Flood Lava Flow Fields on the Plains of Venus

A thesis submitted for the Degree
of
Doctor of Philosophy of the University of London
by
Michael Gavin Lancaster

University of London Observatory Annexe
Department of Physics and Astronomy
University College London
University of London

1994

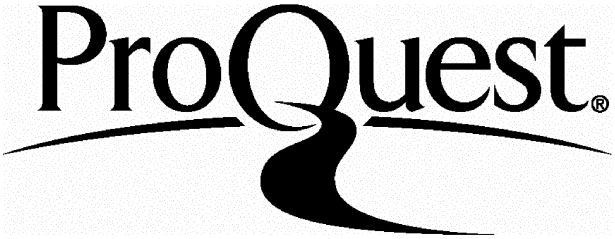

To Mum and Dad

We do not ask for what useful purpose the birds do sing, for song is their pleasure since they were created for singing. Similarly, we ought not to ask why the human mind troubles to fathom the secrets of the heavens...The diversity of the phenomena of nature is so great, and the treasures hidden in the heavens so rich, precisely in order that the human mind shall never be lacking in fresh nourishment.

– Johannes Kepler, *Mysterium Cosmographicum*

Statement of originality of research

I claim originality for the research presented in this thesis, except where the work of other authors is clearly referenced. The work presented in Chapters 3 and 4 is strictly my own, but was conducted as part of a collaborative exercise with K. M. Roberts (also known as K. Magee Roberts and K. P. Magee). In particular I wish to stress that I made the following contributions to the work on great flows (Chapter 3) and Mylitta Fluctus (Chapter 4):

Chapter 3

- Selection of the set of fifty great flows direct from examination of C1MIDRs
- Development of morphological classification scheme
- Measurement of all flow field dimensions, topographic slope and radar backscatter
- Selection of the seven flow fields for detailed examination
- The stratigraphy and detailed description of the fields
- Creation of all maps
- Estimates of eruption rates and durations

Chapter 4

- The regional setting of Mylitta Fluctus and Figure 4.2
- Figure 4.3
- The detailed mapping and stratigraphy of Mylitta Fluctus
- Measurement of all flow field dimensions
- Figure 4.9
- Estimates of eruption rates and durations

The research on Mylitta Fluctus is included in Magee Roberts et al. (1992)*; which is inserted at the back of the thesis. My specific contributions to this paper include Figures 3, 4, and 6, and Tables 1, 2 and 3. Plate 1 (reproduced as Figure 4.5 in this thesis) was the combined work of K. Magee Roberts, J. E. Guest and myself.

*Note that Magee Roberts et al. (1992) is also referred to as Roberts et al. (1992) in the literature.

M G Lancaster

J E Guest

ABSTRACT

The Magellan spacecraft has mapped nearly 99% of the surface of Venus with high resolution synthetic aperture radar (SAR) images, radiometry and altimetry. These data are used to study the characteristics and distribution of volcanic deposits on Venus, specifically the large flood-type lava flow fields, and their relationship to tectonic features. Regional stratigraphy and the nature of plains formation are also investigated. A set of fifty flood-type lava flow fields on Venus with total areas greater than 50,000 km^2 (great flow fields) are analysed. These fields have typical lengths of several hundred kilometres and estimated volumes of 10^3 to 10^4 km^3. The fields have been classed into five morphological types, with the basic distinction being drawn between sheet-like and digitate morphologies. The sheet flow fields may represent single massive volume limited eruptions from laterally extensive fissures, while the digitate fields were formed by the repeated eruption of individual lobate flows. Six eruptive episodes are identified in Mylitta Fluctus, which is studied in detail. Most of the great flow fields may be characterised by extremely smooth pavement-like surface textures, with some occurrences of aa. First order estimates of eruption rate of between 10^5 and 10^6 m^3s^{-1} have been made for typical flow units within the digitate fields. Most of the great flows are associated with zones of lithospheric extension and thinning, and represent comparatively recent volcanism. However, a population of indistinct flows on the plains may represent an extended period of plains resurfacing. The great flow fields are considered to be Venusian analogues of terrestrial flood basalt provinces. A specific regional study of Rusalka Planitia and Atla Regio has indicated three main phases in the geological history of that area, including early tessera formation, widespread plains formation and the burial of tessera, and later mantle upwelling and the formation of coronae, large volcanoes and rift zones.

Global mosaic of Cycle 1 Magellan synthetic aperture radar (SAR) data, centred upon 180° E longitude. The colour is based on image data of the surface returned by Venera 13 and 14. Data gaps are filled with Pioneer Venus topographic data, where available. Eastern Aphrodite Terra runs from left centre to right centre and includes Thetis Regio (left centre), Artemis Chasma (lower left), Dali and Diana Chasmata (lower centre) and Atla Regio (right centre). Rusalka Planitia is located at the centre of the image. The radar-dark areas are associated with impact craters. Image P-39225.

CONTENTS

LIST OF TABLES

LIST OF FIGURES

CHAPTER 1

INTRODUCTION

> Astronomy compels the soul to look upward, and leads us from this world to another.
>
> – Plato, *The Republic*

1.1 AIMS, OBJECTIVES, AND RESEARCH UNDERTAKEN

The Magellan spacecraft has mapped nearly 99% of the surface of Venus with high resolution synthetic aperture radar (SAR) images, altimetry and radiometry. These data allow the volcanic and tectonic characteristics of the entire planet to be studied in unprecedented detail. The main aims of this research were to use the Magellan dataset to study the characteristics and distribution of volcanic deposits on Venus, the relationship between these deposits and tectonic features, and to elucidate regional volcanic and tectonic history. Due to the wealth of information provided by the Magellan dataset, it was decided to focus the analysis on to a specific set of volcanic features and their tectonic associations, rather than attempt a global study of all volcanic deposits and tectonic features. To some extent the direction of research was dictated by those features which were covered during the early stages of the mission, and which proved to be particularly noteworthy of investigation. One such feature was the Mylitta Fluctus lava flow field in southern Lavinia Planitia, which formed the subject of a detailed mapping exercise. Mylitta is one example from a set of particularly extensive flood-type flow fields which exhibit a variety of morphologies and tectonic associations. It was decided that a survey of these features should be undertaken, as they are appear to represent the most recent volcanic activity, provide useful constraints on volcanic style and flow emplacement, and present many examples of the relationships between tectonic and volcanic activity. These fields also give an insight into the nature of plains resurfacing.

In order to place these flow fields and tectonic features into the context of regional geology and stratigraphy, a study and mapping of volcanism and tectonism in eastern Rusalka Planitia and northern Atla Regio was conducted. The region was chosen because it contains most of the types of volcanic and tectonic features observed on Venus, is fully covered by Cycle 1 data, and covers plains as well as highlands. This regional study also forms a link between local volcanic and tectonic activity and more global patterns, providing insight into global volcanic and tectonic history, interior dynamics, and the nature of plains formation.

1.2 LAYOUT OF THE THESIS

The remainder of this introductory chapter gives a background to the Magellan mission, data products and data interpretation. After providing the astronomical background to the planet Venus, Chapter 2 provides a summary of the major geological results obtained from spacecraft exploration of Venus prior to the Magellan mission. Particular emphasis is placed on the understanding of volcanism and tectonism on the planet, and outstanding questions for the Magellan mission are posed. A review of the major results of the Magellan mission at the time of writing is then given. Chapter 3 gives a survey of fifty great flow fields on Venus, discussing both their aggregate properties, and giving more detailed descriptions of seven specific fields. A highly detailed analysis of the Mylitta Fluctus flow field is provided in Chapter 4. A regional study of Rusalka Planitia and Atla Regio is presented in Chapter 5, which includes maps, detailed descriptions and interpretations of volcanic and tectonic features, and a stratigraphic history of the area. The main conclusions of this investigation are brought together in Chapter 6, which also gives suggestions for further research.

1.3 THE MAGELLAN MISSION

1.3.1 Goals

The goals of the Magellan mission were "to improve the knowledge of the geological history of Venus by analysis of the surface morphology and electrical properties and the processes that control them, and to improve the knowledge of the geophysics of Venus, principally its density distribution and interior dynamics", Saunders et al. (1991), p.249. The detailed science objectives are described in Saunders, et al. (1990), and specifically focus on volcanic, tectonic, impact, surficial, isostatic and convective processes. In order to achieve these goals the experimental objectives of the mission were to map at least 70% of the surface with radar imagery at a resolution of better than 300 m (Saunders et al., 1992) and to determine the global topography at a horizontal resolution of about 10 km and a vertical accuracy of 80 m or better (Ford and Pettengill, 1992). In addition the spacecraft tracking data will allow a refinement of the global gravity field of Venus.

1.3.2 Instrumentation

The Magellan spacecraft carries only one scientific instrument, the 12.6 cm wavelength radar system. This radar system is shared between synthetic aperture radar

(SAR), altimetry, and thermal emission radiometry modes. The SAR imaging and thermal radiometry employ a 3.7 m diameter parabolic high-gain antenna, while the altimetry uses a smaller nadir-directed horn antenna (Figure 1.1). The high gain antenna is also shared with the spacecraft's telemetry system, and following a mapping pass it is used to transmit the recorded radar data back to Earth. The spacecraft observing geometry is illustrated in Figure 1.2. In the SAR imaging the cross-track or range resolution is obtained from the time-delay co-ordinate, while the along-track or azimuth resolution is obtained from Doppler-frequency analysis. In this way the time delays and Doppler frequency shifts of the echoes are used to isolate particular areas of the surface.

1.3.3 The Flight

Magellan was launched from the Space Shuttle Atlantis on 5 May 1989 (Figure 1.3), and spent 15 months cruising to Venus. Venus orbit insertion occurred on the 10 August 1990. The spacecraft was placed into an elliptical orbit, with an inclination of 85.5°, a period of 3.26 hours, and a periapsis altitude of 294 km, at 9.9° N (Saunders and Pettengill, 1991). On 15 August 1990 the radar was switched on, and the first test radar images were obtained the following day. These first images had a resolution of 120 m and included the impact crater Golubkina (60.3° N, 286.6° E). Two loss of signal incidents then followed. The first occurred on 16 August 1990 when control was lost for 15 hours, and the second on the 21 August 1990, control being regained after 8 hours (Saunders and Pettengill, 1991). Normal radar mapping operations began on 15 September 1990.

1.3.4 Mapping Strategy

Mission plans called for a sequence of global mapping cycles, each lasting 243 days. Each 243 day period constituted one axial rotation of Venus beneath the spacecraft orbital plane. The first mapping cycle, or primary mission, began on 15 September 1990 during orbit 376 (the first orbit about Venus was designated number 100 for bookkeeping purposes); ending on 15 May 1991. During the primary mission, Magellan acquired 7.3 orbits of image data per day (Saunders and Pettengill, 1991). During each orbit an image swath measuring 20 km x 17,000 km, spanning latitudes 90°N to 70°S, and containing 100 Mb of data was generated. Each swath constitutes the Full Resolution Basic Image Data Record, or F-BIDR (Table 1.1). Cycle 1 images are left-looking and have a variable incidence angle (Figures 1.4 and 1.5) of 15° near the north pole to 45° at periapsis (9.9° N). This variable incidence was chosen to optimise the coverage for resolution of geological features and obtain stereo capability with later cycles (Saunders and Pettengill, 1991). Eighty-four percent of the planet was covered by SAR images during the first cycle

Figure 1.1 Diagram of the Magellan spacecraft as it appears in Venus orbit. After Saunders et al. (1990).

Figure 1.2 Magellan observing geometry for SAR and altimetry data collection. After Saunders et al. (1990).

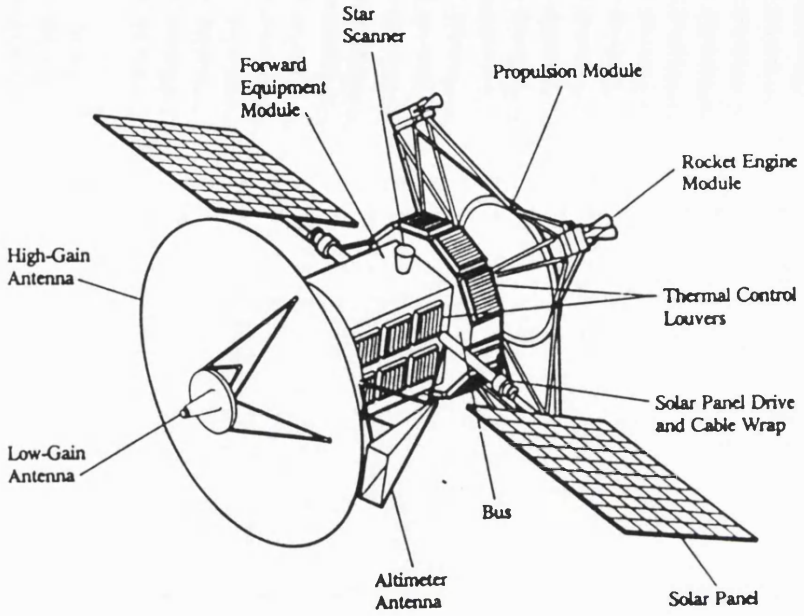
Star
Scanner
Forward
Equipment
Module
Propulsion Module
Rocket Engine
Module
High-Gain
Antenna
Thermal Control
Louvers
Solar Panel Drive
and Cable Wrap
Low-Gain
Antenna
Bus
Altimeter
Antenna
Solar Panel

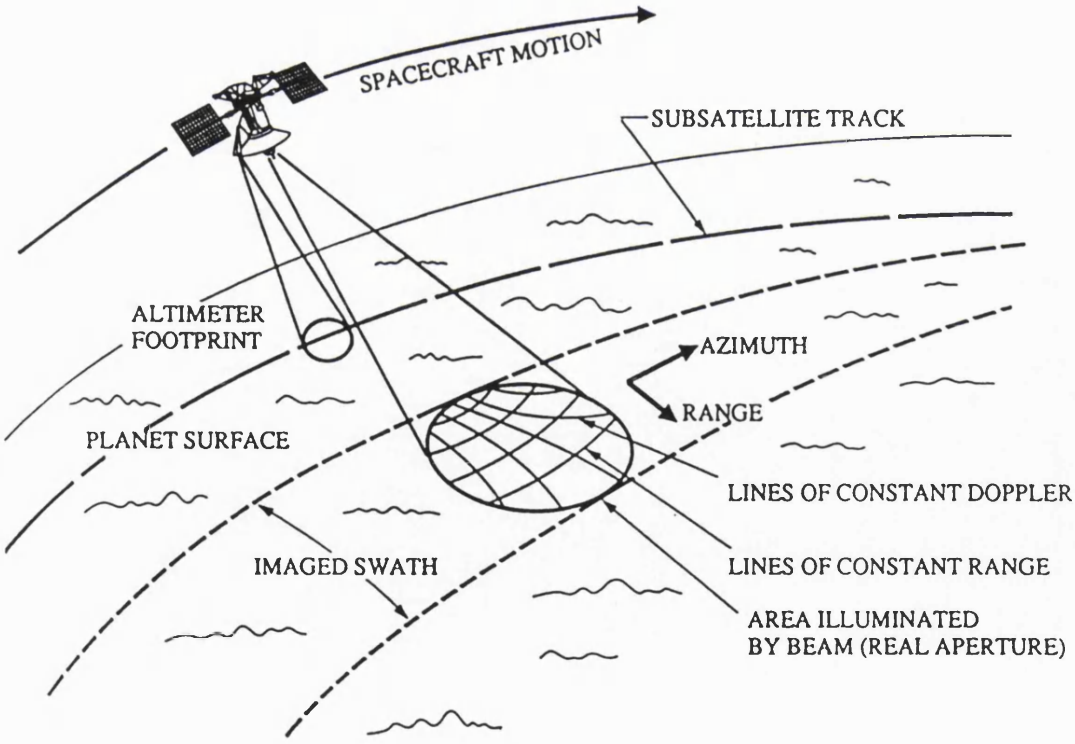
SPACECRAFT MOTION
SUBSATELLITE TRACK
ALTIMETER
FOOTPRINT
AZIMUTH
RANGE
PLANET SURFACE
LINES OF CONSTANT DOPPLER
IMAGED SWATH
LINES OF CONSTANT RANGE
AREA ILLUMINATED
BY BEAM (REAL APERTURE)

Figure 1.3 The launch of Magellan from the Space Shuttle Atlantis on 5 May 1989.


USA

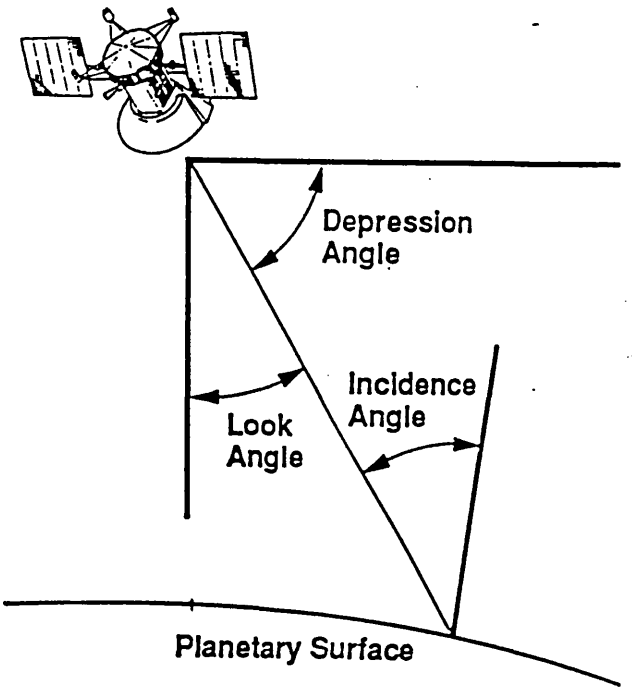

LEFT-LOOKING NOMINAL

(Incidence Angle vs. Latitude)

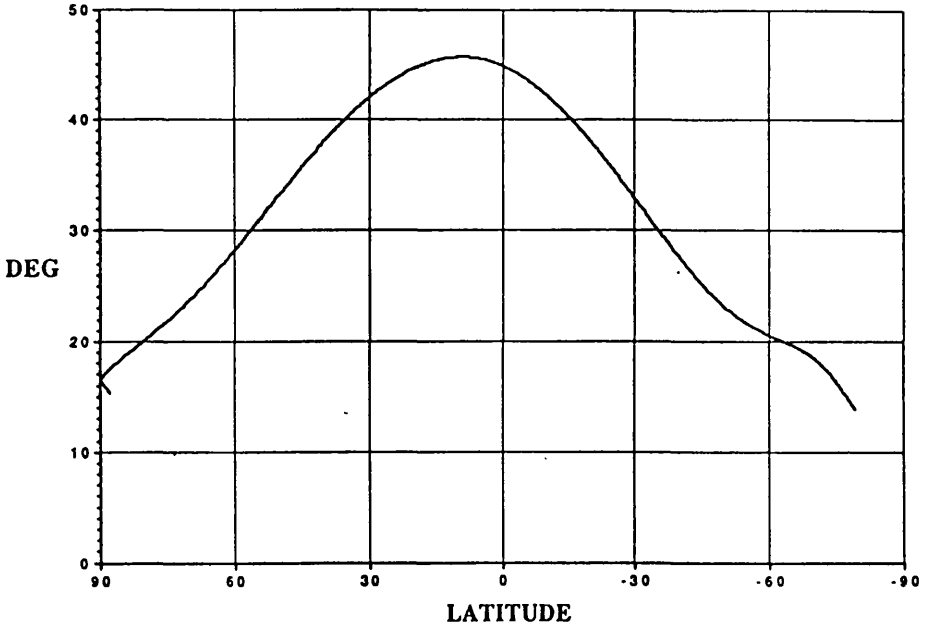

Table 1.1 Magellan data products.

Acronym	Product	Area	Resolution
F-BIDR	Full Resolution Basic Image Data Record	20 x 17000 km	75 m/pixel
F-MIDR	Full Resolution Mosaicked Image Data Record	5° x 5°	75 m/pixel
C1-MIDR	Compressed-Once Mosaicked Image Data Record	15° x 15°	225 m/pixel
C2-MIDR	Compressed-Twice Mosaicked Image Data Record	45° x 45°	675 m/pixel
C3-MIDR	Compressed-Thrice Mosaicked Image Data Record	120° x 120°	2025 m/pixel
GEDR	Global Emissivity Data Record	Global	5 km/pixel
GREDR	Global Reflectivity Data Record	Global	5 km/pixel
GSDR	Global Slope Data Record	Global	5 km/pixel
GTDR	Global Topographic Data Record	Global	5 km/pixel

(Saunders et al., 1992). Data gaps were caused by superior conjunction, Earth occultation, the inability to image the south polar region with left-looking radar, and tape recorder and pointing problems (Saunders and Pettengill, 1991).

The Extended Mission consisted of all activity beyond Cycle 1, and included two further radar mapping cycles and the collection of high resolution gravity data. Cycle 2 mapped approximately 50% of the planet with right looking gap filling sequences between May 15, 1991 and January 15, 1992, bringing the global coverage to 97% (Saunders et al., 1992). Cycle 3 lasted from January 15 to September 15, 1992, and covered 21.3% of the surface with left-looking images at smaller incidence angles than Cycle 1, in order to provide some stereo coverage. An additional 2% of the planet was imaged with the Cycle 1 incidence profile to fill in the last major gap in coverage during the last part of this cycle, bringing the total coverage to 99% (Thompson et al., 1993). By high resolution Doppler tracking of the spacecraft in elliptical orbit, Mission Cycle 4 (15 September 1992 to 24 May 1993) provided gravity observations of Venusian near-equatorial regions which were reduced to a 60° by 60° spherical harmonic field (Thompson et al., 1994). In order to allow the collection of global high resolution gravity data, the orbit of the Magellan spacecraft was circularised by an aerobraking procedure between late May and early August 1993. At the time of writing Magellan is in a near-circular orbit about Venus, and is providing gravity measurements with a nearly uniform resolution.

1.4 DATA PRODUCTS AND INTERPRETATION

1.4.1 SAR Images

Magellan data products are listed in Table 1.1. The F-BIDRs were mosaicked into Full-Resolution Mosaicked Image Data Records or F-MIDRs. Each F-MIDR covers 5° x 5° and has a resolution of 75 m/pixel (representing a slight oversampling of the original data). During the early stages of Cycle 1, 29 initial F-MIDRs were produced to target specific areas of interest including Maxwell Montes, Sif and Gula Mons, and Alpha Regio (Saunders and Pettengill, 1991). The remaining F-MIDRs and other SAR mosaics were placed at pre-determined positions on the planet. These other mosaics comprise a series of products of increasing area and decreasing resolution, covering 15° x 15°, 45° x 45°, and 120° x 120° regions, with resolutions of 225 m, 675 m. and 2025 m per pixel respectively (Table 1.1, Figure 1.6). They are known as C1, C2 and C3-MIDRs respectively, with C1, C2, and C3 standing for compressed once, twice and thrice. These products have been produced in various numbers and locations for all 3 mapping cycles. Each product is identified in the general form of PxxHyyy;C, where P denotes the type of photoproduct (F, C1, C2 or C3), xx stands for the approximate centre latitude in degrees, H represents the hemisphere (N for north, S for south), yyy is the centre longitude and C denotes the cycle

Figure 1.6 Magellan SAR image data products and their coverage. After Saunders et al. (1990).

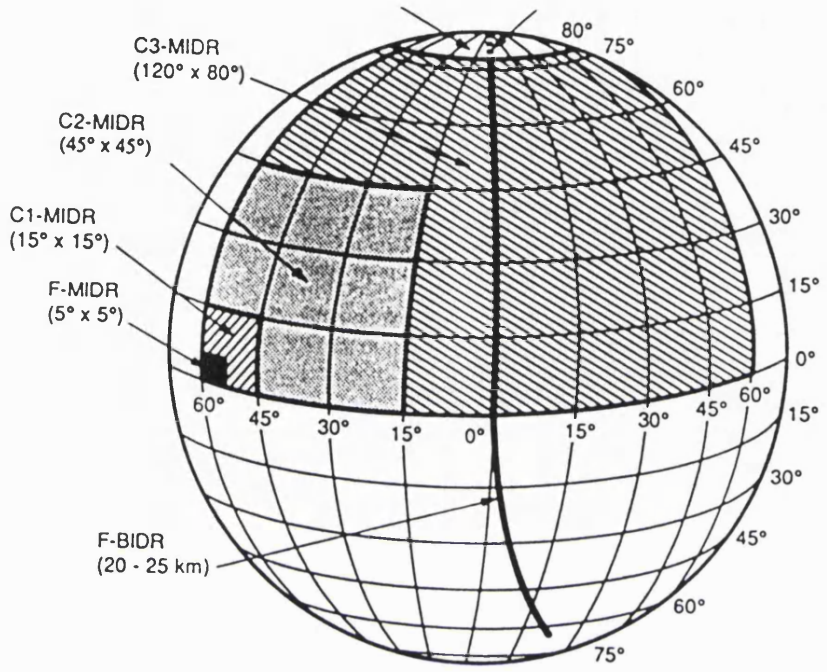
C3-MIDR
(120° x 80°)
C2-MIDR
(45° x 45°)
C1-MIDR
(15° x 15°)
F-MIDR
(5° x 5°)
F-BIDR
(20 - 25 km)
80°
75°
60°
45°
30°
15°
0°
15°
30°
45°
60°
75°

(1, 2 or 3). For example, C115N197;1 denotes a Cycle 1 C1-MIDR which is approximately centred on 15° N, 197° E.

"Realworld" pixel values in the F-BIDRs represent the actual observed radar backscatter coefficient value σ_{obs} (or *specific radar backscatter*) normalised to an empirically derived backscatter model (Muhleman, 1964; Pettengill et al., 1988) that describes the average backscatter σ_{Muh} as a function of incidence angle θ. The "realworld" pixel values are expressed in decibels (dB) such that:

$$\text{Pixel value in dB} = 10 \times \log_{10}(\sigma_{obs}/\sigma_{Muh}) \qquad \text{Eq. 1.1}$$

The relationship between the "realworld" pixel values and image brightness (pixel DN) is given by the expression (Saunders et al., 1992):

$$\text{Pixel value in dB} = 0.2\ (\text{pixel DN} - 101) \qquad \text{Eq. 1.2}$$

The 8 bit pixel DN values range from 1 to 251, with 0 and 252 to 255 reserved as marker flags. A pixel value of 101 corresponds to a measured backscatter which is equal to that of the model. The backscatter model employs the Muhleman function (Muhleman, 1964) as follows:

$$\sigma_{Muh} = K_1 \cos\theta/(\sin\theta + K_2\cos\theta)^3 \qquad \text{Eq. 1.3}$$

where the constants $K_1 = 0.0188$ and $K_2 = 0.111$ are empirically derived from Pioneer-Venus results and describe the radar scattering behaviour of the "average" Venus surface (Pettengill et al., 1988). However, the SAR processor was implemented with an erroneous value for K_1 of 0.0118, and a further error was introduced such that a value of $(\theta + 0.5°)$ was used instead of θ. Thus the pixel values in the F-BIDRs are based on an approximation of the intended backscatter function (Saunders et al., 1992; Figure 1.7) such that:

$$\sigma_{Muh} = 0.0118\cos(\theta + 0.5°)/[\sin(\theta + 0.5°) + 0.111\cos(\theta + 0.5°)]^3 \qquad \text{Eq. 1.4}$$

Brightness variations in the Magellan SAR images result from three different surface properties: (1) topography, (2) roughness, and (3) electrical properties. The radar incidence angle and/or illumination direction also influence the extent to which each of these factors affect the image brightness. The effect of topography is such that slopes that face towards the radar sensor appear bright and spatially compressed relative to slopes that

Figure 1.7 Plot of the average radar backscatter against incidence angle prescribed by the correct and incorrect Muhleman formulas. Magellan SAR data employed the incorrect formula. After Michaels (1992).

Figure 1.8 Radar backscatter versus incidence angle for surfaces with different roughnesses. Differences in topographic slope dominate the backscatter for incidence angles less than about 25°. After Ford et al. (1989).

CORRECT AND INCORRECT MUHLEMAN FORMULAS

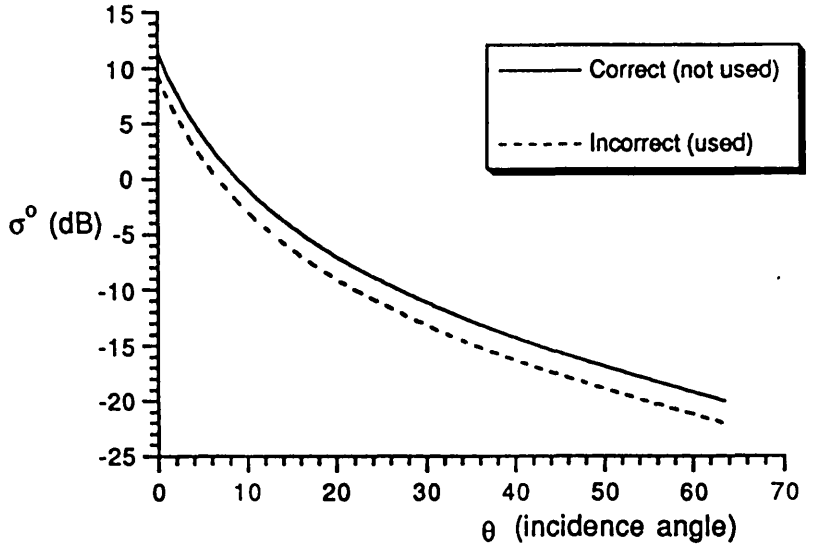

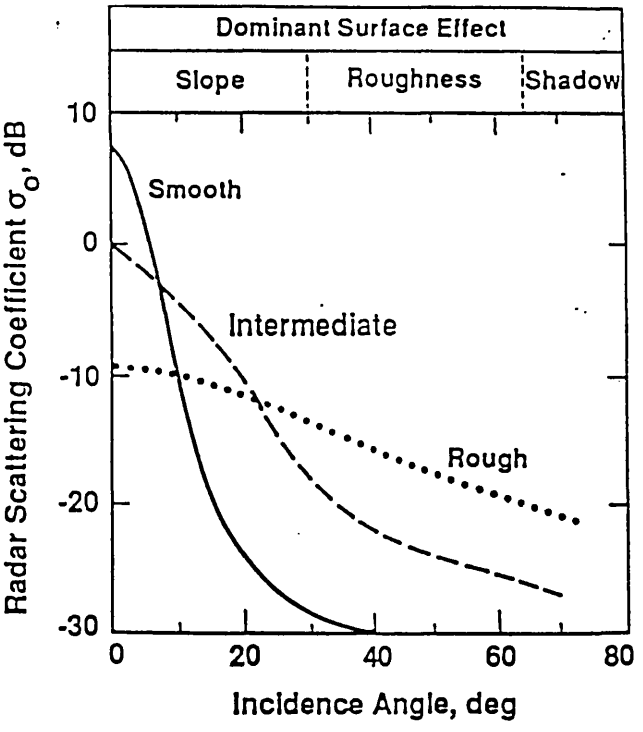

face away, which appear dark and spatially expanded. Figure 1.8 plots radar backscatter as a function of incidence angle for three different surfaces with varying degrees of roughness. Each surface is characterised by a particular curve or scattering law. A flat scattering law is consistent with an extremely rough surface, while a steep scattering law implies a smoother surface. Where incidence angles are less than about 25°, small changes in slope give large changes in backscatter. In the absence of topographic effects the surface roughness at the scale of the radar wavelength may dominate the backscatter when the incidence angle is between about 25° and 60° (Figure 1.8). In the Magellan images rough surfaces have notably higher backscatter than smooth surfaces, even though the data have been normalised to the average backscatter of Venus. In addition to the effects of topography and surface roughness, the intrinsic reflectivity of the surface can have a major effect on image brightness. A surface with a given roughness and an intrinsically high reflectivity will have a higher absolute backscatter than the same surface with a lower intrinsic reflectivity (see Section 1.4.2).

1.4.2 Altimetry and Radiometry

The altimeter, with its nadir-looking geometry, is designed to precisely determine the distance between the spacecraft and the surface directly below. The size of the surface footprint illuminated by the altimeter varies with altitude between about 10 km and 30 km, between 10° N and 80° N respectively. A typical altimetry orbit consists of about 1000 footprints. An echo "profile", representing the strength of the received echo as a function of time delay, was generated for each footprint (Pettengill et al., 1991; Ford and Pettengill, 1992). For relatively flat surfaces most of the echo power is received in a short time, producing a sharp peak in the echo profile. More complex and broader echo profiles are produced by surfaces with topographic undulations which vary rapidly at scales larger than the radar wavelength. Before Magellan arrived at Venus a library of altimeter echo profiles or "templates" was developed (Ford and Pettengill, 1992). Each template gives the predicted response of a surface with three known parameters: the distance from the spacecraft, the root-mean-square (rms) slope of surface undulations at scales greater than the radar wavelength, and the intrinsic Fresnel reflectivity of the surface. During data processing the three parameters are found for each footprint by matching the best template to the observed profile. The distance is determined by the position of the strongest peak in the profile, the rms slope from the dispersion of the echo in time, and the reflectivity from the overall strength of the echo. The templates are derived from the Hagfors scattering function (Hagfors, 1970), which predicts the intensity of radar backscatter as a function of incidence angle θ, Fresnel reflectivity ρ, and a large-scale roughness parameter C:

$$\sigma^0 = (\rho C/2)(\cos^4\theta + C\sin^2\theta)^{-3/2}$$

Eq. 1.5

The roughness parameter is equivalent to 1/(rms slope in radians)^2. This scattering function has proven to be appropriate for most of the surface of Venus at the near-nadir incidence angles (less than about 15°) employed by the altimeter.

Fresnel reflectivity is a measure of the efficiency of a surface in reflecting electromagnetic radiation. A reflectivity of 1.0 represents perfect, total reflection. Typical plains regions on Venus have a reflectivity of about 0.1. Reflectivity is an intrinsic property of the surface material, and is related to the dielectric constant (e) of the surface:

$$\rho = [(1-\sqrt{e})/(1+\sqrt{e})]^2$$

Eq. 1.6

In practice, sub-wavelength roughness tends to randomly scatter a nadir-pointing signal, diminishing the received echo power (Pettengill et al., 1988). If this scattering effect is not taken into account, a rough surface will appear to have a lower reflectivity than a smooth surface composed of the same material. The SAR backscatter cross section is used to estimate the amount of random scattering within each altimeter footprint, and a correction is applied to the reflectivity derived from the template matching procedure. The rms slope quantifies the topographic undulation of the terrain at scales of tens of centimetres to a few kilometres. Rms slopes derived from Magellan altimetry are typically in the range of 1 to 3° for plains regions, and may be as high as 10° for highly fractured tectonic terrains.

The radiometry experiment used the high gain antenna in a passive mode to detect thermal radiation emitted from the surface at radio wavelengths (Pettengill et al., 1992). The amount of radiation emitted, or radiance, depends on the surface temperature and emissivity, and is expressed by Stefan's Law:

$$R = \sigma e T^4$$

Eq. 1.7

where R = total radiance in Wm^{-2}.

$\sigma = 5.67 \times 10^{-8}\ Wm^{-2}K^{-4}$ (Stefan-Boltzmann Constant)

e = emissivity

T = temperature, K

Magellan acquired the radiance measurements, while the surface temperature was assumed to be a well-behaved function of surface elevation, allowing the surface emissivity to be derived. Emissivity is a measure of how well the surface approaches a perfect

blackbody radiator, and is primarily controlled by the dielectric constant. Emissivity ranges from 0 to 1, and is the complement of reflectivity, although in practice the sum of these two quantities ranges between 0.90 and 0.95 in Magellan data (Ford et al., 1993). The mean surface emissivity observed by Magellan is 0.845, which corresponds to a dielectric constant of about 4.0 (Pettengill et al., 1992). Like the altimetry, the size of the emissivity footprint varies with latitude and ranges between about 20 and 80 km.

The altimetry and radiometry data are available in the form of two products: the Altimetry-Radiometry Composite Data Record (ARCDR) and the Global Data Record (GxDR). The ARCDR is a non-image data set that contains the derived values of planetary radius, rms slope, reflectivity, and emissivity for each altimeter and radiometer footprint. Latitude and longitude are provided in the ARCDR data to allow identification with features seen in the image data. The GxDR takes the form of a global image map of topography (GTDR), rms slope (GSDR), reflectivity (GREDR), and emissivity (GEDR), Table 1.1. The GxDR maps are given in several map projections on CD-ROM at a full resolution of 5 km/pixel. The map projections include a global sinusoidal equal area projection, a Mercator projection between latitudes 65° N and 65° S, and north and south polar stereographic projections extending to 47° north and south respectively. The Mercator and polar stereographic projections of the GTDR are shown in Figure 1.9.

1.4.3 Data Availability and Image Processing Facilities

A wide range of photographic and digital data was accumulated at the University of London Observatory Regional Planetary Image Facility during the course of the research and the Magellan mission. SAR images were most readily available in the form of 10" x10" photoproducts (including both prints and negatives) of F-MIDRs and C-MIDRs. These products are produced in sinusoidal equal area projection, are contrast enhanced, and framed by margins giving latitude and longitude. The bulk of the data analysis was carried out using the C1-MIDRs, as these were available for the whole of Cycle 1 and provided a convenient scale for the analysis and mapping of geological features. Higher resolution views were provided by the F-MIDR photoproducts, but only a limited part of Cycle 1 was available in this format due to the budgetary constraints of the mission. However, enlargements of particular areas or features were frequently made from the set of 10" x 10" C1-MIDR negatives. A small number of 20" x 20" prints of selected F and C1-MIDRs covering particular features were also at hand, as were two 40" x 40" prints covering the Mylitta Fluctus lava flow field (C160S347 and C145S350). Altimetry and radiometry photoproducts included a number of contour plots, and colour and greyscale images of topography, rms slope, reflectivity and emissivity of a limited number of regions. These regions coincided with a selection of F-MIDRs and C1-MIDRs, and the products included some contour and colour-scale overlays of altimetry and radiometry data on SAR

Figure 1.9 Magellan Global Topographic Data Record (GTDR) in Mercator and polar stereographic projections.

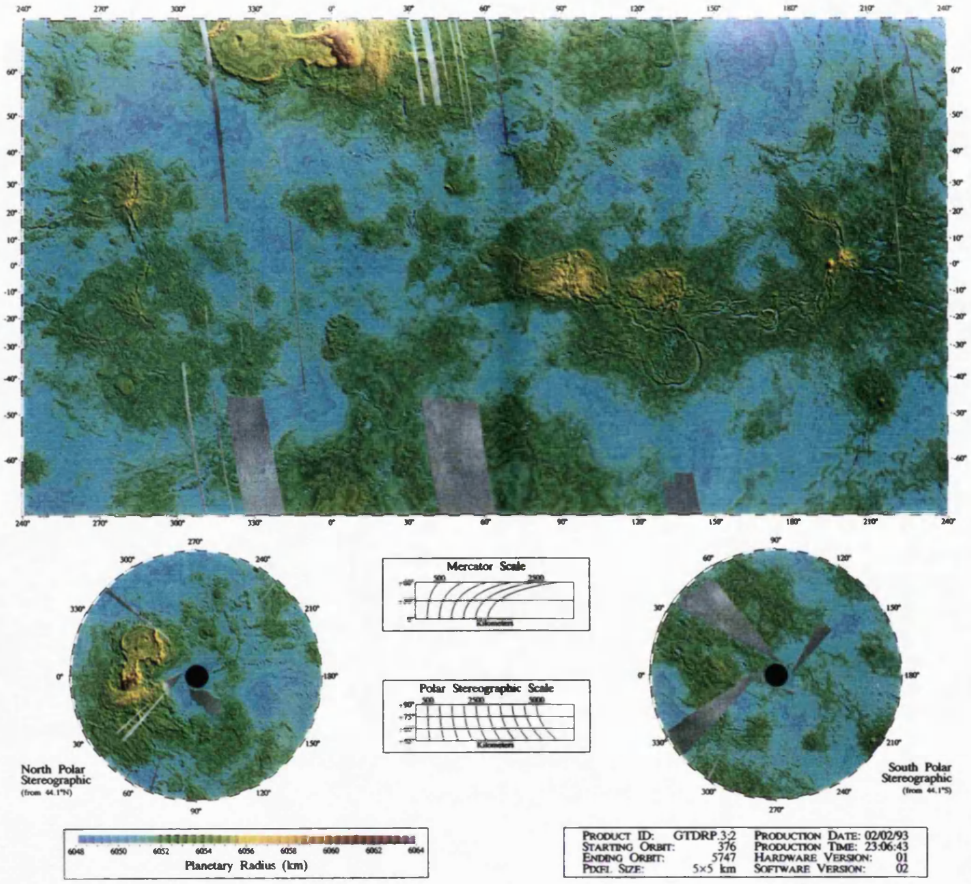
Mercator Scale
Polar Stereographic Scale
North Polar Stereographic
South Polar Stereographic
Planetary Radius (km)
6048 6050 6052 6054 6056 6058 6060 6062 6064
PRODUCT ID: GTDRP.3-2
STARTING ORBIT: 376
ENDING ORBIT: 5747
PIXEL SIZE: 5×5 km
PRODUCTION DATE: 02/02/93
PRODUCTION TIME: 23:06:43
HARDWARE VERSION: 01
SOFTWARE VERSION: 02

images. In addition to all these photoproducts, a wide range of special products were also available. These special products are mainly SAR images of specific features of interest such as impact craters or large volcanoes, and some altimetry, radiometry, and perspective views.

The F-MIDR, C-MIDR, and GxDRs were also available in digital form on Compact Disk Read-Only-Memory (CD-ROM). Each F or C1-MIDR is stored on the CD-ROM as 56 individual framelets. Each framelet is a 1024 line x 1024 sample section of the complete 7168 line x 8192 sample mosaic. The framelets are accompanied by a 1/8 th scale browse version of the MIDR measuring 896 lines x 1024 samples. The SAR images are un-enhanced and in sinusoidal equal area projection. All the GxDRs were available on a single CD-ROM, with each GxDR stored as framelets and a browse version. In addition the ARCDR data were available on 17 CD-ROMs.

In order to access the data contained on the CD-ROMs, two main computer platforms were used. A Sun Sparcstation running General Image Processing System (GIPS) software (Ford, 1992) constituted the main platform for browsing, enhancing, and analysing Magellan image data on-screen. The second platform was an Apple Macintosh computer running NIH Image version 1.45. In addition to these facilities some use was made of the IMDISP image processing software provided on Planetary Data System (PDS) CD-ROMs and implemented on an IBM compatible personal computer.

CHAPTER 2

THE EXPLORATION AND GEOLOGICAL UNDERSTANDING OF VENUS - A REVIEW

There was the Door to which I found no Key;
There was the Veil through which I might not see.

– Omar Khayyam

2.1 THE PLANET VENUS

Venus attains the brightest apparent magnitude of any planet visible from the Earth's surface, and has received much attention since Galileo turned his small telescope towards the planet in 1610. Galileo was the first to record the changing phases of the planet, noting that these were comparable to those displayed by the Moon, and that Venus was therefore not self-luminous. Observation through the following centuries revealed that Venus has approximately the same size and mass as the Earth, and is our nearest planetary neighbour (Table 2.1). Because of these similarities in bulk properties and distance form the sun, Venus has been referred to as Earth's twin. However, ground-based and spacecraft measurements during this century have disclosed a planet with radically different surface and atmospheric conditions from those of the Earth (Table 2.1). Nevertheless, much of our geological understanding of Venus is based on comparisons with the Earth.

It was realised during the latter part of the eighteenth century that Venus was surrounded by an extensive atmosphere. Improvements in instrumentation failed to reveal any permanent markings that could be attributed to surface features, and led to the conclusion that the planet is covered in a perpetual cloud layer. The composition of the atmosphere remained unknown until the 1930s, when spectroscopy and infrared radiometry divulged the presence of massive amounts of carbon dioxide. Polarimetric and spectroscopic measurements conducted during the 1970s revealed that the clouds were composed of sulphuric acid droplets, and disclosed the presence of sulphur dioxide within the atmosphere. From the tracking of cloud features, the atmosphere was found to rotate with a period of 5 days.

The advent of radio and radar astronomy in the late 1950s enabled the first measurements of the solid body of Venus to be obtained. The planet was found to emit a substantial radio flux, from which a brightness temperature of approximately 600 K was determined, indicating an extremely hot surface and lower atmosphere. These

Table 2.1 Comparison of the physical properties of Venus and Earth. Modified from Beatty et al. (1981).

Property	Venus	Earth
Mean distance from Sun	108.2×10^6 km	149.6×10^6 km
Orbital period	224.701 days	365.265 days
Sidereal rotation period	243.01 days retrograde	23.93 hours
Obliquity	-2.6°	23.45°
Mass	4.871×10^{24} kg	5.976×10^{24} kg
Mass (Earth = 1)	0.81503	1.0000
Equatorial radius	6051.3 km	6378 km
Equatorial radius (Earth = 1)	0.949	1.000
Mean density	5.24 g/cm^3	5.52 g/cm^3

measurements agreed with theoretical predictions extrapolated from cloud top temperatures, and a surface pressure of several tens of bars was indicated. A hot surface was later confirmed by measurements of limb darkening at microwave wavelengths obtained by the Mariner 2 spacecraft in 1962. Major investigations into the role of CO_2 in heating the planet via the greenhouse effect were also made at this time. In addition the early radar studies revealed that the solid body of Venus rotates with a period of 243 terrestrial days in a retrograde direction. Coupled with the orbital motion of Venus about the sun this rotation yields a venusian day equal to 116.75 earth days. During the 1970s and 1980s the Goldstone and Arecibo radar observatories obtained images of the Earth-facing part of Venus with a spatial resolution of up to 1 to 2 km (Goldstein, et al., 1976, 1978; Campbell and Burns, 1980; Campbell et al., 1989). Together with the Pioneer Venus and Venera 15/16 data (see below), these images provided the framework upon which the further interpretation of surface features on Venus from Magellan images could proceed. The geological understanding of Venus that has emerged both prior to and from Magellan is discussed in detail in the next sections.

2.2 THE PRE-MAGELLAN GEOLOGICAL UNDERSTANDING OF VENUS

2.2.1 Spacecraft exploration prior to Magellan

The first successful flyby of Venus was achieved by Mariner 2 in 1962. This probe confirmed the high surface temperature and disclosed the absence of a magnetic field. Venera 4 was the first probe to enter the Venus atmosphere during 1967, and was followed by the Mariner 5 flyby, and the Venera 5 and 6 entry missions between 1967 and 1969. Venera 7 achieved the first soft landing in 1970, and was followed by seven successful landers of the Venera and Vega series between 1972 and 1984. These landers returned surface images and data on the physical properties and composition of surface materials at sites near Beta Regio and in Aphrodite Terra. Meanwhile Mariner 10 provided detailed images of the atmosphere in visible and ultraviolet wavebands in 1974, confirming a cloud circulation rate of 5 days.

In 1978 the Pioneer Venus Orbiter (PVO) mapped the surface of Venus with low resolution radar images between 40° N and 10° S. Altimetry data was recovered between 78° N and 63° S, with a vertical resolution exceeding 200 m, and a spatial resolution of better than 150 km (Pettengill et al., 1980). A global relief map of Venus derived from PVO data is provided in Figure 2.1, while a corresponding contour map with named features is given in Figure 2.2. Pioneer Venus also mapped the gravity field of Venus and was accompanied by several entry probes. Major results are given in Masursky et al. (1980) and Pettengill et al. (1980). Pioneer Venus was followed by the Venera 15 and 16 orbiters in 1983, which mapped the surface with radar images at a resolution of 1 to 2 km

Figure 2.1 Global relief map of Venus in Mercator projection obtained by the Pioneer Venus Orbiter. The colours correspond to the contour levels indicated in the bar at right. The spatial resolution of the map varies from 100 to 200 km. After Pettengill et al. (1980).

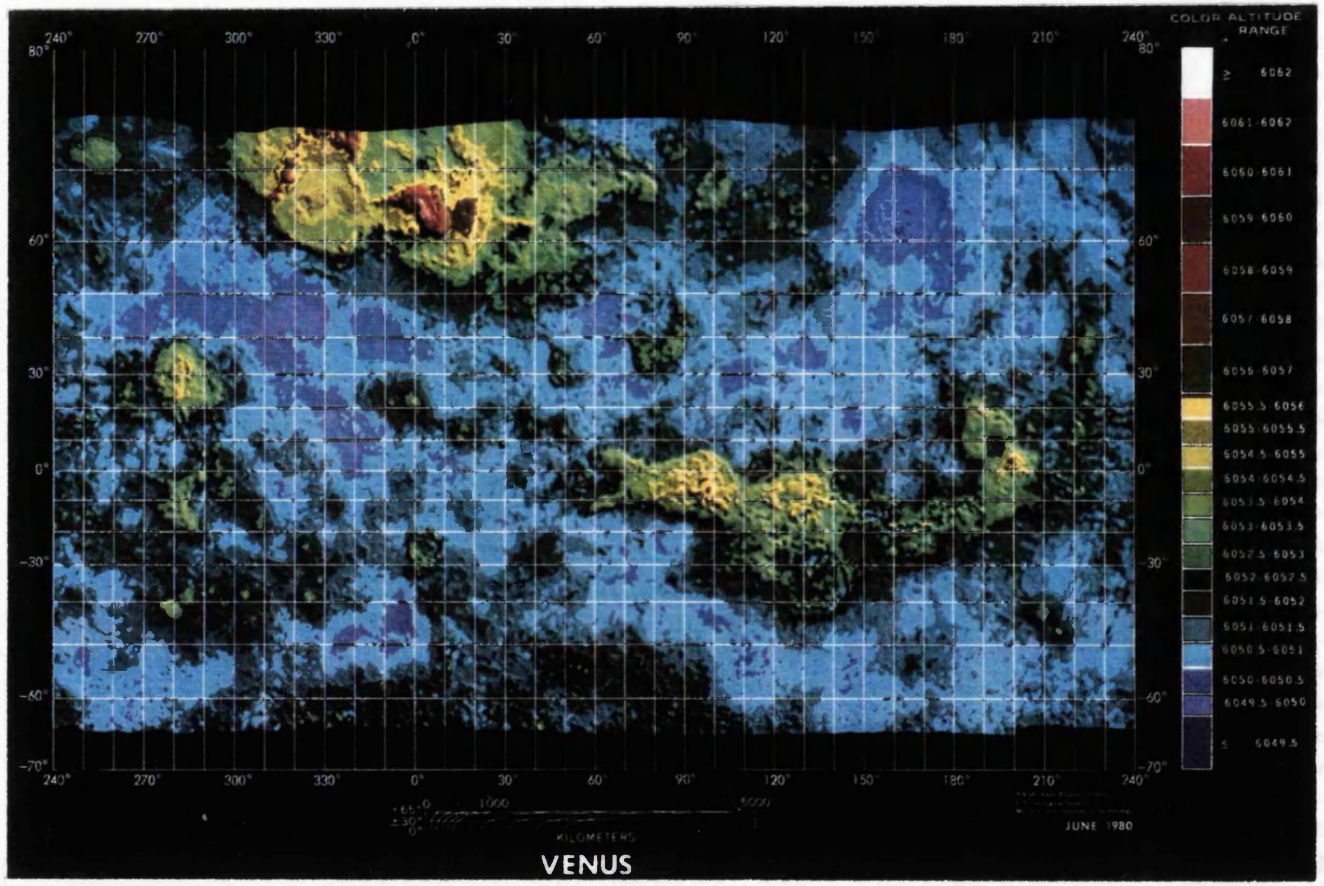
COLOR ALTITUDE RANGE
≥ 6062
6061-6062
6060-6061
6059-6060
6058-6059
6057-6058
6056-6057
6055.5-6056
6055-6055.5
6054.5-6055
6054-6054.5
6053.5-6054
6053-6053.5
6052.5-6053
6052-6052.5
6051.5-6052
6051-6051.5
6050.5-6051
6050-6050.5
6049.5-6050
≤ 6049.5
240° 270° 300° 330° 0° 30° 60° 90° 120° 150° 180° 210° 240°
80° 60° 30° 0° -30° -60° -70°
1000
5000
KILOMETERS
JUNE 1980
VENUS

Figure 2.2 Contour map of Venus from Pioneer Venus data. Contour interval is 1 km and the datum is at 6051.0 km. Major surface features are named and the positions of the Venera 8, 9, and 10 landers are shown by triangles. After Masursky et al. (1980).

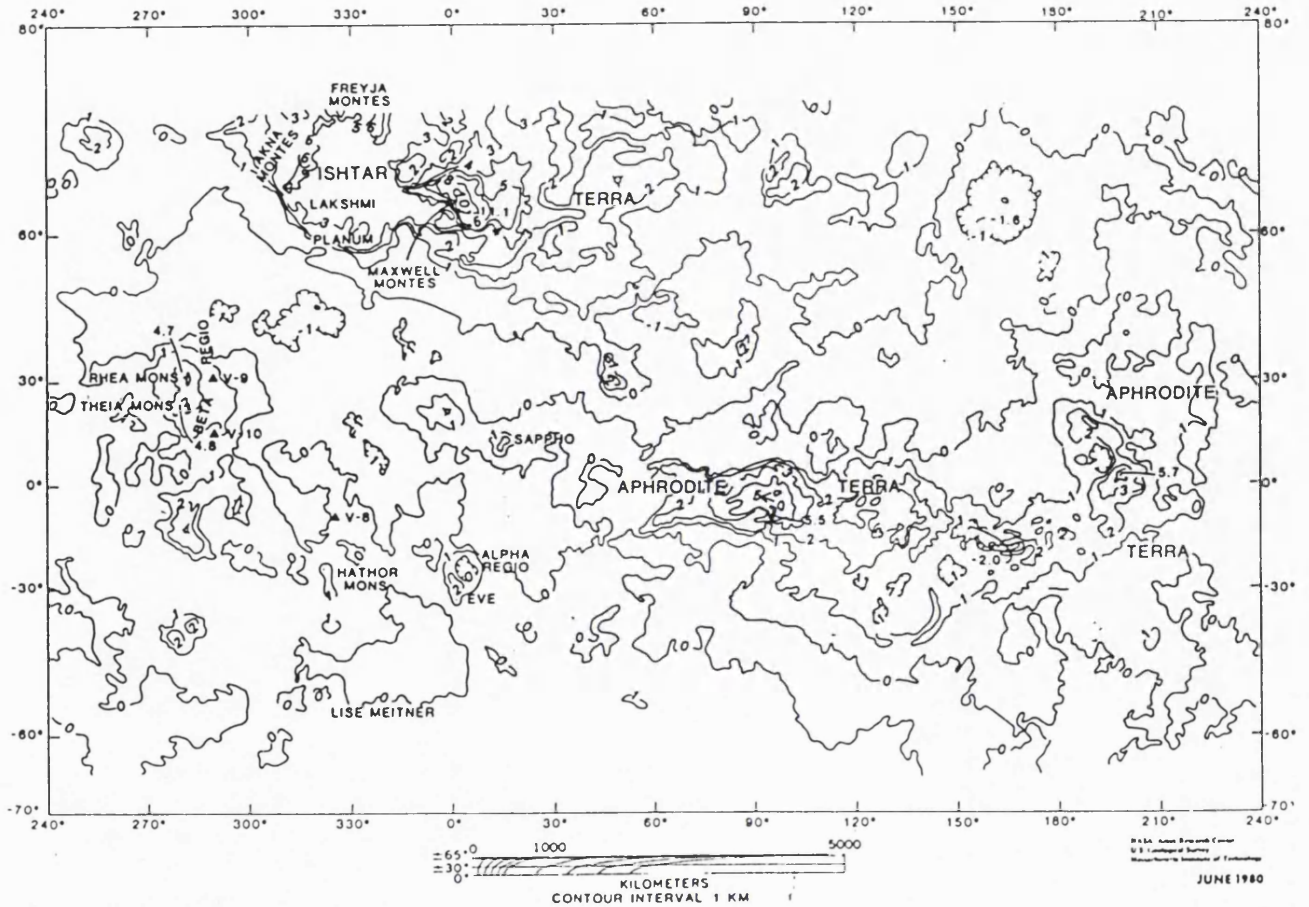

CONTOUR MAP OF VENUS

between 78° N and 30° N. Altimetry with a vertical resolution of 50 m over a footprint size of 40-50 km was also obtained. The geology and geomorphology of the surface as revealed by the Venera 15 and 16 missions are described by Barsukov, et al. (1986a), Basilevsky, et al. (1986), Ivanov, et al. (1986), Basilevsky and Head (1988), and Schaber (1990).

2.2.2 Physiography and Topography

Pioneer Venus data revealed the planet to consist of 65% rolling plains, 27% lowlands, and 8% highlands (Figure 2.1; Masursky et al., 1980). In contrast to the unimodal distribution of surface elevation on the Earth, the elevations on Venus exhibit a bimodal distribution (Pettengill, et al., 1980). The physiography is dominated by the high latitude uplands of Ishtar and Lada Terrae, the equatorial highlands of Aphrodite Terra, Eistla, Beta and Atla Regiones, and the mid-latitude lowland planitiae (Figure 2.2). Ishtar contains the highest mountains on Venus, Maxwell Montes, which rise to 11 km above a datum of 6051.0 km.

In contrast to the Earth, the long wavelength gravity and topography were found to be strongly correlated (Phillips et al., 1981; Sjogren et al., 1983; Bills et al., 1987). This correlation indicates that the highlands are isostatically compensated, as a result of either passive support through crustal thickening or dynamic support by mantle upwelling (Masursky et al., 1980).

2.2.3 Surface Environment and Composition

There were a total of seven geologically useful landings between 1972 and 1984; the Venera 8, 9, 10, 13 and 14 missions, and Vega 1 and 2. Venera 9, 10, 13, and 14 provided television panoramas allowing the surface morphology in the vicinity of the lander to be determined (Florensky et al., 1977; Basilevsky et al., 1985). Venera 9 landed on a 30° slope, densely covered by decimetre sized rocks with loose soil between them. Veneras 10, 13, and 14 recorded squat, flat topped outcrops of bedded rocks, with variable amounts of loose soil in between. The surface environmental conditions as measured by the Venera and Vega landers were a temperature of 475 K, an atmospheric pressure of 90 bar, and a wind velocity of up to 1 $m.s^{-1}$.

The composition of the surface was measured at the seven landing sites by either gamma-ray spectroscopy (Venera 8, 9 and 10, and Vega 1 and 2), or x-ray fluorescence (Venera 13 and 14, and Vega 2). Venera 9, 10, 14, and Vega 1 and 2 found compositions consistent with tholeiitic basalt. Venera 13 measurements suggested a subalkaline basalt, while Venera 8 compositions were more akin to alkaline basalts, shoshonites and syenites.

Nikolayeva (1990) has concluded that the Venera 8 material has a quartz monzonite-quartz syenite affinity resembling Earth's continental crust. The surface material measured by the Venera landers was friable and porous, with a bearing capacity of 40-50 $Mg.m^{-2}$. The density of the material was 1.4-1.5 $Mg.m^{-3}$, except at the Venera 10 site where it was as high as 2.8 $Mg.m^{-3}$, Basilevsky et al. (1985).

Sedimentary processes appear to be relatively unimportant on Venus. The lack of water and thermal cycling means little chemical or physical weathering occurs, and the dense atmosphere blocks the passage of small meteoroids which would otherwise produce a regolith. Impact craters, tectonics and limited pyroclastic volcanism may nevertheless provide local sources of sediment, which may then be transported by aeolian activity (Greeley and Arvidson, 1990). Only a small proportion of the surface appears to have a significant thickness of soil deposits (Pettengill et al., 1988; Bindschadler and Head, 1988).

2.2.4 Volcanism

Pre-Magellan data has revealed that volcanic deposits form more than 70% of the surface which was well imaged. The regional plains were interpreted to be of volcanic origin (Sukhanov et al., 1989) on the basis of their regional topography and smoothness, associated lava flows and abundant small volcanoes. The small volcanoes include shields and domes with diameters of several km to 15-20 km, and often occur in clusters (Sukhanov et al., 1989; Aubele and Slyuta, 1990). Veneras 15 and 16 mapped 800 volcanoes in the 20 to 100 km diameter size range (Slyuta and Kreslavsky, 1990), and with Arecibo observations revealed 50 volcanic centres greater than 100 km in diameter, including shields and calderas (Slyuta, 1990; Sukhanov et al., 1990; Schaber, 1991). Large volcanic centres associated with topographic rises are discussed in a separate section below. Lava flow fields were identified on the plains in both Venera 15 and 16 and Arecibo data. Radar-bright and dark lava flows were identified in Venera 15 and 16 images of northern Sedna Planitia by Barsukov et al. (1986), and Arecibo images revealed flow fields in the southern hemisphere including Mylitta Fluctus (Campbell et al., 1991; Senske et al., 1991a; Chapter 4). Barsukov et al. (1986) concluded that the plains themselves are essentially the product of flooding by basaltic lava.

2.2.5 Volcanic Rises and Rift-Zones

The largest scale tectono-volcanic features on Venus are the volcanic rises. Collectively they form the equatorial highlands (Phillips et al., 1981), including Aphrodite Terra, Asteria, Beta, Atla, Eistla, and Phoebe Regiones (Figure 2.2). They occur in linear to arcuate belts and individual rises are circular to quasi-circular in plan, and have

diameters of 1000 to 3000 km (Sukhanov et al., 1989; Campbell et al., 1989; Stofan and Saunders, 1990; Senske, 1990). They occur both as broad types, such as those in Beta, Bell, and Atla Regiones, and as plateau-like features such as Ovda and Thetis Regiones. The rises are commonly associated with rift zones, large volcanoes and lava flow fields (McGill et al., 1981; Schaber, 1982; Campbell et al., 1984; Campbell et al., 1989;. Campbell and Campbell, 1990; Senske, 1990). The rises display a large apparent depth of compensation (ADC) of long wavelength topography of 100 to 200 km (Smrekar and Phillips, 1991), which suggests that they may be partially supported by mantle dynamics at a regional scale (Phillips et al., 1981; Phillips and Malin, 1983). Phillips and Malin (1983) have proposed that one or more hot-spots may underlie the volcanic rises, providing buoyancy forces together with a thermally thinned lithosphere. In addition Head and Crumpler (1990) have suggested that rises within Aphrodite Terra are the sites of crustal spreading.

The rift zones are 100-300 km wide, thousands of kilometres in length, with up to 5 km of relief. The largest were found in the equatorial highlands in Beta and Phoebe Regiones, and tectonic junctions were identified in Beta and Atla Regio (Schaber, 1982). Beta Regio exhibited evidence of only limited extension of up to a few tens of kilometres, comparable to intracontinental rifts on Earth (McGill et al., 1981). In contrast the rifts in Aphrodite Terra were interpreted as sites of crustal spreading analogous to mid-ocean ridges (Kaula and Phillips, 1981; Head and Crumpler, 1987; Head and Crumpler, 1990). Evidence given in favour of this hypothesis included a bilateral topographic symmetry about the highland axis, and regional cross-strike discontinuities in topography and radar reflectivity perpendicular to the topographic axis which show some similarities to oceanic fracture zones (Crumpler et al., 1987; Crumpler and Head, 1988). However, a crustal spreading origin for the volcanic rises has largely been rejected in the light of the Magellan data.

2.2.6 Plains Deformation

Venera 15 and 16 images revealed that the plains are deformed by narrow (up to 10-25 km) lineaments, including low ridges, shallow grooves and radar-bright bands of unclear origin (Basilevsky and Head, 1988). Deformation belts with lengths of hundreds to thousands of kilometres and exhibiting up to several hundred metres of relief were also found in Venera 15 and 16 and Arecibo images of the plains (Barsukov et al., 1986a; Campbell, et al., 1991). They include both ridge and fracture (or groove) belts, although this distinction did not become clear until Magellan data was available (Solomon et al., 1991, 1992; Squyres et al., 1992b; Section 2.3.4). Ridge belts were identified in Venera 15 and 16 data of the northern hemisphere, occurring in Atalanta Planitia and the northern polar plains (Basilevsky et al., 1986; Kryuchkov, 1988; Frank and Head, 1990), and are

composed of numerous sub-parallel long and narrow ridges. Deformation belts were also identified in Arecibo images of the southern hemisphere (Campbell et al., 1991), containing sub-parallel radar-bright lineaments with a 10 to 40 km spacing. Deformation belts are concentrated in or near the broad topographic lowlands, occurring both as sub-parallel networks and fans in Lavinia and Atalanta Planitiae, and as orthogonal patterns adjacent or sub-parallel to tessera (Frank and Head, 1990; Campbell et al., 1991). The cumulative length of ridge belts measured in Venera 15 and 16 images is 40,000 km (Frank and Head, 1990). Many authors have concluded that the ridge belts were predominantly formed by crustal shortening (Barsukov et al., 1986a; Basilevsky et al., 1986; Frank and Head, 1990; Kryuchkov, 1988), as suggested by their topographic form, spacing, and similarity to lunar mare ridges (Zuber, 1990). In contrast Sukhanov and Pronin (1989) argue for an extensional origin, citing the parallel pattern of ridges within some ridge belts, their occurrence in topographic lows, examples of split and separated features and the fan-like arrangement of ridge belts within Atalanta Planitia.

2.2.7 Mountain Belts

Mountain belts contain the greatest compressional deformation, and have elevations of more than 10 km above the mean planetary radius (mpr) of 6052.0 km,. They were first discovered in the PVO data (Pettengill et al., 1980), and are found around the perimeter of Ishtar Terra, comprising Akna, Danu, Freyja, and Maxwell Montes. Details seen in Venera 15 and 16 and Arecibo data include broad bright and dark bands within and striking sub-parallel to the trend of Freyja Montes (Barsukov et al., 1986a; Campbell et al., 1983), and sinuous subparallel scarps on Lakshmi Planum adjacent to the Freyja belt (Sukhanov et al., 1989; Schaber and Kozak, 1990; Roberts and Head, 1990). All the mountain belts are composed of ridges which are tens to hundreds of kilometres in length. On the basis of Arecibo and Venera 15 and 16 images these ridges were interpreted as compressional folds and thrust faults (Campbell et al., 1983; Phillips and Malin, 1984; Barsukov et al., 1986a; Crumpler et al., 1986). From Venera 15 and 16 and Arecibo data the mountain belts have been inferred to be sites of compression, crustal shortening, and thickening (Barsukov et al., 1986a; Crumpler et al., 1986). On the basis of topographic profiles there is evidence to suggest that some of this deformation may be the result of lithospheric shortening and underthrusting (Head 1990a; Head et al., 1990; Solomon and Head, 1990). This deformation may be driven by shear tractions at the base of the lithosphere caused by a cylindrical downwelling mantle flow beneath Ishtar Terra (Kiefer and Hager, 1991; Bindschadler et al., 1990b). Alternatively, the mountain belts may be the sites of downward return flow surrounding a region of cylindrical upwelling beneath Lakshmi Planum (Pronin, 1986; Basilevsky, 1986), where strain has been localised along a discontinuity between the thermally weakened plateau and its surroundings (Grimm and

Phillips, 1990). Upwelling would help to explain the volcanic plains of Lakshmi, including Colette and Sacajawea Paterae (Sukhanov et al., 1989; Schaber and Kozak, 1990; Basilevsky et al., 1986). Upwelling is also consistent with large apparent depth of compensation of long wavelength topography of 130 km, which is difficult to reconcile with simple downwelling (Grimm and Phillips, 1990).

2.2.8 Tessera

First identified in Venera 15 and 16 data, the tessera (or complex ridge terrain) are equidimensional elevated regions of intense deformation containing two or more intersecting sets of linear to arcuate troughs, ridges, and scarps (Barsukov et al., 1986a; Basilevsky et al., 1986). These features are typically spaced between 10 and 20 km apart. On the basis of Venera 15 and 16 images, Bindschadler and Head (1991) identified three types of tessera: disrupted, linear ridged, and trough and ridge terrain. Disrupted terrain is the most common, and is characterised by chaotic structural patterns, while linear ridged terrain is less abundant and contains sub-parallel ridges and troughs and cross-strike lineations (Bindschadler and Head, 1991); the trough and ridge terrain is comparatively rare and characterised by sub-parallel troughs and orthogonal ridges and troughs.

Ten to fifteen percent of the area imaged by Venera 15 and 16 was found to be covered by tessera (Sukhanov, 1986; Bindschadler and Head, 1989). Areas of tessera over 1000 km across are typically steep-sided plateaus, and most tessera lies 1 to 2 km above the plains. Tessera exhibits an unusually high surface roughness at scales of up to a metre (Bindschadler and Head, 1988, 1989), and comparisons of regions with similar radar properties in PVO data to those of known areas of tessera, suggest that it is widespread (Bindschadler et al., 1990a). It was predicted that Alpha, Beta, Asteria, Ovda, Thetis and Phoebe Regiones are dominated by tessera, as well as Lada Terra and Nokomis Montes. Alpha Regio was confirmed as tessera from Arecibo observations by Campbell et al. (1991).

Unlike the volcanic rises (see below), large areas of tessera show relatively shallow apparent depths of compensation of less than 100 km (Sjogren et al., 1983; Smrekar and Phillips, 1991), suggesting that they are mainly supported by enhanced crustal thickness rather than mantle upwelling. Various models for tessera formation have been proposed, including gravitational sliding (Kozak and Schaber, 1986; Sukhanov, 1986), the interaction between a mantle plume and a spreading centre (Head, 1990b), mantle downwelling and attendant crustal thickening (Bindschadler and Parmentier, 1990), late stage deformation of elevated and thickened crust (Herrick and Phillips, 1990), and a combination of crustal compression and subsequent gravitational relaxation (Bindschadler and Head, 1991; Phillips et al., 1991b).

2.2.9 Coronae

Coronae were first identified in Venera 15 and 16 data, where they were defined as circular to oval features, 200 - 1000 km in diameter, with an elevated centre and a narrow deformed annulus of concentric ridges (Barsukov, et al., 1984; Barsukov, et al., 1986a). They are unique to Venus, and are characterised by elevated topography, interior and exterior volcanism, interior extensional and compressional features, and a peripheral trough (Barsukov, et al., 1984; Barsukov, et al., 1986a; Pronin and Stofan, 1990; Stofan and Head, 1990). Individual coronae may lack or only partially display some of these features. Their circular symmetry, and the presence of volcanic sources and deposits in their interiors suggested they may be the surface manifestations of mantle plumes (Barsukov et al., 1986a; Basilevsky et al., 1986; Pronin and Stofan, 1990; Stofan and Head, 1990, Stofan et al., 1991). As the coronae decrease in diameter they merge into another group of tectono-volcanic features called arachnoids. The arachnoids are 50 to 200 km in diameter and consist of concentric and concentric-radial systems of narrow ridges (Basilevsky and Head, 1988). The term arachnoid derives from the similarity of this feature to spiders along "webs" of linear fracture belts (Barsukov et al., 1986a). The origin of the arachnoids is not clear, but their morphological similarity and tectonic association with coronae suggest that these features may share a similar origin.

Thirty-six coronae and corona-like features were mapped in the area covered by Venera 15 and 16 (Pronin and Stofan, 1990), with many clustered around Themis Regio and east and west of Ishtar Terra. A linear collection was identified in Themis Regio using Arecibo data (Stofan et al., 1984). Like the other volcanic centres no absolute ages could be determined, but aspects of coronae morphology suggest there may be several developmental stages and a possible age sequence (Stofan and Head, 1990). A three-stage evolutionary scheme was derived including an early phase of uplift, faulting and volcanism, followed by a second stage of annulus and trough formation accompanied by topographic degradation; the final stage involving continued volcanism and topographic degradation (Stofan and Head, 1990; Pronin and Stofan, 1990). Arecibo images have provided detailed views of particular coronae, such as Quetzalpetlatl on the northern margin of Lada Terra (Campbell et al., 1991).

2.2.10 The Impact Cratering Record

All terrains imaged by Venera 15 and 16 are sparsely covered by impact craters of between 8 and 140 km in diameter, of which 139 were discovered (Ivanov et al., 1986). The abundance of impact craters in the areas imaged by both orbiting and Earth-based radar was found to be about 1 per 10^6 km^2 for craters greater than 8 km in diameter, the size-frequency distribution implying a surface age of between 0.5 to 1.0 billion years

(Ivanov et al., 1986; Schaber et al., 1987; Campbell et al., 1990). The average surface age is thus very much less than that of the Moon, Mars, and Mercury, but older than that of the Earth. Despite this information it was not possible to determine absolute or relative ages for most volcanic and tectonic features, due to the sparse population of craters resolved in the images. Nevertheless, the occurrence of many pristine craters implies a low rate of surface reworking.

2.2.11 Summary and Conclusions

To conclude, 45% of the surface was imaged by radar before Magellan, while 90% was covered by long wavelength topographic data. Volcanism is widespread and has been responsible for forming plains which cover 70 % of the planet, as well as numerous edifices at a variety of scales. There has been intensive horizontal deformation as manifested by the presence of both linear deformational belts and the tessera. Little or no evidence for plate tectonics was seen in the pre-Magellan datasets, and the presence of the coronae and volcanic rises suggests that hot-spot tectonics may characterise the planet instead.

The similar bulk properties of Venus and Earth lead to thermal models which predict essentially earth-like conditions in the interior of Venus (McGill, et al., 1983). However the high surface temperature implies a thin lithosphere (Phillips and Malin, 1983), which may explain the apparent absence of plate tectonics as the lithosphere may not be dense enough to subduct (Anderson, 1980, 1981; Phillips et al., 1981). The lack of plate tectonics implies that Venus must lose internal heat by other mechanisms such as extensive volcanism and/or local thinning and enhanced heat loss over hot spots (Phillips and Malin, 1983; Kaula and Muradian, 1982). The greatest heat loss may occur at the volcanic rises such as Beta Regio and Aphrodite Terra, where volcanism accompanies lithospheric thinning and limited extension. These conclusions are consistent with the large apparent depths of compensation of the rise topography (e.g. more than 100 km for Aphrodite), which implies dynamic support (Phillips and Malin, 1983). A dynamically supported topography is also a general requirement in the case of a thin lithosphere. McGill et al. (1983) suggest that these rises might have become divergent plate boundaries if subduction had been possible elsewhere.

2.2.12 Questions for Magellan

Pre-Magellan studies of Venus left many questions unanswered (e.g. Head and Crumpler, 1990; Solomon and Head, 1991). Volcanism has clearly played a dominant role in Venusian geology as seen in Pioneer-Venus, Venera and Arecibo images, but what is

the present global volcanic flux and how has it varied in the past? A global inventory of volcanic features and an assessment of their relative ages, together with the impact crater distribution visible in Magellan imagery is required to help answer this question. It is evident from previous imagery that volcanism must provide the single most important resurfacing mechanism, but what is the present rate of crustal formation and how has this varied over time? To what extent has resurfacing proceeded by hot-spot volcanism as opposed to the generation of crust at linear spreading centres?

Crustal formation implies that one or more mechanisms of crustal recycling must be occurring. Possible sites of recycling include the orogenic belts identified around Ishtar Terra, but the extent of recycling and the mechanisms and magnitude of the horizontal motions needs to be established. Earlier examples of orogenic belts may be visible in the Magellan imagery, and these would allow a better understanding of the evolution of such belts after convergence. Further to the understanding of crustal deformation, the sense and magnitude of the strain in ridge belts, and their distribution and relation to global tectonics needs to be addressed. The origin and evolution of tessera pose an outstanding question for Magellan data to resolve. Observations of the style of deformation, the relationship between deformation and slope, the gravitational signatures and developmental sequence of tessera is required.

An analysis of the surface deformation and magmatism as seen in Magellan images should provide clues as to the interior pattern of mantle convection. Magellan provides the opportunity to test for dynamic uplift beneath volcanic rises by tectonic signature, but evidence may be obscured by multiple episodes of deformation and volcanism (Solomon et al., 1991). Another outstanding question is the nature of the early climate on Venus, although most of the evidence for this has probably been erased by subsequent volcanic and tectonic processes.

2.3 VENUS IN THE MAGELLAN ERA

2.3.1 Physiography and Topography

Magellan has confirmed that Venus is mostly covered by lowland volcanic plains which occupy 85% of the surface, and are covered with thousands of individual volcanic edifices. The remaining 15% of the surface is occupied by tectonically deformed highlands dominated by the tessera. The mean radius obtained from the new altimetry data is 6051.84 km, and more than 80% of the surface lies within 1 km of this mean. These results confirm the unimodal distribution of elevation obtained from previous missions. Magellan has revealed that average kilometre-scale slopes of more than 30° are common on the south-west slope of Maxwell Montes, southern Danu Montes and chasmata east of Thetis

Regio (Ford and Pettengill, 1992). The presence of such steep slopes indicates recently active tectonics.

2.3.1 Volcanism

Magellan data has allowed more than 1600 volcanic land forms and deposits to be identified (Head et al., 1992). These features include over 550 shield fields (clusters of small volcanoes less than 20 km in diameter), 274 intermediate volcanoes between 20 and 100 km in diameter, 156 large volcanoes over 100 km in diameter, 86 caldera-like structures not otherwise associated with large volcanoes, 175 coronae, 259 arachnoids, 50 "novae" (prominent radial fracture patterns without concentric structure), 53 flood-type lava flow fields, and 50 sinuous lava channels.

The majority of the small volcanoes are shields which are generally less than 10 km in diameter and are most abundant on the plains (Guest et al., 1992). Volcanic cones are also found in the same size range as the shields, and both are inferred to be of basaltic composition. Steep-sided domes are also found, and range in diameter from about 15 to 90 km, are usually circular in plan, and have heights of a few hundred metres. These domes have morphologies similar to terrestrial domes formed by viscous, andesitic, dacitic, and rhyolitic lavas (Pavri et al., 1992). Evolved compositions are also supported by the occurrence of steep-sided domes within Magellan images of the Venera 8 and 13 landing sites, where non-tholeiitic compositions were measured (Basilevsky et al., 1992). There is evidence for localised pyroclastic volcanism in some areas including Guinevere Planitia, despite the fact that the high atmospheric pressure on Venus should inhibit explosive activity (Lancaster and Guest, 1991; Guest et al., 1992). The large volcanic shields are characterised by extensive radial flow aprons and positive topography, and are frequently associated with a concentric or circular central feature (Head et al., 1992). They preferentially occur in or near the highlands, and are only sparsely scattered in the lowlands. Many are found on the broad rises and tectonic junctions of the equatorial highlands (Senske et al., 1992). There is a morphological transition between some of the large volcanoes and the coronae, and many coronae are surrounded by extensive radial flow aprons. Coronae are associated with a wide range of volcanic deposits, including interior lava flows and small shields, and exterior flow aprons (Head et al., 1992; Stofan et al., 1992). Extrusive volcanism is less commonly associated with arachnoids and novae, which may contain a greater component of intrusive magmatism (Head et al., 1992). The 86 calderas mapped by Head et al. (1992) most commonly range between 40 and 80 km in diameter and are defined as circular to elongate depressions not associated with a well defined topographic edifice. They are characterised by concentric patterns of enveloping fractures and smooth or radar-dark central regions indicative of late infilling by lava. The term caldera is used by Head et al. (1992) to signify that these features are interpreted as

due to collapse following removal of subsurface magma. The distinction between large volcanoes, coronae, arachnoids, novae and calderae is based on their structural, volcanic, and topographic characteristics, but they all appear to represent different manifestations of broadly similar magmatic processes.

The most extensive volcanic deposits are the flood lava flow fields. These have typical areas of several hundred thousand square kilometres, exhibit a range of radar backscatter characteristics, and are commonly related to zones of limited extension and rifting (Chapter 3). Baker et al. (1992) have identified 200 sinuous channel features whose morphologies suggest formation by fluids which could include ultramafic silicate melts, sulphur, and carbonatite lava. The channels include sinuous rilles which resemble similar features on the Moon, and a newly recognised long sinuous form of channel with a high width to depth ratio and remarkably constant width (Baker et al., 1992). The channels range from a few kilometres to a few tens of kilometres wide, and several tens to several thousands of kilometres in length. Komatsu et al. (1993) have recently suggested that canali-type channels may have been responsible for large-scale plains formation, although few examples of associated flow fields are seen (Chapter 3).

Magellan has confirmed that volcanism is the most important and widespread phenomenon on Venus. The large size of many volcanic constructs implies that large magma reservoirs have developed. There is a deficiency of volcanic edifices in the lowlands, where most flood lava flow fields are located, and most large edifices are found at higher elevations. Head et al. (1992) explain this as due to an altitude dependent influence of atmospheric pressure on volatile exsolution and the production of neutral buoyancy zones sufficient to form magma reservoirs. In this scenario large reservoirs are formed at higher elevations, while magma at lower elevations undergoes little or no storage before eruption. The greatest concentration of volcanic features (2 - 4 times the global average) is found in the Beta-Atla-Themis region, which covers approximately 20% of the planet and may be a region of anomalous mantle (Head et al., 1992).

2.3.3 Volcanic Rises and Rift Zones

Senske et al. (1992) provide an account of the geology of rises within Western Eistla, Beta and Atla Regiones as revealed by Magellan data. Magellan images confirm that the rises have been the sites of significant volcanic flux and are characterised by the presence of large shield volcanoes. Western Eistla Regio is an elongated domical rise containing the large volcanoes Sif and Gula Mons. Within Beta Regio the presence of a split and extended crater in Devana Chasma indicates that the rift has undergone up to 20-30% extension. Magellan reveals that tessera is a major unit within Beta, and that Rhea Mons is highly deformed, possesses characteristics of tessera, and does not appear to be a volcanic construct (Senske et al., 1992). Stratigraphic relations indicate that several

episodes of fracturing and volcanism have occurred in Western Eistla and Atla Regiones (Senske et al., 1992; Chapter 5). Chains of coronae are associated with fractures and rift zones in Beta and Atla Regio, suggesting that upwelling has occurred along zones of extension. The presence of widespread volcanism within the rises and the details of extensional tectonism revealed by the Magellan data strengthen the case for an origin by mantle plumes (Bindschadler et al., 1992b; Senske et al., 1992).

2.3.4 Plains Deformation

Magellan has shown that most areas of plains show considerable evidence for deformation (Saunders et al., 1991; Solomon et al., 1991). The high resolution of Magellan images allows numerous individual structural features to be seen for the first time. These structures include families of graben and sinuous ridges with spacings of a few kilometres to tens of kilometres, which indicate areally distributed strain of modest magnitude (Solomon et al., 1992). Most of these features belong to areally extensive swarms and sets which cover hundreds to thousands of kilometres. The coherence of these patterns over such large areas implies that local features reflect a crustal response to mantle dynamics (Solomon et al., 1992). For example, Solomon et al. (1991) identified several types of lineated terrain in the region between Sedna and Guinevere Planitiae, including extensive NW trending lineations and graben, orthogonal sets of lineations, complex lineations and regularly spaced ridges. Solomon et al. (1992) describe N-S trending radar-bright graben in Niobe Planitia. Individual graben have lengths of 5-40 km, and widths of up to 1 km, with typical spacings of a few kilometres. They are evidence of a modest amount of extension, and their persistent trends imply the existence of structurally coherent sheets that are thin and extensive (Solomon et al., 1992). Sinuous ridges with regular spacings are commonly found on the plains, and are particularly well developed in Rusalka Planitia (Solomon et al., 1992; Chapter 5). These ridges are similar to lunar and Martian wrinkle ridges attributed to modest horizontal compression and shortening (Plescia and Golombek, 1986; Watters, 1988). Their spacing of about 20 km implies the deformation of the entire thickness of the strong upper crustal layer (Zuber, 1987; Zuber and Parmentier, 1990).

Magellan data has provided a clearer distinction between ridge and fracture belts, although in some cases the belts appear to be composite (Solomon et al., 1991, 1992; Squyres et al., 1992b). Notable concentrations of ridge and fracture belts are found in Lavinia, Atalanta, and Vinmara Planitiae. Belts may be up to 250 km wide, with lengths that can exceed 1000 km, and heights of a few hundred metres to 1 km. Ridge belts within Lavinia Planitia contain ridges of variable width up to 10 km, which are most commonly smooth and arch-like in profile, although some have superposed ridges, and some are cross-cut by one or more sets of groove-like lineaments, which both predate and post-date

the ridge belt (Solomon et al., 1991, 1992). Individual ridges are typically 200 to 300 m in height (Squyres et al., 1992b). Modest amounts of compressive strain and shear (around 20%) are manifested by ridge belt deflected lineaments. Examples are also seen in north-east Rusalka Planitia (Chapter 5).

Fracture belts are characterised by broad topographic ridges, resolvable in Magellan altimetry, with a complex array of linear to arcuate faults and fractures, some of which are paired to from grooves of 1 to 2.5 km width and 5 to 20 km spacing (Solomon et al., 1991, 1992). Also called groove belts by Solomon et al. (1991), they are best seen in Lavinia Planitia (Squyres et al., 1992b). They contain evidence for at least two scales of deformation, modest shear, and interior volcanism.

The overall similarities between ridge and fracture belts, including their elevated nature, suggests that both were formed by crustal shortening and thickening (Solomon et al., 1991). The fracture belts may involve near-surface extension and fracturing of a shallow layer over the broader uplift. Some deformation belts in the Atalanta-Vinmara Planitia area change from fracture to ridge dominated along their length, which supports the case for a common origin (Solomon et al., 1992). Alternatively, the fracture belts may be dominantly extensional in origin, having been localised by lithospheric heating patterns or igneous intrusion (Solomon et al., 1992). This second hypothesis is consistent with the close association between fracture belts and plains volcanism, including fields of small volcanoes. The deformation belts are evidence for a strong link between interior dynamics and surface deformation and are comparable to areas of intracontinental deformation on Earth (Solomon et al., 1991). Further discussion of deformation belts is to be found in Chapter 5.

2.3.5 Mountain Belts

Magellan has provided a detailed and more complicated picture of the mountain belts surrounding Ishtar Terra than previously seen. Graben and normal faults trend perpendicular to topographic slopes within western Ishtar Terra, and suggest that gravitational spreading has occurred (Smrekar and Solomon, 1992). Models of gravitational relaxation suggest that either the crust of western Ishtar Terra is stronger than that predicted by flow laws, or the relief has been actively built within the last few tens of millions of years. The mountain belts deform the adjacent plains of Lakshmi Planum, indicating that horizontal compression was active more recently than the youngest plains-forming lava flows (Kaula et al., 1992). Volcanic plains with little or no deformation occur within Itzpapalotl Tessera to the north of Freyja Montes at a similar elevation to Lakshmi Planum. The location and relatively recent nature of this volcanism suggest that some magmatism in Ishtar is the product of re-melting of thickened crust (Bindschadler et

al., 1990b; Roberts and Head, 1990), rather than that due to a mantle plume beneath Ishtar (Pronin, 1986; Basilevsky, 1986).

2.3.6 Tessera

Magellan has tripled the known area of tessera, and revealed the details of the extremely complex deformation. As predicted by Bindschadler et al. (1990a) the main areas of tessera occur in Ovda, Thetis, Phoebe, Beta and Asteria Regiones, and in the Lada Terra and Nokomis Montes regions (Nokomis Montes is discussed in Chapter 5). Magellan data have shown that tessera is the most areally extensive highland tectonic unit (Bindschadler et al., 1992b). The largest contiguous region of tessera comprises Ovda Regio and much of the westward extension of Aphrodite Terra, and covers 10^7 km^2 (Solomon et al., 1992). Magellan data confirm that most large regions of tessera contain compressional ridges and troughs, with a spacing of 10 to 20 km, with numerous superposed graben and other extensional structures with widths and spacings which range down to the resolution limit (Solomon et al., 1992). Individual structures continue for up to 100 km, and groups of structures may hold consistent orientations for up to 1000 km. The Magellan data suggest that the classification of tessera from Venera 15 and 16 data by Bindschadler and Head (1991) remains useful. According to Bindschadler et al. (1992a,b) the morphology of tectonic features within Alpha Regio and their stratigraphic relationships support a mantle downwelling model for tessera formation. Linear deformation zones within Alpha are interpreted to be shear zones, while small graben are interpreted as the product of late-stage gravitational relaxation of the tessera (Bindschadler et al., 1992a). However, Solomon et al. (1992) point out that the tesserae may simply be long-lived blocks of thickened crust that have been subjected to repeated episodes of tectonic deformation imposed by exogenic and large-scale stresses. They also point out that such elevated regions are less susceptible to volcanic burial and thus record a longer history of deformation than the surrounding plains. The complexity and diversity of tessera are such that a number of these processes, either alone or in combination, may have operated in particular regions.

2.3.7 Coronae

The population of known coronae was increased to 362 by the time Magellan had mapped 90% of the surface of Venus. These coronae range from 60 to more than 2000 km across, with extensional, compressional, and combined extensional/compressional annuli of 10 to 150 km in width (Stofan et al., 1992). Magellan has revealed a complex and diverse range of morphologies and topographic characteristics (Solomon et al., 1991; Head et al.,

1991; Squyres et al., 1992a). Stofan et al. (1992) identify five classes of coronae based on tectonic characteristics, including concentric, concentric-double ring, asymmetric, radial/concentric and multiple; radial and volcanic classes of corona-like features are also identified. These classes are interpreted to represent coronae in different states of evolution, and that have been affected by different amounts of uplift, interior tectonism and volcanism, and annulus formation (Squyres et al., 1992). Coronae have been modified by varying amounts of regional tectonic activity, this being particularly so for the asymmetric and multiple classes. The corona-like features may be examples of relatively young or "failed" coronae.

Magellan data has revealed that a greater proportion of corona annuli are typified by extensional faults and troughs, than the predominantly compressional annuli in coronae mapped by Venera 15 and 16 (Pronin and Stofan, 1990). Most coronae interiors are dominated by smooth plains deposits, but such interior deformation which does occur commonly includes oblique fractures which parallel regional deformation in the surrounding plains (Stofan et al., 1992). No conclusive evidence of interior compressional deformation was found by Stofan et al. (1992), but regional trending ridges are seen within Eigin Corona (5.0° S, 175.0° E), Chapter 5. A range of volcanic styles and intensities is found in the interior of coronae, with most displaying a moderate amount of volcanic features, smooth plains and domes being the most common deposits (Stofan et al., 1992). Topographically the coronae are mostly plateau-like, but domes, plateaus with interior lows, rimmed depressions, and rimless depressions interpreted as calderas also occur (Stofan et al., 1992).

Analyses of Magellan data have confirmed that the characteristics and evolution of coronae are consistent with a formation by mantle plumes or diapirs (Squyres et al., 1992a; Stofan et al., 1992; Janes et al., 1992). Stofan et al. (1992) highlight the similarities between coronae and large volcanic shields and rises, such as Western Eistla Regio; the largest corona, Artemis, is actually larger than several volcanic rises. Coronae may occupy an intermediate position between major volcanoes and rises, manifesting the presence of significant melt as under large volcanoes, but with less volcanism, and either smaller scale or shorter lived upwellings than the volcanic rises (Stofan et al., 1992). The three-stage evolutionary sequence derived from Venera 15 and 16 data (Stofan and Head, 1990; Pronin and Stofan, 1990), is supported by the Magellan observations (Stofan et al., 1992), most coronae being in the middle to late stages of this evolution. Unlike hot-spot chains on Earth, Stofan et al. (1992) found no evidence to suggest any systematic variation in age along chains of coronae; although limited crustal movement above a mantle plume may be indicated by multiple and overlapping coronae.

Magellan data has confirmed that the distribution of coronae is complex, with some located at apparently random places within the plains, while others occur in several concentrations and chains. The largest concentration of coronae is found along Parga Chasma, where a north-west-south-east trending chain of coronae superpose troughs and

faults interpreted as extensional in origin (Stofan et al., 1992). Parga extends south-west from Atla Regio, and may be a zone of rifting and extension associated with an alignment of mantle plumes which have formed both Atla and the coronae (Stofan et al., 1992).

2.3.8 The Impact Cratering Record

Schaber et al. (1992) list 840 craters observed in Magellan data covering 89% of the surface. Crater diameters range between 1.5 and 280 km, but there are few below 35 km in diameter because of the shielding effect of the atmosphere. Most of the impact craters appear to be unmodified by weathering processes, which attests to the very low rate of surface modification on Venus. Crater morphology ranges with increasing diameter from flat floored, central peak, peak ring, to multiring craters (Schaber et al., 1992). Craters smaller than 30 km are usually irregular or multiple, resulting from disrupted projectiles. Radar-bright and dark "splotches" with typical diameters of 20 km are interpreted as the signatures of atmospheric shock waves resulting from bodies which did not survive atmospheric passage. Many of the impact craters are associated with large parabolic haloes, which may be radar-bright or dark, and are always open to the west. The haloes are usually associated with radar-bright craters and are among the youngest surface features. The haloes are interpreted as deposits of small particles injected into the atmosphere by the impact and transported by the east-west zonal winds.

The density of craters is too low to allow estimates of surface ages other than on a global scale, providing an average surface age of between 200 Ma and 700 Ma. Two resurfacing histories have been proposed to account for the cratering record. Phillips et al. (1992) propose an ongoing equilibrium resurfacing, where randomly distributed areas are resurfaced and craters are obliterated at approximately the same rate they form, maintaining a spatially random crater population and an average surface age of about 500 Ma. Alternatively, Schaber et al. (1992) favour a global resurfacing event ending at about 500 Ma ago, which completely obliterated the previous cratering record and was followed by reduced volcanic activity and the accumulation of the current population of craters. Global resurfacing is supported by Monte Carlo simulations that indicate that equilibrium resurfacing models are not consistent with the observed cratering record (Bullock et al., 1993). Global resurfacing has been modelled as the result of catastrophic mantle overturn, in the form of episodic crustal recycling due to the growth of instabilities in a thickened depleted upper mantle layer (Parmentier and Hess, 1992) or as episodic plate tectonics (Turcotte, 1993). The plains may have been produced during such catastrophic mantle overturn by a large number of widespread eruptions with high volume fluxes.

2.3.9 Summary and Conclusions

Magellan has confirmed that the assessment of the global importance of plains and highlands based on Pioneer Venus and Venera 15/16 data was essentially correct. Volcanism is the most widespread and important geological phenomenon, but unlike the Earth the volcanic features have a broad global distribution[1]. More than 1660 volcanic land forms and deposits have been identified, including clusters of small volcanoes, larger individual volcanoes with diameters from 20 km to over 100 km, caldera-like structures, coronae, arachnoids, novae, lava flow fields and sinuous lava channels (Head et al., 1992). The majority of the volcanic features are consistent with basaltic compositions However, the steep-sided domes may represent more evolved compositions, and some of the sinuous lava channels may have been formed by more fluid, ultramafic magma. The areal distribution, abundance and size-frequency distribution of large volcanic features suggests that they are the surface manifestations of mantle plumes or hot spots.

Magellan has revealed tectonic features with a wide variety of styles and spatial scales from a few kilometres to thousands of kilometres. Deformation occurs both as widely distributed strain of modest magnitude, and as areas of concentrated extension and shortening. Some regions display evidence of lateral extension and collapse both during and after crustal compression. Extensional deformation appears to be limited to a few tens of kilometres. Several large offset strike-slip faults are found, but limited local horizontal shear across zones of crustal shortening is more common. There is evidence for multiple episodes of deformation in many areas, which suggests that Venus has been tectonically active over an extended period of time. Current tectonic activity is implied by the presence of slopes in excess of 20° to 30° over scales of tens of kilometres. Mantle convection, and the associated dynamic stress and heat transport, is likely to drive the long wavelength topography at scales of hundreds to thousands of kilometres, and is evident in the long wavelength gravity. The volcanic rises with their abundant volcanism, geoid anomalies and extensional deformation suggest mantle upwelling, while downwelling may be occurring beneath the lowland plains. No evidence for Earth-style plate tectonics has been found, although some features associated with coronae and arcuate trenches within the Dali-Diana chasmata have morphologies that resemble terrestrial subduction trenches (McKenzie et al., 1992a). Venus tectonics is most comparable to actively deforming continental regions on the Earth, where deformation is distributed across broad zones up to several hundred kilometres across, separated by less deformed blocks of stronger crust (Solomon et al., 1991).

Both the intensity of deformation and the state of preservation appear to be a function of elevation (Solomon et al., 1991). Regional lithospheric strain appears to be concentrated by areas of elevated and thickened crust, where the thicker layer of weaker crust is more susceptible to ductile flow. Such elevated regions are also less susceptible to volcanic resurfacing and remain to preserve multiple episodes of deformation, which may

[1] If the Earth's continents alone are considered.

ultimately become regions of tessera (Solomon et al., 1992). Volcanic burial is more likely to occur in lowland regions as represented by the plains. The impact crater data and volcanic distribution support a catastrophic resurfacing at 500 Ma ago which may be represented by the large expanses of plains, while the population of volcanic features that are largely superimposed on the plains may be the product of ongoing hot-spot type volcanism.

CHAPTER 3

GREAT LAVA FLOW FIELDS

A time would come when Men should be able to stretch out their Eyes...they should see the Planets like our Earth.

– Chrisptopher Wren, Inauguration Speech, Gresham College, 1657

3.1 INTRODUCTION

Magellan images have revealed many extensive flood-type lava flow fields on Venus (Guest, et al., 1992; Head ét al., 1992). Flow fields and field assemblages with areas greater than 50,000 km^2 are termed "great" flow fields (Lancaster et al., 1992a), following terminology used for major units within the Columbia River Basalt Group (Tolar et al., 1989). This area defines an arbitrary lower bound, taken to distinguish the more areally extensive fields and field assemblages, which make up large expanses of plains forming lava.

A survey of fifty great flow fields was undertaken. These fields were chosen on the basis of not only area, but the visibility and contrast of flow units, flow structure, mappability, and recognition of source regions (Table 3.1). Each of these examples consists in itself of either an assemblage of stratigraphically related and superposed flow fields, which were erupted from the same source region, or less commonly a single flow field. The group represents a working and manageable set of flow fields, and is not intended to be an exhaustive list or a statistically complete set. The list includes many but not all of the class of lava floods defined and identified in the survey of Crumpler et al. (1993), as well as many of the lava fields classed under large volcanoes, shield fields, and coronae. These fifty fields are also a sub-set of the more comprehensive population of 208 large flow fields documented by Magee and Head (1994). The flow fields in this set are not randomly distributed about the planet, and concentrations can be seen in and around Beta and Eastern Atla Regiones, and Navka and Lavinia Planitiae (Figure 3.1). To an extent these follow the global concentrations of volcanic features noted by Head et al. (1992). Nevertheless the small sample size and somewhat subjectively chosen set of the great flows dictates caution in explaining their distribution.

The great flow fields display a variety of morphologies, with five types having been recognised (Figure 3.2)[2]. These different morphologies primarily reflect variations in emplacement style, source characteristics, and local topography. A basic distinction has been drawn between sheet-like and digitate flow fields. The sheet flow fields appear to represent single large flow fields with irregular margins and an absence of distinctive individual flow units, while the digitate flow fields are composed of several or many discrete flow units.

[2]In this study

Table 3.1 Locations, morphology and dimensions of the 50 great flow fields.

Name/Source	Latitude	Longitude	Morphology	Total Area/km^2	Maximum Length/km
Metis Regio	67N to 75N	240 to 270E	Apron	336,000	540(max), 380(av)
Lauma Dorsa	55N to 65N	176 to 191E	Sheet	304,000	540
Iris Dorsa	53N to 59N	216 to 224E	Fan	86,000	360
Pandrosos Dorsa	43N to 56N	207 to 215E	Sub-parallel	234,000	590
Feronia Corona	62N to 68N	261 to 289E	Apron	161,000	630 (max)
Aitra Mons	48N to 56N	260 to 275E	Apron	201,000	660(max), 270(av)
Neago Fluctus	43N to 60N	338 to 357E	Transitional	744,000	1900
Sekmet Mons	42N to 50N	239 to 245E	Apron	81,000	520(max), 150(av)
Mist Fossae	37N to 43N	242 to 255E	Sub-parallel	106,000	450
Kawelu Planitia	40N to 52N	253 to 275E	Sheet	780,000	630
Hroswitha Patera	34N to 41N	021 to 037E	Sheet	197,000	880
Eastern Tepev Mons	21N to 35N	040 to 055E	Apron	638,000	850 (max)
Rusalka Planitia	11N to 27N	148 to 159E	Transitional	504,000	600 (S), 720 (N)
Ulfrun Regio/ Ganiki Planitia	24N to 32N	215 to 225E	Sub-parallel	198,000	670
Ulfrun Regio/ Kawelu Planitia	33N to 37N	224 to 232E	Sub-parallel	50,000	500
Theia Mons	19N to 29N	273 to 287E	Apron	469,000	680 (max)
South Sappho	6N to 19N	009 to 020E	Apron	301,000	450 (max)
Sapas Mons	7N to 12N	185 to 190E	Apron	175,000	320 (max)
Ganis Chasma	14N to 20N	191 to 197E	Apron	217,000	300 (max)
Hecate Chasma	11N to 14N	231 to 237E	Sub-parallel	91,000	860
Asteria Regio	18N to 22N	266 to 271E	Apron	105,000	220 (max)
Large Volcano at 10.5N, 275E	7N to 13N	272 to 277E	Apron	225,000	400(max), 240(av)

Table 3.1 continued

Name/Source	Latitude	Longitude	Morphology	Total Area/km^2	Maximum Length/km
Large Volcano at 9.5N, 309E	6N to 14N	304 to 312E	Apron	250,000	630 (max)
Shield Field at 13N, 314.5E	11N to 19N	310 to 319E	Apron	102,000	450 (max)
Corona at 9.2N, 315.5E	8N to 13N	314 to 320E	Sheet	66,000	450
N Eigin Corona	5S to 6N	170 to 180E	Transitional	204,000	900
Maat Mons	3S to 5N	189 to 198E	Apron	191,000	590
Northern Ozza Mons	4N to 10N	194 to 205E	Apron	325,000	770
SE Ozza Mons, Atla Regio	7S to 2S	200 to 212E	Sub-parallel	121,000	1,460
Large Volcano at 3.5N, 270E	1N to 6N	266 to 273E	Apron	138,000	420(max), 260(av)
Shield Field at 1.5N, 277.5E	1S to 4N	276 to 281E	Sub-parallel	87,000	340
Large Volcano at 2N, 316E	7S to 5N	310 to 320E	Apron	353,000	680(max), 250(av)
Kuanga Chasma	22S to 10S	085 to 094E	Transitional	342,000	1,310
Corona at 21S, 119E	23S to 18S	112 to 119E	Apron	337,000	770 +
SE Thetis Regio	18S to 14S	138 to 144E	Sub-parallel	96,000	820
Rift Zone at 19.8S, 145E	26S to 18S	140 to 151E	Transitional	404,000	580
Dali Chasma	23S to 16S	175 to 183E	Sub-parallel	200,000	770
Corona at 17.5S, 244E	21S to 13S	242 to 250E	Apron	223,000	630(max), 360(av)
Large Volcano at 12.5S, 261.5E	16S to 10S	258 to 264E	Apron	135,000	425(max), 245(av)
Large Volcano at 18S, 285E	25S to 14S	280 to 292E	Sub-parallel	222,000	800
Navka Planitia from 14S, 310E	15S to 11S	310 to 317E	Fan	117,000	720

Table 3.1 continued

Name/Source	Latitude	Longitude	Morphology	Total Area/km^2	Maximum Length/km
Large Volcano at 27.5S, 262E	32S to 23S	243 to 262E	Transitional	338,000	2,840
Parga Chasma at 30S, 265E	35S to 28S	258 to 267E	Transitional	304,000	990
Eriu Fluctus	40S to 34S	354 to 003E	Sub-parallel	278,000	630
Ammavaru	52S to 43S	015 to 032E	Fan	164,000 (fan)	460 (fan)
Kaiwan Fluctus	53S to 43S	353 to 010E	Sub-parallel	868,000	870
Themis Regio	46S to 39S	275 to 289E	Apron	247,000	540(max), 250(av)
Mylitta Fluctus	63S to 49S	349 to 359E	Sub-parallel	300,000	1000
SE of Aino Planitia	65S to 52S	123 to 142E	Sheet	554,000	720
Quetzalpetlatl Corona	76S to 69S	000 to 030E	Apron	1,500,000	813

Figure 3.1 Location map of the set of 50 great flow fields. Flow field types are indicated as are flow directions for subparallel (direction of arrows) and transitional (convex side of symbol in flow direction) fields. Flow field area is not implied by symbol size.

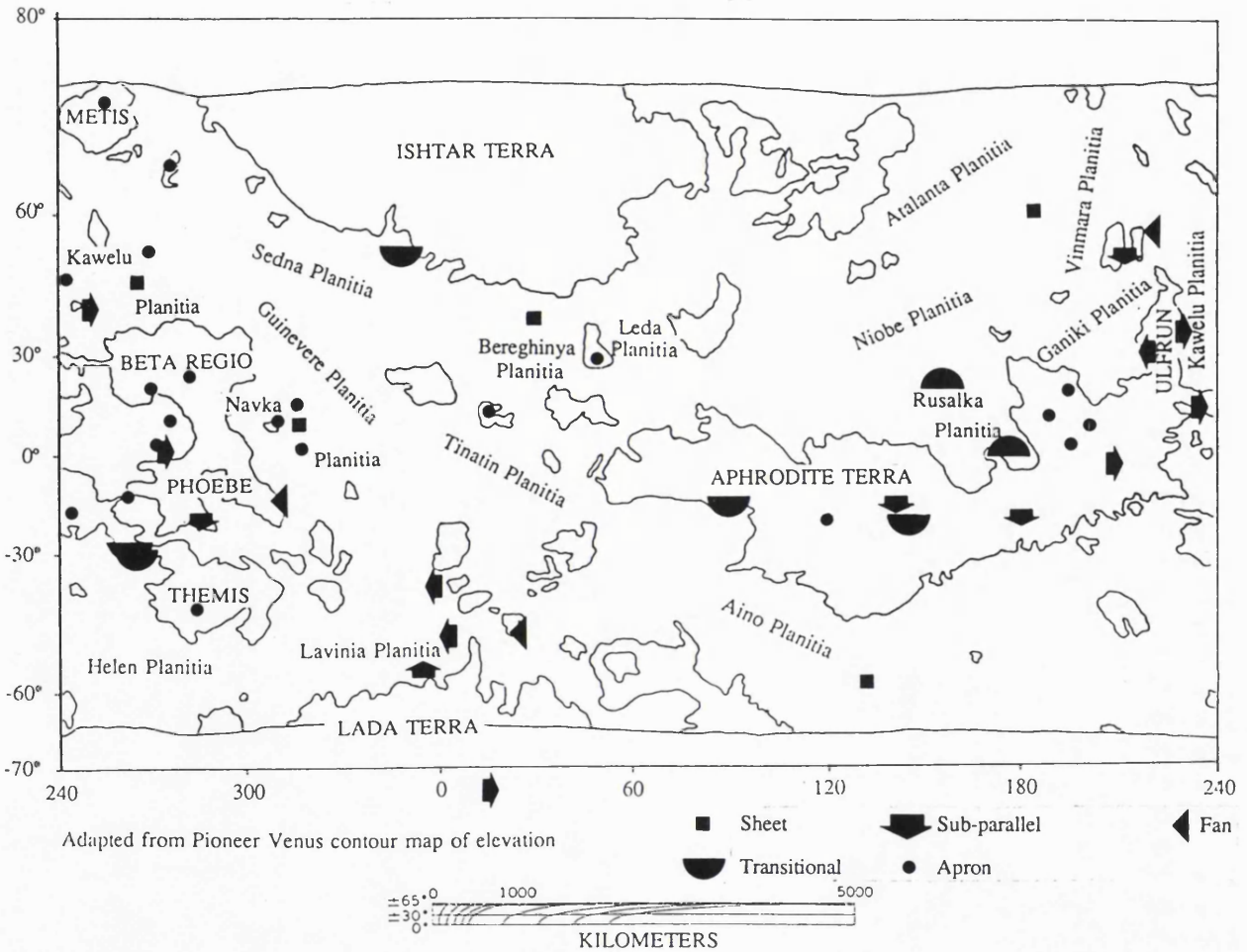

Adapted from Pioneer Venus contour map of elevation

Figure 3.2 Morphological types of great flow fields (not to scale). Fields of each type may not display all the indicated features and source characteristics of that type.

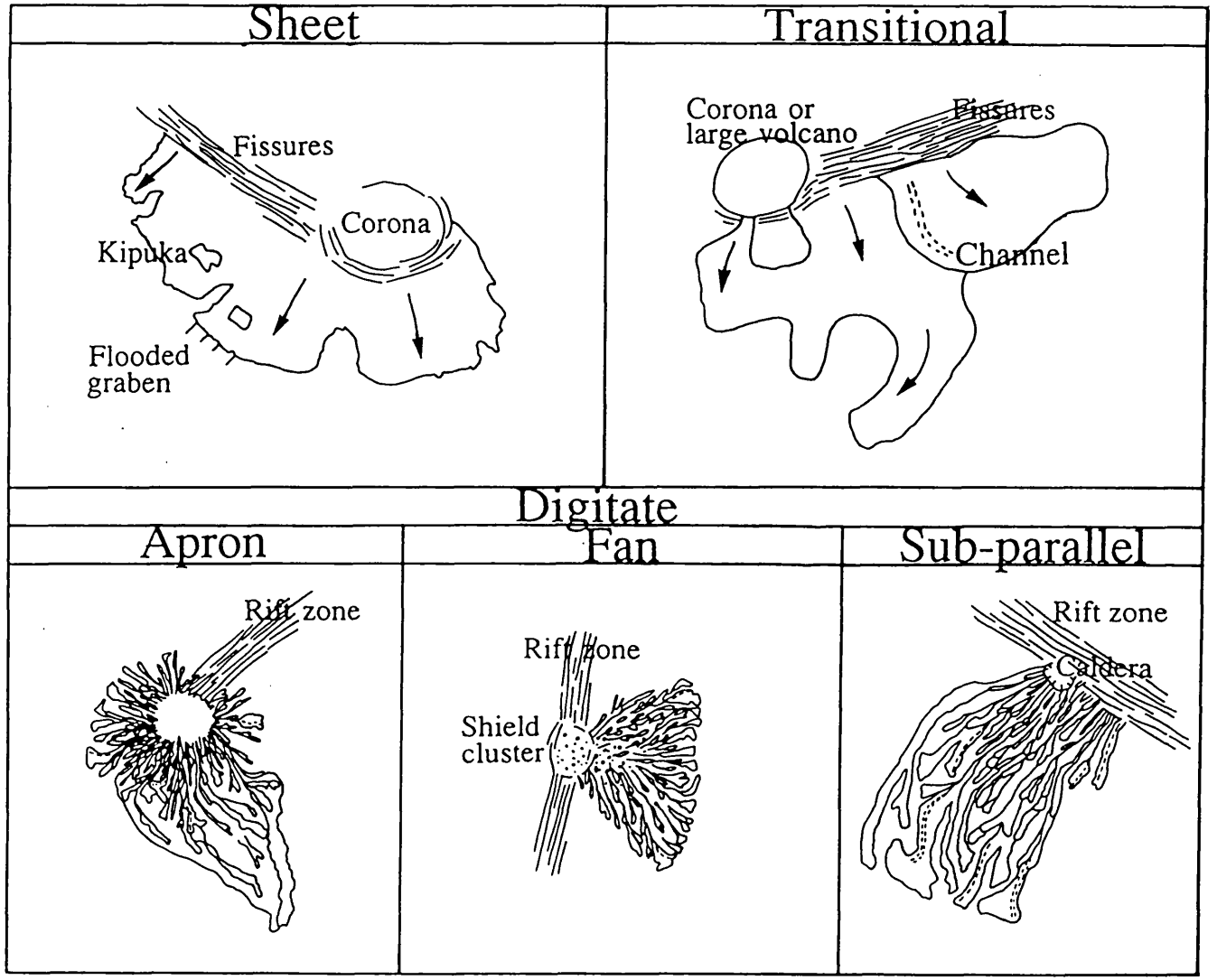
Sheet
Transitional
Fissures
Corona
Kipuka
Flooded graben
Corona or large volcano
Fissures
Channel
Digitate
Apron
Fan
Sub-parallel
Rift zone
Rift zone
Shield cluster
Rift zone
Caldera

The term "flow unit", as used in this chapter, refers to a portion of a flow field that may be mapped as a distinct entity, having a discernible boundary and usually representing a single flow lobe or lava stream, commonly with distinct radar properties and age relationships to other units in the same field. A problem encountered during mapping was the inability to completely define and close some flow unit and field boundaries due to changes in radar properties along the length of the unit or field. Thus a degree of uncertainty exists in the definition, position and dimensions of mapped flow units and fields. Nevertheless in most cases these components are quite distinct and have been mapped with reasonable confidence. Adjacent units and fields of similar surface texture may not be distinguishable in the radar imagery (Gaddis et al., 1989; Theilig, et al., 1989). Mapping may therefore underestimate the number of exposed flow units in a given field, or the number of fields in an assemblage.

The total areas of great flow fields range between 50,000 and 1,500,000 km^2 (Table 3.1, Figure 3.3a). Maximum lengths are broadly distributed between 150 and 2,840 km (Table 3.1, Figure 3.3b). Source elevations lie between 1.0 km below to 8.7 km above the mean planetary radius (mpr) of 6051.8 km (Table 3.2, Figure 3.3c), with most between 0 and 2.2 km above the mpr. Topographic slopes (the average topographic slope along the entire length of each flow field) range up to 0.77° (Table 3.2, Figure 3.3d, Figure 3.4). The areas of the great flow fields (Figure 3.3a) compare well with those of terrestrial flood basalt provinces, which are typically a few hundred-thousand square kilometres in extent (Table 3.3); the same holds true for maximum lengths (several hundred kilometres).

The thickness of flow units is difficult to determine, as individual units are not distinguishable in the altimetry. This is partly due to the spatial resolution of the altimetry (10 to 30 km) as compared to the size of individual flow units, but even the largest flow units of several tens up to a hundred kilometres across show no topographic expression in the altimetry. This suggests that in many cases these flows may less than 50 m in thickness (the vertical resolution of the Magellan altimetry). Estimates of flow thickness may also be made from the control on flow emplacement exerted by ridges and small shields whose heights have already been estimated by other means. Flow unit thicknesses of up to 100 m have been determined for the flow field south-east of Ozza Mons (Section 3.2.3.2.1), and less than 50 m for Mylitta Fluctus (Chapter 4). These estimates agree well with typical thicknesses of several tens to over 100 meters for individual flows within terrestrial flood basalts (Table 3.3).

Estimates of minimum flow field volumes may be obtained by multiplying the thickness estimates by flow field area and summing the contributions from multiple overlapping flow units in the proximal regions of the digitate fields. Estimates of several thousand to several tens of thousands of cubic kilometres are obtained by using flow thicknesses of 50 to 100 m. These volumes are comparable those of major units within terrestrial flood basalt provinces (Table 3.3).

In order to provide some insight into surface texture, average normalised radar backscatter cross sections for each of the great flow fields were taken from the Cycle 1 C1MIDR products by averaging all the pixel values within the boundary of each field (or assemblage). This process averages the contribution from individual flow units and is only

Figure 3.3 Histograms for the entire population of great flows with the indicated percentage values of (a) total area in km^2, (b) maximum length in km, (c) source elevation expressed as the planetary radius in km, (d) average topographic slope in degrees. The numbers above each bar give the number of flow fields in each bin.

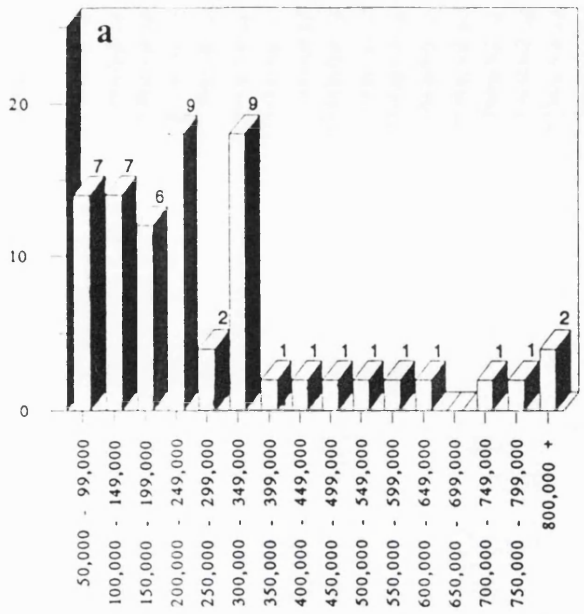

Total area/km^2

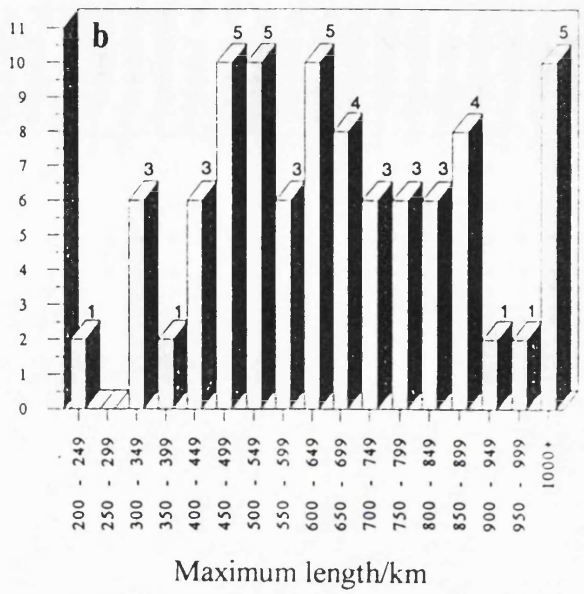

Maximum length/km

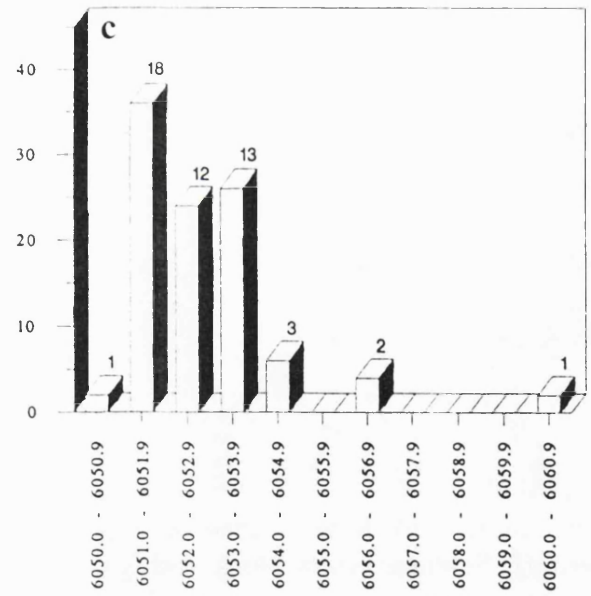

Elevation (planetary radius)/km

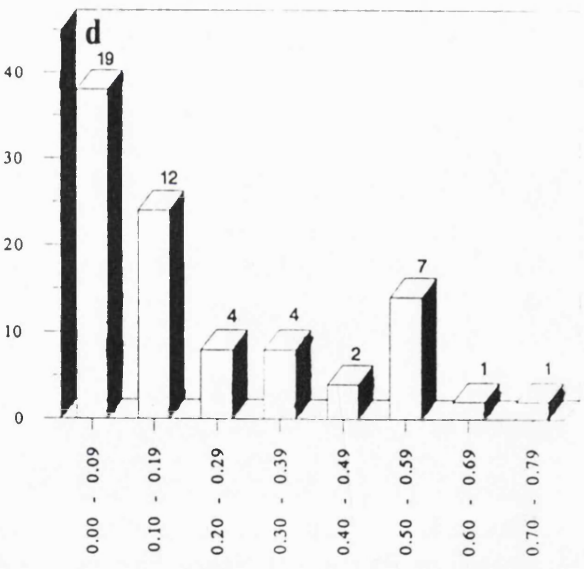

Average topographic slope/degrees

Figure 3.4 Topographic profiles of (a) Lauma Dorsa, (b) Kawelu Planitia, (c) Hroswitha Patera, (d) Neago Fluctus, (e) Ammavaru, (f) Southeast Ozza Mons, and (g) Kaiwan Fluctus. Heights are expressed as planetary radius in km, and distances are given in km. Scales and vertical exaggerations vary. S and X correspond to the source and distal parts of the field respectively, and in all profiles the source is to the left. Lines of section are given on the corresponding maps. Topographic data was extracted from the GTDR products.

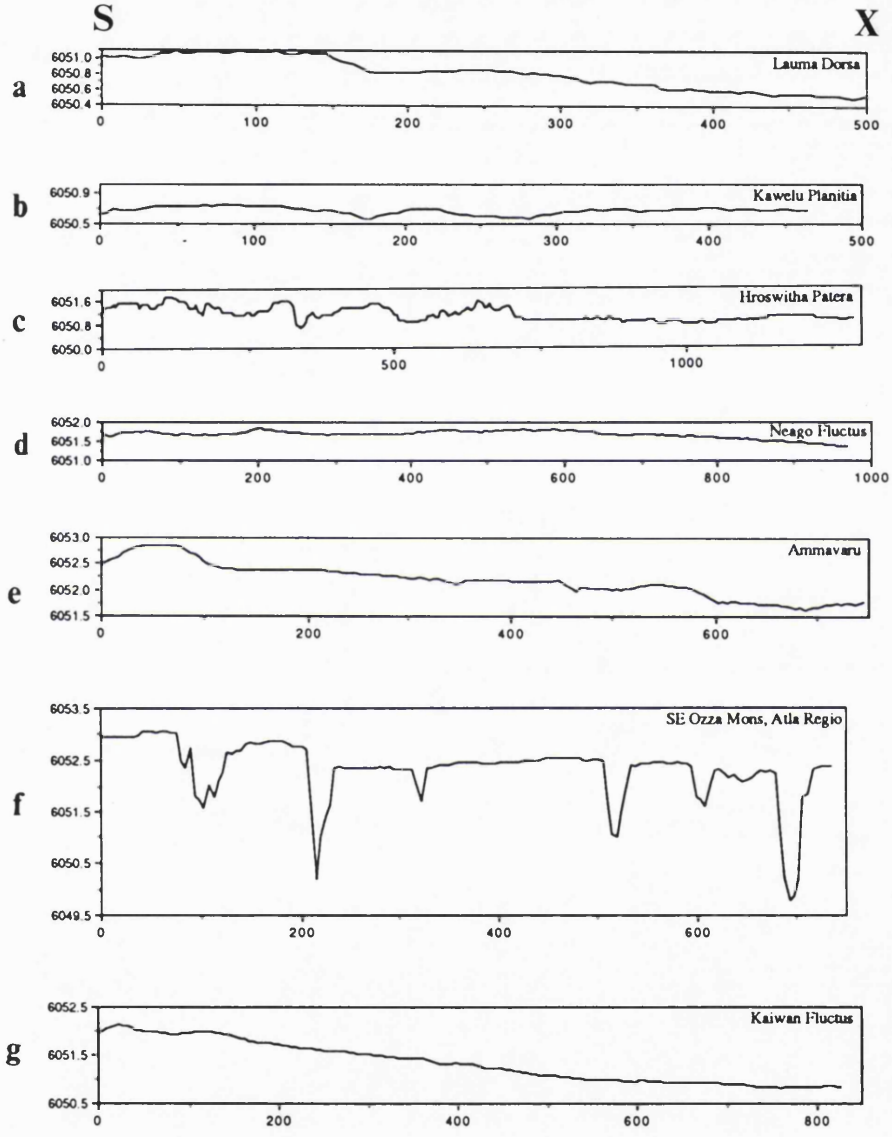
S
X
a
Lauma Dorsa
6051.0
6050.8
6050.6
6050.4
0
100
200
300
400
500
b
Kawelu Planitia
6050.9
6050.5
0
100
200
300
400
500
c
Hroswitha Patera
6051.6
6050.8
6050.0
0
500
1000
d
Neago Fluctus
6052.0
6051.5
6051.0
0
200
400
600
800
1000
e
Ammavaru
6053.0
6052.5
6052.0
6051.5
0
200
400
600
f
SE Ozza Mons, Atla Regio
6053.5
6052.5
6051.5
6050.5
6049.5
0
200
400
600
g
Kaiwan Fluctus
6052.5
6051.5
6050.5
0
200
400
600
800

Table 3.2 Topographic data and average specific backscatter cross sections of the 50 flow fields.

Name/Source	Source Elevation/km	Average Topographic Slope	Specific Backscatter Cross Section/dB
Metis Regio	6053.4	0.32	-10.4
Lauma Dorsa	6051.0	0.07	-12.3
Iris Dorsa	6051.9	0.08	-12.1
Pandrosos Dorsa	6052.3	0.29	-12.9
Feronia Corona	6051.4	0.12	-14.9
Aitra Mons	6051.8	0.11	-4.7
Neago Fluctus	6052.0	0.01	-14.3
Sekmet Mons	6053.4	0.50	-11.8
Mist Fossae	6051.3	0.12	-12.8
Kawelu Planitia	6050.8	0.00	-13.3
Hroswitha Patera	6051.4	0.03	-15.1
Eastern Tepev Mons	6052.8	0.13	-14.3
Rusalka Planitia	6051.4	0.60	-14.5
Ulfrun Regio/ Ganiki Planitia	6051.6	0.17	-17.7
Ulfrun Regio/ Kawelu Planitia	6052.3	0.00	-15.1
Theia Mons	6056.2	0.41	-7.7
South Sappho	6053.2	0.52	-7.4
Sapas Mons	6054.5	0.52	-10.4
Ganis Chasma	6053.5	0.54	-8.0
Hecate Chasma	6051.7	0.02	-13.3

Table 3.2 continued

Name/Source	Source Elevation/km	Average Topographic Slope	Specific Backscatter Cross Section/dB
Asteria Regio	6051.8	0.37	-12.3
Large Volcano at 10.5N, 275E	6052.9	0.55	-16.1
Large Volcano at 9.5N, 309E	6053.0	0.05	-14.8
Shield Field at 13N, 314.5E	6051.9	0.12	-15.8
Corona at 9.2N, 315.5E	6051.3	0.05	-13.8
N Eigin Corona	6051.7	0.05	-8.8
Maat Mons	6060.5	0.77	-10.0
Northern Ozza Mons	6056.8	0.56	-17.3
SE Ozza Mons, Atla Regio	6053.5	0.05	-14.8
Large Volcano at 3.5N, 270E	6053.6	0.03	-17.3
Shield Field at 1.5N, 277.5E	6051.9	0.01	-12.4
Large Volcano at 2N, 316E	6052.1	0.06	-13.9
Kuanga Chasma	6054.7	0.24	-15.7
Corona at 21S, 119E	6053.4	0.30	-13.9
SE Thetis Regio	6053.3	0.01	-12.5

Table 3.2 continued

Name/Source	Source Elevation/km	Average Topographic Slope	Specific Backscatter Cross Section/dB
Rift Zone at 19.8S, 145E	6053.0	0.17	-12.7
Dali Chasma	6052.7	0.15	-14.3
Corona at 17.5S, 244E	6052.1	0.21	-13.6
Large Volcano at 12.5S, 261.5E	6053.3	0.41	-14.5
Large Volcano at 18S, 285E	6054.1	0.36	-12.7
Navka Planitia from 14S, 310E	6052.2	0.15	-13.2
Large Volcano at 27.5S, 262E	6052.4	0.06	-16.0
Parga Chasma at 30S, 265E	6052.6	0.12	-13.3
Eriu Fluctus	6051.4	0.07	-12.1
Ammavaru	6052.1	0.05	-7.4
Kaiwan Fluctus	6051.9	0.10	-11.6
Themis Regio	6053.3	0.58	-10.5
Mylitta Fluctus	6051.5	0.20	-9.2
SE of Aino Planitia	6051.5	0.05	-9.1
Quetzalpetlatl Corona	6053.0	0.15	-6.4

Table 3.3 Comparison of flow fields on the terrestrial planets. References: [a]Maack (1952), [b]Beurlen (1970), [c]Leinz et al. (1966), [d]Basaltic Volcanism Study Project (1981), [e]Richards et al. (1989), [f]Cox (1972), [g]Navlivkin (1973), [h]Green (1972), [i]Tolan et al. (1989), [j]Reidel et al. (1989), [k]Ghose (1972), [l]Sukeswala and Poldervaart (1958), [m]Lopes and Kilburn (1990), [n]Schaber (1973a, b).

Flow field or Province	Present (and possible original) area, km^2	Maximum (and average) thickness, m	Approximate total volume, km^3	Individual flow areas, km^2	Individual flow thicknesses, m	Individual flow volumes, km^3
Paraná Basin	1.2×10^6 [a] (2×10^6?)	1,500 - 1,800[b] (650)	650,000[c] (1.5×10^6?)		average = 50[d] maximum > 100	
Karroo Province	140,000 (2×10^6?)[f]	8,000 - 9,000[d] (1,000?)	420,000[f] (2×10^6?)[e]		average = 10[d] (= Lesotho)	
Siberian Platform	> 1.5×10^6 [g] includes intrusions	3,500[d] (1,000)	250,000[g]		average = 30[d]	
Lake Superior Basin (Keweenawan)	100,000 in Lake Superior area[d] (125,000?)	800 - 12,000[d] (5,000?) for several basins[d]	> 300,000 in Lake Superior area[d]		3 - 30[h] average = 25[h] maximum = 400[h]	
Columbia River Basalt Group	163,700 ± 5,000[i]		174,300 ± 31,000[i]	149,000 (= Grande Ronde Basalt)[j]	~ 3 to > 100 average = 30 (= Grande Ronde Basalt)[j]	maximum = 2,000 to 3,000[i]
Deccan Traps	520,000[k]	2,000[l]	700,000[k] (1.5×10^6?)			
Alba Patera, Mars				S-type fields: 33 - 1,800 M-type fields: 25,500 - 28,880[m]	S-type fields: 34 - 97 M-type fields: 80 ± 50%[m]	S-type fields: 1.6 - 174.8 M-type fields: 2,040 - 2,310[m]
Mare Imbrium			3×10^6 [d]		average = 30 - 35[n]	
Mylitta Fluctus, Venus	300,000	400 - 250?	19,982	7,900 - 117,960 (flow episodes)	10 - 30 ?	80 - 16,970 (using 10m thickness)

intended to provide a first order measure of the overall scattering behaviour of each field. During the averaging process a minor component (≤ 5%) from the plains between some flow lobes was included where the overall field boundary is particularly intricate. However the effect of this contamination is insignificant. In order to compare these results with backscatter data of terrestrial lava flows of known surface texture, the averaged pixel values were converted to specific backscatter cross-sections (i.e. the Muhleman scattering law was removed). The relationship between the averaged pixel DN and the specific backscatter cross-section was obtained by combining equations 1.1, 1.2, and 1.4:

$$\sigma_{obs} = 10^{0.02(\text{pixel DN} - 101)} \times (0.0118\cos(\theta + 0.5°)/[\sin(\theta + 0.5°) + 0.111\cos(\theta + 0.5°)]^3)$$

Eq. 3.1

The specific backscatter values were then converted to decibels using the relation:

$$\sigma_{obs} \text{ in dB} = 10 \times \log_{10}(\sigma_{obs})$$

Eq. 3.2

The average incidence angle for each field was taken into account and the results are given in Table 3.2 and Figure 3.5. Figure 3.5 plots the specific cross sections against incidence angle along with the Venus global average specific backscatter curve derived from 18 cm wavelength Pioneer Venus data (Pettengill et al., 1988). This curve provides a first order indication of the scattering behaviour of the background plains, which comprise 85% of the Venus surface. In order to compare the specific backscatter cross section of the great flow fields with terrestrial lava flows of known surface texture, AIRSAR data of aa and pahoehoe flows on Kilauea Volcano, Hawaii (Campbell and Campbell, 1992) are plotted on Figure 3.5. These terrestrial data include aa from 4 sites, and pahoehoe from 3 sites, which for simplicity have been combined into single aa and pahoehoe groups. The same data are plotted as separate sites and compared with the backscatter of flow fields within Mylitta Fluctus in Chapter 4, Figure 4.17. Variations in the radar backscatter between flow fields or across different portions of a single flow field in Magellan images are interpreted as primarily denoting changes in surface roughness at the scale of the radar wavelength (12.6 cm). The dielectric properties and viewing geometry may also affect the radar brightness of the flow fields. At different incidence angles the sensitivity of backscatter to variations on roughness and dielectric constant may differ (Plaut and Arvidson, 1992). Cycle 2 and 3 data provide additional viewing geometries, but were not included in the analysis for reasons of brevity, and lack of complete coverage. However, both Cycle 1 and 2 data are included in the analysis of the radar properties of flow fields within Mylitta Fluctus (Chapter 4). The backscatter data of the great flow fields are widely scattered about the Venus average surface, reflecting differences in incidence angle, surface texture and dielectric properties (Figure 3.5). Most of

Figure 3.5 The average specific backscatter cross section of each flow field plotted against incidence angle (Cycle 1 data). The Venus global average curve from Pioneer Venus data, after Pettengill et al. (1988), is plotted for comparison. Data for terrestrial aa and pahoehoe flow surfaces on Kilauea Volcano, Hawaii, from Campbell and Campbell (1992) are also shown for comparison.

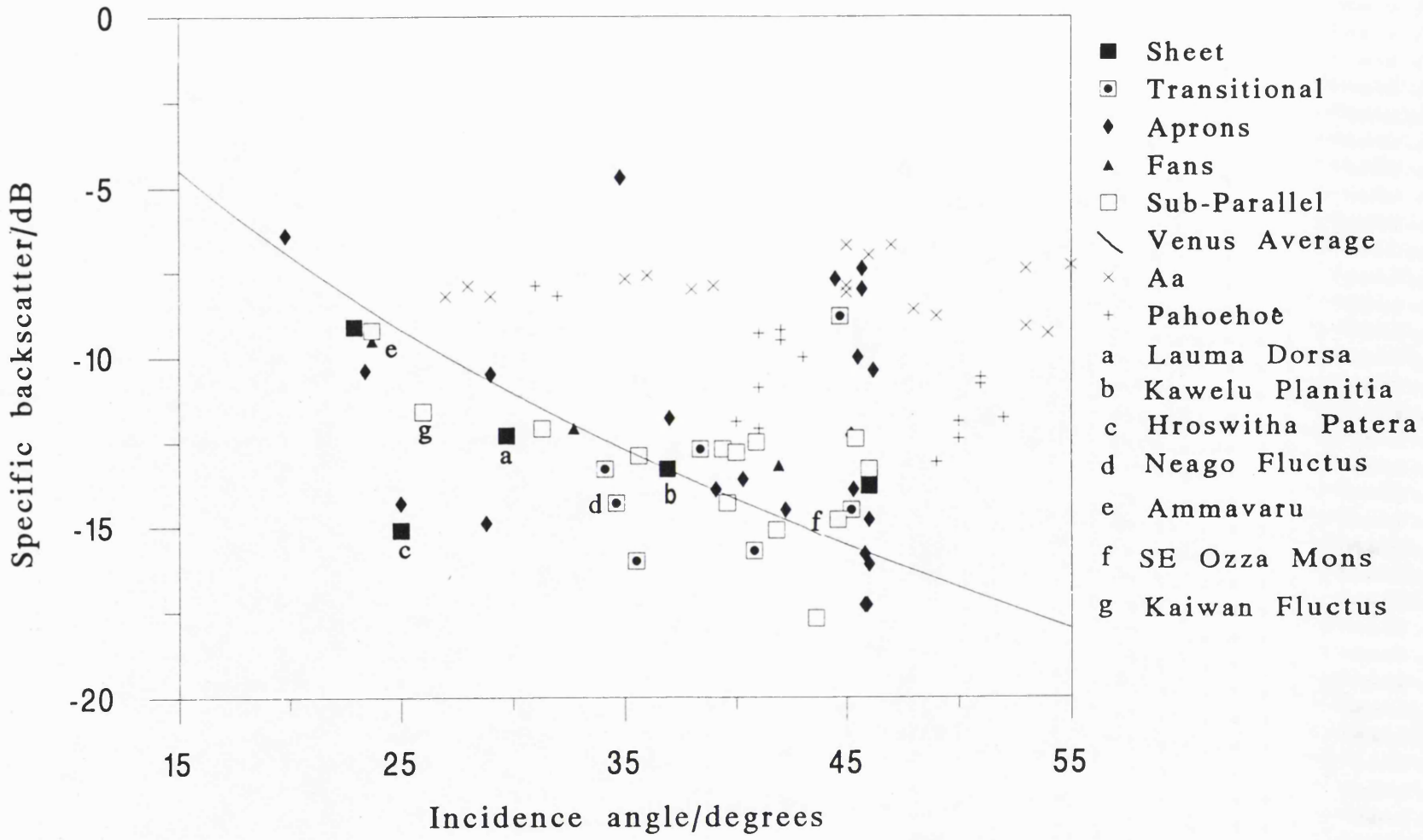
0
-5
-10
-15
-20
15
25
35
45
55
Specific backscatter/dB
Incidence angle/degrees
Sheet
Transitional
Aprons
Fans
Sub-Parallel
Venus Average
Aa
Pahoehoe
a Lauma Dorsa
b Kawelu Planitia
c Hroswitha Patera
d Neago Fluctus
e Ammavaru
f SE Ozza Mons
g Kaiwan Fluctus

the data points fall below the backscatter data of terrestrial aa and pahoehoe, implying that most of the great flow fields have very smooth pavement-like surfaces.

Most of the great flow fields are associated with deformation belts, which are interpreted to be zones of limited extension (Solomon et al., 1992) and rifting. The great flow fields are analogous to major units within terrestrial flood basalt provinces such as the Columbia River Flood Basalt Province, Paraná flood basalts and Deccan Traps (Tolan et al., 1989; Piccirillo, et al., 1988; Mahoney, 1988). Of the fifty great flow fields comprising this study, seven of the most outstanding have been chosen as particularly noteworthy of detailed study and mapping; Mylitta Fluctus is given detailed treatment in Chapter 4.

3.2 MORPHOLOGY

The flow fields have been classified as essentially either sheet-like or digitate in morphology (Figure 3.2). Sheet-like flow fields are essentially irregular in outline, with featureless interiors and relatively uniform backscatter, while digitate flow fields are made up of discrete flow lobes with a wider range of backscatter across a given field. Sheet flow fields form a class of their own, and digitate flow fields have been divided into three sub-classes, based on the degree of divergence between the constituent flow lobes. This distinction in morphology is interpreted to primarily be a result of emplacement style and source characteristics, with the digitate flow fields erupted as many discrete cooling-limited flows from mostly centralised sources, and the sheet flows as massive volume-limited eruptions from laterally extensive fissure systems onto essentially horizontal terrain. Several flow fields are transitional in form between sheet and digitate types, and a transitional class has therefore been included. Digitate and transitional fields are usually composed of several smaller fields and units, while sheet flow fields may represent single large eruptions.

3.2.1 Sheet Flow Fields

Sheet flow fields are distinguished by their relatively uniform backscatter, lack of internal flow structure such as well defined lava streams or channels, absence of flow lobes, and irregular boundaries (Lancaster et al., 1993). Internal flow boundaries are invisible in these fields, and as such they cannot usually be divided into separate flow units or smaller fields. Some of the larger sheet flow fields may be composed of a series of superposed flow units and/or fields, which, because of their nearly identical radar properties, may not be distinguished in the radar imagery. This is unlike the digitate and transitional flow fields, which can be divided into separate flow units and smaller fields. Some sheet flow fields consist of spatially separate but associated flow units of identical radar characteristics and similar morphology. These units appear to be fed by distributed vents but may derive from the same source region (e.g. Lauma Dorsa, Hroswitha Patera).

The five sheet flow fields included in the survey (Table 3.1) are widely distributed in longitude and lie on the plains. The total area of these fields ranges between 66,000 and 780,000 km^2 (Table 3.1). Maximum lengths from the source to the most distal reach are distributed between 450 and 880 km (Table 3.1). The vast extent and irregular non-lobate boundaries suggest ponding of lava, with local topography controlling the shape of the flow margins. The lack of recognisable internal flow boundaries and structure hinders the determination of flow direction and provenance. Using topographic data and assuming no post-emplacement topographic adjustment, the flow direction is inferred to be down-slope relative to the present topography. Sources may then be inferred from association with up-slope tectono-volcanic features, and include deformation belts inferred to be rift zones (Lauma Dorsa, Kawelu Planitia, and the field south-east of Aino Planitia) and coronae (Hroswitha Patera, and at 9.2° N, 315.5° E). In the case of the rift zones these fields appear to have been erupted concurrently from extensive fissures along continuous stretches of rift, forming extremely large and continuous expanses of lava (e. g. Kawelu Planitia). The sheet-like morphology may primarily be a result of massive volume-limited eruptions from laterally extensive stretches of fissure onto near-horizontal gradients.

The sheet flow fields are also typified by low source elevations which fall between 1.0 and 0.3 km below the mpr. The flows are apparently too thin to be expressed in the altimetry data, which a has an absolute uncertainty of 50 m (Pettengill, et al., 1991). This observation, together with the localised topographic control by narrow graben, ridges etc., suggests the flows to be less than 50 m thick at their distal margins.

Average specific radar backscatter cross sections of the sheet flow fields range between -15.1 and -9.1 dB (Table 3.2, Figure 3.5). The average backscatter values of all the sheet flow fields except the one associated with Hroswitha Patera follow a trend which is suggestive of a scattering law. This implies that the differences in backscatter between these fields are due primarily to incidence angle variations. Apart from Hroswitha, the sheet flow fields lie within 2 dB of the global average curve. This implies that these sheet flow fields display a similar scattering behaviour to that of the background plains. The spatially uniform radar properties and plains-like scattering behaviour of the sheet flow fields supports the contention that much of the plains may be composed of such fields. The average backscatter cross sections of the sheet flow fields are less than those of aa and pahoehoe surfaces plotted on Figure 3.5, implying extremely smooth surface textures. The field associated with Hroswitha Patera is of unusually low backscatter, and this is discussed in Section 3.2.1.3. Three sheet flow fields are described here in detail as examples: Lauma Dorsa, Kawelu Planitia and Hroswitha Patera.

3.2.1.1 Lauma Dorsa (Figure 3.6)

A 304,000 km^2 sheet flow field has flowed up to 540 km west from a 900 km long section of the north-south trending ridge belt of Lauma Dorsa in Vinmara Planitia. The spatial

Figure 3.6a Image of the sheet flow field associated with the western flank of Lauma Dorsa. Image is centred upon 60.0° N, 183.5° E and measures 1280 x 800 km.

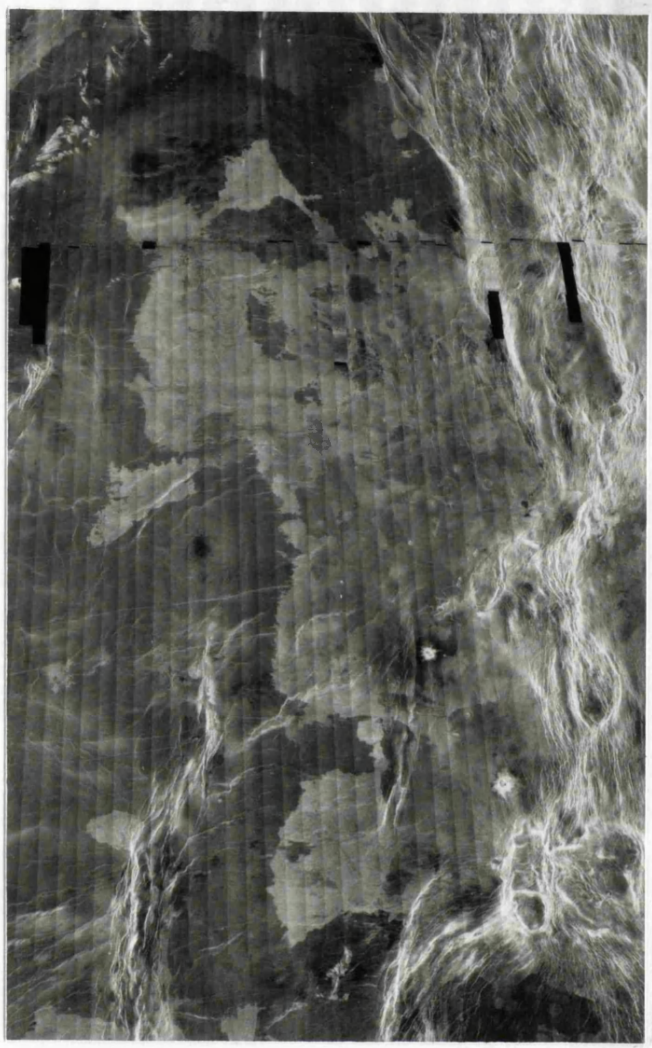
N

Figure 3.6b Sketch map of the Lauma Dorsa sheet flow field. The field is stippled and flow direction is indicated by arrows. S-X = line of topographic section (Fig. 3.4a).

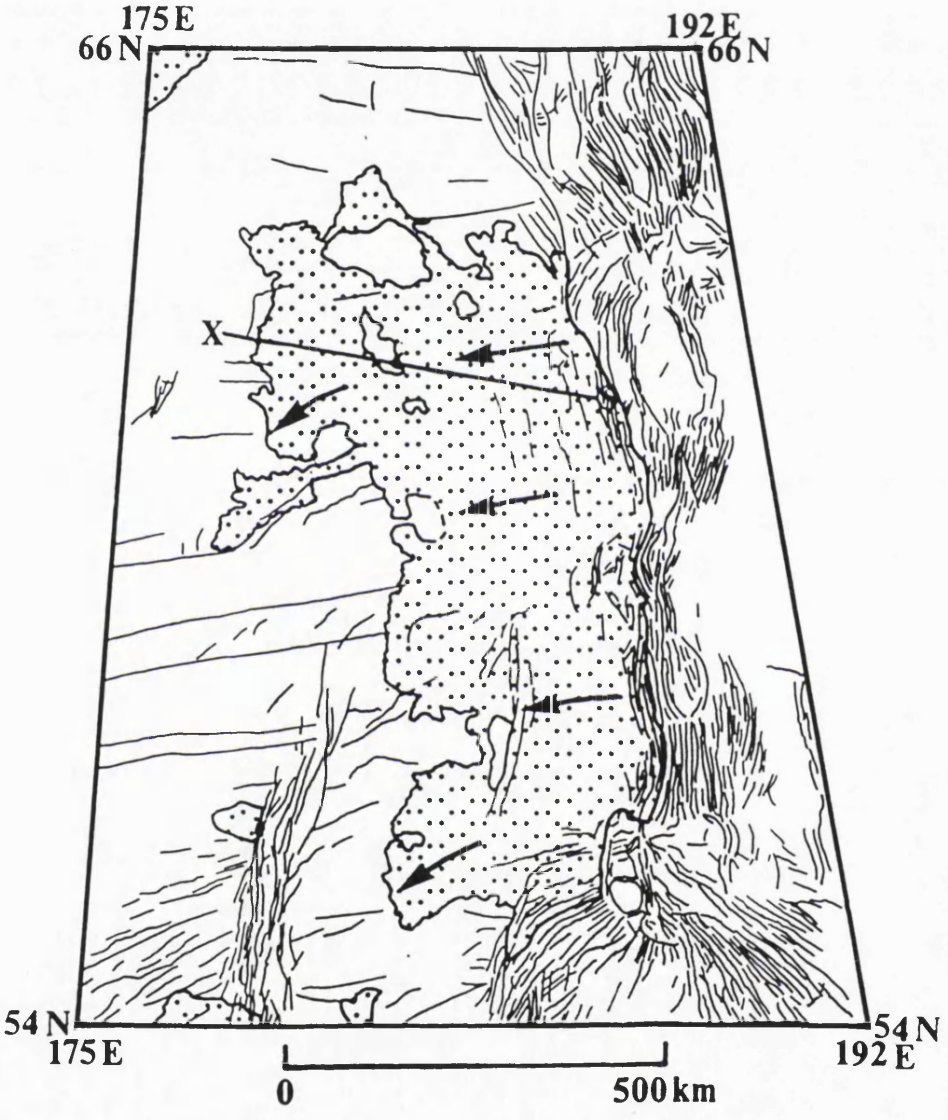
175 E
66 N
192 E
66 N
X
54 N
175 E
54 N
192 E
0
500 km

Figure 3.7 Image of the localised fissure sources (arrowed) in the Lauma Dorsa flow field at 64° N, 183-185° E. Image measures 250 x 340 km and is centred upon 63.6° N, 184.0° E.

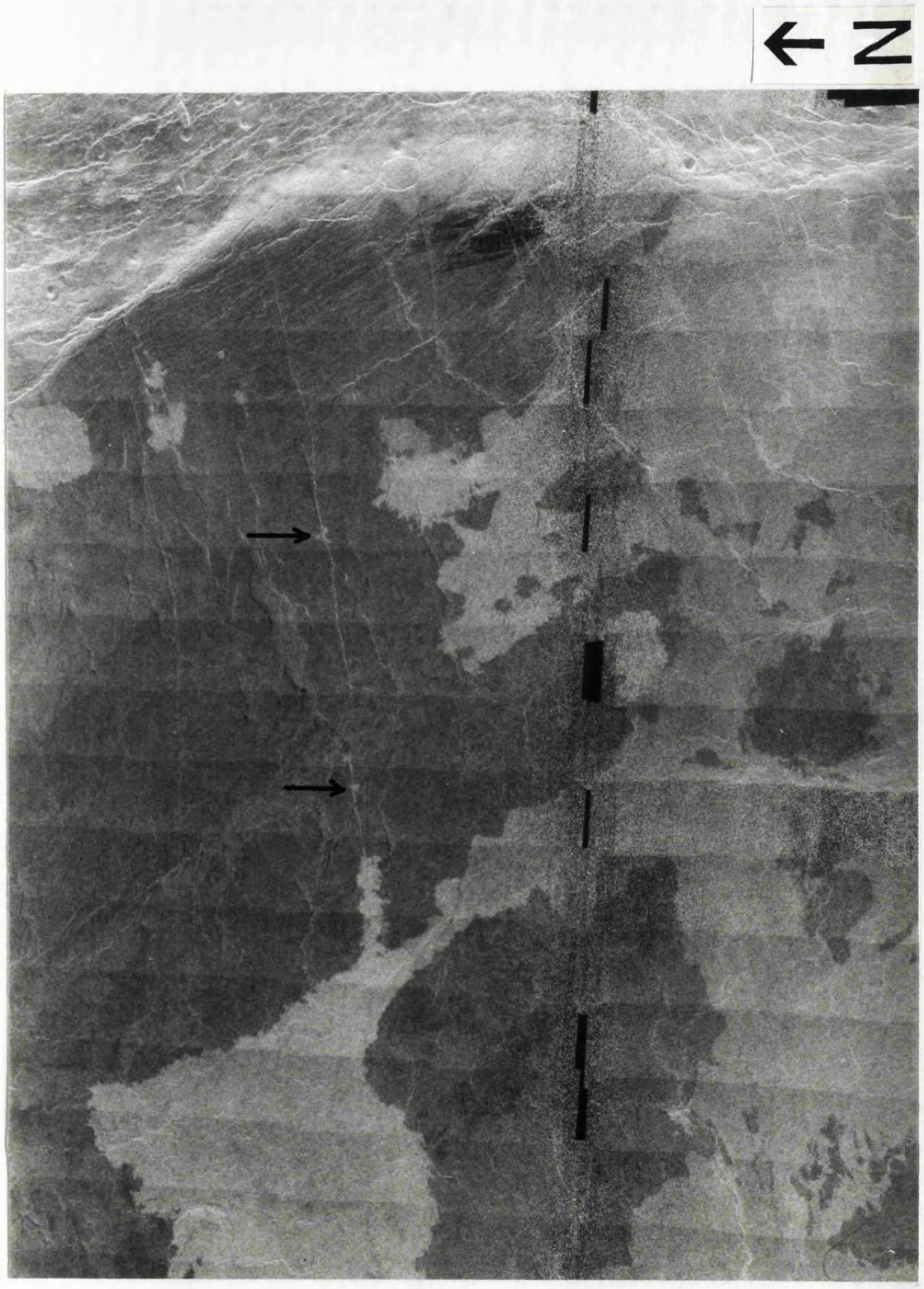
N

association of the flow field with the ridge belt suggests that Lauma Dorsa was the source. A region comprising at least 2 x 10^6 km^2 of sheet-like flows lies to the east of Lauma Dorsa. These flows are of similar backscatter to the western flow field, and may also originate from the same regional source. However, their boundary, particularly in the north, is ill-defined, and local source-flow relations have not been identified. Assuming that the surface topography of the field is representative of the underlying terrain, then the field was emplaced onto a nearly horizontal slope of 0.07° (Figure 3.4a).

Localised sources occur on the plains up to 200 km from Lauma Dorsa. At 64° N, 183-185° E, an east-north-east trending fracture appears to have fed the flow field to the west (Figure 3.7). Short flows also emerge from this fracture at 64° N, 185.2° E and 63.9° N, 183.8° E (arrowed), and are isolated from the main part of the field. Similar relations between east-west trending fractures and radar-bright flows are seen on the plains in the north-east of Figure 3.7. Many examples of extensive fracture systems with distal outflows have been documented by Parfitt and Head (1992a,b, 1993a,b), who suggest that they are the surface expression of dike swarms emplaced under buffered conditions. These observations suggest that some component of the flow field was locally fed by approximately east-west trending dikes, as well as from fissures within Lauma Dorsa itself.

Many north-south trending ridges on the western flank of Lauma Dorsa appear to be post flow emplacement, as they superpose the east-west trending fractures and the radar backscatter of the ridges and the inter-ridge material is very similar to that of the flow field. A compressional origin for Lauma Dorsa has been proposed (Sukhanov and Pronin, 1989; Grosfils and Head, 1992), whereas an extensional regime involving open fissures is required to feed the flows. The compressional structures may be largely post-volcanic, with the volcanism occurring during an earlier phase of rifting. However some post-volcanic extension has occurred as evidenced by en-echelon faults trending north-south and subparallel to Lauma Dorsa in the proximal portion of the field (Figure 3.6b).

The average specific radar backscatter of the field is -12.3 dB, only 2 dB below the Venus global average specific backscatter of - 11 dB at the incidence angle of 30° (Figure 3.5). The backscatter is somewhat variable in the centre of the field between 59° to 61° N and 182.5° to 187° E, giving a "patchy" appearance on the image. These "patches" are about 5 to 20 km in diameter and interpreted as either flows emplaced from ephemeral boccas or small, possibly monogenetic, shield volcanoes with little or no topographic expression. Hence the localised eruption and emplacement of flood lavas such as Lauma Dorsa could occur by both fissure and bocca fed mechanisms at considerable distances from the locus of magmatism.

3.2.1.2 Kawelu Planitia (Figure 3.8)

Kawelu Planitia contains a sheet flow field covering an area of 780,000 km^2, which has flowed up to 630 km south-west of a north-west-south-east trending deformation belt consisting of several tectono-volcanic centres and belts of lineaments. These centres include

Figure 3.8a Image of the sheet flow field in Kawelu Planitia. Image measures 1340 x 1690 km and is centred upon 46° N, 264° E.

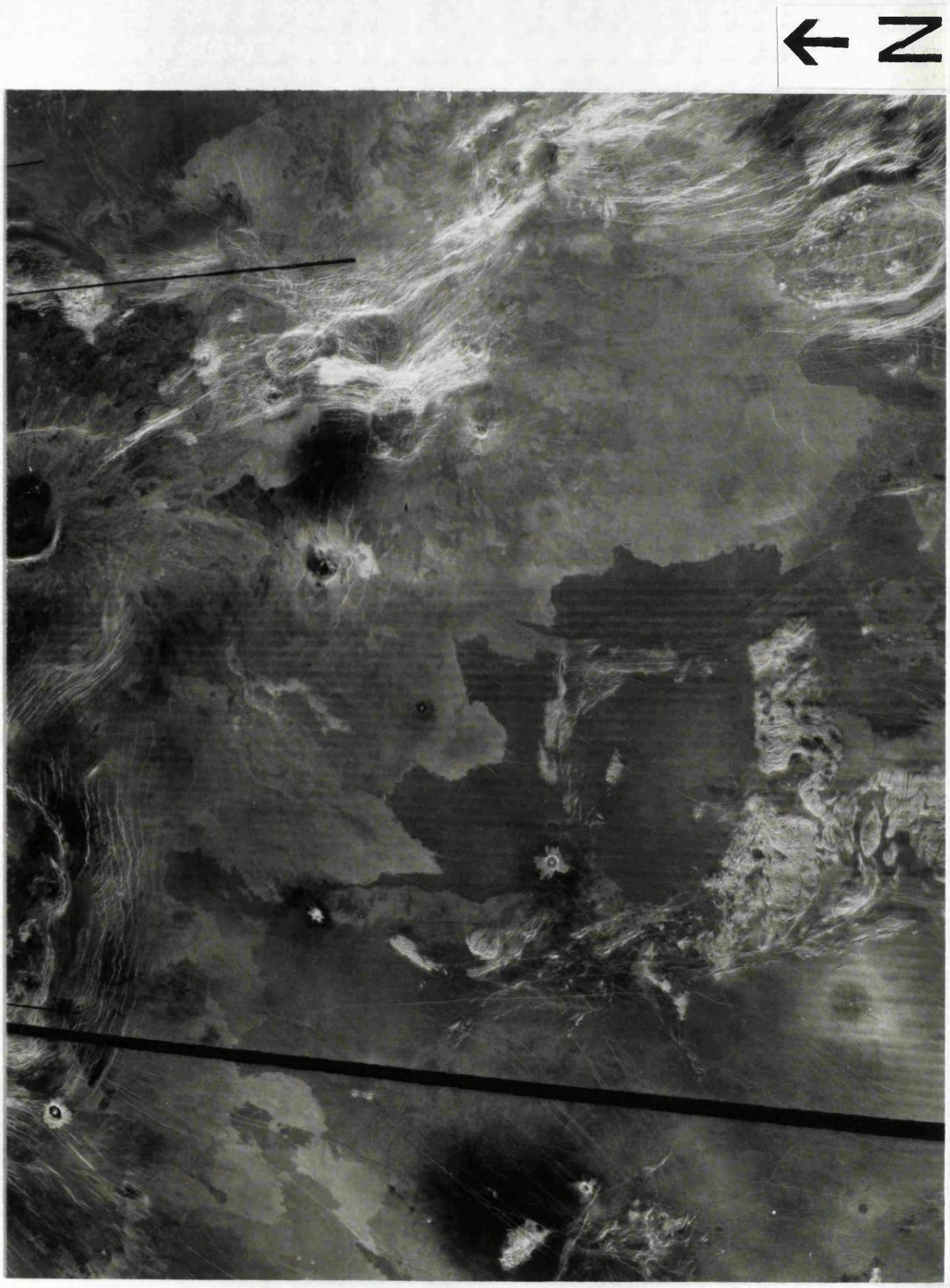
← Z

Figure 3.8b Sketch map of the sheet flow field in Kawelu Planitia. Letters correspond to features described in the text, S-X = line of topographic section (Fig. 3.4b), T = tessera, impact deposits are shown in black and the darkest stipple. Flow direction is indicated by arrows.

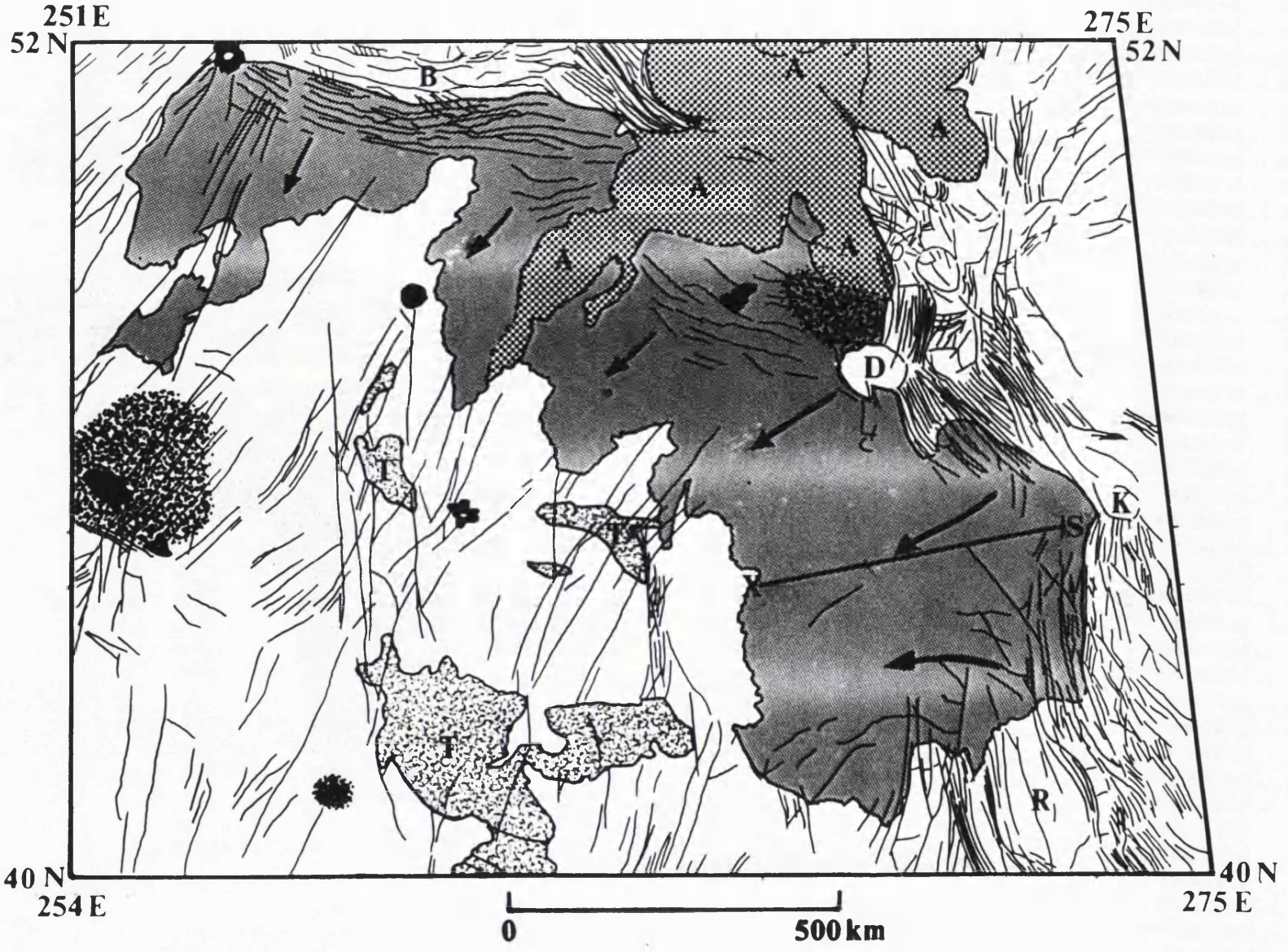
251E
52 N
275E
52 N
B
A
A
A
A
A
D
T
T
T
K
S
R
40 N
254 E
40 N
275 E
0
500 km

Figure 3.9 Close-up of the distal margin of the Kawelu Planitia sheet flow at 46° N, 260° E, showing north-east-south-west trending graben filled by lava. Image measures 240 x 320 km and is centred upon 47.1° N, 261.6° E.


←Z

Davies (47°N, 269°E; D, Figure 3.8b) and Keller (45°N, 273.5°E; K) Paterae, which lie at either end of Dodola Dorsa. Bau Corona (51-55°N, 254-262°E; B) lies at the north-west margin, and flows from Aitra Mons (52.3°N, 267.5°E; A) have been emplaced on the field. The peripheral trough of Rauni Corona (39.3-42.2°N, 271.6-272.3°E; R) is embayed by the field. In common with other sheet flows the backscatter is fairly uniform across most of the field, and lies close to the Venus average at -13.3 dB (Figure 3.5). Thus the field appears to be spatially continuous, but may have been erupted diachronously from different sources and stretches of fissure along the deformation belt, which is interpreted as a series of discontinuous rift zones. The average elevation of these source regions is 1 km below the mpr, and the topographic surface of the field is essentially horizontal (Figure 3.4b, Table 3.2). The distal boundary of the field exhibits local topographic control where lava has flowed up to 10 km along narrow graben (Figure 3.9).

3.2.1.3 Hroswitha Patera (Figure 3.10)

Hroswitha Patera is a corona-like volcano-tectonic centre in Bereghinya Planitia (H, Figure 3.10b), which is the source of radar-dark sheet flows with an unusually low average specific radar backscatter of -15.1 dB (Figure 3.5). This backscatter is nearly 7 dB below the Venus global value for the incidence angle of 25°. The field is also characterised by very low rms slopes of 0.4° to 0.8°. The field displays an spatially uneven reflectivity of around 0.11, which is only slightly enhanced with respect to the surrounding plains, and matches the typical reflectivity of the plains in general. The emissivity of the field, although unstriking, measures about 0.84, consistent with the reflectivity data. These observations suggest that the low radar backscatter is due to a very smooth surface texture rather than a low intrinsic reflectivity. This implies that the surface of the flow underwent little or no disruption during the final stage of emplacement and cooling. Such a smooth surface may have resulted from a lava which remained very fluid throughout its emplacement and formed a surface which solidified only after the flow was finally at rest. The spatially uniform backscatter implies that similar rheological conditions existed throughout the field.

The field covers some 197,000 km^2, is 880 km long, and 410 km in overall width; the average topographic slope of the flow surface is 0.03° (Figure 3.4c). The field has been emplaced as several elongate flows whose margins appear to be controlled by the pattern of narrow ridges on the plains. Some of these ridges appear in the interior of the field itself as radar-bright features. These observations suggest that volcanism occurred both before and after the tectonism in the area. The main expanse of the flow field appears to be isolated from portions closer to Hroswitha, as do smaller areas of lava to the north and south. Each isolated section may be locally fed, or alternatively they may be continuous with each other, the "missing" areas of lava having radar properties almost identical to those of the surrounding plains.

Figure 3.10a Image of the sheet flow field associated with Hroswitha Patera. Image measures 860 x 1380 km and is centred upon 37.5° N, 29.6° E.

←Z

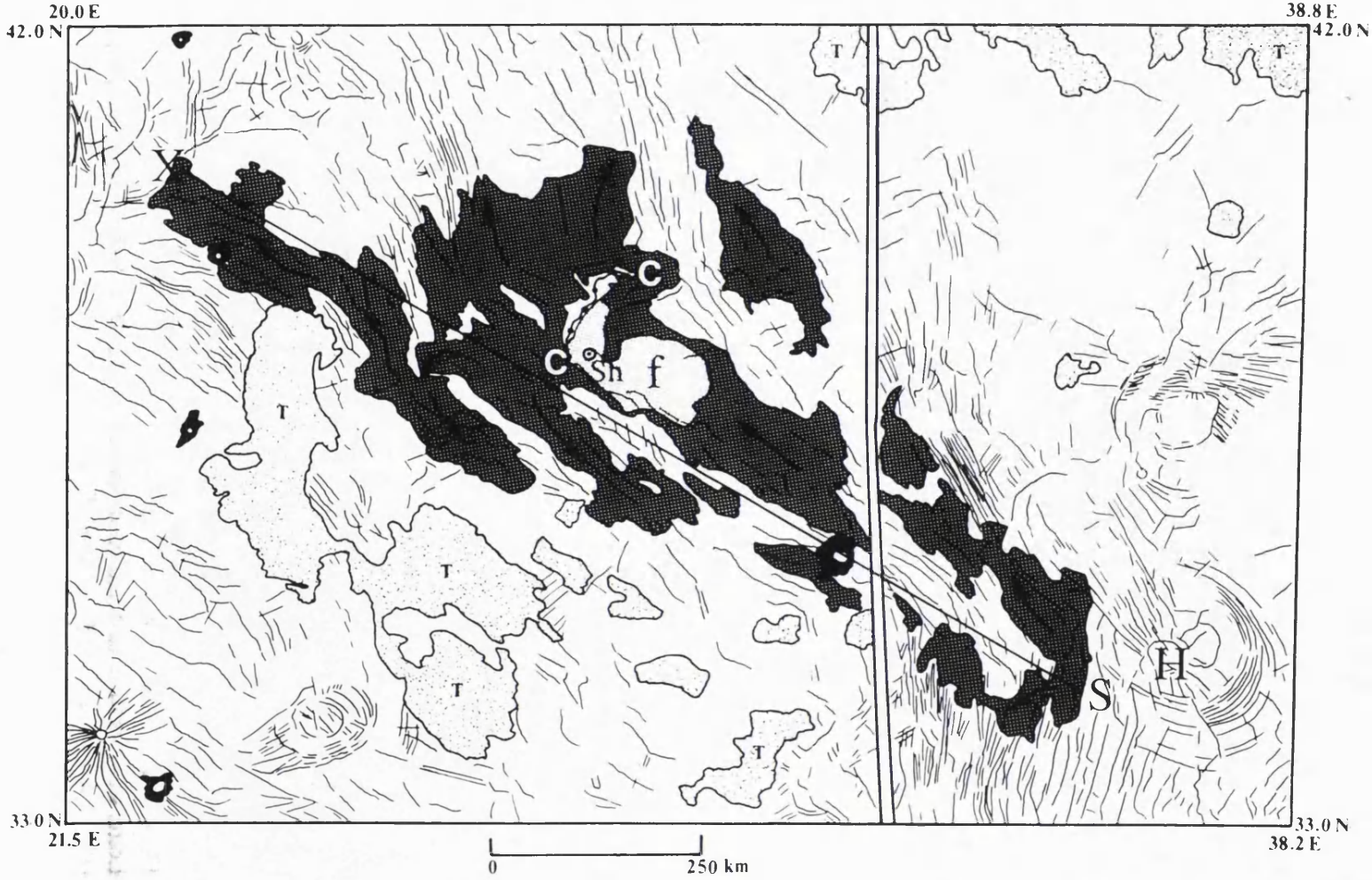
20.0 E
42.0 N
38.8 E
42.0 N
T
C
C
Sh
f
T
T
T
T
S
H
33.0 N
21.5 E
33.0 N
38.2 E
0
250 km

Around 37.5-39.5° N, 27.5-29.5° E several small volcanic shields and pits (Sh, Figure 3.10b) are superimposed on the flow field, as is a 140 km long, 2 km wide lava channel with radar-bright overspills (C-C). The channel may be traced back to a possible source at 37.8° N, 28.8° E, and is associated with a region of lava flows with a higher backscatter than the rest of the field (f). These volcanic features may not be related to the flow field development, but their spatial association with the field is intriguing. They may represent late-stage locally fed volcanism, but from the same source region as the main flow field.

3.2.2 Transitional Flow Fields

These are transitional between sheet and digitate morphologies and contain sheet-like, broad lobate and ponded flow units and fields. These component units and fields display uniform radar properties and may be defined by their characteristic backscatter (e.g. Neago Fluctus), and contain little or no internal structure, although channels are present in some examples (Figure 3.2). Seven transitional flow fields have been included (Table 3.1), of which Neago Fluctus is considered in depth. Total areas of between 154,000 and 744,000 km^2 have been recorded (Table 3.1). Maximum lengths are 450 to 2,840 km (Table 3.1). The more digitate planform of the transitional flow fields results in greater length to width ratios.

Sources for transitional fields include large volcanoes, coronae, and possible rift zones. Source elevations reflect the wider range of source types, and fall between 0.4 km below and 2.9 km above the mpr (Table 3.2). Average topographic slopes lie between 0.01 and 0.6° (Table 3.2). Average specific radar backscatter values of between -16.0 and -8.8 dB have been recorded, with about 85% of the transitional flows having specific cross sections of between -16.0 and -12.0 dB, (Table 3.2, Figure 3.5). These backscatter values are more widely scattered about the Venus global average curve than those of the sheet flow fields, and only cover about 10° in incidence angle. The variations in average backscatter reflect the wider range in backscatter displayed by different flows within and between transitional fields, and are attributed to differences in surface roughness and dielectric properties. Most of the transitional fields have average backscatter values which are below those of the comparison terrestrial fields, suggesting that they are mostly characterised by flow surfaces which are smoother than pahoehoe. However, one of the transitional fields (associated with Eigin Corona), has an average specific backscatter which approaches that of terrestrial aa.

3.2.2.1 Neago Fluctus (Figure 3.11)

Neago Fluctus in northern Sedna Planitia covers 744,000 km^2, measures 1900 km north-south by 800 km east-west, and was erupted from fissures in Clotho Tessera at the south-east border of Ishtar Terra. It is an assemblage of several superposed, radar-bright and dark ponded flow fields, which are broadly lobate and have widths of several hundred

Figure 3.11a Image of Neago Fluctus in Sedna Planitia. Image measures 210 x 1330 km and is centred upon 51.3° N, 350.1° E.


N

Figure 3.11b Sketch map of Neago Fluctus. Stratigraphy after Arvidson et al. (1992). S-X = line of topographic section (Fig. 3.4d). Letters correspond to features described in the text. Arrows indicate flow direction.

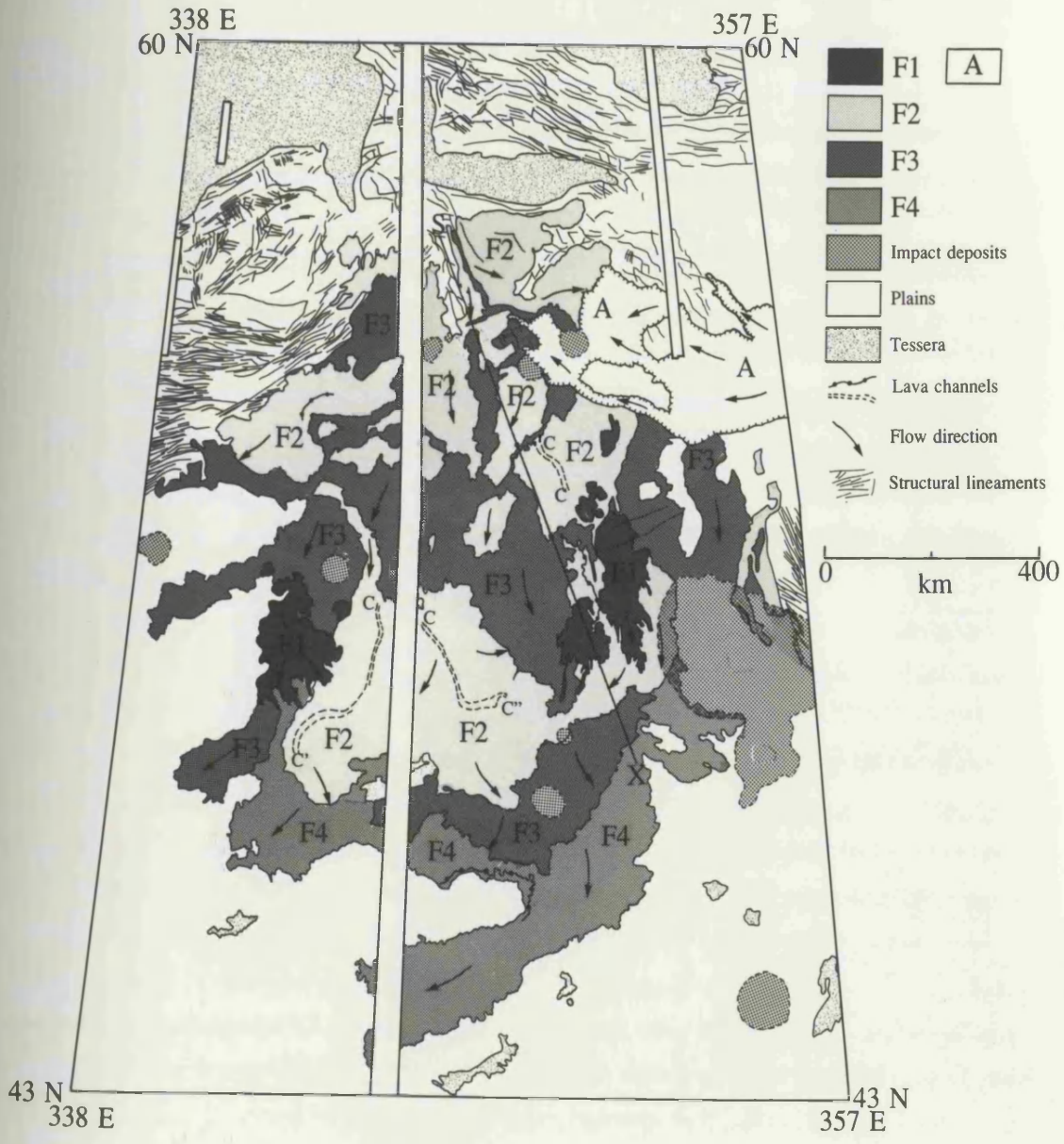
338 E
60 N
357 E
60 N
F1
A
F2
F3
F4
Impact deposits
Plains
Tessera
Lava channels
Flow direction
Structural lineaments
0
km
400
43 N
338 E
43 N
357 E

kilometres. Four flow units (described in this work as fields) were identified by Arvidson, et al., (1992), on the basis of specific backscatter cross section, rms slopes, and stratigraphic relationships. They found a decrease in backscatter cross section and rms slope with relative stratigraphic age, and, by comparison with AIRSAR data, explained this as due to weathering and degradation of the flow units with time. They deduced a surface modification rate of approximately 1 meter per 0.6 Ga for this part of Sedna Planitia.

Following the stratigraphy of Arvidson et al. (1992), the youngest flow field, F1, occupies the smallest area (29,000 km^2) and has the lowest backscatter (-14.4 dB). Rather than being a continuous flow field, it is composed of a number of individual flow units which appear to have erupted from a cluster of small volcanic vents around 50-53° N, 350-353° E. The flows form approximately circular aprons up to about 30 km in diameter around the vents, which have in many cases continued their emplacement to form narrow digitate flows up to 5 km wide, coalescing to form lobate regions up to 75 km across and 290 km long. A similar, but smaller flow field with nearly identical characteristics occurs around 29-31°N, 341.5-344°E, and bears the same stratigraphic relationship to the other fields as the flows around 50-53°N, 350-353°E; it covers 23,000 km^2. The coalescence of identifiably separate flow units into regions of uniform radar properties, where the individual units cannot be discerned where they overlap, supports the contention that many of the flow fields, and indeed large expanses of plains, are composed of many smaller individual flow units. These relatively young, locally fed, and low backscatter fields lie some 900 km from the source of the major units of Neago Fluctus, and therefore may not be related to the same volcanic events and/or source which formed the rest of the field.

F2 has the highest backscatter of the Neago flow fields (-8.2 dB, Arvidson et al., 1992), and covers 355,000 km^2 where exposed. This field may be traced to north-south trending fissures in the southern margin of Clotho Tessera around 55.5° to 57.5°N, 347°E, at an elevation of 0.2 km above the mpr. The largest expanse of F2 occurs in the southern part of the assemblage and comprises a broad sheet covering 167,000 km^2. This section is fed by at least 2 channels, 12 km wide and up to 360 km long (C-C' and C-C", Figure 3.11b). F2 occurs as a patchwork of spatially separate regions north of 52° N. These regions have irregular boundaries and are separated by field F3. In places the regions are separated by only 4 to 10 km (e.g. at 56.7° N, 347.1° E and 53.5° N, 349° E) and there is a channel (C-C) on F2 which appears to be truncated by F3. Thus F3 appears to be younger than F2 in this region, whereas the two fields are stratigraphically reversed to the south. The emplacement of F2 and F3 may have overlapped in time and F3 may actually be two separate fields of similar backscatter, one older and one younger than F2.

F3 (-12.7 dB) is exposed for 649,000 km^2 around the patchwork of F2 in the north, and is the most extensive of the Neago flow fields. This field lies directly on the plains to the west of Neago, but overlaps F4 to the south. A small subparallel flow field has flowed from the west over F2 and F3 in the proximal portion of Neago (A, Figure 3.11b). F4 (-11.2 dB) constitutes the oldest field in the assemblage may only be seen in the south where it lies directly on the plains. F4 cannot be traced to source, both the proximal and medial regions

being buried beneath the later fields. The exposed section of F4 covers 177,000 km^2 and includes a broad lobe of up to 160 km in width and 480 km in length.

The source region of Neago Fluctus lies in the tectonically disrupted terrain of Clotho Tessera at the south-east margin of Ishtar Terra. Mantle upwelling and downwelling have both been proposed as hypotheses for the formation of Ishtar Terra (Kaula et al., 1992). As with all the non-central great flows composed of singularly large flood-like fields, a tectono-volcanic episode involving extension or some form of rifting is envisaged. This is difficult to reconcile with the location of Neago at the compressive margin of Ishtar. Nevertheless these mountain belts and Clotho tessera show many extensional features which Smrekar and Solomon (1992) cite as evidence for gravitational sliding. These extensional features in turn may have facilitated the volcanism in the region (Solomon et al., 1992), which also includes collapse pits and lava channels in the adjacent Danu Montes.

3.2.3 Digitate Flow Fields

Digitate flow fields consist of several or many discrete flow units and smaller fields (Figure 3.2). They are the most common type of flow field on Venus (including scales less than the arbitrary 50,000 km^2), and comprise 76% of this survey, or 38 fields (Table 3.1). Total areas range from 50,000 to 1.5 x 10^6 km^2 and maximum lengths fall between 150 and 1,460 km (Table 3.1). They are usually composed of many individual flow lobes, which have a wide range of dimensions and a variety of specific backscatter cross sections. Both radar-bright and radar-dark flow units and fields occur in the same assemblage. Altogether, digitate flow fields have specific backscatter cross sections of between -17.7 and -4.7 dB, scattered widely about the Venus global average curve (Table 3.2, Figure 3.5). This variation is interpreted as due to a combination of incidence angle, surface roughness and dielectric differences. Source elevations lie between 0.3 km below and 8.7 km above the mpr (Table 3.2). The digitate morphology may primarily reflect the eruption of numerous individual cooling-limited flows from more centralised sources, rather than the eruption of massive volume-limited fields from laterally extensive fissure systems, as in the sheet flow fields.

Within a given digitate flow field, numerous superposition relationships occur between individual flow units and constituent fields, and quite complex flow stratigraphies and eruption histories may be inferred (e.g. Mylitta Fluctus, Chapter 4). On the basis of the distal widening of the overall flow field and the downstream divergence between flow lobes, digitate fields have been subdivided into aprons, fans and subparallel morphological classes (Figure 3.2). Aprons and fans have centralised sources, including clusters of small shields and coronae, while the subparallel flow fields have been erupted from less centralised sources, including sections of rift zone and laterally extensive fissure systems. Aprons completely surround the source whereas fans are confined to a particular range of directions by the local topography.

3.2.3.1 *Aprons and Fans*

The aprons represent the most common type of digitate field, and indeed the most common of all the flow fields in this survey, while the fans are relatively rare. Each apron or fan may be composed of several tens to many hundreds of radar-bright and dark flow lobes, radially arranged about a central source region. Individual flow lobes range from a few hundred to several thousand square kilometres in area, with lengths between a few tens and several hundred kilometres. Individual flows have widths of several to a few tens of kilometres, and they usually undergo some distal widening. The proximal portions are often channelled, or composed of very narrow flows on the order of 1 km wide, and there is considerable overlapping of flow units. Most of the aprons represent large central volcanoes, and often surround coronae or corona-like features. These Venusian examples suggest that the role of centralised volcanism in terrestrial flood basalt provinces merits further attention.

The 22 aprons in this study range in area from 81,000 to 1.5 x 10^6 km^2, average apron radii lie in the range 150 to 380 km, and maximum flow lengths of 220 to 850 km have been measured (Table 3.1). Over 75% of the aprons possess particularly extensive flows, which extend beyond the main apron in one or more directions and onto the surrounding plains. They are often of low backscatter and usually predate the main phase of apron development. These extensive distal lobes are essentially flood-type flow fields in themselves, and may represent earlier, more voluminous eruptions in the development of these centralised fields.

Source elevations fall between 0.4 km below to 8.7 km above the mpr, and topographic slopes range from 0.03 to 0.77° (Table 3.2). The aprons display the widest variation in specific backscatter about the Venus global average, with values of -17.3 to -4.7 dB (Table 3.2, Figure 3.5). The wide range of average specific backscatter between different aprons is due to a combination of different incidence angles and surface properties. However, there is a spread of up to 10 dB for 12 aprons with an incidence angle close to 45°, which may be attributed to variations in both surface texture and dielectric properties (Figure 3.5). The varying proportions of radar-bright and dark flow units, and the presence of high reflectivity summit material in some aprons may contribute to this variation. Details of various aprons are provided in Head et al. (1991, 1992) and Keddie and Head (1992), and no further treatment is given here.

Fans are the least common type of flow field, only three being identified in this survey (Table 3.1). They may be considered as incomplete aprons whose emplacement has been constrained by local topography to a narrow range of directions. Individual flow lobes possess the same dimensions and radar properties as those within the aprons. The fans range in area from 86,000 to 242,000 km^2, with maximum lengths of between 360 and 720 km (Table 3.1). Two of the fans are associated with clusters of small shields at Iris Dorsa and Ammavaru, while the third appears to have been erupted from a set of north-south trending fissures at 14° S, 310° E. Ammavaru is considered in more detail below. The specific backscatter cross sections of the fans range from -13.2 to -7.4 dB, and lie within 2 dB of the Venus global average curve (Table 3.2, Figure 3.5). Differences in incidence angle may account for most of

Figure 3.12a Image of the flow field associated with Ammavaru caldera. Image measures 1180 x 1720 km and is centred upon 46.7° S, 24.9° E.


←Z

Figure 3.12b Sketch map of the flow field associated with Ammavaru caldera. Letters correspond to features described in the text. S-X = line of topographic section (Figure 3.4e).

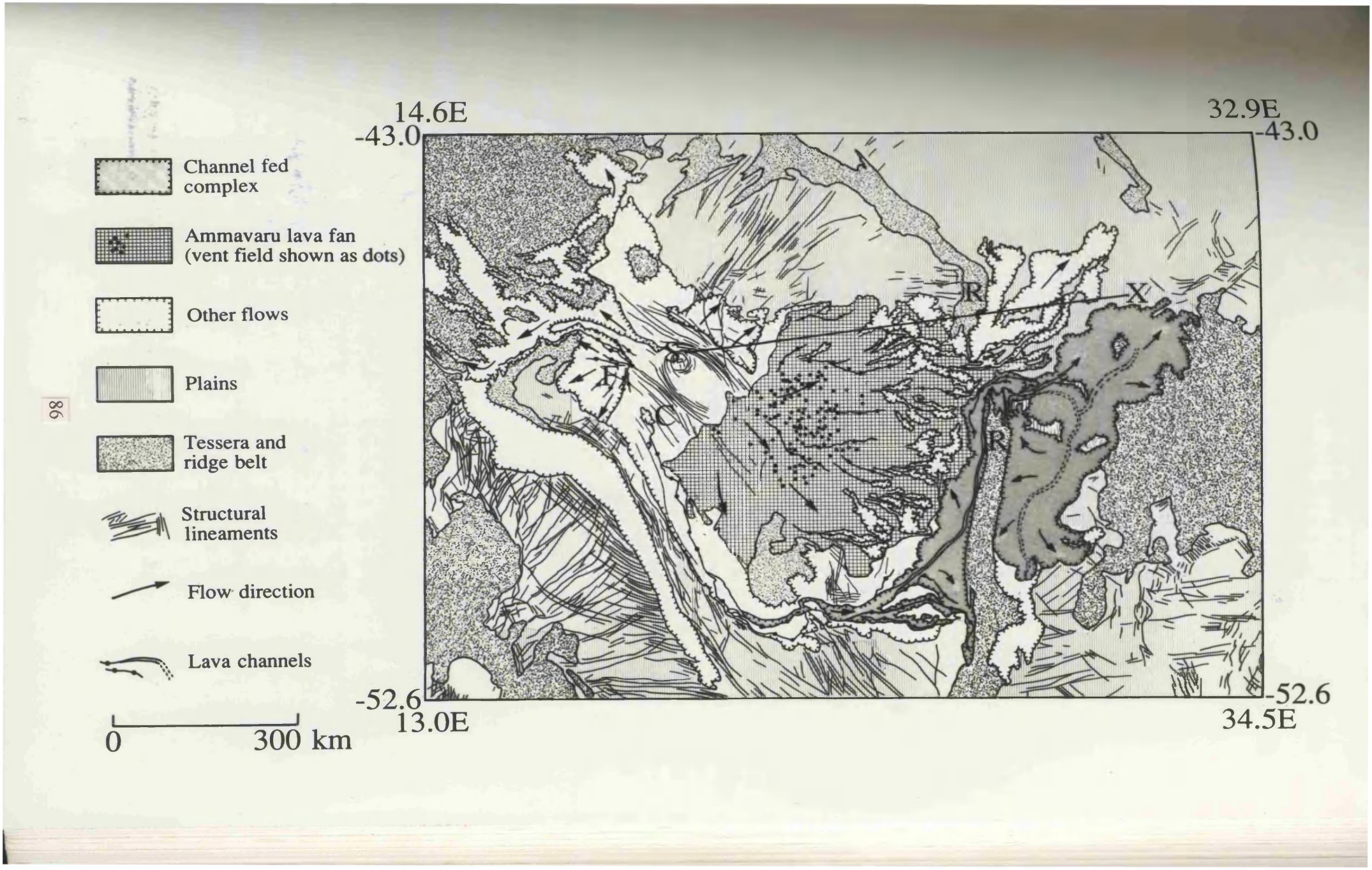
14.6E
32.9E
-43.0
-43.0
-52.6
-52.6
13.0E
34.5E
Channel fed complex
Ammavaru lava fan (vent field shown as dots)
Other flows
Plains
Tessera and ridge belt
Structural lineaments
Flow direction
Lava channels
0
300 km
R
X
F
C
R

this variation, and the three fans all have average backscatter cross sections less than the terrestrial fields.

3.2.3.1.1 Ammavaru (Figure 3.12)

A 470 km wide, 164,000 km^2 lava fan has been emplaced to the south-east of the caldera-like structure named Ammavaru (S, Figure 3.12b), on the northern edge of Lada Terra. The fan has a maximum length of 460 km, and is composed of many small, radar-bright and dark channel fed flows, that have emanated from a field of small volcanoes to the south-east of the caldera. The most proximal lava flows superpose the concentric structures around Ammavaru. Individual radar-bright flow lobes have lengths of up to 110 km and define the distal portions of the fan. Radar-bright flows at the distal portion of the fan have breached a north-south trending ridge belt (R - R) before spreading out to form large digitate lobes covering a total of 78,000 km^2 on the plains to the east of the belt. A small channel fed fan is also located at 47° S, 18° E (F, Figure 3.12b). A topographic profile across the assemblage yields an average slope of 0.05° (Figure 3.4e), and the summit caldera lies at an elevation of 0.3 km above the mpr.

3.2.3.2 Subparallel Fields

Subparallel flow fields consist of numerous, adjacent and sometimes overlapping digitate flow units (and fields), which maintain approximate parallelism at distances far from the source. Thirteen subparallel flow fields have been included in this survey, ranging in area from 50,000 to 868,000 km^2, with maximum lengths of between 340 and 1,460 km (Table 3.1). Of the digitate flow fields, individual units (and component fields) of subparallel fields are the most extensive in terms of area, length and width. Individual units and fields may broaden into wide distal ponds, on the order of 100 km wide.

Nearly 80% of the subparallel fields in this study appear to be related to rift zones, and often to central volcanic sources on rifts (e.g. Mylitta Fluctus, Magee Roberts et al., 1992).[3] Other sources include fields of small volcanoes, coronae, and fissure systems. Source elevations lie between 0.5 km below and 2.3 km above the mpr, with over 90% less than 2.2 km above the mpr (Table 3.2). Average topographic slopes of up to 0.36° have been measured and only 23% have slopes above 0.20°. Specific backscatter cross sections range between -17.7 and -9.2 dB (Table 3.2, Figure 3.5). This variation may be due to a combination of differing incidence angles, textural and dielectric properties. A number of the subparallel fields have specific cross sections which approach those of pahoehoe fields. The assemblage of flow fields on the south-east flank of Ozza Mons and Kaiwan Fluctus in Lavinia Planitia are considered in detail.

[3]Note that Magee Roberts et al. (1992) is also referenced as Roberts et al. (1992) in the literature.

Figure 3.13a Image of the flow field on the south-east flank of Ozza Mons in Atla Regio. Image measures 700 x 1390 km and is centred upon 4.0° S, 206.1° E.


←Z

Figure 3.13b Sketch map of the flow field on the south-east flank of Ozza Mons in Atla Regio. S-X = line of topographic section (Figure 3.4f).

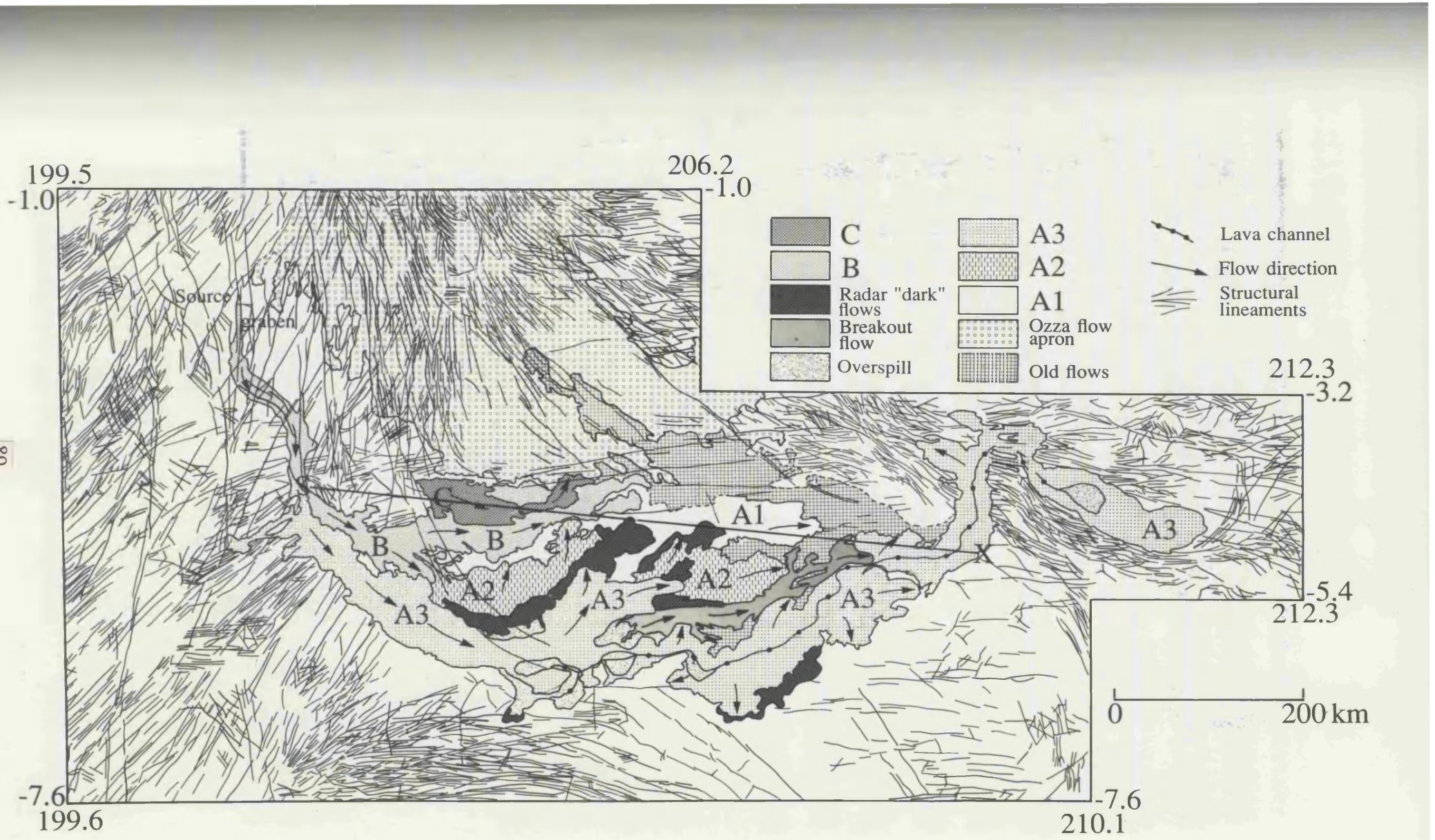
199.5
-1.0
206.2
-1.0
C
B
Radar "dark" flows
Breakout flow
Overspill
A3
A2
A1
Ozza flow apron
Old flows
Lava channel
Flow direction
Structural lineaments
Source graben
212.3
-3.2
A1
A3
B
B
A2
A3
A2
A3
A3
X
-5.4
212.3
0
200 km
-7.6
199.6
-7.6
210.1

Figure 3.14 Close-up of channel overspills on unit A3 of the south-east Ozza Mons flow field (arrows). S = partially embayed shield volcanoes, a and b are sources of radar-dark flows described in the text. Image measures 210 x 280 km and is centred upon 6.2° S, 205.0° E.

N
a
b
s

3.2.3.2.1 South-east Ozza Mons (Figure 3.13)

This remarkable assemblage of flow fields lies along the extreme south-east flank of the large volcano Ozza Mons in Atla Regio. Covering a total of some 121,000 km^2, it can be traced to several wide, north-south trending graben which are radial to Ozza Mons. The overall length and width of the assemblage is 1,460 by 270 km respectively, and a topographic profile is provided in Figure 3.4f. Head et al. (1992) identify 4 flow units within this complex, however a more detailed mapping of this field has been undertaken, and at least 6 constituent flow fields are identified on the basis of superposition relationships, breakouts, channels and backscatter characteristics.

The oldest "field" identified is that of "old flows" of low backscatter (-14.4 dB) which are exposed over 23,000 km^2 in the north-central part of the complex. They are partly superposed by the flow apron on the extreme southern flank of Ozza Mons. It is not clear to what extent these old flows are part of the subparallel complex, although a common source is suggested by faintly visible flow lobes which are subparallel with those of the main assemblage.

The main phase of flow emplacement took place with the eruption of flow fields A1, A2 and A3. These fields share a similar morphology and a specific backscatter of -7.2 dB. A1 and A2 were emplaced first, and each covers 24,000 km^2 (where exposed) in the form of lobes up to 50 km wide. A1, the earliest field, displays a variable backscatter of -7.2 to -16.1 dB, which may represent differences in surface texture or dielectric properties along the length of the flow. The main phase of flow emplacement culminated in the eruption of A3, which may be traced to north-south trending graben on the extreme southern flank of Ozza Mons. A3 has a total area of 59,000 km^2, and measures 1500 km in total length, making it the longest flow field observed in this survey. The field bifurcates in its medial region, forming a 150 km long, 60 km wide lobe which was emplaced north-east onto A2. At 1100 km from source A3 turns northwards for 130 km before flowing east through a network of subparallel graben to pond along a 50 by 190 km long region at its most distal reach.

The medial and distal reaches of the field were fed by a 750 km long channel, which has drained into an oval region of ponded lava in the distal section of A3. The upper portion of this channel is dominated by several late-stage overspills (Figure 3.14, arrows). These overspills have individual areas of around 600 km^2, lava having flowed up to 15 km on either side of the channel. Slabs of radar-bright flow crust appear to have separated before coming to rest within these overspills (Guest et al., 1992). The slabs are separated by radar-dark regions interpreted to be smoother, rapidly chilled lava.

A number of radar-dark lava flows occur at the margins of A2 and A3. Their low backscatter of -15.5 to -15.1 dB implies a relatively smooth surface, which is smoother than the surrounding plains. A radar-dark flow on the northern margin of A3 may be traced to a "disturbed" region at the edge of A3 which has a similar appearance to the channel overspills (a, Figure 3.14). A possible mechanism for the formation of these margins is late-stage breakout of low-viscosity lava from the base of A3 and A2, which rapidly chilled upon

emplacement without forming a broken crust. Another breakout from A3 (b, Figure 3.14) has produced a 280 km long flow of intermediate backscatter (-13.6 dB). This flow covers more than 4000 km^2 and was erupted onto A2 and the "old flows". The toe of this flow oversteps A3 for a short distance, indicating that A3 must already have been emplaced over 1000 km from source before more proximal activity which produced the breakout ceased. A3 has also flowed around several small shield volcanoes, leaving them as kipukas (S, Figure 3.14). By comparing these partly buried shields with the dimensions of similar unburied shields in the area and elsewhere on Venus (Guest et al., 1992), the thickness of A3 is estimated as 75 to 100 m.

The main phase of flow field emplacement was followed by waning activity, with the emplacement of fields B and C. Flow field B (-7.7 dB) covers 16,000 km^2 and may be traced to its source in the north-south trending graben around 3° S, 201.5° E. Field B is superposed by flow field C (-6.4 dB) which covers 4,000 km^2. On the basis of comparisons between Cycle 1 and 2 data, and emissivity measurements, Ford et al. (1993) propose that field C is composed of lava with a high dielectric constant, which they suggest may be caused by a greater bulk density and/or unusual composition. C was erupted from a north-west -south-east trending arcuate fissure at 4.2° S, 202.2° E. This fissure cuts the older flow fields further south, but is subparallel to the main source graben further north. These structures are radial to Ozza Mons, and may be the surface manifestations of dykes which have were fed from a source beneath that centre. These observations suggest that the eruption of C may derive from the same source region as the rest of the complex, but represents somewhat later activity.

3.2.3.2.1 Kaiwan Fluctus (Figure 3.15)

Kaiwan Fluctus, in Lavinia Planitia, is an assemblage of at least two separate subparallel fields, which have flowed westwards from Selu Corona (42° S, 6° E; C, Figure 3.15b) and a north-south trending deformation belt. The northern section of the assemblage (42.5 to 48.5° S, 353 to 3.5° E) comprises a subparallel field which is formed by flows whose average specific backscatter is -8.5 dB and covers an area of 608,000 km^2. They were erupted from sources at the margin of Selu Corona and flowed westwards before ponding between deformation belts in Lavinia Planitia. Channels of 5 to 9 km width, and up to 250 km in length have developed on these flows, which are themselves up to 870 km long and 170 km wide. A radar-dark flow unit (-12.7 dB) occurs in the south-east portion of this field, and was emplaced between units of higher backscatter. This flow may have a smoother surface texture or different dielectric properties from the radar-bright units which both preceded and followed the radar-dark flow.

Between 46.5 - 49° S and 2 - 10° E flow lobes have been emplaced from north-north-east - south-south-west trending fissures at the western boundary of a region of fractures, ridges and tessera to form the 260,000 km^2 southern Kaiwan Fluctus flow field. The structures are part of a north to north-east trending fracture belt interpreted to be a zone of rifting and

Figure 3.15a Image of Kaiwan Fluctus in Lavinia Planitia. Image measures 1000 x 1300 km and is centred upon 46.0° S, 2.2° E.


←Z

Figure 3.15b Sketch map of Kaiwan Fluctus in Lavinia Planitia. Letters correspond to features described in the text. S-X = line of topographic section (Figure 3.4g).

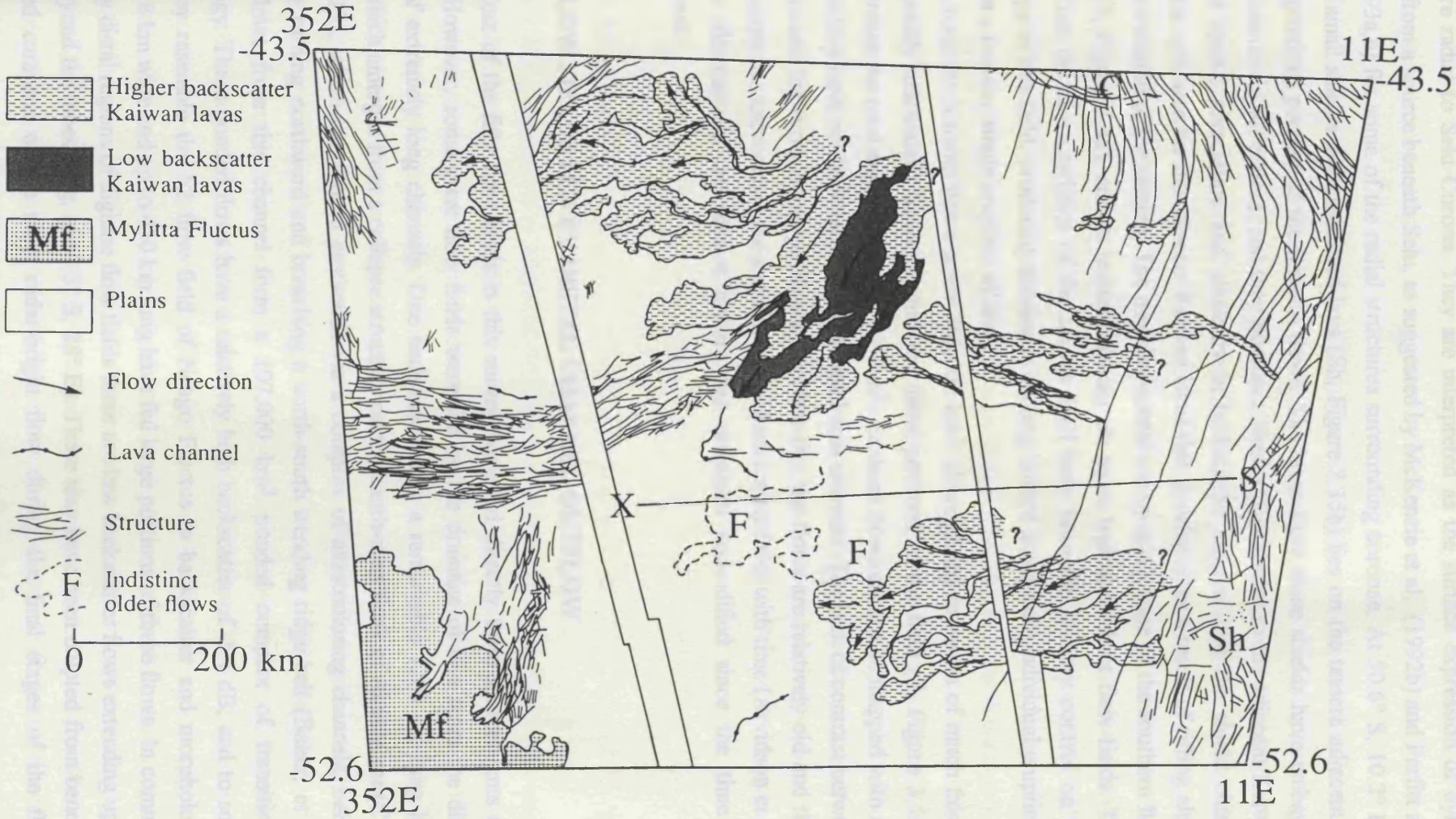
352E
-43.5
11E
-43.5
Higher backscatter Kaiwan lavas
Low backscatter Kaiwan lavas
Mf
Mylitta Fluctus
Plains
Flow direction
Lava channel
Structure
F
Indistinct older flows
0
200 km
X
S
F
F
Sh
Mf
-52.6
352E
-52.6
11E

extension (Campbell et al., 1991; Senske et al., 1991; Roberts et al., 1992). Some of these fissures are radial to Selu Corona. They are interpreted as the surface expression of dykes radiating from a source beneath Selu, as suggested by McKenzie et al. (1992b) and Parfitt and Head (1993a,b) for some of the radial structures surrounding coronae. At 50.6° S, 10.2° E a cluster of small shields and associated lava (Sh, Figure 3.15b) lies on the tessera adjacent to the most proximal portion of the Kaiwan flows. The lavas from these shields have embayed local depressions in the tessera, and they possess a similar backscatter to the adjacent Kaiwan lavas. The spatial association and similarity in backscatter suggest that the shield cluster represents a vent area for the adjacent Kaiwan lavas that developed as a result of rifting along the western margin of the tessera. The near-horizontal topographic slope of the southern flow field (0.01°, Figure 3.4g), and its tectonic setting are more typical of sheet flow fields. This suggests that the characteristics of the source itself have been the primary control on the morphology of this field, producing numerous cooling-limited flows from individual eruptions, rather than a massive single eruption of lava.

In total the Kaiwan flows cover 868,000 km^2, although the inclusion of much fainter (but apparently associated) flows beyond the distal portions of the field (F, Figure 3.15b) would increase the total area to over 1 x 10^6 km^2. As these flows cannot be mapped with any confidence they have not been included in the total area estimate. The lack of contrast between these flows and the surrounding plains may indicate that the flows are relatively old and their surface texture has approached the average Venus backscatter level with time (Arvidson et al., 1992), or alternatively the surface texture has remained unmodified since the time of emplacement.

3.3 FLOW FIELDS FED BY DISTAL CHANNEL OUTFLOW

Most of the fifty flow fields in this survey were fed directly from source vents and fissures. However, some great flow fields were fed by the drainage of lava from the distal reaches of extremely long channels. One such example is a remarkable 1200 km long lava channel which emerges from a collapse structure on the south-west flank of Ammavaru (C on Figure 3.12), which has flowed eastwards via a complex of anastomosing channels, before eventually turning northward and breaching a north-south trending ridge belt (Baker, et al., 1992). Flows from this channel form a 107,000 km^2 ponded complex of transitional morphology. These ponded flows have a relatively high backscatter of -5.1 dB; and to some extent they resemble the F2 flow field of Neago Fluctus in backscatter and morphology. Channels 8 km wide and up to 430 km long have fed large portions of these flows. In common with many distal regions of digitate flow fields there are low backscatter flows extending up to 80 km beyond the lobes (e. g. at 50.5° S, 28° E). These may have been erupted from beneath the cooled carapace of the main radar-bright flow during the final stages of the flow emplacement.

3.4 COMPOSITION, SURFACE TEXTURE AND EMPLACEMENT STYLE

3.4.1 Composition

Direct measurements of surface composition have only been obtained from seven locations by the Venera and Vega landers, and results from five of these sites (Vega 1 and 2, Venera 9, 10 and 14) have been interpreted as indicating tholeiitic basalt (Keldysh, 1977; Surkov, 1977; Surkov et al., 1984; Barsukov et al., 1986b; Surkov et al., 1986). Each of these five sites contain extensive flow fields, radar-dark plains, and possible rift zones within or near the error circle of the lander position (Basilevsky, et al., 1992; Kargel, et al., 1993). The Vega 2 site is located on the flow field associated with the corona chain in Rusalka Planitia which includes Eigin Corona (Table 3.1 and Chapter 5). Vega 2 measurements suggest a normal mid-ocean ridge basaltic tholeiite composition. Venera 14 settled directly on or near the flow apron of a volcanic shield at 14° S, 310° E in Navka Planitia (Table 3.1). This shield is located next to a fracture zone and associated with a fan-like flow field which extends 700 km to the east. Venera 14 measurements also indicated a normal mid-ocean ridge basaltic tholeiite composition, and television panoramas revealed a smooth and horizontal or slightly sloping surface with thinly layered or platy outcrops (Surkov et al., 1984), which Garvin et al. (1984) have compared to pahoehoe flows on the Snake River Plain. Although a sedimentary origin has been proposed for these outcrops (Florensky et al., 1983), the Magellan images and Venera 14 data support a volcanic origin for these rocks.

3.4.2 Surface Texture

Backscatter variations in Magellan SAR images of lava flows on Venus are usually ascribed to differences in wavelength-scale roughness. This is supported by the generally positive correlation of backscatter, rms slope and emissivity (Plaut and Arvidson, 1992). However, some lava flows display trends which are contrary to these, suggesting intrinsic dielectric differences and/or a scale dependence in roughness characteristics between rms slope and wavelength-scale roughness. Several studies have compared Magellan backscatter and rms slope data of Venusian lava flow fields and plains to terrestrial flow fields. Campbell (1992) compared Magellan rms slope estimates for a number of volcanic provinces to surface height profiles of 10 widely varied basaltic lava flows on Kilauea Volcano, Hawaii, and concluded that, in general, large-scale roughness on Venus is similar to that of rather smooth pahoehoe surfaces on Earth. In a separate study, Arvidson et al. (1992) compared Magellan rms slope data and specific backscatter cross sections of flows within Sedna Planitia (Neago Fluctus) to AIRSAR data of Quaternary basaltic aa and degraded flows in the Lunar Crater Volcanic Field, Nevada. They argue that Venusian lava flows have been degraded to varying extents by in situ mechanical and chemical weathering over the approximately 500 Ma age of the surface. They estimate that the removal of only about one metre of surface roughness would be enough

to change even the roughest Venusian flows to the typically smooth signature of the plains surfaces. From an analysis of the dependence of like-polarised circular backscatter on incidence angle in Goldstone radar data of Venus, Goldstone circular polarisation ratios, and comparisons between Magellan backscatter and terrestrial AIRSAR data, Campbell and Campbell (1992) found that volcanic surfaces in Eistla Regio are analogous to terrestrial pahoehoe flows, with limited occurrences of aa. They also found that emissivity values suggest dielectric constants in the range from 3 to 7, consistent with terrestrial basalt and a possible mixture of soil. Similar results were obtained for Bell Regio by Campbell and Rogers (1993), who analysed the relationships between Magellan backscatter and rms slope data, together with terrestrial AIRSAR data, and found the vast majority of the flows in Bell Regio have radar-brightnesses comparable to pahoehoe. In a recent survey of more than 300 effusive volcanic units on Venus, Hultgrien and Gaddis (1994) interpreted the Magellan radar data as indicating the presence of basaltic lava flows with surface textures included within the full range of pahoehoe-transitional-aa types. However, they also found that even the highest rms slope values (6° to 8°) are consistent with textures comparable only to those of the roughest terrestrial pahoehoe flows.

In a completely different approach to the question of surface texture, Taylor et al. (1994) measured the fractal dimensions of the margins of 13 large-volume lava flows on Venus. Their results suggest all but two of the lava flows have fractal dimensions greater than 1.15, consistent with pahoehoe. The other two flows are in Flow Field 4 of Mylitta Fluctus (Chapter 4) and have fractal dimensions of 1.04 and 1.09, consistent with aa. These results imply that most of the great flow fields form pahoehoe textures, consistent with the radar results.

An analysis of the average specific radar backscatter cross section of the fifty great flow fields as compared to terrestrial aa and pahoehoe fields on Kilauea Volcano, Hawaii (Campbell and Campbell, 1992), suggests that most of these fields are characterised by flow surfaces which are smoother than pahoehoe (Figure 3.5). However, a number of subparallel flow fields have radar cross sections which approach those of pahoehoe, and many of the aprons plot within the range of backscatter values typical of both pahoehoe and aa. These results are in general agreement with those of the previous studies outlined above, which together suggest that most of the surfaces of the great flow fields have textures comparable to terrestrial pahoehoe, with limited occurrences of aa type surfaces. Many of the smoothest surfaces, in particular the background plains, may have been degraded from rougher pahoehoe textures by in-situ weathering.

3.4.3 Emplacement Style

The great flow fields exhibit a wide range of emplacement styles, from the broad sheet-like flows to the channel fed flow lobes of digitate fields. The sheet flow fields appear to be the products of single massive eruptions, where the lava was erupted from continuous stretches of

fissure as very broad sheets of lava onto essentially horizontal surfaces. The spatially uniform radar characteristics of the sheet flow fields imply that rheological conditions were similar throughout the field during the final stage of emplacement, and either produced textures that were generally smoother than pahoehoe, or pahoehoe that has now degraded to a smoother texture. The sheet flows were probably less than 50 m thick, by analogy with major flow units within terrestrial flood basalt provinces, and due to the lack of topographic expression within the altimetry. The sheet-flow fields lack lava channels, and were probably volume-limited, the final planform morphology being controlled by local topography, and producing irregular flow margins. Some sections of these fields may have been erupted from local fissure eruptions at distance from the main source fissures, and bocca-fed eruptions may have occurred in some cases.

The transitional flows were emplaced as broadly lobate sheet-like lava flows which in some cases ponded in topographic lows. Some of these broad lobes were channel-fed, and may have been partly cooling-limited. The wider range of backscatter exhibited by the transitional flows attests to a more diverse range of surface textures than the sheet flow fields (including pahoehoe and some aa surfaces), and may thus reflect a wider range of rheological conditions. The digitate fields were emplaced as numerous individual centralised eruptions, which formed channel-fed, lobate flows that were probably cooling-limited. Numerous channels which commonly display radar-bright levées are often found in the proximal portions of these fields. The flow lobes generally undergo much distal widening to form flows up to several tens of kilometres wide, which may ultimately form ponded regions of lava on the order of 100 km across. A wide range of surface textures from very smooth, through pahoehoe and aa is inferred for the digitate flow lobes within any given field. Some flow surfaces exhibit extreme heterogeneity in radar-brightness, which may indicate the presence of numerous overlapping flow units.

To summarise, the great flow fields contain a wide range of flow morphologies and surface textures, from extensive sheet-like flows of uniform texture, to channel-fed flow lobes with a range of textures. These different characteristics may reflect a wide variation in lava rheology, effusion rates, cooling rates and preservation states. Some first order estimates of the effusion rates that may have characterised the emplacement of the great flows are made in the next section.

3.5 ERUPTION RATE AND DURATION

The Venera lander data, radar characteristics, and planimetric morphology all suggest that the great flows are basaltic in composition, and the following analysis will proceed on this assumption. The complete interpretation of the emplacement and cooling history of lava flows requires knowledge of many parameters which are not readily available for Venus. For the purposes of estimating the eruption rates and durations of the great flows, only the inferred

surface textures, final planimetric morphology, dimensions and estimated volumes are available.

It has been established that the majority of the great flow fields have radar characteristics and fractal dimensions consistent with pahoehoe, with more limited occurrences of aa. For terrestrial flows on Hawaii, Rowland and Walker (1990) showed that aa typically forms when volumetric flow rates (the actual rate within a single flow) exceed 5 to 10 m^3s^{-1}, and pahoehoe forms at lower rates. If the Venusian flows behaved in a similar manner to the Hawaiian flows, then the majority may have been formed at flow rates less than about 10 m^3s^{-1}. However, the surface texture of a lava flow is only that which formed at the very last moment of flow emplacement and cooling, and may not be truly representative of the surface texture which existed during the most active phase of emplacement.

Head and Wilson (1986) undertook a theoretical analysis of lava flow emplacement under Venus conditions, and predicted few major differences between Venusian and terrestrial flows in terms of length and surface morphology, unless there are significant differences in lava rheology. The high atmospheric temperature slows flow cooling, but this is offset by the high atmospheric pressure, which enhances convective heat loss. Nevertheless, the enhanced convection is predicted to cause the more rapid formation of a cool crust on Venus, such that active flows form aa surfaces in only two-thirds of the time required for similar changes to occur on Earth. Such flows may be represented by the channel-fed, higher backscatter flows visible in the great flow fields, such as flow A3 in the subparallel field south-east of Ozza Mons (Section 3.2.3.2.1), and flows within Field 4 of Mylitta Fluctus (Chapter 4). These flows have widths of several tens to nearly 100 km, and lengths of the order of 1000 km. Using the model of lava flow morphology of Hulme (1974), Head and Wilson (1986) predicted eruption rates of 10^5 to 10^6 m^3s^{-1} over periods of 6 to 14 days for channel-fed flows with similar dimensions on slopes of 0.17° (assumptions include a lava density of 2600 $kg.m^3$, a yield strength of 100 Pa, and a viscosity of 1500 Pa.s). The more rapid formation of a cool crust on Venus may also lead to the enhanced development of roofed-over channels and tube-fed flows, with pahoehoe type flow surfaces (Head and Wilson, 1986). This may explain the abundance of flows with radar properties approaching those of pahoehoe. The eruption rates for tube-fed flows over 100 km in length may then be much less than those predicted for the flows in open channels. Another possible mechanism for the emplacement of pahoehoe flows on Venus is the injection of lava into pre-existing, cooler flow units - the inflation-dominated "lava rise" mechanism (Self et al., 1991). This hypothesis stems from observations of compound pahoehoe flow units within the Columbia River Basalt province, suggestive of low effusion rates. However, as noted above, the final surface texture reflects the rheological conditions and flow regime at the very last stage of emplacement, and may not be a reliable indicator of the average effusion rate.

The relationship of flow dimensions to eruption parameters remains the subject of some controversy. Several models have attempted to predict eruption conditions on the assumption that flow field growth is strongly correlated to effusion rate, eruption duration, and local topography. From an examination of 41 terrestrial basalt, basaltic andesite, and

Figure 3.16 Plot of maximum flow length (km) against effusion rate (m^3s^{-1}) showing the upper and lower limits of Walker's trend used in estimating the effusion rates of the great flow fields. Modified from Walker (1973).

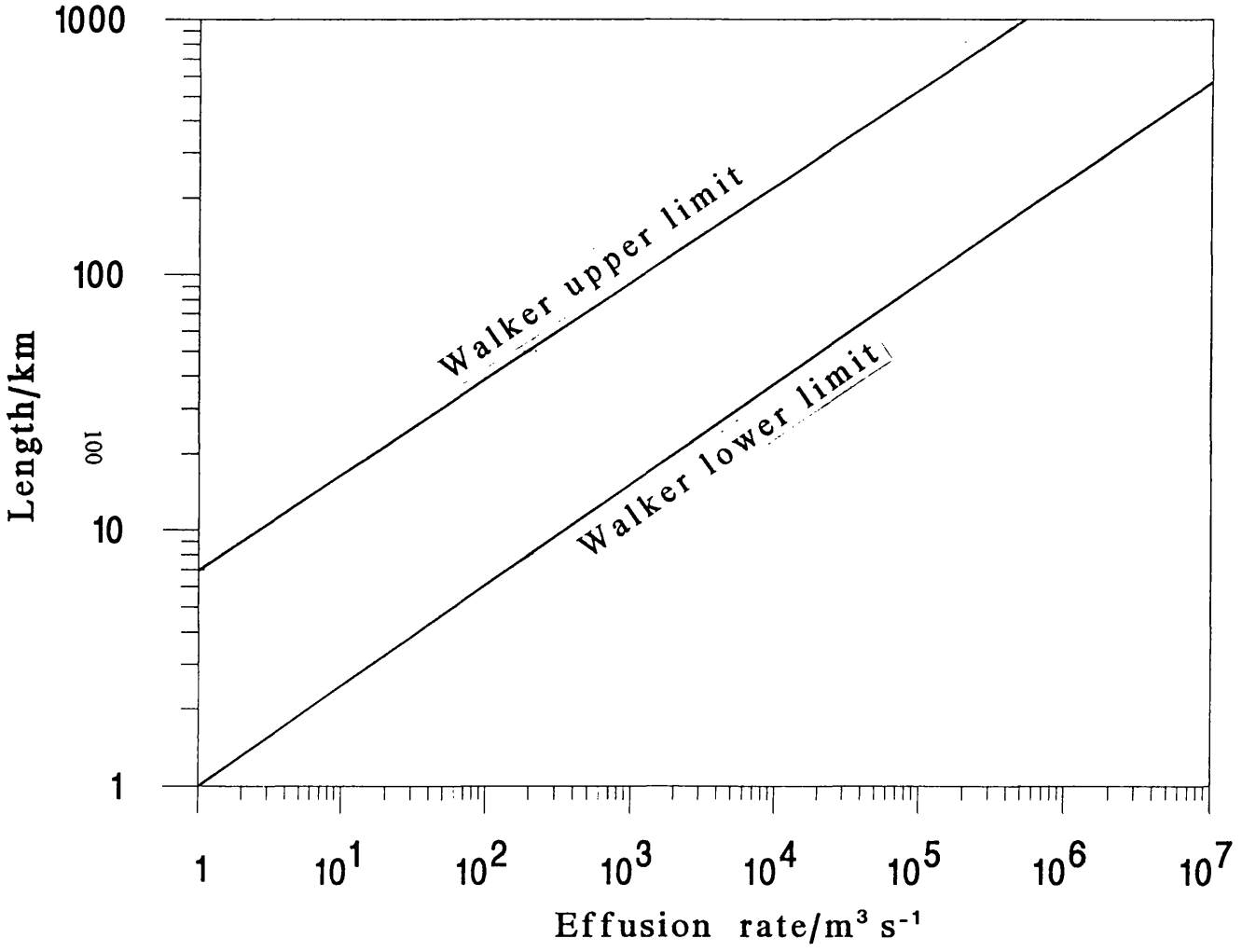
1000
100
10
1
Length/km
100
Walker upper limit
Walker lower limit
1
10^1
10^2
10^3
10^4
10^5
10^6
10^7
Effusion rate/m^3 s^-1

dacite flows, Walker (1973) concluded that lava flow length is largely determined by eruption rate. The model is simple and allows eruption rates to be determined from flow length alone (Figure 3.16). However, this relationship has been criticised, and correlations have also been found between flow length and total flow volume (Malin, 1980), and eruption rate and planimetric area (Pieri and Baloga, 1986) for several Hawaiian basaltic flows. Despite its simplicity, the relationship has been confirmed for all mature, channel-fed flows, and may be used to predict flow length within a factor of 7 (Pinkerton and Wilson, 1992). The relationship does not hold for tube-fed flows, or those with an eruption duration less than about two days (Pinkerton and Wilson, 1988, 1992). The positive relationship between eruption rate and flow length is related to cooling, and has been confirmed from observations of channel-fed flows on Mount Etna (Guest et al., 1987; Kilburn and Lopes, 1988). In order to estimate effusion rates of Venusian great flows, Walker's plot has been extended to lengths of the order of 1000 km (Figure 3.16). For a given flow length, the upper and lower bounds of Walker's trend were then used to predict the minimum and maximum effusion rates respectively. Many of the channel-fed flows in the great flow fields have lengths of several hundred kilometres, and some have lengths of 1000 km or more. The Walker(1973) model predicts effusion rates of between 10^4 and 10^7 m^3s^{-1} for these flows. Eruption durations may then be calculated by dividing estimates of flow volume by the effusion rate. As an example, consider flow A3 of the subparallel field south-east of Ozza Mons. This flow has an area of 59,000 km^2, and an estimated minimum thickness of 75 m, yielding a volume of 4425 km^3, The flow has a total length of 1500 km, which using the Walker (1973) model gives minimum and maximum effusion rates of 2.0×10^6 and 1.3×10^8 m^3s^{-1}. These figures yield an eruption duration of between 9.5 hours and 25.6 days. It has already been noted that the Walker (1973) model is not applicable to flows with eruption durations of less than two days; therefore the higher effusion rate of 1.3×10^8 m^3s^{-1} may be rejected. Similar calculations for flows within Mylitta Fluctus give eruption rates of between 10^4 and 10^6 m^3s^{-1}, and typical durations of weeks or months (ignoring eruption durations of less than two days; Chapter 4, Tables 4.4 and 4.5). These predictions compare well with those made by Head and Wilson (1986) for flows of similar dimensions.

Kilburn and Lopes (1991) derived a first order model for aa and blocky lavas in which only the mean discharge rate and underlying slope determine the final dimensions of these flows, such that:

$$L = (2/3)^{½} [(h/k) \sin a]^{½} Q^{½}$$

Eq. 3.3

where, L = final flow length in metres, h = mean frontal thickness in metres, k is the lava thermal diffusivity (7×10^{-7} $m^2.s^{-1}$ for Venus conditions), a is the angle of the ground slope in degrees, and Q is the mean discharge rate in m^3s^{-1}. Applying this model to flow A3 of the field south-east of Ozza Mons (whose radar backscatter is consistent with aa), using h = 75 m, and a = 0.05° gives a mean discharge rate of 3.6×10^7 m^3s^{-1}. Together with the flow volume this

gives an eruption duration of 34 hours. For Mylitta Fluctus the Kilburn and Lopes (1991) model gives eruption rates of between about 10^6 and 10^7 m^3s^{-1}, and durations of hours to months (Chapter 4, Tables 4.4 and 4.5). Many of the shortest predicted durations are clearly unrealistic, especially for the longer flows, as they imply average flow velocities of up to 1000 $km.h^{-1}$. The problem stems from applying the Kilburn and Lopes (1991) model to flows erupted onto the near-horizontal slopes characteristic of many of the longer flows on Venus, when the model was developed for flows erupted onto the steeper slopes characteristic of terrestrial volcanoes.

Eruption rates may also be predicted by considering the typical dimensions and likely rise rates of magma within fissure systems feeding many of the sheet flow fields. Assuming a spatially continuous eruption along a fissure with a length of 100 km, and typical terrestrial values of say 5 m and 5 $m.s^{-1}$ for the fissure width and magma rise velocity, then an eruption rate of 2.5×10^6 m^3s^{-1} is obtained.

To a first order, the predictions of Head and Wilson (1986), the Wilson (1973) and Kilburn and Lopes (1991) models, together with the consideration of laterally extensive fissure eruptions all give consistent results. Rejecting the highest eruption rates and lowest durations, these results imply typical eruption rates of between 10^5 and 10^6 m^3s^{-1}, and durations of weeks to months. These values compare favourably with those obtained from modelling by Swanson et al. (1975) and Shaw and Swanson (1970) for cooling units within the Columbia River Basalt Group (eruption rates of about 10^6 m^3s^{-1}, and emplacement times of about 1 week), reinforcing the analogy between the great flow fields and terrestrial flood basalts.

3.6 TECTONIC ASSOCIATIONS

The majority of the great flow fields are associated with belts of fractures and grabens interpreted to be zones of limited extension and rifting, while a lesser number are related to isolated sources on the plains. Essentially four rift-related settings can be recognised: (1) volcanic rises, (2) corona-chains, and (3) highland-marginal fracture belts, and (4) mixed ridge and fracture belts. The volcanic rises exhibit the most copious amounts of volcanism, which usually occurs in the form of large volcanoes, and non-centred volcanism is usually absent. Examples in the survey of fifty great flow fields include Atla Regio with Maat and Ozza Mons (Chapter 5), Beta Regio (Theia Mons) and Bell Regio (Tepev Mons). On the basis of their broad regional topography, large apparent depths of isostatic compensation, the presence of rifts, and large volcanoes, the volcanic rises are interpreted as the sites of major mantle upwelling or deep mantle plumes (Senske et al., 1992). A major question regarding the formation of terrestrial flood basalts is the importance of pre-existing extension and lithospheric thinning in producing enhanced decompression melting within a large plume head or mantle anomaly (e.g. McKenzie and Bickle, 1988; White and McKenzie, 1989; Hooper, 1990; Hill, 1991; Saunders et al., 1992). In most cases on Venus the rifting pre-dates the formation of the large volcanoes. The volcanic activity may therefore have been either initiated

or enhanced by decompression melting. The flow aprons of the large volcanoes are often cut by rift-related faults and graben, indicating that rifting continued during the period of volcanism.

Many great flows are also associated with chains of coronae and corona-like features. These chains are characterised by irregular topography and semi-continuous troughs which contain swarms of fractures and graben, which link the coronae and corona-like centres together. The chains occur in the plains, and often radiate from the volcanic rises. Centre-to-centre spacings are typically 400 km. Most volcanism is centred on the coronae and corona-like features, in the form of flow aprons and transitional-type fields. Examples are the fields associated with Eigin Corona in Rusalka Planitia, and Hecate Chasma (Table 3.1). The chains are interpreted to be major zones of extension, along which diapiric upwellings form the coronae and corona-like features (Stofan et al., 1984; 1992). In many cases the centres both post-date and are cut by rift-related structures. The formation of these centres may in part be due to the upwelling of melts formed by upper mantle decompression as a result of the extension and thinning of the overlying lithosphere. However, the origin of the extension is in many cases unclear, and may itself be due to upper mantle upwelling. Ghail and Wilson (1994) propose that the corona chains may arise from the alignment of upper mantle plumes along great circles to form integrated networks of upwelling and rifting. If this is the case then the volcanic activity may be a result of both active and passing upwelling.

A number of great flows are associated with highland-marginal fracture belts. These also contain coronae and corona-like centres, but with a greater spacing of about 600 km on average. The belts are characterised by a discontinuous chain of topographic lows and relatively broad zones of fracturing (Senske and Head, 1992). Both centred and non-centred volcanism occur in this setting, and both aprons and sub-parallel fields are found. These zones are usually located at the margins of highlands, such as southern Aphrodite Terra and northern Lada Terra (the Lada rift). Senske and Head (1992) have suggested that the highland-marginal fracture belts may have resulted from slope failure and gravity sliding at the highland margins. More recently, Magee and Head (1993) have proposed that the Lada rift, which is associated with Mylitta Fluctus (Chapter 4), is due to passive rifting at the margin of Lada Terra. They propose that this passive rifting developed in response to extensional strains generated by mantle downwelling beneath Lavinia Planitia. The volcanism may then be linked to upwelling and decompression melting of the upper mantle due to rifting, and possibly to counterflow associated with the adjacent downwelling (Magee and Head, 1993).

Several sheet-like flow fields are often associated with mixed ridge and fracture belts. These belts are characterised by sub-parallel ridges and fractures, contain few coronae or corona-like centres, have essentially no topographic expression, and are found on the lowland plains. The association with sheet-like volcanism is consistent with non-central sources and low topographic slopes. As these belts are not sited upon broad topographic rises, and contain few individual centres, they may have been formed by passive extension. The origin of this extension is unclear, but it may be related to stresses generated by local patterns of mantle convection beneath the surrounding plains. Volcanism is semi-continuous along the length of

these belts, suggesting linear zones of melting, rather than individual diapirs. This melting may be the result of extension related decompression. The ridges usually post-date the fractures and flow fields, and may have been formed by gravitational relaxation and subsidence of the belt after upwelling had ceased. Examples of these belts include Lauma Dorsa, and the belt associated with the sheet-flow field in Kawelu Planitia (Dodola Dorsa).

The non-rift-related settings include both centred and non-centred volcanism which is found on the plains. Centres include large volcanoes and coronae which have produced large flow aprons, sheet-like and transitional flow fields. These centres may be the product of isolated diapirs or upper mantle plumes, and generally form less extensive or voluminous flow fields than those associated with the rift zones. Isolated non-centred volcanism is the least common of all, and is usually represented by less extensive sheet-like flow fields with no obvious source. These non-centred fields may have been erupted from fissure-systems which are no longer visible due to subsequent burial by lava flows. This non-centred volcanism may result from localised melting due to regions of thinner lithosphere or minor extension.

To summarise, the rift-related settings reflect a spectrum of volcanic and tectonic activity, related to varying amounts of active and passive upwelling. Major deep mantle upwellings produce the volcanic rises and generate the largest volumes of melt through a combination of both active upwelling and rift-generated decompression melting. Smaller amounts of upper mantle upwelling produce the corona chains, while passive rifting produces the highland-marginal fracture belts and mixed ridge and fracture belt associations. Isolated upwellings and localised extension and melting beneath the plains produce smaller aprons, transitional and sheet flow fields. Comparisons have already been drawn between the great flow fields and terrestrial flood basalt provinces, which occur in a similar tectonic environment, with the largest volumes of lava being erupted where extension and mantle plumes coincide. Moreover the role of central volcanism in generating terrestrial flood basalts may merit further attention.

3.7 IMPLICATIONS FOR RESURFACING

A major question regarding the great flow fields is how do they relate to plains resurfacing? Have the types of great flows visible today and the eruptions they represent been responsible for the bulk of plains resurfacing in the past, or have the plains to a large extent been formed by some other volcanic process? The set of fifty great flows do not represent a statistically complete population and therefore cannot be used to adequately address questions of global resurfacing. Nevertheless, several observations are of relevance in developing ideas on the mode of plains emplacement. As they were chosen for visibility and contrast against the surrounding plains, nearly all of the great flow fields are stratigraphically younger than the background plains. In addition, the visible population of great flow fields is mostly related to zones of lithospheric extension and thinning, and to centres which have developed in the pre-existing plains. These observations are consistent with models which propose that the bulk of

the background plains were formed during a period of catastrophic mantle overturn and global resurfacing (Schaber et al., 1992; Parmentier and Hess, 1992; Turcotte, 1993).

The plains may have been emplaced as extensive sheet flow fields from widespread high effusion rate fissure eruptions. The current population of sheet flow fields exhibit spatially uniform radar properties and little or no flow structure. The general invisibility of the plains-forming flow fields might then be explained if the plains were formed from sheet-flow fields with similar characteristics to those of the current population, whose surface properties have subsequently undergone "homogenisation". Similar conclusions were reached by Magee Roberts and Head (1993) with regard to identifying coronae related flow fields, which they suggest may be a significant contributor to plains formation and resurfacing, as coronae are numerous and widespread. The emplacement of plains may also be related to canali-type lava channels (Komatsu et al., 1993), although few examples of associated flow fields have been seen.

The radar backscatter of flows is thought to progressively approach that of the Venus average with age due to in-situ weathering, small-scale mass wasting, aeolian activity, and the emplacement of impact ejecta that slowly homogenise initial surface properties (Arvidson et al., 1992). It is possible that many plains-forming great flow fields are now unrecognisable due to this process. However, many indistinct flows are recognised, such as the "mottled plains" visible in association with some great fields such as Kaiwan Fluctus (Figure 3.15) and Mylitta Fluctus (Chapter 4). The population of indistinct flows may represent the waning stages of global resurfacing, and/or ongoing volcanism since that time. More detailed analysis of the global population of all scales and morphologies of flow field in the plains, to the limits of contrast and visibility, is required before resurfacing questions can be adequately addressed.

3.8 CONCLUSIONS

Great flow fields typically cover areas of a few hundred-thousand square kilometres, with lengths of a few hundred to over one thousand kilometres and widths of several hundred kilometres (Table 3.1). They principally occur as either sheet-like or digitate morphologies, although a few fields with transitional morphologies are also found. The digitate fields may be subdivided further into aprons, fans and subparallel fields. The principle difference in morphology is attributed to a combination of emplacement style and source characteristics, with the digitate flow fields erupted as many discrete cooling-limited flows from mostly centralised sources, and the sheet flows as massive volume-limited eruptions from laterally extensive fissure systems onto essentially horizontal terrain.

An analysis of the average specific radar backscatter of the great flow fields as compared to terrestrial pahoehoe and aa fields on Kilauea Volcano, Hawaii, suggests that most of these fields are characterised by extremely smooth pavement-like flow surfaces. The backscatter of individual sheet flow fields is remarkably uniform over large areas. However there is much variation in the backscatter of different flow units within individual digitate and

transitional fields, from below to above the Venus average and surrounding plains. Many of the flow units with the highest backscatter may have aa-type textures. The sparse Venera lander data, radar properties, planform morphology and tectonic associations of the great flows imply that they are basaltic in composition.

Many of the flow units within the digitate fields were apparently channel-fed and cooling-limited. First-order estimates of eruption rate of between 10^5 and 10^6 m^3s^{-1} have been made for flow units of several hundred to a thousand kilometres in length in these fields, by application of the Walker (1973) relation between flow length and effusion rate. The flow units have typical volumes of several hundred to over one thousand cubic kilometres. Together with the estimated effusion rates these volumes yield typical eruption durations of weeks to months.

The majority of the great flows are associated with zones of mantle upwelling, extension and rifting, including volcanic rises, corona-chains, highland marginal fracture belts, and mixed ridge and fracture belts. In most cases this volcanism is centred and has produced flow aprons about coronae, corona-like features and large volcanoes. A lesser number of great flows are related to both centred and non-centred volcanism on the plains. The set of fifty great flows represent comparatively recent volcanism, which is mainly related to lithospheric extension and mantle upwelling, and the plains may have formed during an earlier episode of catastrophic mantle overturn and global resurfacing. This plains resurfacing may have been characterised by sheet type flow fields, which are now largely invisible due to "homogenisation" to uniform radar properties. Indistinct flows with no obvious tectonic associations which are seen on many areas of plains may have been formed during global resurfacing, or may have been formed during ongoing volcanic activity since that time. In terms of planimetric dimensions, predicted eruption rates, inferred compositions and surface textures, together with an association with zones of lithospheric thinning and extension, the great flow fields are considered to be Venusian analogues of terrestrial flood basalt volcanism.

CHAPTER 4

MYLITTA FLUCTUS

I would rather understand one cause than be King of Persia.

– Democritus of Abdera

4.1 INTRODUCTION

Mylitta Fluctus is a remarkable sub-parallel flow field that covers approximately 300,000 km^2 in southern Lavinia Planitia. The field was first recognised in images acquired by the Arecibo Observatory (Campbell et al., 1991; Senske et al., 1991a). In these and later images acquired by Magellan the radar-bright flow lobes of Mylitta contrast particularly clearly against the surrounding plains. The location of Mylitta (55° S, 355° E) allowed Magellan to provide images of the field during the early stages of Cycle 1 (Head et al., 1991; Roberts et al., 1991; Figure 4.1). Specially enlarged 40" x 40" photo products of C160S347 and C145S350 were available and these were used to produce a detailed preliminary map of Mylitta Fluctus and surrounding structures (Guest et al., 1991).[4] This mapping enabled the detailed stratigraphy of the flow field to be obtained from superposition relations. In addition the broad scale sequence of regional tectonics was established from the cross-cutting relations of regional structures. The results of this work warrant a dedicated chapter, and appear in a different form in Magee Roberts et al. (1992).

Mylitta is characterised by generally radar-bright lava flow lobes with uniform radar properties which have been emplaced on radar-dark plains (Figure 4.1). Many of the flows contain central channels and levées, and complex superposition relationships are apparent. The field measures 1000 km north-south by 460 km east-west, and was emplaced down slope to the north into Lavinia Planitia from a source at the northern margin of Lada Terra. The source is a 400 km diameter asymmetric shield volcano located along an east-west trending lineament belt interpreted to be a rift zone.

In this chapter the regional setting of Mylitta is established, followed by a detailed analysis of the flow field stratigraphy and development based on superposition relations. The flow morphology is also discussed in detail. An interpretation of eruption style, including first-order estimates of eruption rates and duration based on measured and estimated flow dimensions is given. Finally the origin of Mylitta with respect to the local tectonic environment and possible rifting in northern Lada Terra is discussed.

[4]Guest, J. E., M. G. Lancaster, K. Roberts, and M. H. Bulmer, Volcanic Geology and Stratigraphy at Part of the Boundary Between Lavinia Planitia and Lada Terra (abstract), *Lunar Planet Sci. XXII*, 505, 1991.

Figure 4.1 Magellan image mosaic of Mylitta Fluctus and surrounding regions. Image measures 2000 x 900 km, and is composed of portions of C160S347 and C145S350.


343.2
356.2
-48.0
-48.0
-67.5
-67.5
354.6
9.4

Figure 4.2 Structural map of the Mylitta Fluctus region showing the outline of Mylitta Fluctus, the distribution of small volcanic shields, and structural lineaments. The diagonal bars are data gaps. A = source of Mylitta Fluctus, B, C and D = other tectono-volcanic centres discussed in text.

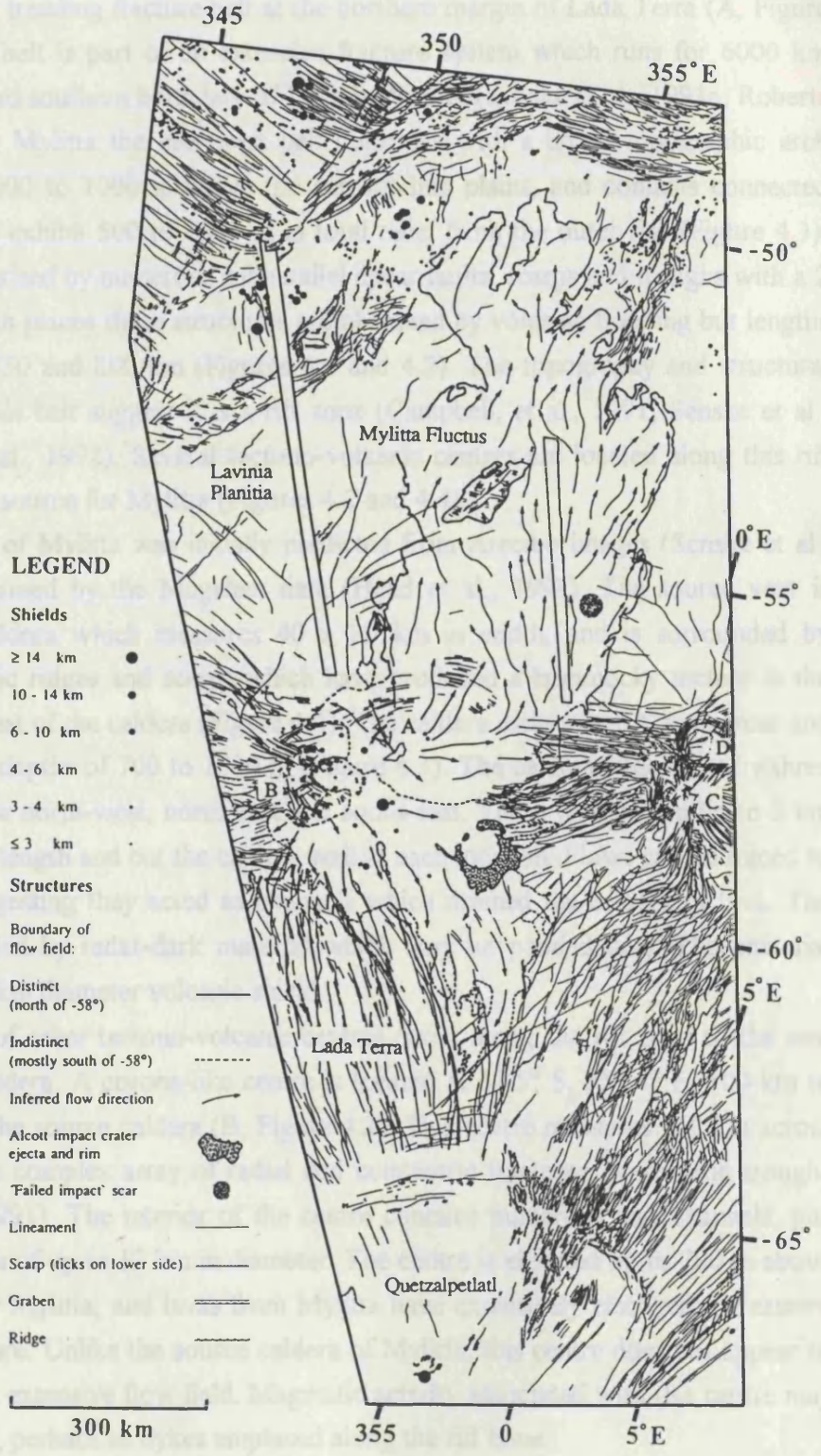
345
350
355°E
-50°
Mylitta Fluctus
Lavinia
Planitia
0°E
-55°
A
B
C
D
-60°
5°E
Lada Terra
F
-65°
Quetzalpetlatl
355
0
5°E
LEGEND
Shields
≥ 14 km
10 - 14 km
6 - 10 km
4 - 6 km
3 - 4 km
≤ 3 km
Structures
Boundary of flow field:
Distinct (north of -58°)
Indistinct (mostly south of -58°)
Inferred flow direction
Alcott impact crater ejecta and rim
'Failed impact' scar
Lineament
Scarp (ticks on lower side)
Graben
Ridge
300 km

4.2 TECTONIC SETTING AND ORIGIN

Mylitta Fluctus is set in a region of complex geology (Figure 4.2). The source lies within an east-west trending fracture belt at the northern margin of Lada Terra (A, Figure 4.2). This fracture belt is part of an extensive fracture system which runs for 6000 km along the eastern and southern boundary of Lavinia Planitia (Senske et al., 1991a; Roberts et al., 1992). Near Mylitta the east-west belt coincides with a broad topographic arch which is elevated 400 to 1000 m above the surrounding plains, and contains connected[5] interior lows which exhibit 500 to 1000 m in total relief from the outer rise (Figure 4.3). The belt is characterised by numerous subparallel linear faults, scarps and troughs with a 2 to 25 km spacing. In places these structures are obscured by volcanic flooding but lengths measure between 250 and 800 km (Figures 4.1 and 4.2). The topography and structural characteristics of this belt suggest it is a rift zone (Campbell, et al., 1991; Senske et al., 1991a; Roberts et al., 1992). Several tectono-volcanic centres are located along this rift zone, including the source for Mylitta (Figures 4.2 and 4.4).

The source of Mylitta was initially predicted from Arecibo images (Senske et al., 1991a) and is confirmed by the Magellan data (Head et al., 1991). The source vent is composed of a caldera which measures 40 x 20 km in width, and is surrounded by numerous concentric ridges and scarps which have produced a hummocky texture in the area to the south-east of the caldera (Figure 4.4). The caldera measures 100 km across and is characterised by depths of 700 to 1500 m (Figure 4.3). The caldera wall is cut by three radial troughs in the north-west, north-east and south-east. These troughs are up to 5 km wide and 60 km in length and cut the caldera wall at each location. Flows can be traced to these troughs, suggesting they acted as channels which drained the caldera of lava. The caldera itself is filled by radar-dark material which may be ponded lava. This material partially buries a 3 km diameter volcanic shield.

A number of other tectono-volcanic centres occur along the rift zone to the east and west of the caldera. A corona-like centre is located at 57.5° S, 351.1° E, 100 km to the south-west of the source caldera (B, Figure 4.2). This centre measures 160 km across and is defined by a complex array of radial and concentric fractures, scarps and troughs (Solomon et al., 1991). The interior of the centre contains numerous lava channels, pits and volcanic shields of up to 12 km in diameter. The centre is elevated up to 700 m above the source vent for Mylitta, and lavas from Mylitta have extensively embayed the eastern portion of the feature. Unlike the source caldera of Mylitta, this centre does not appear to be the source of an extensive flow field. Magmatic activity associated with this centre may be largely intrusive, perhaps as dykes emplaced along the rift zone.

A structurally complex tectono-volcanic centre is located at 58.1° S, 2.5° E, about 470 km to the east of the Mylitta source vent (C, Figure 4.2). This centre contains a 50 km diameter circular structure, which is the locus of an array of radial fractures. These fractures may be the surface manifestations of dykes. Another circular feature, some 195

[5]or semi continuous.

Figure 4.3 Magellan topography of the Mylitta Fluctus region. Contour interval is 100 m, with a datum of 6052.0 km. Mylitta Fluctus itself is stippled. The vertical bar is a data gap.

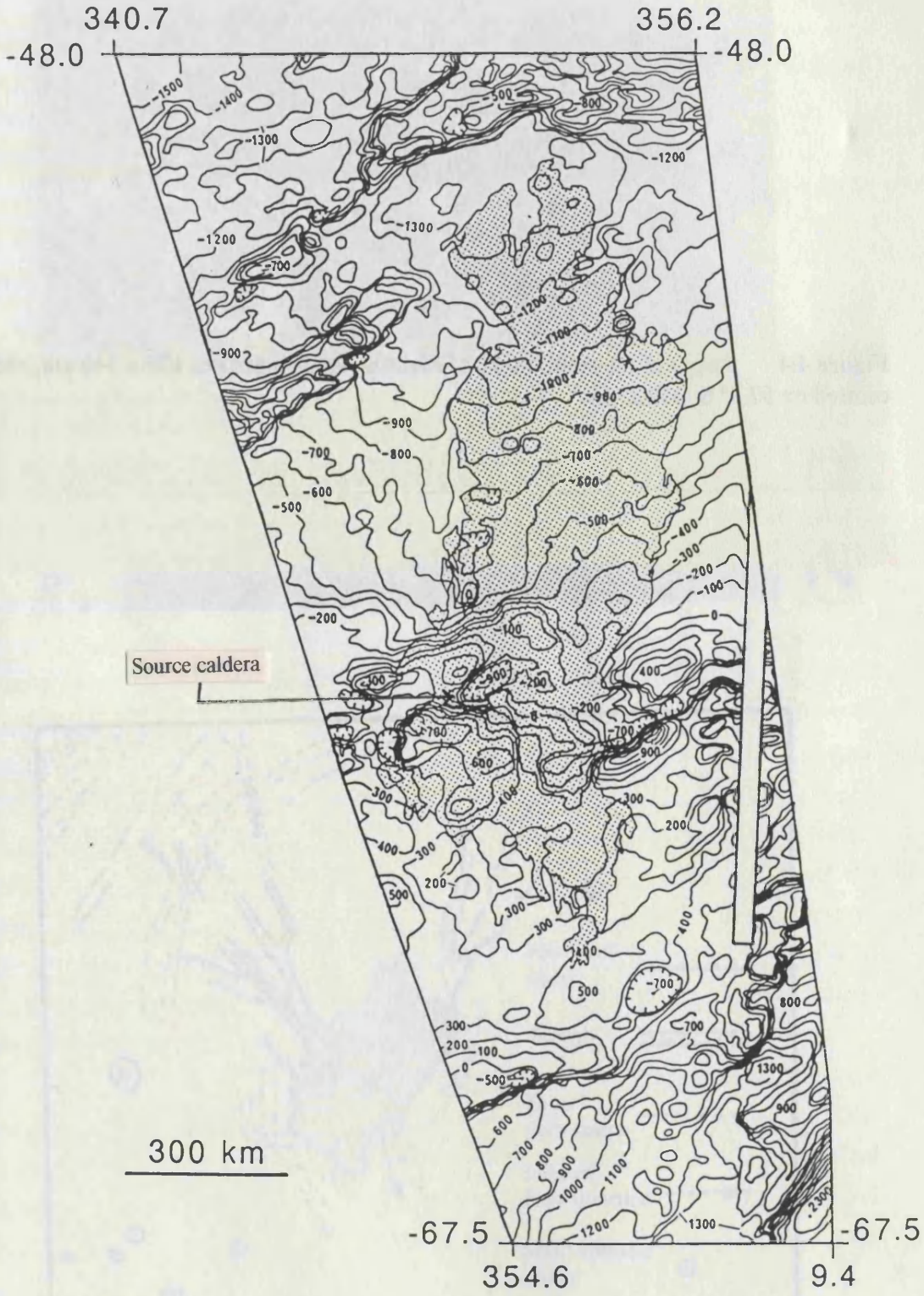
340.7
356.2
-48.0
-48.0
Source caldera
300 km
-67.5
-67.5
354.6
9.4

Figure 4.4 Image and interpretation map of the source vent of Mylitta. Image measures 120 x 140 km, and is centred on 57.3° S, 352.2° E. The source caldera (shaded) is defined by a semi-continuous scarp which is illuminated on the eastern side of the caldera. The south-west side of the caldera is marked by a steep outward facing scarp slope. Troughs directed lava from the north-west, north-east and south-east margins of the caldera. These troughs may have been formed by lava erosion and that in the north-west has cut arcuate faults which are concentric with the source of Mylitta.

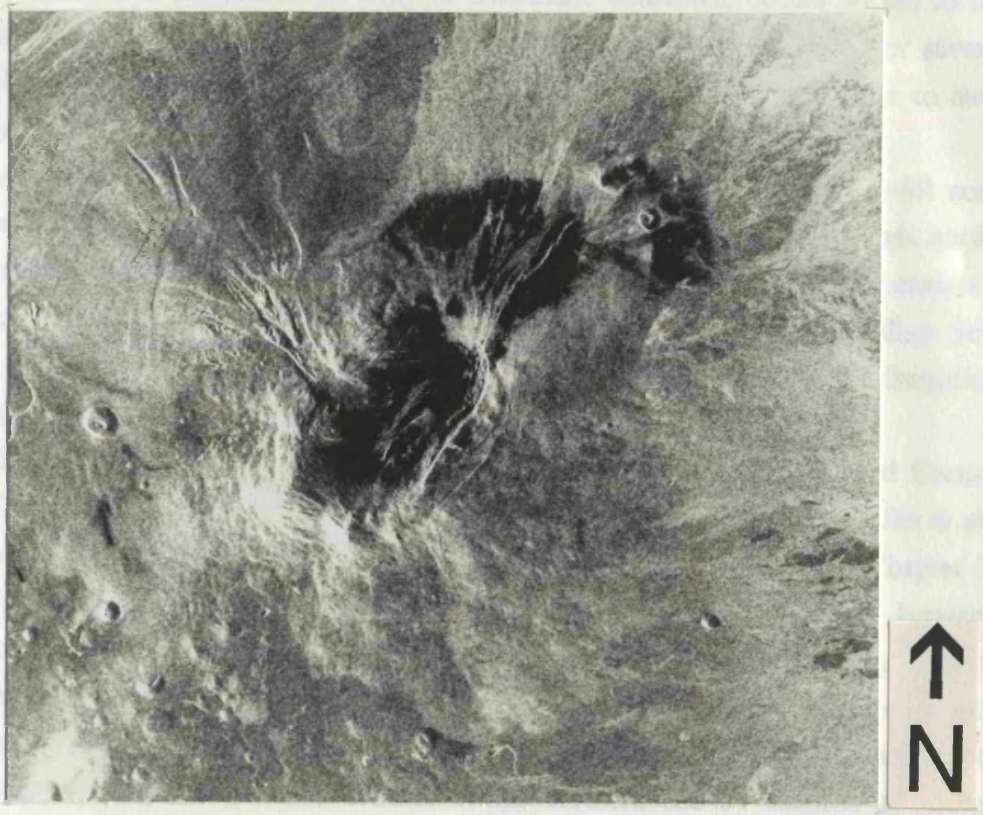
N

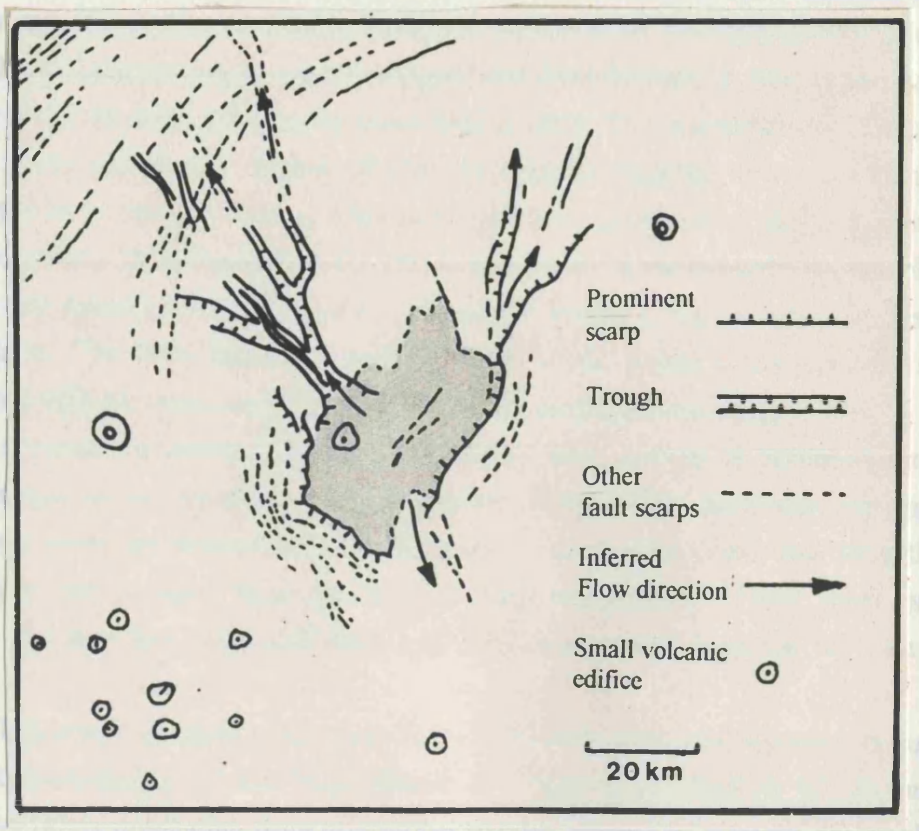
Prominent scarp
Trough
Other fault scarps
Inferred Flow direction
Small volcanic edifice
20 km

km in diameter, and defined by an array of concentric structures, occurs 90 km to the north-east of this centre (D, Figure 4.2). This latter structure is the source for several lobate flows extending for 50 km to the north-west. Both these centres appear to have developed at the same time as the rift zone in which they are located.

A 500 to 600 km diameter corona is located at the eastern end of the rift zone (Campbell et al., 1991). To the north of this corona, a deformation zone extends north-north-westwards for about 2000 km towards Atla Regio. This deformation zone crosses a region of tessera, is punctuated by additional tectono-volcanic centres including Selu Corona, and is the source for Kaiwan Fluctus (Chapter 3, Figure 3.15). This deformation zone is also interpreted as a zone of rifting and extension.

South of Mylitta the regional tectonics are dominated by Quetzalpetlatl Corona (67.0° S, 0.0° E). Quetzalpetlatl is an 800 km diameter asymmetric corona (Stofan et al., 1992) surrounded by an extensive lava flow apron covering 1.5 $x10^6$ km^2 (Chapter 3, Table 3.1). Linear fractures and graben up to 530 km in length extend between Quetzalpetlatl and the Mylitta Fluctus source and other centres along the rift zone (Figure 4.2). North-north-west trending fractures extend from Quetzalpetlatl to the corona-like centre at 57.5° S, 351.1° E. These fractures cut the lava flows to the south of the Mylitta Fluctus source area, and are characterised at the northern end by collapse structures indicative of magma drainage in dykes below the fractures. East-north-east trending fractures also radiate from centres at the eastern end of the rift zone. In addition to these structures, north-north-east trending fractures radiate from the north-eastern portion of Quetzalpetlatl. Cross-cutting relations suggest that these fractures at least in part post-date activity in the rift zone, and they are interpreted as the surface manifestations of dykes.

North and west of Mylitta Fluctus the regional tectonics of Lavinia Planitia are dominated by north-east trending ridge belts, and west-north-west trending fracture belts (Solomon et al., 1992; Squyres, et al., 1992). These belts are embayed by the lava flows of Mylitta and Kaiwan Fluctus (Figure 4.1; Chapter 3, Figure 3.15), as well as by the radar-dark plains. The belts appear to predate most of the volcanic and tectonic activity associated with the rifting and flow emplacement in northern Lada Terra.

A region of indistinct flows which display little contrast in backscatter to their surroundings, lie on the plains west of Mylitta. They exhibit north-east trending flow directions which are inconsistent with the present topographic slope, indicating that the topography has changed since the time of their emplacement. These flows pre-date Mylitta, and may have originated from a now obscure source along the rift zone to the south.

The source of Mylitta Fluctus is located within the east-west trending fracture belt at the northern margin of Lada Terra. Magee and Head (1993) attribute this fracture belt to passive rifting originating from extensional stresses created by adjacent downwelling in Lavinia Planitia. The volcanic activity may then be linked to upwelling and decompression melting of the upper mantle due to rifting and possible counterflow associated with the

downwelling (Magee and Head, 1993). At Mylitta the volcanism post-dates the rifting, consistent with this hypothesis. The rift is associated with several other centres which are the source of minor amounts of volcanism (B, C, and D, Figure 4.2). This system of rifting and upper mantle upwelling is similar to rifts containing corona-like centres in north-east Atla Regio (Chapter 5). This volcanism, together with concentric and radial structures associated with the centres, largely post-dates the rift zone. As with Mylitta, it is likely that these centres were formed after most of the rifting occurred, in response to decompression melting and a weakened lithosphere. This contrasts with the situation in north-east Atla Regio, where rift zones and corona-like features have developed simultaneously. The tectonic setting of Mylitta within a zone of rifting and extension is similar to that of many terrestrial flood basalts, in agreement with comparisons of flow dimensions and eruption parameters (see below).

4.3 FLOW STRATIGRAPHY

Six major flow fields are identified in Mylitta Fluctus, and are interpreted to represent different eruptive episodes within the emplacement of the flow complex. The sequence of flow field emplacement is shown in Figure 4.5. The individual flow fields were identified by continuities in flow boundaries and central channels, by branching and superposition relations between flow units, and by similarities in radar backscatter and textural appearance. Most of the individual flow units within the medial and distal portions of Mylitta appear distinct and contrast well with their surroundings. However, a number of flow units in the proximal portion are not so easily separated due to their close spacing, narrow widths, and complex branching and anastomosing morphologies.

4.3.1 Flow Field 1

The initial eruptions in the history of Mylitta produced a flow field (shown in green on Figure 4.5) which is characterised by an asymmetric flow apron in the form of a shield some 200 km in radius and elevated up to 700 m above the adjacent plains of Lavinia. These eruptions may have initially been fissure fed, although no evidence for such eruptions can now be seen. Evidently the main source centralised at an early stage, and this probably occurred at the same time as the caldera was formed. This is supported by the association of the caldera with the flows of the shield, and by the partial burial by later flows of channels radiating from the caldera. The northern flank of the shield is composed of numerous, closely spaced flow lobes of 1 to 4 km in width, and extending up to 200 km from source (Figure 4.6). Multiple arcuate lineaments with widths of about 1.5 km and spaced between 1 and 3 km apart cross-cut the shield, and appear to be scarps or troughs

Figure 4.5a Legend for the flow maps in Figures 4.5b and 4.5c. After Magee Roberts et al. (1992).

FLOW MAP LEGEND

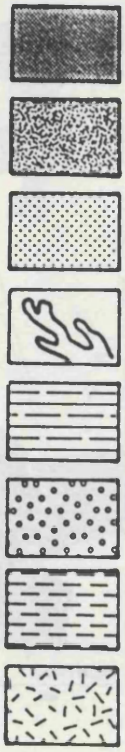

flows associated with phase depicted

diffuse dark deposits of possible impact origin

ovoid

outline of flows from previous phases

rift zone

impact materials

ridge belt

tectonically deformed terrain

Figure 4.5b Sequence of maps illustrating the evolution of Mylitta Fluctus through the emplacement of six successive flow fields. Each field is highlighted in a different colour. After Magee Roberts et al. (1992).


352
356
-50
-54
-58
-62
348
100 km
FLOW FIELD 1

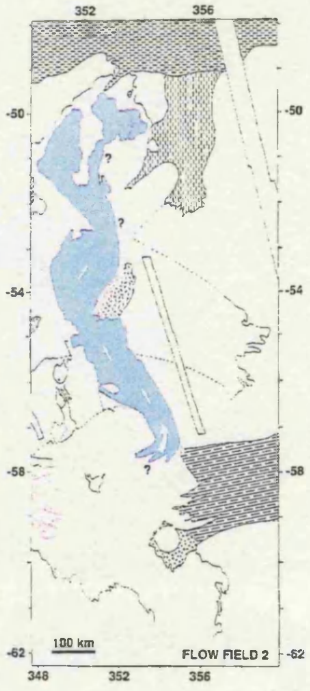
352
356
-50
-54
-58
-62
348
100 km
FLOW FIELD 2

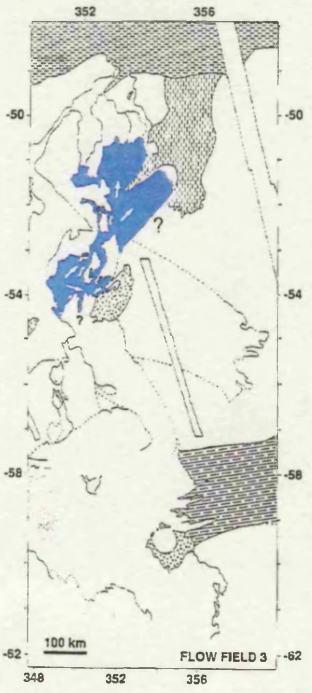
352
356
-50
-54
-58
-62
348
100 km
FLOW FIELD 3

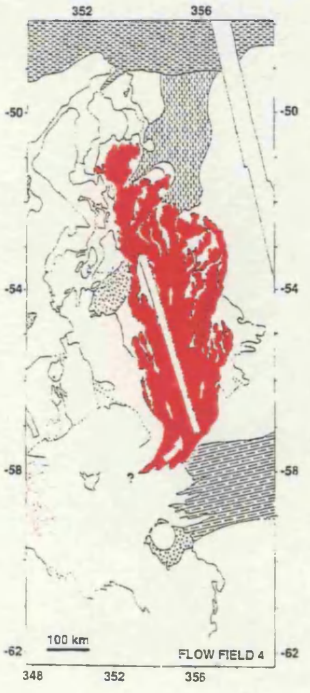
352
356
-50
-54
-58
-62
348
100 km
FLOW FIELD 4


352
356
-50
-54
-58
-62
348
100 km
FLOW FIELD 5

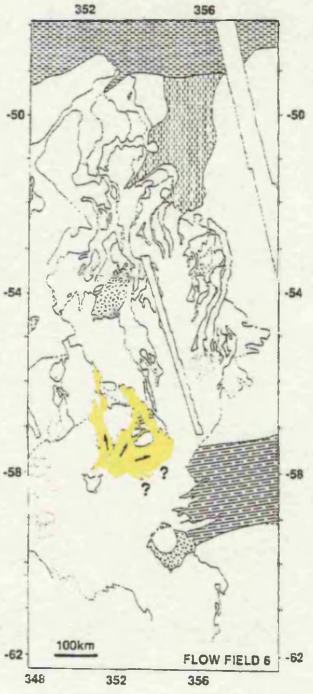
352
356
-50
-54
-58
-62
348
100km
FLOW FIELD 6

Figure 4.5c Map showing the complete Mylitta Fluctus flow complex. Flow field colours as for Figure 4.5b. After Magee Roberts et al. (1992).

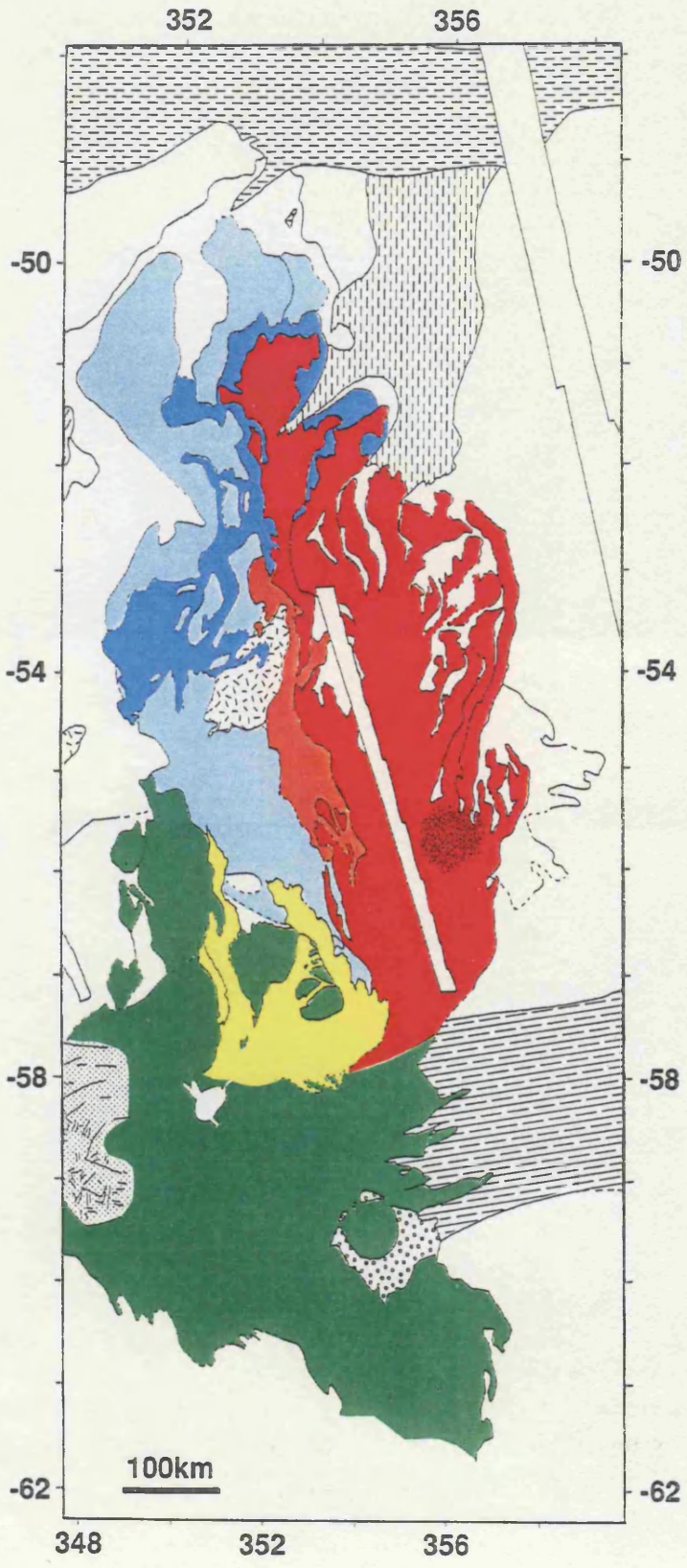
352
356
-50
-54
-58
-62
100km
348
352
356

Figure 4.6 Image of the closely spaced radial flow lobes on the northern flank of the shield developed during episode 1. Multiple arcuate lineaments cut these flow lobes and are interpreted as troughs or scarps. The radar-bright flow units in the lower and right hand portions of the image belong to episode 6. Some of the flow units within episode 6 appear to have been arrested or deflected by the arcuate structures. Image measures 90 x 110 km, and is centred on 57.0° S, 352.9° E.

Figure 4.7 Image showing the distal reaches of flow field 2, where the flow units pond and widen, embaying north-west trending ridges on Lavinia Planitia. The distal margin of flow field 4 (phase A_2) is visible at the lower edge of the image. The radar-dark flows of flow field 3 lie between flow fields 2 and 4. Image measures 160 x180 km, and is centred on 50.2° S, 353.0° E.


N

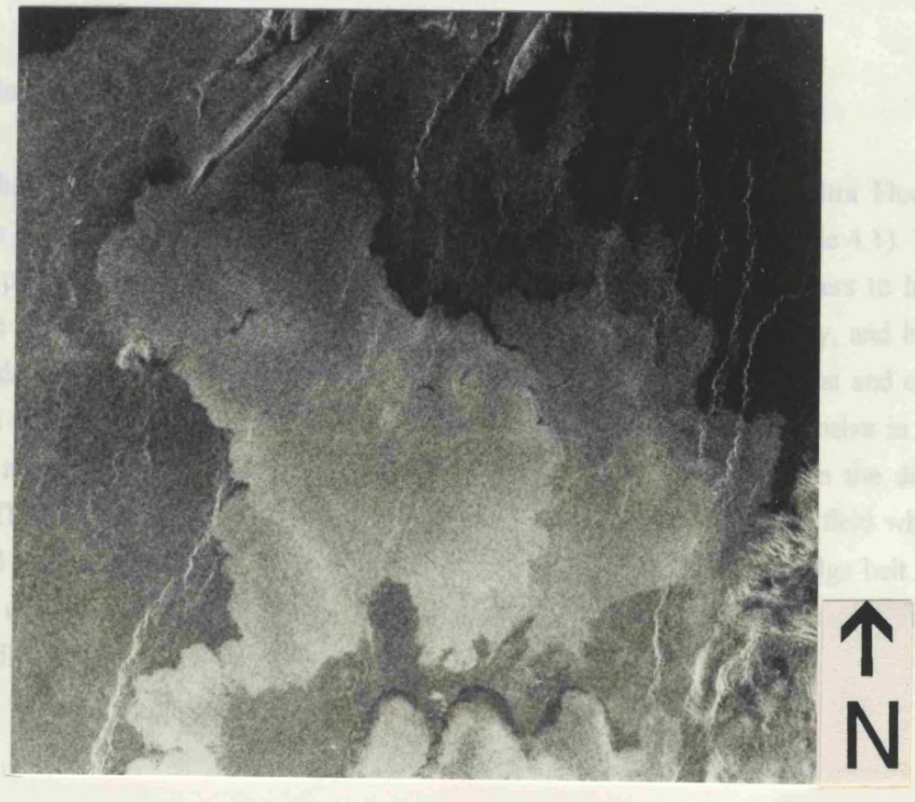
N

(Roberts et al., 1991). These structures may have resulted from continued extension along the rift, or from gravitational relaxation of the northern flank of the shield. Two troughs of 100 to 400 m depth occur on the northern flanks of the shield (Figure 4.3), and have directed most of the flows down slope onto Lavinia Planitia (Figures 4.2 and 4.5b).

To the south of the caldera the impact crater Alcott (59.5° S, 354.6° E) rests on sheet-like flows which may have been erupted either from fissures within the rift zone or from the corona-like centre at B, Figure 4.2. This is supported by the topographic data which indicates that flows may have travelled down slope from those sources (Figure 4.3). These flows may have been emplaced at a very early stage within the formation of flow field 1. Alcott was subsequently flooded by later flows from the caldera, which also formed the shield surrounding the source of Mylitta.

Flows extend over 200 km from the base of the shield to the north. These flows have widths of up to 6 km, and a maximum length of 440 km has been measured (Table 4.1). The flows are closely spaced and appear to radiate from channels superimposed on the shield, suggesting they are the youngest flows of flow field 1. A lava channel, lava fan, and a 50 km diameter shield volcano are situated to the west of these flows, and appear to have been erupted before the activity in episode 1 was complete. The total volume of flow field 1 has been estimated as approximately 1.7×10^4 km^3 (Table 4.1), and the field was evidently emplaced as multiple eruptions over an extended period of time. These eruptions constitute an early episode of edifice building, and together account for 85% of Mylitta Fluctus by volume.

4.3.2 Flow Field 2

The second major episode produced the longest flow field in Mylitta Fluctus (shown in light blue on Figure 4.5), with a maximum length of 1000 km (Table 4.1). The proximal portion of the field is buried by later flow units, but the field appears to have originated form the caldera. The flows have followed the regional topography, and have travelled down slope to the north-east of the caldera, before turning north-west and onto the plains to form the western part of Mylitta. Channel development is extensive in the proximal and medial portions of the field, but are only poorly developed in the distal regions. The flows widen to between 60 and 100 km in the distal part of the field where they pond and embay ridge belts in Lavinia Planitia (Figure 4.7). An older ridge belt has also been embayed in the medial portion of the field. The flows are generally radar-bright (-8 to -5 dB) with a uniform textural appearance.

Table 4.1 Dimensions of the Mylitta Fluctus flow fields.

Flow Field	Area, km^2	Maximum Length[a], km	Maximum Width[b], km	Volume[c], km^3
1	117,960	440	-	16,966[d]
2	62,320	1000	140	623
3	32,100	390[e]	100	321
4	106,660	960	160	1,741
5	7,900	630	60	79
6	16,180	340	140	162
Entire flow complex	300,000[f]	1000[g]	460	19,892

[a]The maximum continuous length of each flow field, measured from the source caldera to the most distal part.

[b]The maximum continuous width of individual flow fields. Flow field 1 completely surrounds the source caldera. The maximum width of the whole complex includes several flow fields.

[c]Volumes are based on a minimum estimate of flow unit thickness of 10 m. Figures are quoted to the nearest cubic kilometre to avoid rounding errors during summation, but this precision is not implied. The volume for flow field 4 was derived separately (see Table 2*).

[d]Based on a cone 700 m in height with a basal radius of 150 km representing the source edifice, surrounded by a 10 m thick pile of flow field 1 lavas.

[e]Measured from the most proximal to distal part along the longest continual portion (flow unit) of the field. The length was not extended to the source caldera, since for this field the source appears to be local.

[f]Area of the envelope formed by the flow fields (which overlap), includes the southern extension of the flow field beyond 58.5°S.

[g]The maximum length of the longest flow field, namely, flow field 2.

Table 4.2 Dimensions of flow phases within flow field 4.

Flow Phase	Area[a], km^2	Total Length[b], km	Maximum Width[c], km	Volume[d], km^3
A	27,410	A_1 460 A_2 960	80	274[d]
B	45,010	B_1 930 B_2 810 B_3 640	80	450[d]
C	4,580	560	30	46[d]
D	7,180	810	30	72[d]
Medial Region	15,420	510	130	617[e]
Proximal Region	7,060	200	50	282[e]
Whole Field	106,660	960[f]	160	1,741

[a]For flow phases the distal area is quoted.
[b]Measured from the source caldera to the most distal part of the flow phase.
[c]The maximum continuous width.
[d]Distal volumes use, as an example, an average flow unit thickness of 10 m (see text). Figures are quoted to the nearest cubic kilometre to avoid rounding errors during summation, but this precision is not implied.
[e]Medial and proximal volumes use a thickness of 40 m (four overlapping flow units of 10 m thickness).
[f]The maximum length of the longest flow phase, namely Phase A.

4.3.3 Flow field 3

The third episode of flow emplacement appears to be unrelated to the rift zone, with flows originating from an obscure source on the plains at the western margin of Mylitta (dark blue on Figure 4.5). Near the source the flows are relatively narrow, with widths of between 3 and 6 km, and follow complex pathways. The flows have travelled up to 390 km from source towards the north-east over flow field 2 and the underlying plains. In the distal portion the flow field ponds and reaches a maximum width of 100 km.

The field is characterised by radar-dark flows (-12 to -8 dB) of uniform appearance, with little evidence for flow structures such as channels. The field contains the most radar-dark flow unit in the entire complex, with a specific backscatter of around -12 dB (Figure 4.8). There are some uncertainties in the local stratigraphic relations between flow fields 2 and 3, such that in places the stratigraphy appears to be reversed. These apparent stratigraphic reversals are interpreted as indicating some overlap in the emplacement of these fields. Such an overlap in emplacement is consistent with the fields having different source regions.

4.3.4 Flow Field 4

The fourth episode of flow emplacement formed the entire eastern half of Mylitta (shown in red in Figure 4.5). Flow units within this field are the most distinctive and easily separable of the entire complex, and possess a remarkably uniform radar backscatter of between -10 and -5 dB. These properties have allowed this field to be mapped in greater detail and subdivided into four smaller flow fields which are termed flow phases to avoid confusion with the six flow fields which comprise Mylitta as a whole (Figure 4.9). These phases are labelled A to D, and individual lobes within the distal portions of phases A and B are given the notation A_1, A_2 and B_1 to B_3 (Figure 4.9). Individual phases are between 460 and 960 km in length, and between 30 and 80 km wide (Table 4.2). The entire flow field has a maximum continuous width of 160 km, and covers over 100,000 km^2 in area, making it the second most extensive field in the complex. Phases A, B and C have been emplaced in successively eastward positions. This trend may be a response to changes in the local topographic slope caused by the emplacement of previous flow phases. Phase D does not fit into this sequence however, and the position of feeding channels within the medial region may have also been important. There is also a trend towards decreasing length and estimated volume with each successive flow phase except phase D (Table 4.2). These decreases are attributed to a waning effusion rate.

The proximal portion of the flow field is dominated by well developed channels and levées (Figure 4.10). Such features are less common in the distal parts of the field. The medial section of the field contains a circular, diffuse, radar-dark feature, approximately 75

Figure 4.8 Image showing the relationships between the radar-bright flow units of flow field 2 and the generally younger and radar-dark flow units emplaced during episode 3. In places the stratigraphy between flow fields 2 and 3 appears reversed (e.g. the radar-bright lobes in the lower portion of the image appear to postdate the radar-dark flow units of flow field 3). A flow unit of very low backscatter (-12 dB) belonging to flow field 3 is located in the left hand portion of the image. Image measures 240 x 170 km, and is centred on 53.6° S, 351.2° E.

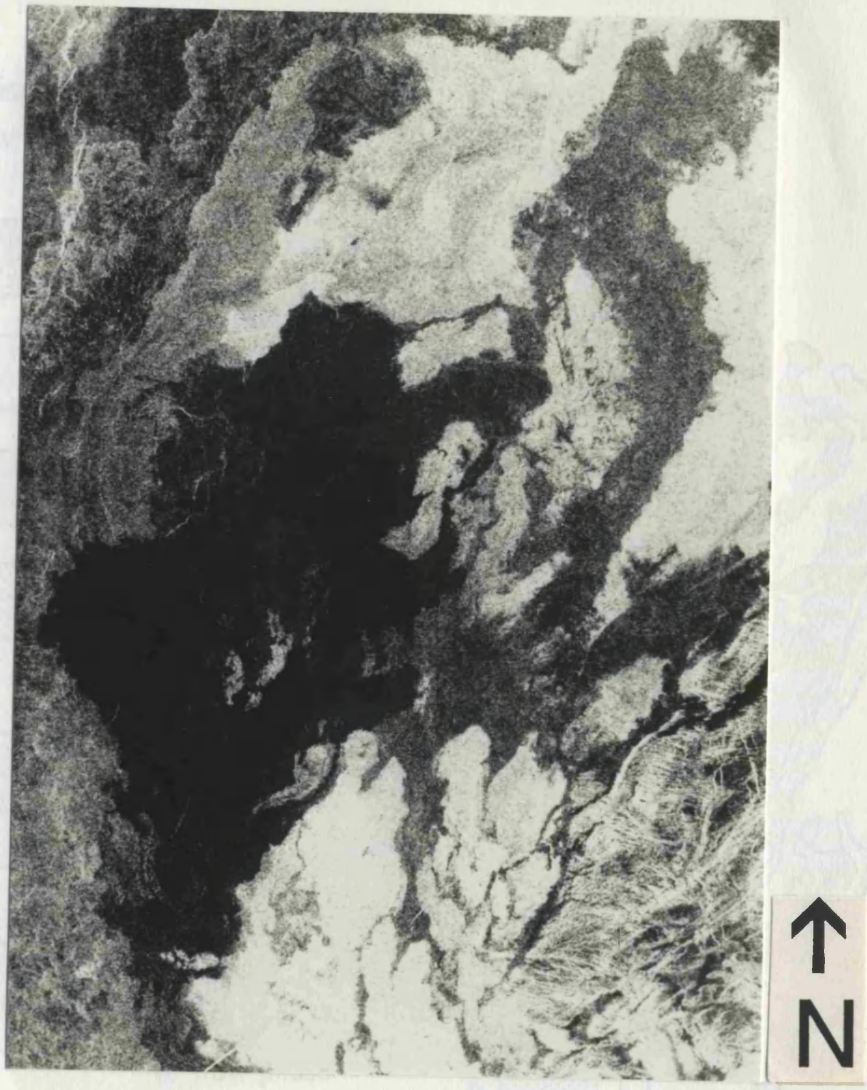
N

Figure 4.9 Sketch map showing the position and relative ages of flow phases within flow field 4. Flow dimensions are given in Table 4.2.

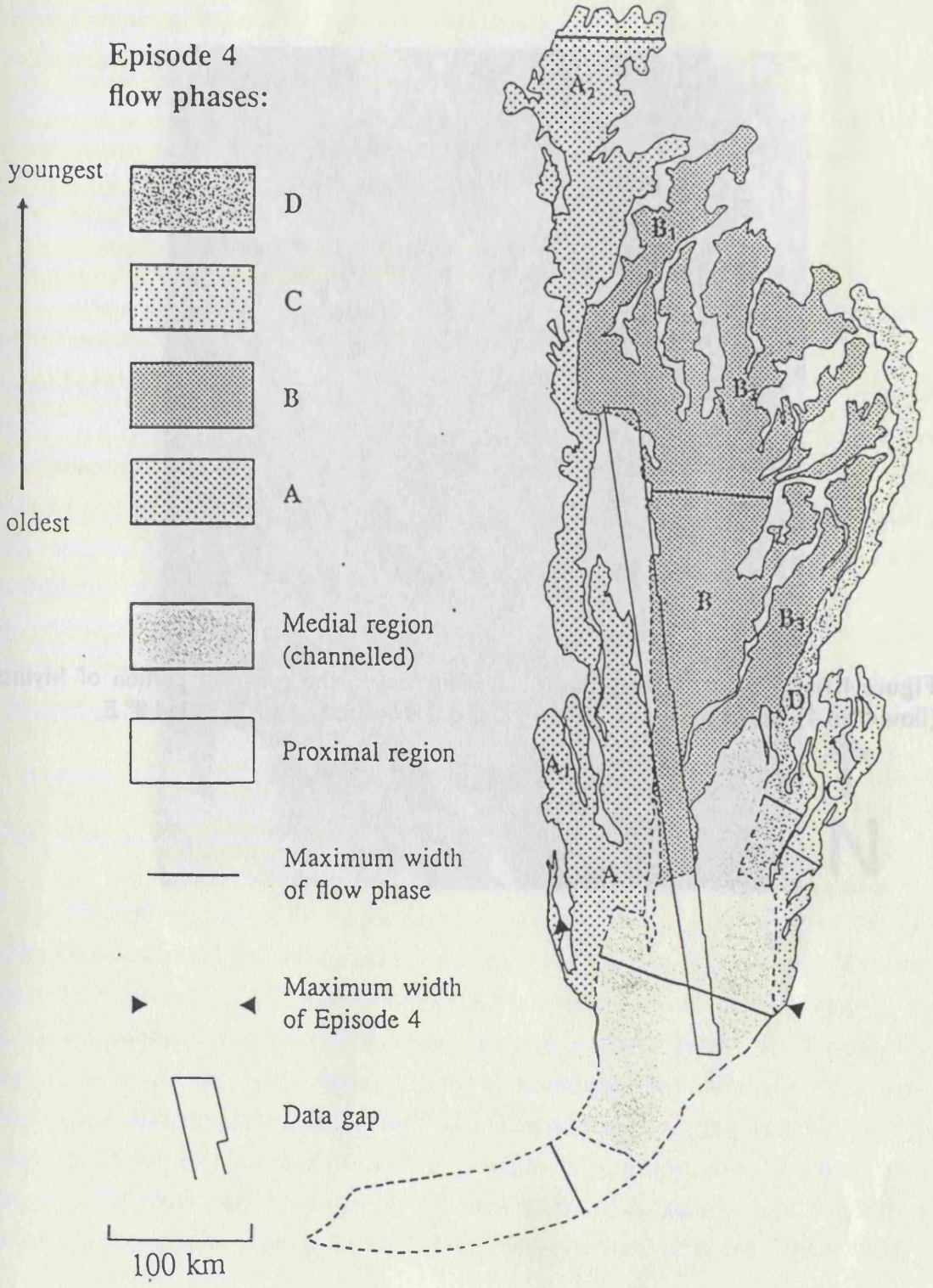
Episode 4
flow phases:
youngest
oldest
D
C
B
A
Medial region
(channelled)
Proximal region
Maximum width
of flow phase
Maximum width
of Episode 4
Data gap
100 km
A2
B1
B2
B
B3
D
C
A1
A

Figure 4.10 Image showing channel development in the proximal portion of Mylitta (flow field 4). Image measures 120 x 90 km, and is centred on 56.7° S, 354.8° E.

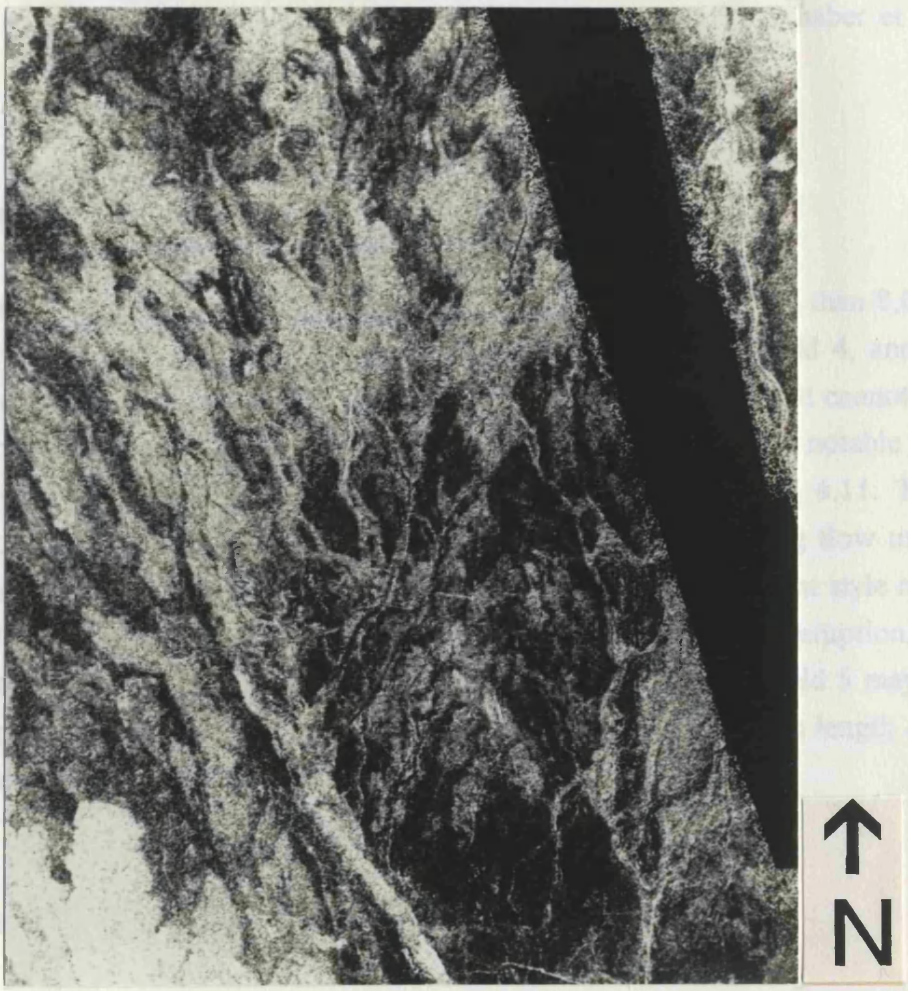
N

km in diameter. This feature is interpreted as a "failed impact" scar produced by the atmospheric shock wave of an incoming meteoroid which was destroyed before reaching the surface. The feature is similar in appearance to others documented by Schaber et al. (1992).

4.3.5 Flow field 5

This is the smallest flow field identified in Mylitta, with an area of less than 8,000 km^2 (Table 4.1). The field was emplaced on the western margin of flow field 4, and is mapped in orange on Figure 4.5. This field is not superposed by later flows and cannot be traced back to source, hence it may therefore have been tube-fed. The field is notable for its mottled and spatially variable radar backscatter (-10 and -4 dB); Figure 4.11. This mottling is interpreted as being due to the presence of numerous overlapping flow units with relatively short lengths and varying surface textures. Such an emplacement style may be attributed to lowered effusion rates characterising the waning stages of an eruption, as has been documented for terrestrial eruptions by Guest et al. (1987). Flow field 5 may in fact represent the waning stage in the eruption of flow field 4, and is similar in length and estimated volume to phase D of that field.

4.3.6 Flow field 6

The final episode of flow emplacement produced flows which extend up to 340 km to the north and north-east of the source caldera, to which they may be directly traced (shown in yellow in Figure 4.5). Near the source the flows are generally radar-bright (-7 to -4 dB) and exhibit well developed lava channels with levées (Figure 4.12). Beyond the base of the shield the flows display a mottled appearance with relatively radar-dark interiors and radar-bright margins. These radar characteristics suggest that the surface roughness of the flow increases towards its margins. This pattern may be related to a change in the rheological properties of the flow towards its margin, together with a decrease in topographic slope as the base of the shield is crossed (arrowed, Figure 4.12).

4.3.7 Summary

The earliest activity in the history of Mylitta flooded the rift zone and built a large shield with a summit caldera. Continued eruptions from this source flooded the impact crater Alcott and produced some sheet-like flows to the north of the shield. These initial eruptions are estimated to account for 85% of Mylitta by volume. The second episode

Figure 4.11 Image of the mottled flow units and varying backscatter characteristics of flow field 5. Radar-bright flow units of episode 4, with more uniform radar properties, are visible in the upper-right portion of the image. Image measures 120 x 80 km, and is centred on 55.2° N, 353.5° E.


N

Figure 4.12 Image demonstrating changes in radar characteristics along a flow unit within flow field 6. Arrows indicate where there is an abrupt change in the radar backscatter of the flow unit as it crosses the base of the shield. Note the radar-bright distal margins of the same flow unit towards the top of the image. Image measures 235 x 70 km, and is centred on 56.6° S, 351.8° E.

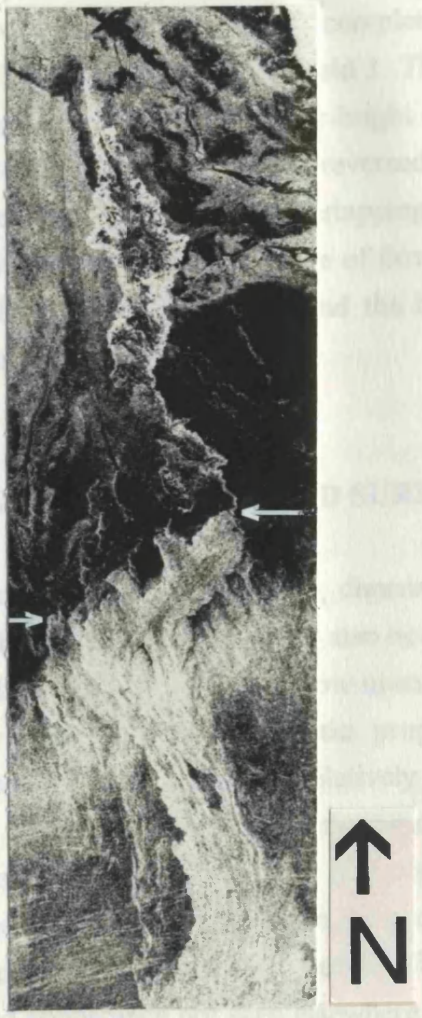
N

produced radar-bright digitate flow lobes which ponded up to 1000 km from the source. The emplacement of these flows may not have been completed before the localised eruption of the radar-dark flows which distinguish flow field 3. This activity was followed by the progressive easterly emplacement of the long, radar-bright digitate flow units which comprise flow field 4. This easterly emplacement trend reversed with the final phase of flow field 4, and the subsequent eruption of numerous overlapping flow lobes in the central part of the complex to form flow field 5. The final episode of flow emplacement produced flows of variable backscatter which extend to just beyond the base of the shield to the north and north-east of the caldera.

4.4 FLOW MORPHOLOGY, DIMENSIONS, AND SURFACE TEXTURE

There is considerable variation in the morphology, dimensions and surface textures of individual flow units within Mylitta Fluctus. Variations also occur between the phases of individual episodes, and along the length of individual flow units. Nevertheless, each flow field is distinguished by flow units with characteristic properties. Flow field 1 is characterised by multiple overlapping flow units with relatively narrow widths and short lengths. Flow fields 2 and 4 are both characterised by generally radar bright flow units (-8 to -5 dB) with homogenous radar properties. These units are notable for their great lengths and distal widening, with channels being very common in the proximal regions. Flow field 3 is unusual for being composed of very radar-dark, sheet-like flows, while flow field 5 is distinguished by a highly mottled appearance not seen elsewhere in Mylitta. Flow field 6 is also unique for the changes in backscatter which it exhibits both along and across the flow units. These differences in morphology and texture are interpreted as indicating differences in effusion rate and duration, and topographic slope. The longest and most areally extensive flow fields (i.e. 2 and 4) are those with the most uniform radar properties, and consist of small number of large flow units. The shorter flow fields have more heterogeneous radar properties and mottled appearances, and generally consist of numerous overlapping flow units. The proximal region of Mylitta is characterised by greater channel development.

4.4.1 Dimensions

Table 4.1 lists the overall dimensions of flow fields within Mylitta, while Table 4.2 gives the detailed dimensions of flow phases within episode 4. The overall areas of the flow fields show no systematic variation with age. However, if the first episode and the locally fed flow field 3 are excluded, then there is a systematic decrease in maximum length with time for flow fields 2, 4, 5, and 6. This relationship is also exhibited by phases within

flow field 4. Such decreases in overall length are attributed to a reduction in the effusion rate and/or duration with time (see Section 4.5).

Table 4.1 gives the maximum widths of entire flow fields, while the maximum widths of individual flow phases are given in Table 4.2 for flow field 4 only. The widths of individual flow units vary systematically with distance from source. They are typically 1 to 8 km wide in the proximal region of Mylitta, although some flows measure up to 20 km across. Channels are also common in this area (Figure 4.10), and the number and density of individual flow units is highest in this portion of the complex. Flow units broaden to about 15 to 40 km in the medial portion of Mylitta, and locally exceed 50 km (Figure 4.13). Maximum flow widths occur in the distal portions, where flow units pond and form lobes which typically measure more than 100 km across (Figure 4.14). The flows may broaden with distance from source as a result of decreasing topographic slopes, and due to ponding on Lavinia Planitia. Maximum width to length ratios range between 0.04 and 0.17 for flow phases within flow field 4 (Table 4.2). These values are similar to those obtained by Kilburn and Lopes (1988) for basaltic aa flow fields on Mount Etna.

As with many of the other flow fields described in Chapter 3, precise estimates of flow thickness are difficult to obtain due to the large footprint size of the Magellan altimeter, which measures approximately 20 km in diameter over this portion of Venus (Pettengill et al., 1991). Deflection of 100 m interval contours is not seen in the regional topography (Figure 4.3), suggesting that the flows are no more than 100 m thick in the distal portions of the flow field where the units do not overlap. Additional information on maximum possible flow thicknesses is provided by the control on flow emplacement exerted by structures whose height may be estimated. Flows in the proximal and medial portion of Mylitta are arrested by narrow lineaments, which are interpreted to be fault scarps (Figures 4.6 and 4.15). These structures are less than 1.5 km wide, and exhibit no signature in the Magellan altimetry, which has a vertical resolution of between 5 and 50 m (Pettengill, et al., 1991). Hence the flows are probably less than 50 m thick where they are stopped by these structures. This value is within the range of flow unit thicknesses found within terrestrial flood lava provinces (Chapter 3, Table 3.3).

In order to make a first-order estimate of the minimum likely volume of each flow field, a flow thickness of 10 m has been used (Table 4.1). The volumes of flow fields 2, 3, 5 and 6 were obtained by multiplying this thickness by flow field area. The volume of flow field 1 was obtained by representing the shield as a cone of height 700 m, with a basal radius of 150 km, and using 10 m for the thickness of the surrounding flow field. It is not known how much of the 700 m elevation is due to lava emplacement, and how much may be due to uplift along the rift zone. However any overestimate in the height of the shield may be balanced by using a minimum flow unit thickness of 10 m. The volume of flow field 4 was estimated separately by summing the contributions from each distal flow phase, and adding these to the estimated volumes of the proximal and medial portions of that field (Table 4.2). Similarly, the volume of the entire flow complex was obtained by summing the

Figure 4.13 Image of flow units within the medial portion of flow field 4 (phases B_2, B_3, and C on Figure 4.9). Note the overall uniformity in radar brightness of the flow units (-5 to -7 dB), and the radar-dark material between them. Image measures 290 x 95 km, and is centred on 53.9° S, 356.1° E.

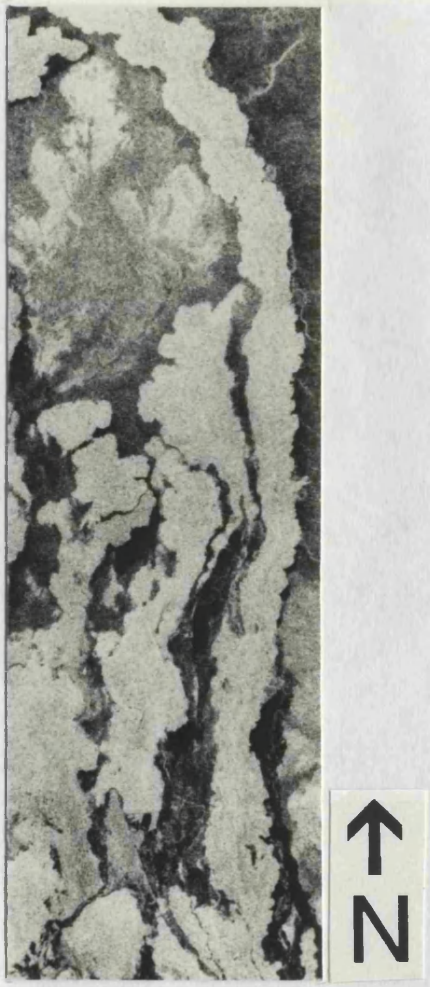
N

Figure 4.14 Image of the distal portion of flow field 4 (phase A_2 on Figure 4.9). Note the narrow radar-dark margins of this flow field, which in turn lie on the radar-dark flow units of flow field 3. The radar-bright flow units of flow field 2 are located at the top of the image. Image measures 200 x 160 km, and is centred on 51.2° S, 353.2° E.

Figure 4.15 Image showing the containment of flow units within flow field 2 by narrow lineaments (arrowed) interpreted to be fault scarps. The flow units are probably less than 50 m thick where they are stopped by these structures, which have no expression in the altimetry. Image measures 80 x 85 km, and is centred on 55.1° S, 351.2° E.

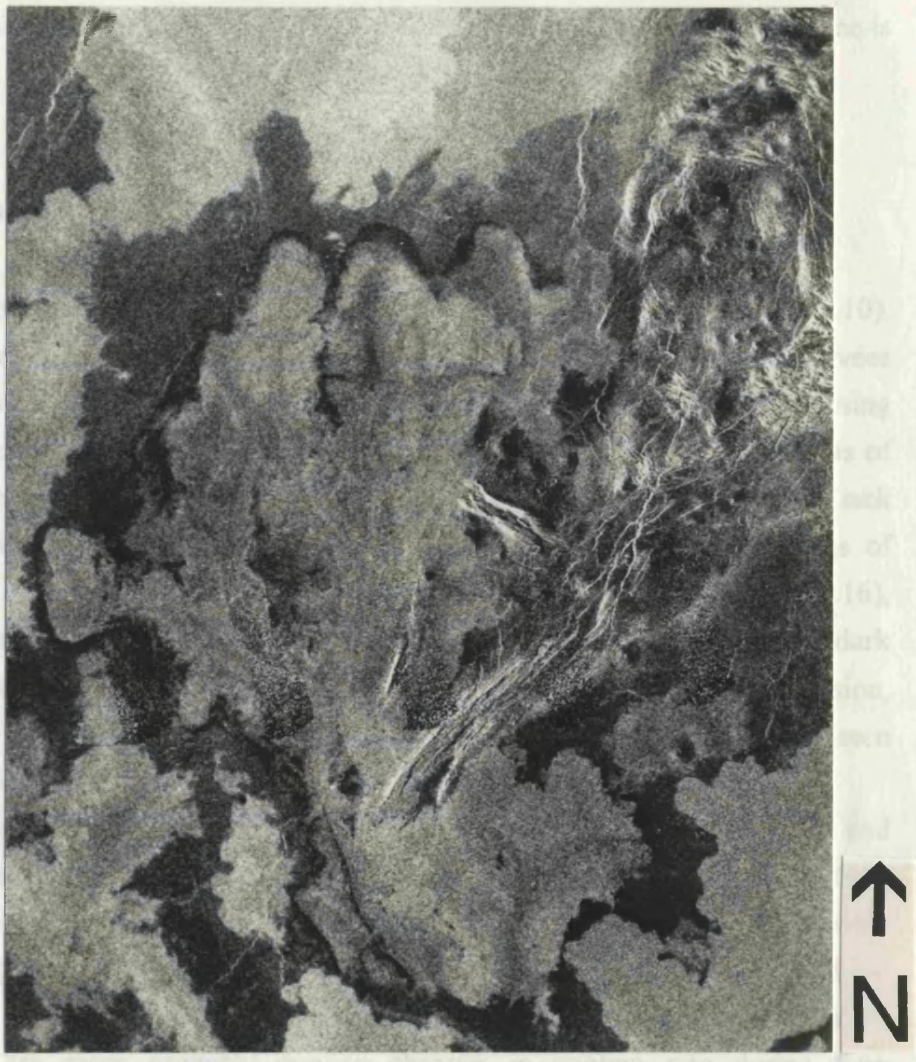
N

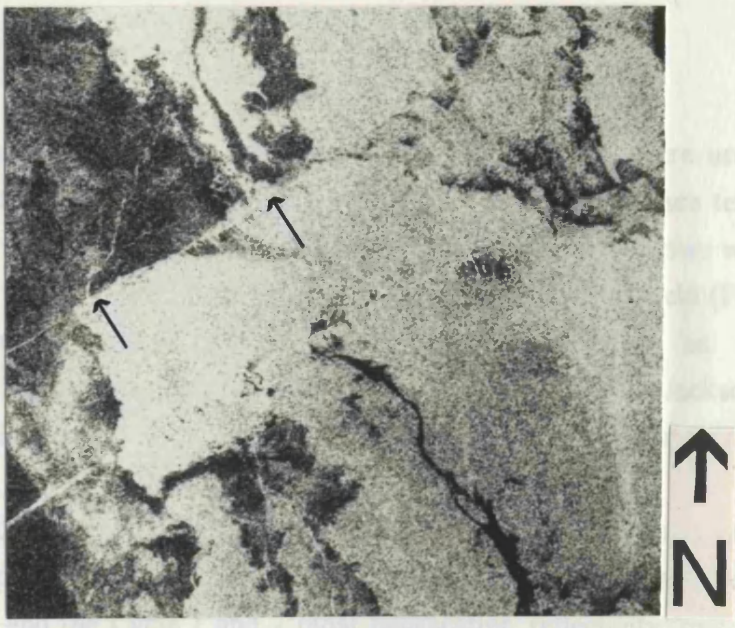
N

contributions from each component flow field. These calculations result in an estimated minimum total volume for Mylitta Fluctus of about 20,000 km^3 (Table 4.1). This volume is comparable to that of major flow fields within terrestrial flood basalt provinces.

4.4.2 Channel Development

Channel development is extensive in the proximal portion of Mylitta (Figure 4.10). These channels are usually less than 2 km wide, and are defined by radar-bright levées enclosing radar-dark interiors. They are arranged in complex branching and anastomosing networks, and often end in distal lava fans. Channels in the medial and distal portions of Mylitta Fluctus are less common, and are generally radar-dark, broadly sinuous, and lack obvious levées (Figure 4.16). The medial and distal channels have uniform widths of between 2.5 and 6 km. Some of these channels are indistinct (b-b on Figure 4.16), suggesting that less drainage occurred within them than in the more prominent radar-dark examples. Some of the radar-dark channels may be attributed in part to thermal erosion, and are similar in length, sinuosity and constant width to the extensive channels seen elsewhere on Venus (Baker et al., 1992).

The differences between proximal and distal channels in terms of abundance and morphology are similar to those documented by Guest et al. (1987) for terrestrial flow fields, and may be due to differences in topographic slope and/or cooling rate. However since there is no significant difference in topographic slope between the proximal and distal regions of channel development on Mylitta Fluctus, the differences in channel abundance and morphology are more probably due to changes in cooling rate during flow emplacement.

4.4.3 Surface Texture

In the previous chapter, the radar characteristics of the great flows were used to establish their surface texture by analogy with terrestrial flows of known surface texture and radar properties. The majority of Mylitta Fluctus consists of radar-bright flows with a homogenous backscatter, particularly in the medial and distal portions of the field (Figure 4.1). Nevertheless, there are some particularly radar-dark flows such as those characterising flow field 3 (Figure 4.8), and considerable heterogeneity in backscatter occurs within the proximal portions of flow field 4 (Figure 4.10) and in flow field 5 (Figure 4.11).

In order to provide finer constraints on the radar properties and hence surface texture and dielectric properties of flows within Mylitta, representative sites were chosen on flow fields 2, 3 and 4, and the Cycle 1 and 2 radar backscatter, reflectivity, rms slope

Figure 4.16 Channels in the medial to distal portion of flow field 4 (phases A_2 and B_1 on Figure 4.9). A prominent radar-dark channel occurs in the centre of phase A_2 at left. This channel is crossed and locally infilled by a radar-bright flow unit from episode 5 (arrowed). A channel may also be faintly traced on phase B_1 of flow field 4 (b-b). Image measures 230 x 95 km, and is centred on 53.9° S, 353.8° E. The black bar is a gap in the Cycle 1 data.

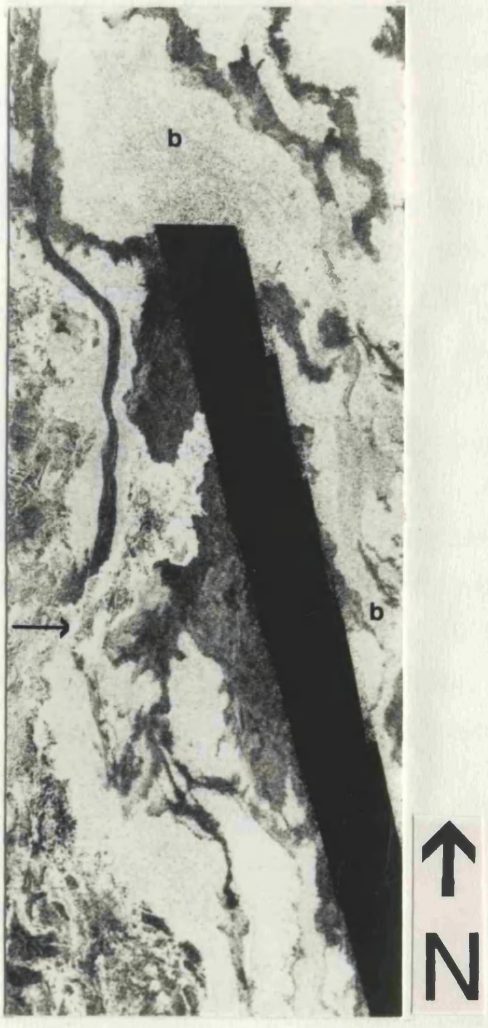
b
b
N

Table 4.3 Radar characteristics of flows within Mylitta Fluctus.

Flow Field	Location	Cycle 1 Backscatter/dB	Cycle 1 Incidence	Cycle 2 Backscatter/dB	Cycle 2 Incidence	Reflectivity	Emissivity	Rms slope
2	55.1° S, 350.9° E	-6.0	21.6°	-7.2	24.7°	0.09	0.88	4.5°
3	53.4° S, 351.0° E	-12.4	22.0°	-13.8	24.9°	-	0.86	-
$4/B_3$	53.6° S, 356.4° E	-6.4	22.0°	-7.4	24.9°	0.07	0.88	2.6°

and emissivity were recorded (Table 4.3). Each site was chosen for its spatially uniform backscatter, and in terms of radar properties the sites on flow fields 2 and 4 are representative of many of the distal flows of Mylitta. For each site the average DN value of a region covering about 1000 pixels was obtained about the location given in Table 4.3, for both Cycle 1 and 2 data. The average DN was then converted to specific radar backscatter by equations 3.1 and 3.2 (Chapter 3). These values of specific backscatter are plotted against incidence angle on Figure 4.17, together with data for terrestrial aa and pahoehoe fields on Kilauea Volcano, Hawaii, from Campbell and Campbell (1992). The average scattering behaviour of Venus as obtained from Pioneer Venus data (Pettengill et al., 1988) is plotted for comparison.

In general, for a given surface, the steeper the trend of backscatter versus incidence angle, the smoother the surface. It can be seen from Figure 4.17 that the Hawaiian aa flows form nearly horizontal trends, consistent with the roughest surfaces, while the pahoehoe flows form steeper trends, consistent with smoother surfaces. The three flow fields from Mylitta form relatively steep trends which are sub-parallel to the Venus average curve, suggesting that they may represent relatively smooth surfaces. However, since only two data points are plotted for each flow (Cycle 3 coverage was not available) this interpretation requires caution.

Both flow fields 2 and 4 have high absolute cross-sections, which plot within the range of the Hawaiian aa flows. This observation agrees with the low fractal dimensions (1.04 and 1.09) of flow margins within flow field 4, which are consistent with aa (Taylor et al., 1994). The rms slopes of flow fields 2 and 4 are 4.5° and 2.6° respectively, which are not inconsistent with an aa-type surface, and indicate generally rougher surfaces than the background plains (plains rms slopes are typically 1° to 3°). The low reflectivities of 0.09° and 0.07° for flow fields 2 and 4 support the interpretation that the high backscatter cross-sections are due to surface roughness rather than intrinsic dielectric properties. The emissivity data gives a value of 0.88 for flow fields 2 and 4, consistent with the reflectivity data.

Flow field 3 has an unusually low backscatter and plots well below the terrestrial lava flows and Venus average curve. Unfortunately the field is located within a gap in the reflectivity and rms slope data. Nevertheless, the emissivity of 0.86 implies a low reflectivity (assuming reflectivity = 1 - emissivity). These observations suggest that the low backscatter of this field may due to a very smooth surface texture and/or low intrinsic reflectivity. It is interesting to note that these flows are not derived form the source caldera, but from an obscure source on the plains away from the rift zone. It is possible that these lavas have a somewhat different composition and/or rheology from the rest of Mylitta, perhaps related to their different source region.

The uniformity in backscatter of flows in the medial and distal portions of Mylitta is interpreted as indicating a remarkably homogenous surface texture. This observation suggests that the rheological properties and final emplacement regime of the flows were

Figure 4.17 The average specific backscatter cross section of Mylitta Fluctus flow fields 2, 3 and 4 plotted against incidence angle (Cycle 1 and 2 data). The Venus global average curve from Pioneer Venus data, after Pettengill et al. (1988), is plotted for comparison. Data for terrestrial aa and pahoehoe flow surfaces on Kilauea Volcano, Hawaii, from Campbell and Campbell (1992) are also shown for comparison.

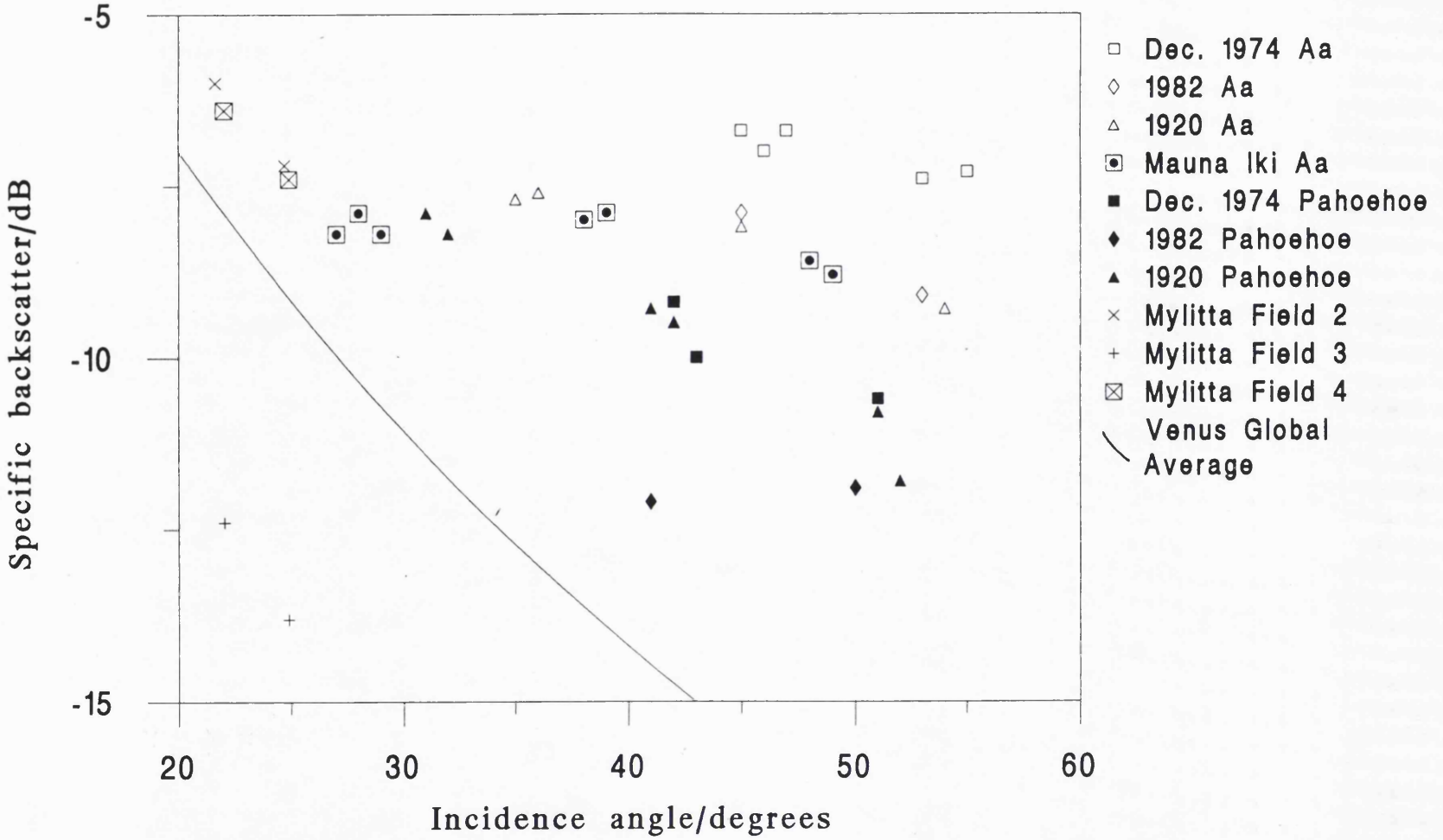
-5
-10
-15
Specific backscatter/dB
20
30
40
50
60
Incidence angle/degrees
Dec. 1974 Aa
1982 Aa
1920 Aa
Mauna Iki Aa
Dec. 1974 Pahoehoe
1982 Pahoehoe
1920 Pahoehoe
Mylitta Field 2
Mylitta Field 3
Mylitta Field 4
Venus Global Average

similar over very wide areas, supporting the case that these flow fields represent single massive eruptions, rather than multiple overlapping units. The backscatter of flows in the proximal region of flow field 4, and within flow field 5 is somewhat more heterogeneous, with rapid spatial variations in backscatter of -10 to -5 dB over incidence angles of only 21.0° to 21.5°. This variation in radar brightness may be due to channel and levée formation in the proximal region of flow field 4 (Figure 4.10), and numerous overlapping flow units within flow field 5 (Figure 4.11). Changes in radar brightness across the distal lobes of flow field 6 (Figure 4.12) may be due to enhanced roughness towards the flow margin. These variations in radar brightness may indicate a full range of textures from smoother than pahoehoe, through pahoehoe to aa, and/or differences in dielectric properties related to variations in the density or vesicularity of the lava. Unfortunately the resolution of the reflectivity, rms slope, and emissivity data is too coarse to allow discrimination of these often kilometre scale variations, and hence discrimination between roughness and dielectric effects.

Radar-dark regions are found at the margins of some flow units within flow field 4 and elsewhere in Mylitta (Figures 4.13 and 4.14). These margins appear to be intimately related to the radar-bright flows which they surround, rather than being underlying flow units. They are similar to radar-dark margins seen in other great flow fields such as that south-east of Ozza Mons (Figure 4.14, Chapter 3), and may be due to late-stage emplacement of lava from the base of the radar-bright flow unit. This lava may have chilled rapidly upon emplacement to form a relatively smooth surface texture without a broken crust. An alternative explanation is that these margins may have formed by the scouring of wavelength-scale material from the adjacent terrain by strong atmospheric convection cells caused by the rapid emplacement of the hot lava flow. Such effects have been documented for active flows on Mount Etna (Whitford-Stark and Wilson, 1976; Chester et al., 1985). However, the boundary between the radar-dark margins and the adjacent plains is usually sharp, suggesting a flow boundary rather than the more diffuse boundary that might be expected from an atmospheric effect. Therefore these radar-dark-margins are interpreted as relatively smooth lava flows emplaced with the associated radar-bright unit.

4.5 ERUPTION RATE AND DURATION

A first order estimate of the eruption rate of flows within Mylitta has been made by extrapolating the plot of flow length versus effusion rate given by Walker (1973) to lengths of 1000 km (Figure 3.16). The presence of abundant channels within Mylitta, together with the lobate morphology of most of the flow units, suggests that the majority of flows were channel-fed and cooling limited. Therefore the application of the Walker model is considered appropriate for most of the flows within Mylitta, at least to a first order. Minimum, maximum, and intermediate eruption rates for each flow field or flow

phase were determined from the upper and lower bounds and the average trend of the Walker plot respectively. Eruption duration was estimated by dividing total volumes by the corresponding eruption rate. The results are presented in Tables 4.4 (flow fields) and 4.5 (episode 4 flow phases). Omitting flows of less than two days duration (see Chapter 3, Section 3.4), eruption rates of between 8.1 x 10^3 and 4.5 x 10^6 m^3s^{-1} have been estimated for flows between 200 and 1000 km in length (Tables 4.4 and 4.5). The corresponding range of eruption duration has been estimated at between 3 days and 67 years. Flow field 1, based on an average flow length of 200 km and the volume from Table 4.1, took between about 1 and 70 years to erupt. As has been mentioned above, the field was probably emplaced as multiple eruptions over an extended period of time. Since the estimated figures are based on a single continuous eruption, they probably underestimate the emplacement period of this field. The rest of Mylitta was emplaced over an estimated total period of between 27 and 185 days (omitting all periods less than two days). Again, this figure does not include periods of inactivity between the emplacement of individual flow fields and phases. For episode 4, eruption rates of between 9.3 x 10^4 and 6.0 x 10^5 m^3s^{-1} have been calculated for flows of 500 to 1000 km length, with durations ranging between 3 and 7 days (Table 4.5). These figures correspond to the minimum bound on effusion rate; intermediate and maximum estimates all give periods of less than two days.

Estimates of effusion rate and duration have also been made using the emplacement model of Kilburn and Lopes (1991). The model was originally developed for blocky and aa flows on Mount Etna, so its use for the apparently aa flows within Mylitta is considered appropriate. This model gives effusion rates which are generally one order of magnitude higher than the Walker model, with values between 2.4 x 10^6 and 6.0 x 10^7 $m^3.s^{-1}$ (Tables 4.4 and 4.5). Combined with the estimated volumes, the model gives emplacement times of between 30 minutes and 82 days. However, these emplacement times are clearly unrealistic, especially for the longer flow phases within flow field 4, as they imply average flow velocities of up to 1000 $km.h^{-1}$. The model was developed for flows erupted onto the steeper slopes of terrestrial volcanoes, and the low values of slope on Venus produce the high values of effusion rate.

The estimated eruption rates and duration of flows within Mylitta Fluctus are similar to values estimated for cooling units within the Roza Member of the Columbia River Basalt. Swanson et al. (1975) found a close agreement between predictions obtained from a cooling model and those obtained from extrapolation of Walker's plot for units within the Roza Member. Using a cooling model, Shaw and Swanson (1970) predicted an eruption duration of approximately 7 days for a Roza cooling unit with a volume of 700 km^3. The resultant eruption rate of 1.2 x 10^6 m^3s^{-1} compares favourably with a maximum eruption rate of 1.5 x 10^6 m^3s^{-1} obtained by extrapolation of Walker's plot, from which the corresponding duration is calculated as 5 days. The values for Mylitta and the unit within the Roza Member are also similar to those predicted by Head and Wilson (1986) for extensive flows on the plains of Venus. Basing their calculations on the model of Hulme

Table 4.4 Estimated eruption rates and durations of flow fields within Mylitta Fluctus.

			Walker (1973)		Kilburn and Lopes (1991)	
Flow field	**Flow Length[a]/km**	**Volume[b]/km^3**	**Eruption Rate[c]/m^{3}s^{-1}**	**Eruption Duration**	**Eruption Rate[d]/m^{3}s^{-1}**	**Eruption Duration**
1	200	17,000	8.1×10^3	67 years	6.0×10^6	33 days
			7.0×10^4	8 years		
			5.0×10^5	395 days		
	400	17,000	4.6×10^4	12 years	2.4×10^6	82 days
			4.1×10^5	1 year		
			3.0×10^6	66 days		
2	1000	623	6.0×10^5	12 days	6.0×10^7	3 hours
			4.5×10^6	2 days		
			3.0×10^7	6 hours		
3	400	321	4.6×10^4	80 days	9.6×10^6	9 hours
			4.1×10^5	9 days		
			3.0×10^6	1 day		
4	1000	1741	6.0×10^5	34 days	6.0×10^7	8 hours
			4.5×10^6	5 days		
			3.0×10^7	16 hours		
5	600	79	1.5×10^5	6 days	2.2×10^7	1 hour
			1.3×10^6	17 hours		
			9.0×10^6	2 hours		
6	400	162	4.6×10^4	41 days	4.8×10^6	9 hours
			4.1×10^5	5 days		
			3.0×10^6	15 hours		

[a]Lengths are rounded to the nearest hundred form Table 4.1.
[b]Volumes are from Table 4.1.
[c]Minimum, intermediate, and maximum eruption rates extrapolated from the plot of length versus eruption rate in Walker (1973).
[d]Eruption rates calculated form the first order emplacement model of Kilburn and Lopes (1991), using a flow thickness of 10 m, and topographic slopes of 0.4° for flow field 1, 0.1° for flow fields 2 to 5, and 0.2° for flow field 6.

Table 4.5 Estimated eruption rates and durations of the distal flow phases within flow field 4.

Flow Phase	Length[a]/km	Volume[b]/km^3	Walker (1973) Eruption rate[c]/m^{3}s^{-1}	Walker (1973) Eruption Duration	Kilburn and Lopes (1991) Eruption rate[d]/m^{3}s^{-1}	Kilburn and Lopes (1991) Eruption Duration
A_1	500	59	9.3×10^4 8.0×10^5 6.0×10^6	7 days 21 hours 3 hours	1.5×10^7	1 hour
A_2	1000	216	6.0×10^5 4.5×10^6 3.0×10^7	4 days 13 hours 2 hours	6.0×10^7	1 hour
B_1	900	205	5.0×10^5 4.0×10^6 2.5×10^7	5 days 14 hours 2 hours	4.9×10^7	1 hour
B_2	800	166	3.0×10^5 2.5×10^6 2.0×10^7	6 days 18 hours 2 hours	3.9×10^7	1 hour
B_3	600	79	1.5×10^5 1.3×10^6 9.0×10^6	4 days 17 hours 2 hours	2.2×10^7	1 hour
C	600	46	1.5×10^5 1.3×10^6 9.0×10^6	4 days 10 hours 1 hour	2.2×10^7	35 min.
D	800	72	3.0×10^5 2.5×10^6 2.0×10^7	3 days 8 hours 1 hour	3.9×10^7	30 min.

[a]Lengths are rounded to the nearest hundred from Table 4.2.

[b]Volumes are from Table 4.2. These volumes do not include the medial and proximal sections of the flow phases, whose boundaries are uncertain, and thus the eruption durations may be underestimated.

[c]Minimum, intermediate, and maximum eruption rates are extrapolated from the plot of eruption rate versus duration in Walker (1973).

[d]Eruption rates calculated form the first order emplacement model of Kilburn and Lopes (1991), using a flow thickness of 10 m, and a topographic slope of 0.1°.

(1974), they predicted eruption rates of 10^5 to 10^6 m^3s^{-1} and durations of 6 to 14 days for flows 20 to 50 km wide and from 350 to over 2300 km long.

In summary, flows within Mylitta Fluctus are estimated to have erupted at between 10^4 and 10^6 m^3s^{-1}, with typical durations of between a few days and a few months. Flow field 1 took at least 70 years to be emplaced, with the remainder of the complex taking up to several months to be erupted. These figures are first order estimates, and do not take into account periods of inactivity between the emplacement of flow episodes, phases, and units. The values are similar to estimates of eruption rate and duration obtained for cooling units within the Roza Member of the Columbia River Basalt (Swanson et al., 1970; Shaw and Swanson, 1975), and agree with predictions by Head and Wilson (1986) for extensive lowland flows on Venus.

4.6 CONCLUSIONS

Mylitta Fluctus is a sub-parallel flow field covering 300,000 km^2 in southern Lavinia Planitia. The field is characterised by generally radar-bright digitate flow lobes with uniform backscatter. Maximum flow lengths range from 400 to 1000 km, and flow widths range between 30 and 100 km in the medial and distal portions of the field. The total volume of the complex is estimated at 2×10^4 km^3. The proximal and medial portions of the field are characterised by well developed channels. The flows were emplaced northwards from a source on the northern flank of Lada Terra onto the lowlands of Lavinia to form a complex which measures 1000 km north-south by 450 km east-west. The geological setting of Mylitta is complex. The source lies within an east-west trending belt of numerous subparallel faults, scarps and troughs, which is interpreted as a rift zone. Volcanism at Mylitta post-dates the rifting, and may be a consequence of decompression melting resulting from the rifting. No evidence for fissure-fed eruptions is seen, and the majority of flows appear to have been erupted from a caldera located on the northern flank of the rift zone. Several other tectono-volcanic centres are located along the rift zone, including a 160 km diameter corona-like structure, and smaller centres to the east of Mylitta. Like Mylitta these centres appear to post-date the rifting, but are only associated with minor amounts of volcanism. Flows were also emplaced south from the source and partially bury the impact crater Alcott. These flows are cut by graben which radiate from Quetzalpetlatl Corona.

Six flow fields have been identified, each comprising a separate episode in the emplacement history of Mylitta. The initial episode produced a 400 km diameter shield volcano with a central caldera. This was followed by the emplacement of extensive flow units up to 1000 km long in a progressive easterly sequence forming flow fields 2 to 4. Radar-dark flows from an obscure source on the plains were erupted during the later stages of episode 2 (flow field 3). The development of Mylitta was completed by the

eruption of flow field 5 to the west of flow field 4, and the emplacement of relatively short flows to the north and north-west of the caldera during the final episode.

Estimated eruption rates of between 10^4 and 10^6 m^3s^{-1} have been obtained from extrapolation of the plot of length versus effusion rate derived by Walker (1973). Flow field 1 took at least 70 years to be emplaced, with the remaining fields taking the order of weeks or months to be erupted. These figures are preliminary and do not take into account periods of inactivity between the emplacement of individual flow units.

Mylitta Fluctus is comparable in flow length and total area to major units within terrestrial flood basalt provinces. The estimated eruption rates and duration of flows within Mylitta are similar to values obtained for flow units of similar dimensions in the Columbia River Basalt Group (Swanson et al., 1975). The tectonic setting of Mylitta is also similar to that of many terrestrial flood basalts. Thus Mylitta is interpreted as a Venusian analogue of terrestrial flood basalt volcanism. Detailed mapping of individual flow units within Mylitta should allow a more accurate picture of the development of the flow complex. In addition, the application of more complex flow emplacement models should provide finer constraints on estimates of eruption rate and duration.

CHAPTER 5

RUSALKA PLANITIA AND ATLA REGIO: A REGIONAL STUDY

> Now how elephants should come to be buried in Churches, is a Question not easily answered...
>
> – Robert Plot

5.1 INTRODUCTION

A regional study and mapping of volcanism and tectonism in eastern Rusalka Planitia and northern Atla Regio has been conducted in order to establish (1) the relationships between volcanic and tectonic processes, in particular the relation between rifting and volcanism, (2) the origin of plains and their subsequent history, and (3) the regional stratigraphy. This region was chosen because it contains most of the types of volcanic and tectonic features observed on Venus, is fully covered by Cycle 1 data, and covers plains as well as highlands. The area comprises four adjacent Cycle 1 C1-MIDRs - C100N180, C115N180, C115N197 and C100N197. These MIDRs are arranged as the four quadrants of a rectangular region measuring 3170 km north-south by 3710 km east-west. In total these cover nearly 12 x 10^6 km^2 between latitudes 7.6° S and 22.6° N, and longitudes 171.4° to 206.2° E; Figure 5.1. The optimum number of C1-MIDRs to map was considered to be four. This covered a sufficiently large area so that regional trends could be established, without sacrificing the more detailed tectonic and volcanic relationships.

In order to eliminate overlap and the difficulties in constructing mosaics between adjacent C1MIDRs with local sinusoidal projections, browse versions of each C1MIDR were taken from CD-ROM and transformed from sinusoidal to Mercator projection using GIPS software. Each re-projected browse C1MIDR was then transferred to an Apple Macintosh, contrast stretched, and laser printed as 6 enlarged subscenes. For each C1MIDR the 6 subscenes were mosaicked together into a 540 x 470 mm paper copy, which formed the image base used in mapping. The geological interpretation maps were made on acetate over these base images for each C1MIDR, and with reference to contrast stretched C1-MIDR framelets displayed by GIPS on a Sun Sparcstation to provide a higher resolution guide. Each acetate map was reduced to 235 x 270 mm to fit, with

Figure 5.1 Mosaic of the four adjacent images C100N180, C115N180, C115N197, and C100N197 (clockwise from lower left). Mosaic measures 3170 x 3710 km across and is centred on 7.5° N, 188.8° E.

N

Figure 5.2 Map units and symbols for Rusalka Planitia and Atla Regio.

RUSALKA PLANITIA AND NORTHERN ATLA REGIO
MAP UNITS

Impact deposits. Radar-dark, diffuse, quasi-circular to parabolic, extended ejecta deposits surrounding impact craters. Also includes radar-dark and bright "splotches" produced by non-crater forming atmospheric impacts.

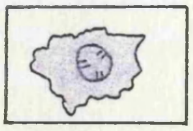

Impact craters. Includes the interior, rim, and radar-bright ejecta of impact craters. Crater names are provisional and subject to ratification by the IAU.

Radar-dark summit material. Radar-dark summit material at the highest elevations in Atla Regio.

Large volcanoes. All centralised flow aprons greater than 100 km in diameter have been mapped as large volcanoes.

Rift-zones. Defined by intense and concentrated faulting, fracturing, and graben development. Includes Dali, Ganis, and Parga Chasmata, and unnamed rift zones northeast of Ozza Mons.

Clusters of small volcanoes. Irregularly shaped clusters of small shield volcanoes and associated deposits.

Lava flow fields. Generally radar-bright (but some radar-dark) plains-forming lava flows (other than the flow aprons of large volcanoes). Includes lava flows associated with tectono-volcanic centres, and those on the plains with no obvious association. Only those fields with recognisable boundaries, and contrasting backscatter to the radar-dark plains have been mapped.

Ridge belts. Generally north-south and northwest trending belts of sub-parallel ridges and arches.

Plains. Generally radar-dark expanses of plains composed of lava flows which cannot otherwise be traced as distinct flow fields, small volcanoes, and aeolian and impact deposits not otherwise mapped.

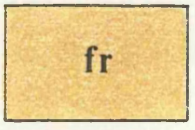

Fracture belt. Defined by generally west-northwest trending fractures and graben.

Figure 5.2 Map units and symbols for Rusalka Planitia and Atla Regio, continued.

RUSALKA PLANITIA AND NORTHERN ATLA REGIO
MAP UNITS AND SYMBOLS CONTINUED

td

Textured terrain. Characterised by a fine scale, diffuse structural fabric composed of multiple sets of faint lineations and ill-defined lava flows.

Tessera. Regions of intense and complex deformation, with multiple, superposed episodes of compression and extension. Characterised by cross-cutting faults, fractures, graben, troughs, and ridges, in a variety of orientations.

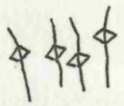

Sinuous ridges

Lineaments. Includes faults, fractures, graben, and other structures whose nature has not been determined.

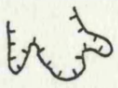

Lava flow margin. The distal margins of lava flows are marked by ticked lines. Ticks are within the lava flow. Applies to large volcanoes and other lava flow fields.

Figure 5.3 Geological map of C100N180. Latitude and longitude are given at 5° intervals around the margins of the map. Crater names are provisional and subject to ratification by the IAU.

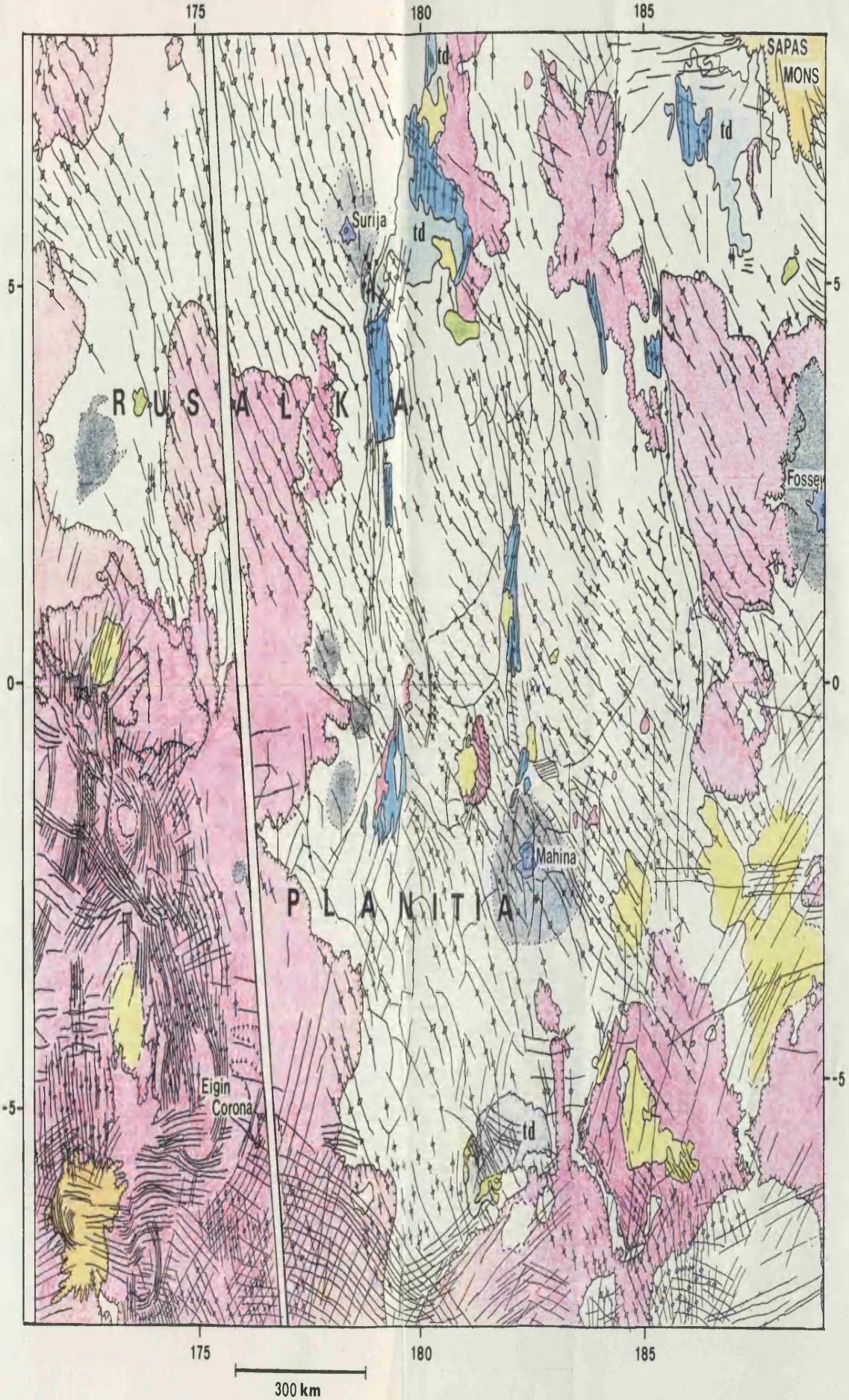
175
180
185
5
0
-5
SAPAS
MONS
td
td
td
Surija
RUSALKA
Fossey
Mahina
PLANITIA
Eigin
Corona
td
300 km

Figure 5.4 Geological map of C115N180. Latitude and longitude are given at 5° intervals around the margins of the map.

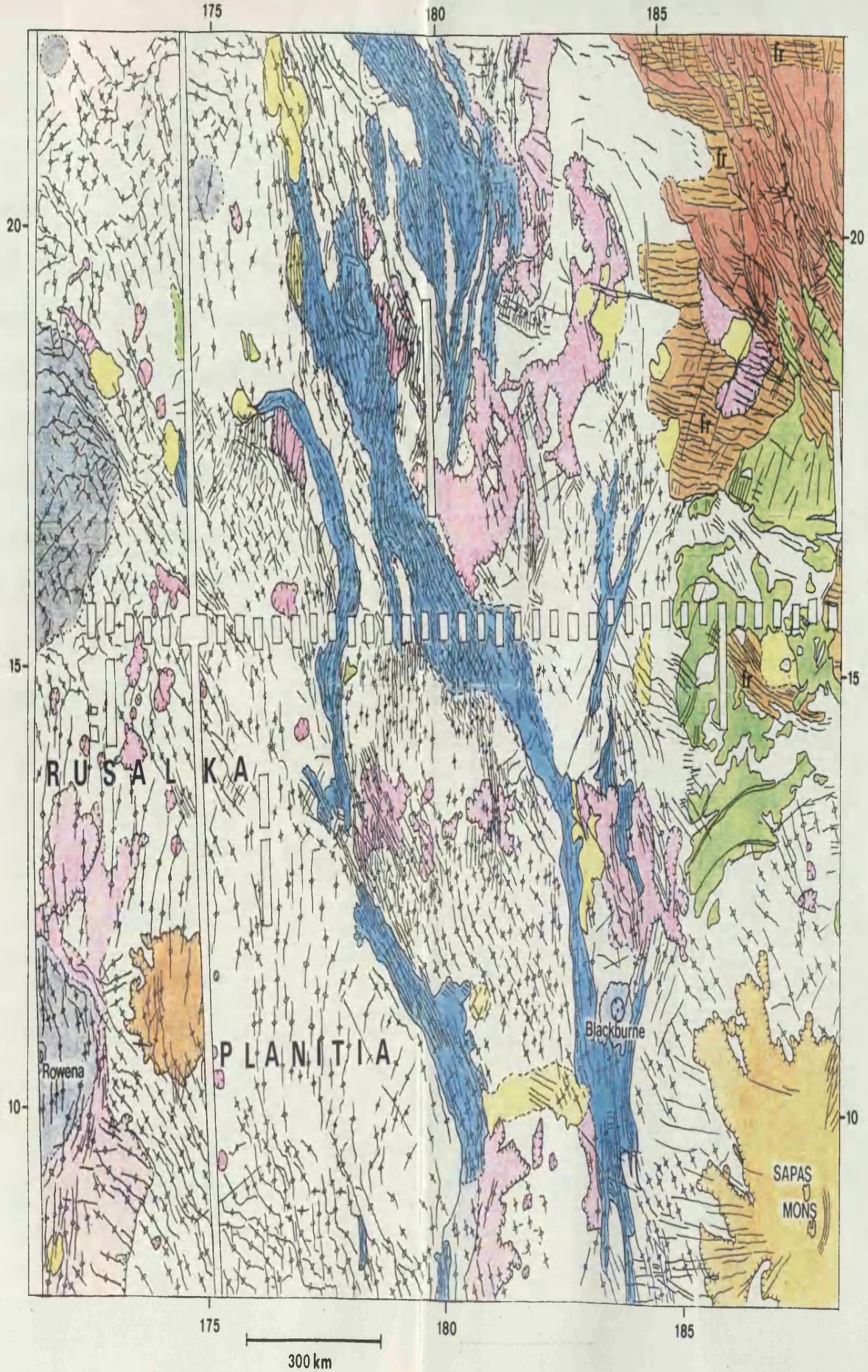
175
180
185
20
15
10
fr
fr
fr
fr
fr
RUSALKA
PLANITIA
Rowena
Blackburne
SAPAS
MONS
300 km

Figure 5.5 Geological map of C115N197. Latitude and longitude are given at 5° intervals around the margins of the map.

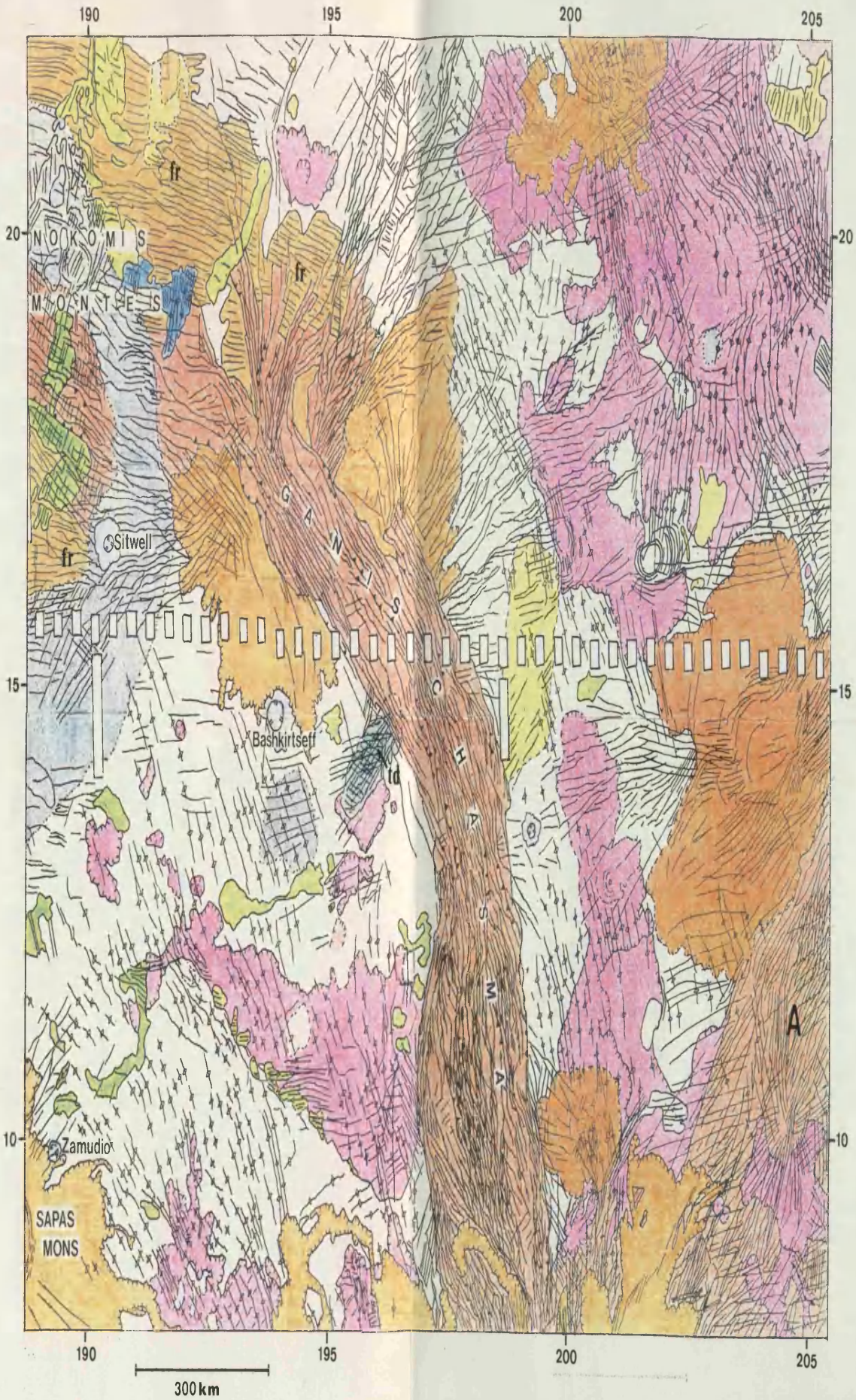
190
195
200
205
20
15
10
fr
NOKOMIS
MONTES
GANIS
CHASMA
Sitwell
Bashkirtseff
td
Zamudio
SAPAS
MONS
A
300 km

Figure 5.6 Geological map of C100N197. Latitude and longitude are given at 5° intervals around the margins of the map. Letters A, B, and C refer to rift zones described in the text.

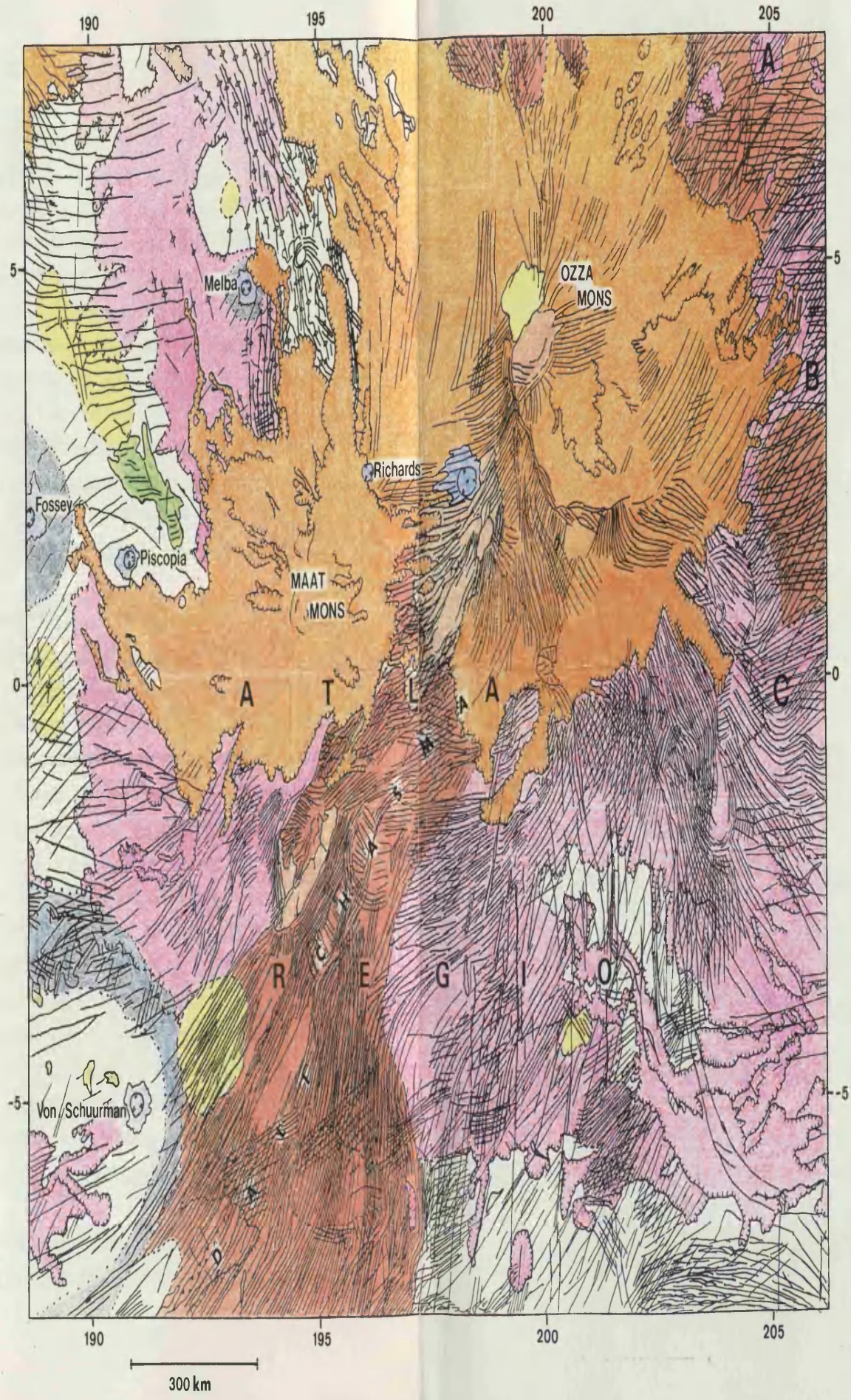
190
195
200
205
5
0
-5
A
B
C
Melba
OZZA
MONS
Richards
Fossey
Piscopia
MAAT
MONS
A T L A N T I S
R E G I O
Von Schuurman
300 km

margins, within the bounds of an A3 size sheet. The final maps appear as Figures 5.2 to 5.6, and have a scale of about 1:6,750,000.

5.2 OVERVIEW

The region mapped is as diverse in terms of physiography, volcanism and tectonism as Venus is globally. All the main types of volcanic and tectonic features, with the exception of mountain belts, are found within its boundaries. The western half of the region comprises the volcanic plains of eastern Rusalka Planitia, which are characterised by a large-scale fabric of north-west trending sinuous ridges that resemble lunar and Martian wrinkle ridges (Solomon et al., 1992, Figures 5.3, 5.7, and 5.8). The sinuous ridges are associated with a number of generally north-west trending ridge belts which occupy the plains in C115N180 (Figure 5.4). These plains lie at or around the mean planetary radius (mpr), but in the centre of C100N180 they are found as low as 700 m below mpr. However, they rise to 500 m above mpr around 5.0° S, in the southern portion of C100N180, where they constitute the northern flank of Aphrodite Terra. A number of coronae and corona-like centres occur in the south-west corner of C100N180 (Figure 5.3). They are associated with extensive lava flow fields and are cut by concentrations of sinuous ridges.

The eastern half of the area is dominated by the broad volcanic rise of Atla Regio, which is centred near 4° N, 200° E, and rises to an elevation of 3 to 4 km above its surroundings, with peaks up to 4 km higher (Bindschadler et al., 1992b; Senske et al., 1992). Pioneer Venus data revealed that Atla is a major tectonic junction centred on convergent deformation zones, and contains mountains interpreted to be volcanoes. It has a significant gravity anomaly with a large apparent depth of compensation of about 200 km (Schaber, 1982; Senske, 1990; Smrekar and Phillips, 1991). Magellan data reveal five rift zones (Figures 5.5 and 5.6), which converge upon the large volcano Ozza Mons at 4.6° N, 201° E, (Senske et al., 1992). These rifts include; Ganis Chasma to the north of Ozza Mons; Dali Chasma to the south-west; Parga Chasma in the south-east; and two un-named rifts to the north-east of Ozza. Ozza Mons itself rises to 6.6 km above mpr, and is surrounded by an extensive flow apron. Maat Mons (0.5° N, 194.4° E), a large volcano rising to 8.3 km above mpr, lies just north of Dali Chasma to the south-west of Ozza Mons (Figure 5.9). Many other lava flow fields lie to the south, west, and east of the Maat and Ozza flow aprons, including a subparallel complex of flow fields to the south-east of Ozza Mons, which was given detailed treatment in Chapter 3. A large volcano is centred on Ganis Chasma at 17° N, 194° E (Chapter 3, Table 3.1), and has been dissected by intense faulting.

Other volcanic centres include the large volcano Sapas Mons at 9.5° N, 187.5° E (Figure 5.10), and a corona at 14.2° N, 204.7° E, which is surrounded by an extensive

Figure 5.7 Northwest trending sinuous ridges in Rusalka Planitia deform both a radar-bright flood lava flow field and radar-dark plains. The flood lava has flowed from tectono-volcanic centres in the south-west of C100N180 onto the radar-dark plains to the east. Image measures 200 x 150 km and is centred on 2.2° N, 177.0° E.

Figure 5.8 Image showing the relationship between textured terrain (td), a north-south trending ridge belt (rb), and the radar-dark plains. The ridge belt deforms the textured terrain, and both are embayed by the radar-dark plains. Note the north-west trending sinuous ridges which deform the plains, textured terrain and the ridge belt. A cluster of small volcanoes is located in the north-east of the image, and deposits associated with this cluster embay the ridge belt to the south. Image measures 230 x 170 km and is centred on 6.5° N, 179.1° E.

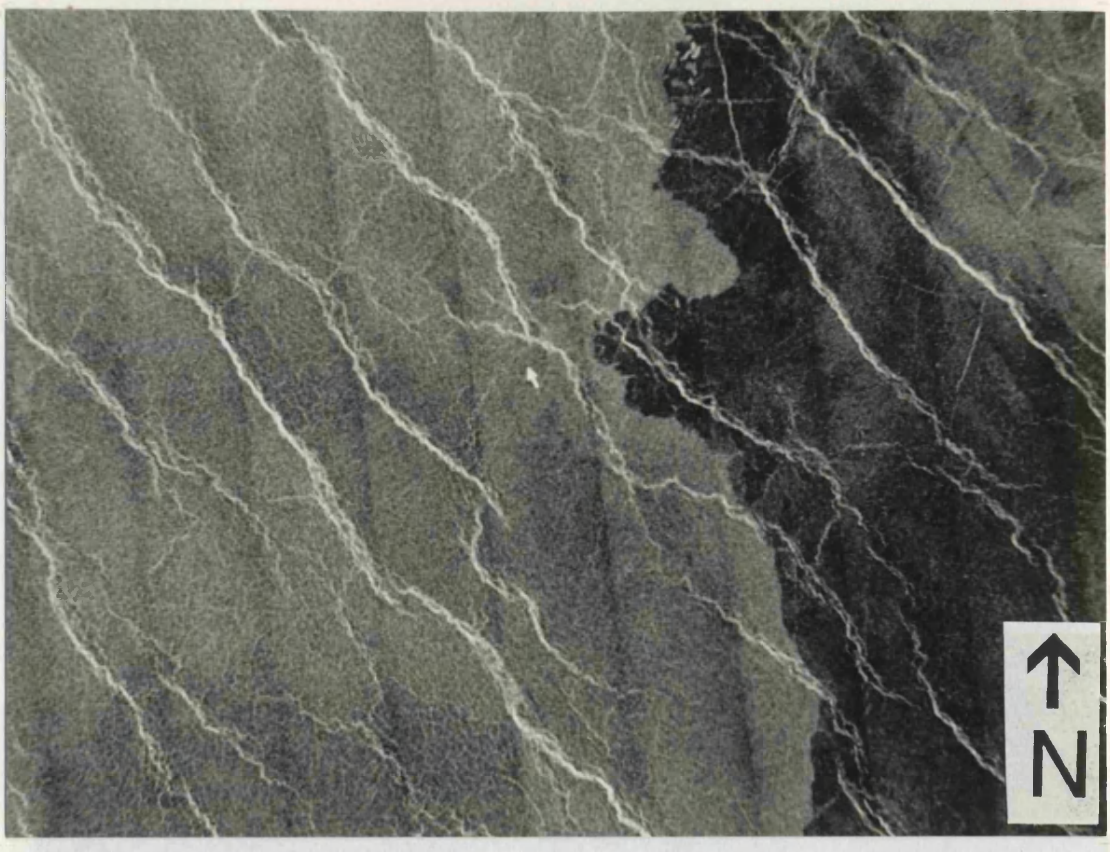
N

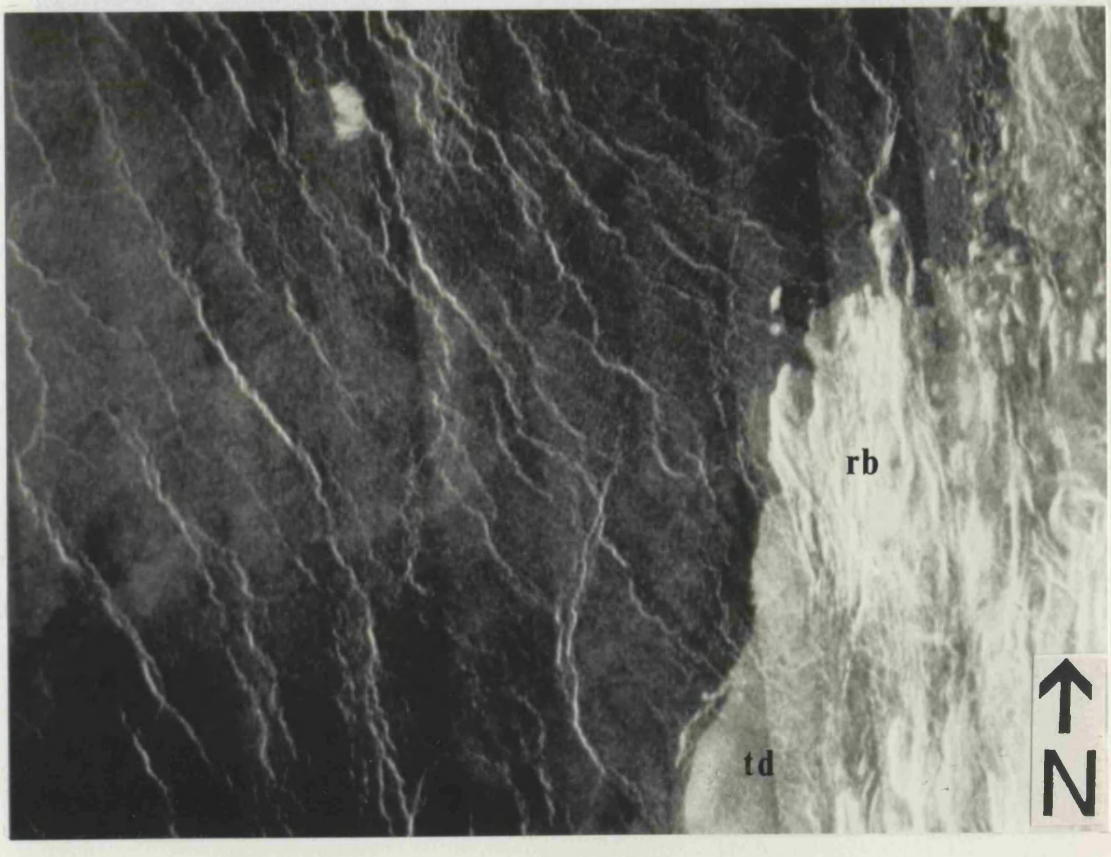
rb
td
N

Figure 5.9 The large volcano Maat Mons (0.5° N, 194.4° E) seen in a false-colour perspective view, based on Magellan altimetry and radar-clinometry. The view looks south and has a vertical exaggeration factor of 10. The radar-bright flow apron of Maat is well seen, and distal digitate flows extend into the foreground where they embay the ejecta of the 23 km diameter impact crater Melba. North-south trending sinuous ridges extend across the radar-dark plains, and are buried by flows from Maat. Magellan image P-40175.

Figure 5.10 The large volcano Sapas Mons (9.5° N, 187.5° E) seen in a false-colour perspective view, based on Magellan altimetry and radar-clinometry. The view looks south and has a vertical exaggeration factor of 10. Sapas lies in the middle distance with radar-bright distal flow lobes extending into the foreground. The twin scalloped margin domes can be seen at the summit of Sapas. Maat Mons lies on the horizon directly beyond Sapas. Magellan image P-40256.

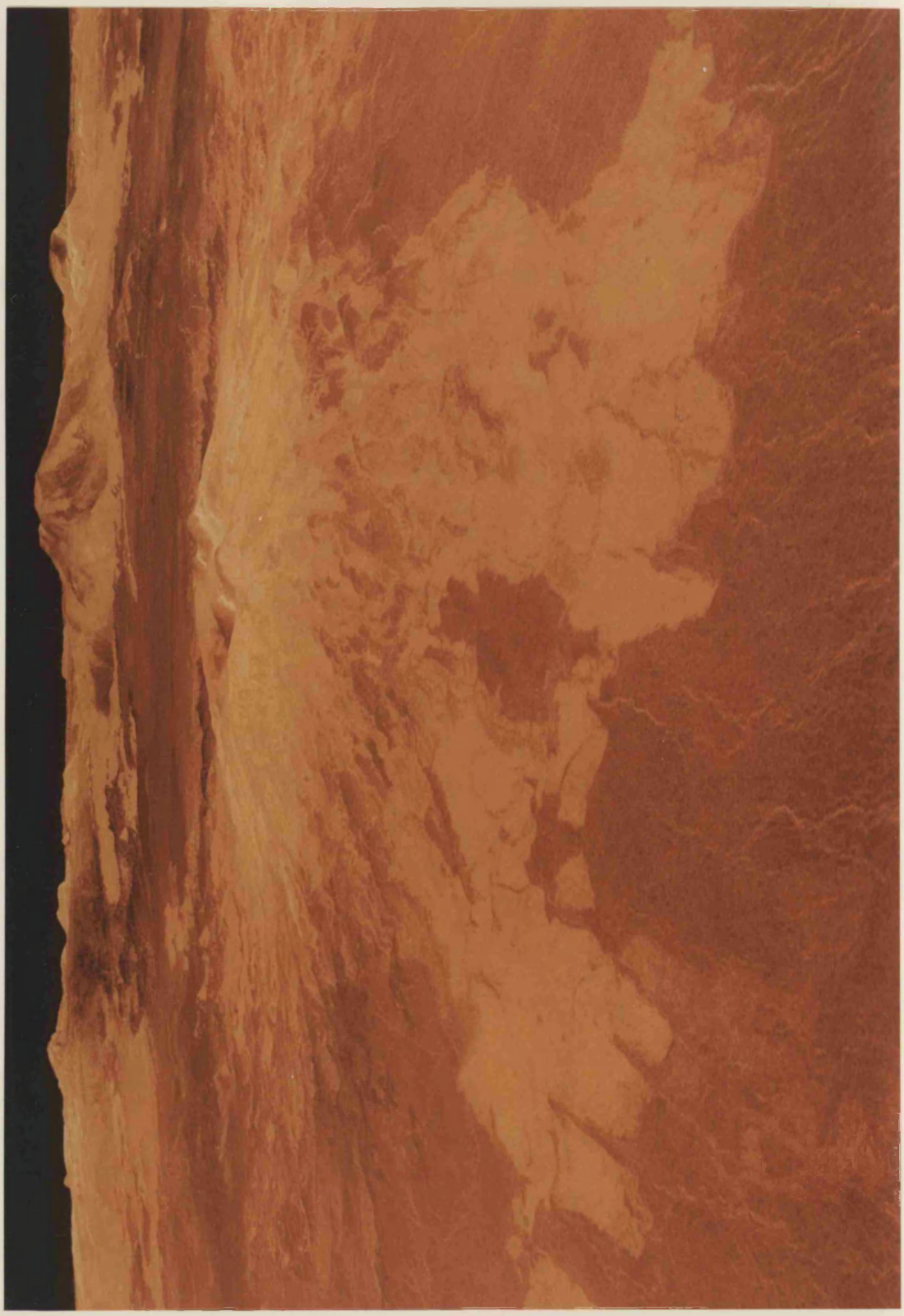

flow apron (Figure 5.5). Several smaller volcanic centres in the north-east of C115N197 are associated with extensive lava flow fields. Numerous smaller flow fields are scattered across the plains throughout the region, as well as many clusters of small volcanoes.

A region of elevated terrain known as Nokomis Montes is located in the north central part of the region at the north-eastern extremity of Ganis Chasma (Figure 5.5). Nokomis is composed of blocks of tessera up to 3.5 km above mpr, which have been extensively rifted, and in this respect is very similar to Rhea Mons in Beta Regio (Senske et al., 1991b). A fracture belt lies to the east and west of Nokomis Montes and predates the rifting and plains in the area (Figure 5.11). An extensive outcrop of un-rifted tessera is found to the south-east of Nokomis Montes, where it has been embayed by plains-forming lavas to form large, irregular islands (Figure 5.12). The least common unit recognised in the region is that of textured terrain, which was first identified and named by Squyres et al. (1992b) in Lavinia Planitia. It is characterised a structural fabric which is similar to that of the tessera, albeit at a finer scale. It is deformed by north-south trending ridge belts in the west-central part of the region, and like the tessera it is embayed by radar-dark plains (Figure 5.8).

As well as sinuous ridges, and apart from the rift zones, the plains contain abundant radar-bright lineaments interpreted to be of extensional origin. These features include swarms of en-echelon fractures, graben, and straight and curvilinear structures which are thousands of kilometres in length. Most of these lineaments belong to regional trends which are usually radial to tectono-volcanic centres, and often normal to sinuous ridges and ridge belts.

A number of impact craters and deposits are scattered throughout the region. Large, radar-dark parabolic haloes occur around many of the craters, most notably those around craters Von Schuurman (5.0° S, 191.0° E) and Sitwell (16.6° N, 190.2° E). The impact craters are generally the most recent features in the area, although four are embayed by the flow aprons of large volcanoes within Atla Regio.

5.3 TECTONISM

The region has been subjected to a long and varied tectonic history, with many different episodes of compressional and extensional deformation. As with much of Venus, tectonic patterns are found at a variety of scales up to regional trends, where structural patterns are coherent across many thousands of kilometres. Tectonism and volcanism appear to have occurred simultaneously in many areas, with structures both cross-cutting and being flooded by lava flows. Each tectonic feature or unit will be discussed in turn, in inferred stratigraphic order, from oldest to youngest.

Figure 5.11 Image of the fracture belt in the north of C115N197. In this area the belt is composed of west-north-west trending fractures and graben, some of which are paired to form bands of 1.5 km width. These structures cut tessera in the north-west part of the image. The fracture belt has been partially flooded by plains-forming lavas. Image measures 200 x 145 km and is centred on 21.2° N, 191.5° E.

Figure 5.12 Image of part of a large island of tessera south of Nokomis Montes. The tessera is characterised by a complex fabric of multiple cross-cutting fractures and graben in a variety of orientations. The latest structures are arcuate graben which, like the rest of the tessera, are extensively embayed by the radar-dark plains. A couple of small volcanoes with radar-bright vents (v) lie on the plains at the western margin of the tessera. Image measures 200 x 150 km and is centred on 12.9° N, 185.9° E.


N

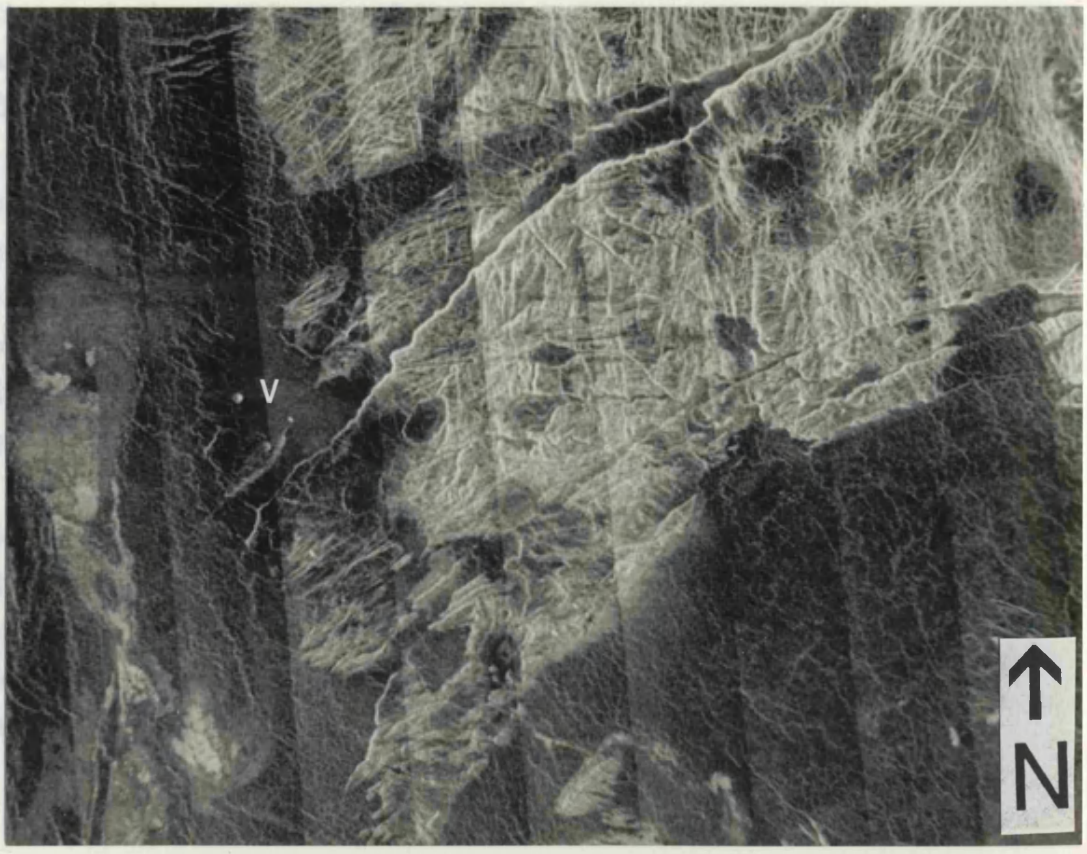
V
N

5.3.1 Tessera

In the northern-central part of the region, between the ridge belts on C100N180 (Figure 5.3) and Ganis Chasma (Figure 5.4) lie a number of islands of tessera. The greatest concentration of this terrain occurs between 12.5 to 18.0° N, 185.0 to 188.5° E, and extends north into Nokomis Montes. This concentration includes several large, irregular shaped islands of tessera up to 300 km across (Figure 5.12). These islands are extensively embayed by the radar-dark plains which surround them, and are separated by between 10 and 70 km. They may be outcrops of a much larger area of basement, which could extend up to 1000 km to the south-east, over a region of scattered, 20 to 200 km sized patches of tessera (Figure 5.5). Magellan altimetry gives elevations of between 400 m and 1.3 km above the adjacent plains for these islands of tessera.

The islands of tessera display a highly complex fabric of multiple cross-cutting lineaments in a variety of orientations (Figure 5.12). These include extensional structures from the resolution limit up to graben of 4 km in width, and several hundred kilometres in length. Arcuate graben cut across the tessera, and are themselves flooded by plains lavas. The arcuate graben may be traced from the tessera into the plains, where they must continue beneath the surface, as their parallel, bounding lineaments are still faintly visible. This provides further support to the contention that the tessera extends as a basement beneath the plains. Similar relationships between tessera, graben and plains, have been documented for southern Guinevere Planitia by Solomon et al. (1992). There is a complete range in the degree of flooding of the tessera between completely flooded and un-flooded areas. This may reflect a spatial variation in the number or thickness of individual lava flows, and/or the local topography of the terrain.

Magellan data confirm that Nokomis Montes itself is an area of tessera, as predicted by Bindschadler et al. (1990a). Nokomis Montes is cut by the north-west extension of Ganis Chasma into blocks of tessera between 30 and 200 km across. These blocks display a complex tectonic fabric, where the latest structures are the north-west trending fractures of the rift zone. Some of these blocks show north-west trending fractures cutting a dense array of poorly defined north-east trending ridges and graben; the latter with a spacing of 1 km.

All the areas of tessera in the region have experienced a long and complex history of compressional and extensional deformation. Except in a few cases (e.g. Figure 5.12), the structures within the tessera are generally un-related to those within the adjacent plains. This observation implies that the tectonic activity responsible for the structural development of the tessera was inactive since before the resurfacing by plains-forming lava.

5.3.2 Textured Terrain

This terrain is characterised by a dense structural fabric at a scale of just a few hundred metres or less; a "texture" which is just resolved in the SAR images. This terrain is very similar in appearance, tectonic association, and general stratigraphic position, to the "textured terrain" found in Lavinia Planitia by Squyres et al. (1992b). It is found in association with several ridge belts which partly deform it. Examples occur at around 5.0° N, 179.7° E, south-west of Sapas Mons around 6.5° N, 186.5° E, and at 5.5° S, 181.5° E, Figures 5.3 and 5.8. The structural fabric does not usually show any preferred orientation and may therefore be composed of multiple cross-cutting structures in a variety of directions, not unlike the tessera but with a higher spatial frequency. In some places it is difficult to distinguish between textured terrain and radar-bright lava flows (for example at around 8.5° N, 180.5° E). Only the structural fabric of the textured terrain allows it to be distinguished in these cases.

The textured terrain is embayed by the radar-dark plains, and may itself represent ancient deformed plains, which have escaped volcanic burial by virtue of their locally elevated topography. Stratigraphically, the textured terrain shares a similar position to the tessera, and it is also appears to be highly deformed. However it is comparatively rare in occurrence. Unlike most areas of tessera, textured terrain has no discernible topographic signature. This could mean that the terrain has a genuinely low elevation with respect to the plains, or that the areas involved are too small to be adequately resolved in the altimetry. The former explanation is favoured, as ridge belts, impact craters, and other features with similar planimetric dimensions to the textured terrain are themselves resolved in the altimetry. A low elevation would explain the rare occurrence of this terrain, as it would be more susceptible to volcanic flooding. These observations suggest that textured terrain represents relatively ancient plains which may be younger than the tessera, but which have survived long enough to record multiple episodes of deformation, including the formation of ridge belts.

5.3.3 Fracture Belt

This belt occurs in the north central part of the region, adjacent to Nokomis Montes, and is cut by the north-west extension of Ganis Chasma (Figures 5.4 and 5.5). Between 19 and 22° N, 190 to 195° E it is characterised by a subparallel pattern of west-north-west trending paired lineaments spaced 1.5 km apart, and forming bands from 40 km to over 100 km in length, the whole having a mottled and subdued appearance (Figure 5.11). Some of the lineaments are revealed to be graben where they cut an outcrop of tessera around 22.0° N, 190.3° E. Along its northern margin and across its interior, the belt is embayed by radar-dark plains, and is covered by several fields of small volcanoes.

Figure 5.13 Image showing the relationship between several volcanic and tectonic features adjacent to the north-west extension of Ganis Chasma on C115N180. The oldest feature is a fracture belt visible as east-west trending radar-bright lineaments in the west of the image (fr). A radar-dark lava flow field (lf) has flooded the fracture belt in the central and south-east part of the image and reveals many east-west trending graben (gr). A cluster of small volcanoes (s) as been emplaced upon the radar-dark flow field, and some of the vents are aligned in sympathy with north-east trending lineaments. The latest deformation is represented by the generally north-west trending fractures and graben of Ganis Chasma in the north-east part of the image. Some of these later structures have developed along earlier east-west lineaments of the fracture belt. Image measures 245 x 190 km and is centred on 19.1° N, 186.0° E.

Figure 5.14 Reticulate network of sinuous ridges deforming plains around 20.9° N, 172.0° E. Image measures 115 x 85 km.

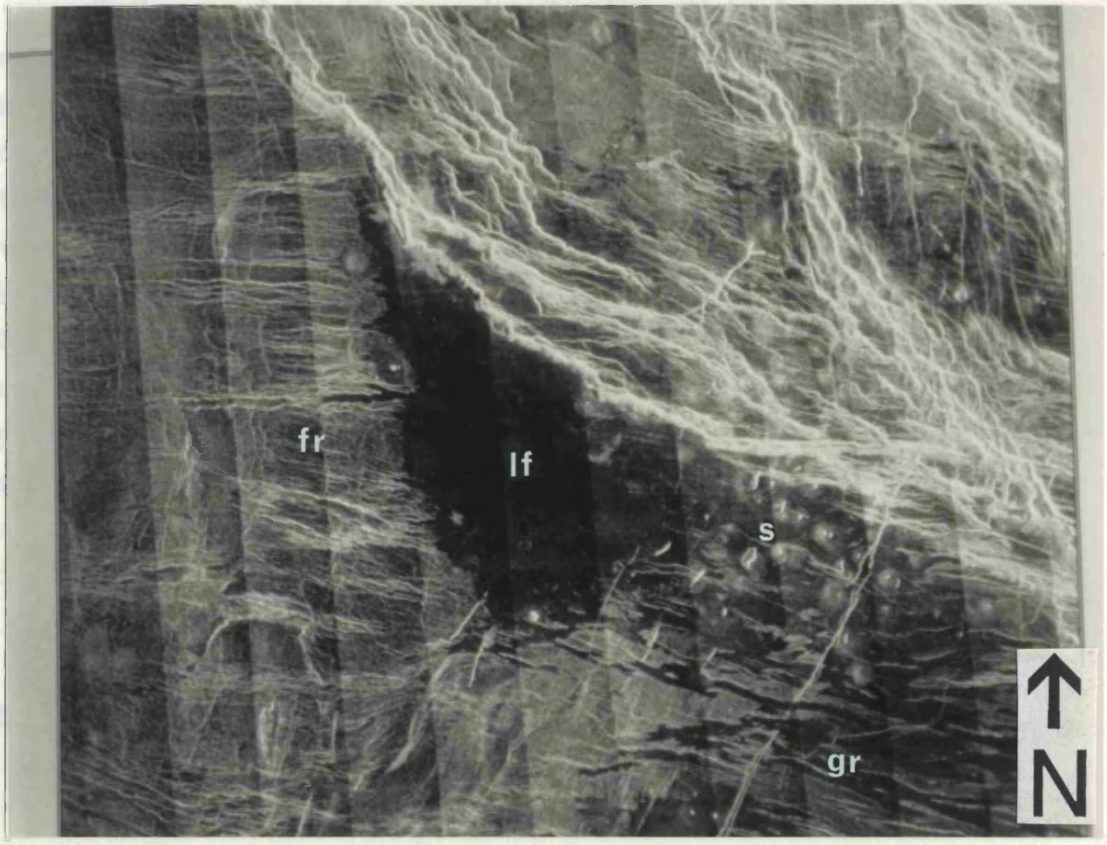
fr
lf
s
gr
N

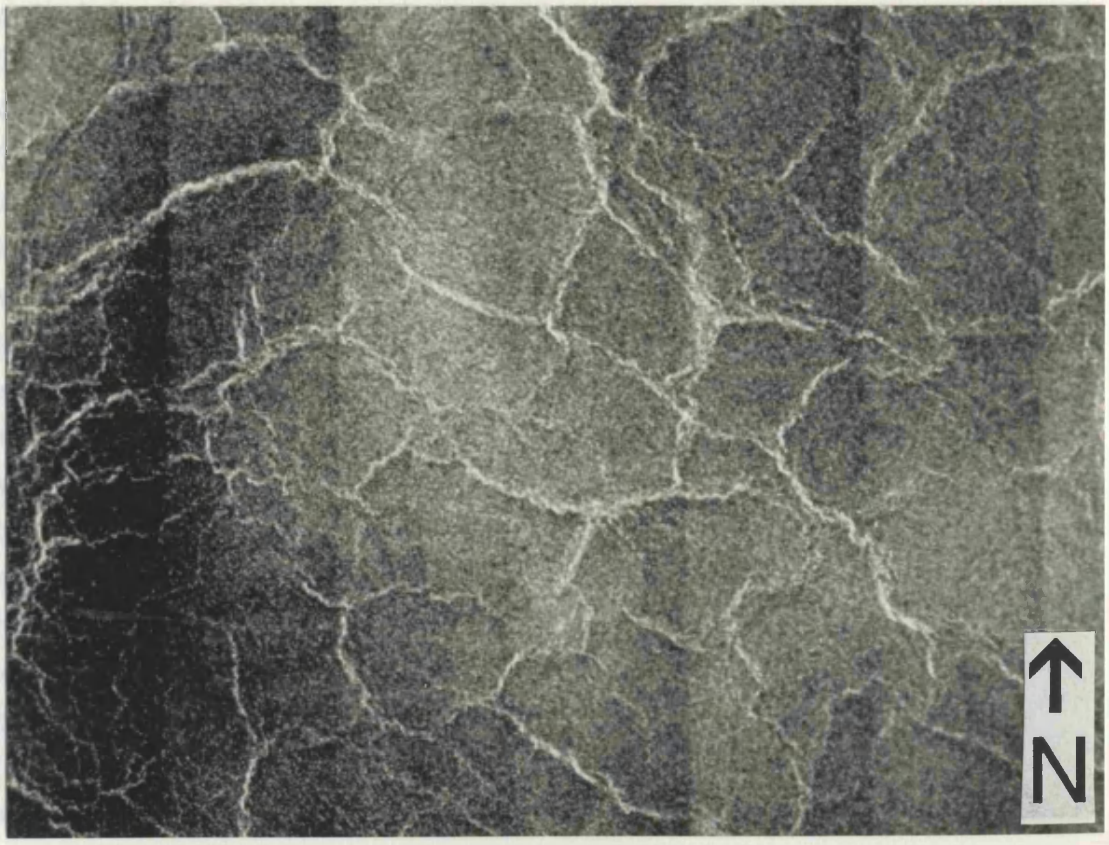
N

Further west the banded pattern is replaced by a fabric of west-north-west trending subparallel radar-bright lineaments. Individual lineaments are at or below the limit of resolution, and occur in swarms up to 8 km wide, as well as in isolation. This fabric is embayed by plains-forming lavas, and cut by fractures of the north-west extension of Ganis Chasma (Figure 5.13). The most westerly of these north-west fractures are composed of west-north-west en-echelon segments which are aligned with the lineaments of the fracture belt. Indeed, the entire section of northern Ganis Chasma between the large volcano at 17° N, 194° E and Nokomis Montes is broadly subparallel to the older fracture belt further north. This observation suggests that the fracture belt was either formed during the early phase of an extended period extensional activity, or that Ganis Chasma was formed in sympathy with the structural trend of the earlier belt, but in a completely different tectonic regime. Since the fracture belt is extensively embayed by plains-forming lavas and clusters of small volcanoes, the latter interpretation is preferred.

5.3.4 Ridge Belts

Ridge belts with a north-south trend are found on the plains of Rusalka Planitia on C100N180 (Figures 5.3 and 5.8). They are similar to ridge belts seen elsewhere on Venus, in Lavinia, Vinmara and Atalanta Planitiae (Sukhanov and Pronin, 1989; Frank and Head, 1990; Solomon and Head, 1992; Squyres et al, 1992). However, there are also some particularly wide ridge belts to the north of approximately 10° N on C15N180 (Figure 5.4), which are different in character to those further south. As a whole the ridge belts are composed of numerous subparallel ridges, which are subparallel to the trend of the belt (Figure 5.8). The belts are between 15 and 150 km across, from 70 to over 1600 km in length, and are typically elevated by 400 m to 1 km above the plains. Typical widths and lengths are 50 km and 500 km respectively, and the typical spacing between ridge belts is a few hundred kilometres. Individual ridges are 20 to 240 km in length, and are around 1 to 10 km in width and separation. Smaller ridges, of a few hundred metres in width, occur in dense swarms between the larger ridges. There are also single wide ridges up to 20 km across, a few tens of kilometres in length, and about 600 m high, which are visible in the altimetry data, but are not otherwise obvious in the SAR images. However, they do coincide with concentrations of sinuous ridges and slope induced brightenings in radar backscatter. Examples are found between 4.2° N, 177.3° E to 9.0° N, 174.0° E, and 11.4° N, 176.6° E to 15.0° N, 174.2° E (Figures 5.3 and 5.4). All the ridge belts in the region were probably formed by belt-normal compression and crustal thickening, as has been proposed for ridge belts seen elsewhere by Barsukov et al. (1986a), Basilevsky et al. (1986), Frank and Head (1990), and Kryuchkov (1988). Individual ridges within belts are interpreted to be folds formed by belt-normal compression.

The ridge belts north of about 10° N follow the same trends as the adjacent sinuous ridges on the plains (see below), which often enter the belts along strike (Figure 5.4). Indeed, these ridge belts appear to be composed of sinuous ridges with wider separations than the ridges in the belts further south. The belts on C100N180 are narrower, and have sharp boundaries with the plains which embay them, whereas the widest sections of ridge belt on C115N180 have no definite boundary, having been mapped by ridge concentration alone. The ridge belts on C115N180 are also longer, and change direction along strike, following the dominant structural trends of sinuous ridges on the plains. For example the longest belt in C115N180 (Figure 5.4) runs north-south by the crater Blackburne (11.0° N, 183.8° E), but turns north-west around 13.5° N, 182.6° E. At 15.2°N, 180.2° E the belt contains both north-south and north-west trending ridges which appear to be contemporaneous, as no cross-cutting relationships can be distinguished. The same ridge belt bifurcates around the position of Blackburne, as do several other sections of ridge belt (Figure 5.4).

Most of the ridge belts within C100N180 are oblique to the trend of the sinuous ridges on the plains (Figures 5.3 and 5.8), and appear to be older than both the sinuous ridges and the wider ridge belts on C115N180. This age difference is supported by the greater embayment of the ridges on C100N180 by the plains, their smaller areas, and their deformation of relatively ancient textured terrain (Figure 5.8). The ridge belts north of about 10° N appear to deform much of the plains themselves, rather than being flooded by plains. The ridge belt that runs between 12° N, 178.5° E and 9° N, 180.5° E is associated with sinuous ridges to the north, but deforms textured terrain to the south (Figures 5.3 and 5.4). Thus it appears that ridge belt formation was active throughout the history of plains emplacement, with more recent deformation being represented by the ridge belts on C115N180. The relationships between sinuous ridges and ridge belts, and their origins, are discussed further under sinuous ridges below.

5.3.5 Sinuous Ridges

Many sinuous radar-bright ridges with pervasively north-west to north-south trends occur throughout most of the region except Atla Regio. They are well developed within Rusalka Planitia on C100N180 where they form a consistently north-west trending pattern that maintains coherence over thousands of kilometres (Figure 5.3). Individual ridges in this area are up to 5 km wide, and between 10 and 200 km in length, with a variable spacing of around 20 km (Figures 5.7 and 5.8). The density and length of ridge segments decreases towards the northern flank of Eastern Aphrodite and Dali Chasma (Figure 5.3). Swarms of north-west to north-south trending ridges are also found in the south-west of C100N180, where they run along a chain of corona-like centres (Figure 5.3), and in the north-east of C115N197 (Figure 5.5).

The north-west trending fabric of sinuous ridges on C100N180 appear to be unrelated to the north-south trending ridge belts which they cross obliquely (Figures 5.3 and 5.8). However, further north on C115N180 the sinuous ridges are intimately associated with generally north-west trending ridge belts (Figure 5.4). Many of the sinuous ridges run parallel to the adjacent ridge belts in this area, which are themselves composed of concentrations of these ridges. Parallelism between sinuous ridges and ridge belts has also been noted by Squyres et al. (1992b) and Solomon and Head (1992) for ridge belts in Lavinia Planitia. The association between these features is taken to indicate that they share a common origin, and were formed at the same time. The sinuous ridges exhibit more variable trends and closer spacings on C115N180 than they do further south. In a number of areas two distinct trends of sinuous ridges form orthogonal or reticulate networks. Examples occur around 8° N, 177° E, and in the extreme north-west of the region (Figures 5.4 and 5.14). The variations in ridge orientation and density may reflect local differences in crustal thickness, structural properties and stress fields.

Northwest trending sinuous ridges are also found between Sapas Mons and Ganis Chasma (Figures 5.5 and 5.6), and in the north-east of C115N197, where their orientations are controlled by pre-existing tectono-volcanic centres as discussed below under coronae (Figure 5.5). Except for a belt of sinuous ridges extending north from Maat Mons (Figures 5.6 and 5.9), such ridges are absent from Atla Regio. The predominance of these ridges on the lowland plains and their absence on the adjacent volcanic rises may reflect the control of tectonic regime on their distribution (see below).

Solomon et al. (1992) have used the term wrinkle ridges to describe the sinuous ridges found in Rusalka Planitia, since their morphology, relief, and spacing is similar to wrinkle ridges observed in the lunar maria and Martian ridged plains (Plescia and Golombek, 1986; Watters, 1988). The ridges are interpreted to be either folds or thrust faults formed by ridge-normal compression. The occurrence of sinuous ridges with pervasive trends across the region suggests regionally compressive stress fields that are coherent over thousands of kilometres. Such regional patterns may result from a strong coupling between the lithosphere and mantle flow. This coupling is predicted by the apparent absence of a low viscosity layer in the upper mantle of Venus as determined from Pioneer Venus gravity data (Kiefer et al., 1986; Smrekar and Phillips, 1991). In a recent study of Magellan gravity data, Bindschadler (1994) interprets Rusalka Planitia as the site of mantle downwelling. Such downwelling may have provided the necessary compression to induce sinuous ridge and ridge belt formation. Other sources for the compression include the upwelling and horizontal spreading of a plume beneath the adjacent volcanic rise of Atla Regio, and its subsequent gravitational relaxation. These processes need not be treated in isolation, but may form an integrated system of mantle upwelling and return flow in the region.

Any tectonic model for sinuous ridge formation must take into account their spatial and stratigraphic relationship to the ridge belts and plains. If a comparatively recent and

ongoing system of mantle dynamics accounts for the sinuous ridge system on Rusalka Planitia (and to the east of Atla Regio), then it must also account for the related north-westerly trending ridge belts on C115N180. However, the existence of older, north-south trending ridge belts on C100N180, which are un-related to the regional pattern of sinuous ridges, has already been noted. These ridge belts are embayed by plains, but semi-continuous with belts further north, which deform the plains instead. These relationships suggest that ridge-belt formation took place over an extended period of time, and was interleaved with plains formation. The ridge belts on C100N180 are clearly buried and embayed by younger volcanic plains, and perhaps were formed in a stress field distinct from that which formed most of the later ridge belts on C115N180 and the sinuous ridges. If the younger ridge belts and sinuous ridges are a consequence of mantle downwelling and adjacent plume spreading, then the presence of the older ridge belts implies either that the system of mantle dynamics existed over an extended period including plains formation, or that some other tectonic regime was responsible for forming the older ridge belts. If most of the plains in the region were formed by one or more episodes of catastrophic global resurfacing, then it is difficult to envision an ongoing system of mantle dynamics and lithospheric compression at the same time as resurfacing. It therefore seems likely that the older ridge belts represent the deformation of an ancient terrain, which was followed by a major period of resurfacing, before the establishment of a more recent period of downwelling and lithospheric compression. The continuity between the older and younger ridge belts may be a result of the structural control of the former belts on the position of the latter, whose orientation is otherwise affected by the more recent stress regime.

The variations in spacing and orientation of sinuous ridges and ridge belts across the region may reflect variations in crustal thickness, rheology and structure, and the magnitude and orientation of stress fields. A common model for crustal and upper mantle rheology on Venus involves a strong upper crust, ductile lower crust, strong upper mantle, and ductile lower mantle (Zuber, 1987; Banerdt and Golombek, 1988). Whereas the characteristic spacing of the sinuous ridges may be attributed to the deformation of the whole thickness of the upper crustal layer, the spacing of the ridge belts may indicate the deformation of the strong upper mantle layer (Zuber, 1987; Zuber and Parmentier 1990).

The sinuous ridges represent the most recent deformation on the plains, but the relative timing between sinuous ridge formation and rifting in this region of Venus remains unclear. It has been proposed that the ridges were formed as a consequence of mantle dynamics, including the upwelling and spreading of buoyant mantle beneath Atla Regio. It is therefore conceivable that rifting and ridge generation occurred simultaneously, as both these processes have been linked to the same system of mantle dynamics. The burial of both ridges (north of Maat) and rift-zones by lava flows within Atla Regio demonstrates that both ridge generation and rifting were underway before the eruption of the large volcanoes in Atla Regio. The comparatively recent stratigraphic position of the sinuous ridges with respect to the plains, together with the gravitational evidence for currently

active mantle dynamics, suggest that sinuous ridge formation may be an ongoing process in the area.

5.3.6 Rift Zones

The eastern half of the region is dominated by rifting, with five rift zones converging on the large volcano Ozza Mons (Senske et al., 1992). The most prominent of these are Ganis Chasma, which extends north from Ozza Mons (Figure 5.5), and Dali Chasma to the south-west of Ozza (Figure 5.6). A portion of Parga Chasma extends from the eastern side of Ozza (C, Figure 5.6), and two un-named rifts extend to the north-east (A and B, Figures 5.5 and 5.6). Ganis Chasma runs for nearly 1600 km between Ozza Mons and Nokomis Montes, and is up to 300 km wide (Figures 5.5 and 5.15). It runs due north for 800 km north of Ozza Mons, before turning north-west around 14.5° N, 197.0° E, and dissecting the large volcano at 17° N, 194° E. The rifting continues through and to the north-west of Nokomis Montes (Figures 5.4 and 5.13).

The north-south section of Ganis Chasma is comprised of a trough bound by elevated flanks which typically rise to 2.6 km above mpr, with local highs of up to 3.9 km. Relative to the adjacent plains these figures translate to 1.6 and 2.9 km respectively. The floor of the trough descends to between 1.4 and 2.8 km below mpr, making the overall rim to floor depth around 5 km. However, there are rapid changes in the GTDR altimetry values from pixel to pixel in the interior of Ganis Chasma. If steep cliffs or troughs are illuminated by the altimeter, several strong echoes may return to the spacecraft at different times, creating an ambiguity in the height determination, and a deviation from the model parameters used in the echo-fitting algorithm (Pettengill et al., 1991; Plaut, 1992). Thus the quoted heights and depths were determined by averaging pixel values in the GTDR image of Ganis Chasma. The interior of the rift in this area contains a highly complex swarm of generally north-south trending faults and graben (Figure 5.15). These structures are confined to the trough, and the rift flanks show little evidence of deformation. The graben are 1 to 10 km wide, and form complex branching and cross-cutting patterns, indicating repeated or progressive deformation. These structures are separated by many elongate regions of less dissected plains, as well as radar-bright regions of highly deformed terrain with a dense structural fabric down to the resolution limit of the SAR images. Many inward facing cliffs mark the sites of normal faults separating down-dropped blocks of crust.

The intensity of faulting increases northwards along the rift towards the large volcano at 17° N, 194° E (Figure 5.5). The summit and much of the flow apron of this volcano have been extensively disrupted by faulting and graben development within the rift zone. Much of the flow apron appears to have been emplaced prior to the majority of the

Figure 5.15 Part of the north-south section of Ganis Chasma. In this area the rift zone is characterised by a highly complex swarm of generally north-south trending faults, graben, and scarps. Individual graben are 1 to 10 km wide, and form a complex branching and cross-cutting pattern. Image is centred on 12.7° N, 198.5° E, and measures 110 x 80 km.

Figure 5.16 A portion of the eastern margin of Dali Chasma centred on 4.4° S, 196.3° E. In this area the predominant structures are north-north-east trending graben up to 1 km wide, which cut an earlier fabric of faint north-east trending lineaments. To the east the graben curve away to the north-east, towards Ozza Mons. Image measures 210 x 155 km.

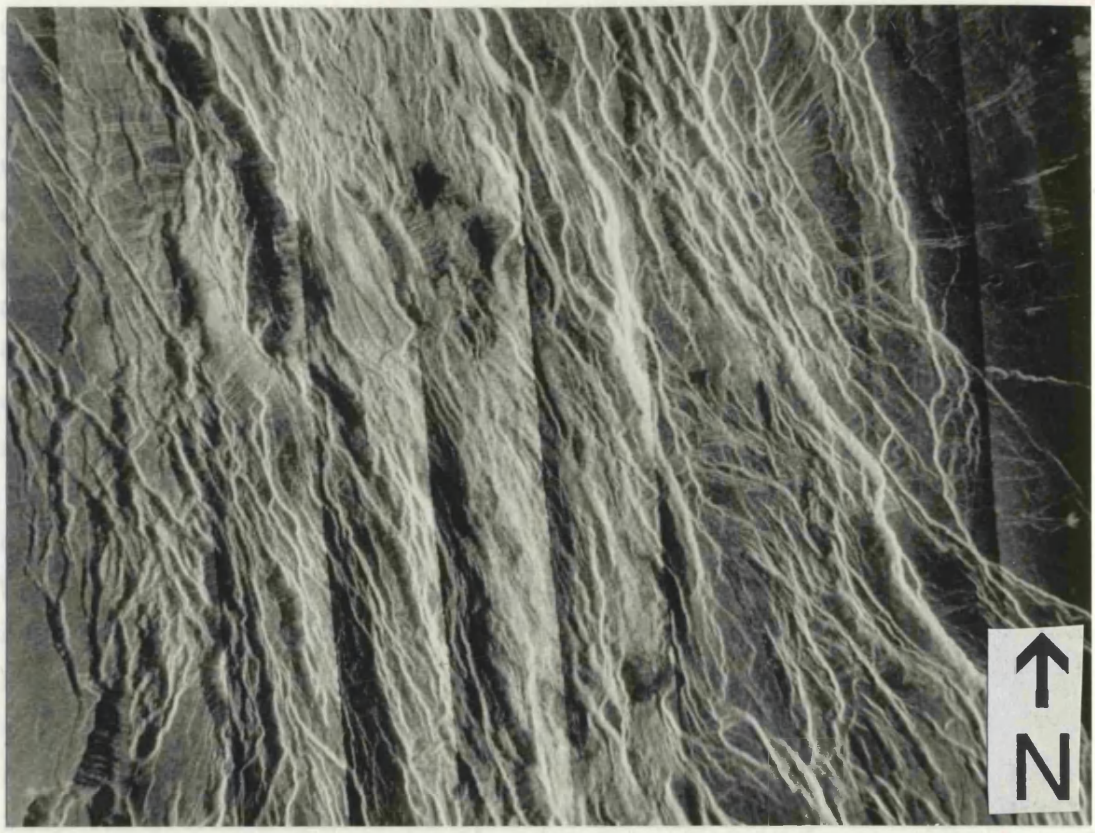
N


N

deformation, but there is some evidence for contemporaneous rifting and volcanism, as some of the graben are flooded by lava from the volcano.

A couple of secondary rifts have developed normal to Ganis Chasma around the area of this large volcano (Figure 5.5). At around 18° N, 195° E a "V" shaped trough opens to the north-east.[6] The floor of this trough lies up to 1.2 km below mpr, and contains a swarm of north-east trending faults and graben. The other rift is composed of a similar arrangement of east-north-east trending faults and graben extending from the margin of Ganis Chasma at 16.5° N, 198.0° E. These secondary rifts are radial to the large volcano at 17° N, 194° E, suggesting that this volcano is the site of a tectonic junction, although not as major as that which is centred upon Ozza Mons.

Beyond the large volcano at 17° N, 194° E, the density of rift-related faulting decreases, and the rift zone turns westwards. Between this volcano and Nokomis Montes, the rift zone consists of east-west and north-west trending fault systems (Figure 5.5). The intensity of deformation increases again through Nokomis Montes, where blocks of tessera have been dissected by the rifting. To the north-north-west of Nokomis Montes, swarms of en-echelon fractures are found, which splay obliquely to the main trend of the rift zone in sympathy with earlier structures in the west-north-west trending fracture belt (Figure 5.13). The en-echelon fractures are typically 1 km wide, but may reach up to 3 km in places, and are between 5 and 40 km in length.

Dali Chasma, to the south-west of Ozza Mons, is broader than Ganis Chasma, and links Atla Regio to the rest of Aphrodite (Figure 5.6). Around 5° S the predominant structures are north-east trending fractures and graben, which are replaced by more northerly trending graben to the east of the rift zone. Around 4.0° S, 196.5° E these northerly trending graben curve around to the north-east, away from the axis of the rift zone, where they become radial to the southern flank of Ozza Mons (Figure 5.16). This pattern may reflect the change in stress regime between Dali Chasma and Ozza Mons. On the western margin of Dali Chasma, around 5.0° S, 192.5° E, the north-east trending graben widen into a chain of collapse pits up to 10 km across. These collapse pits may be purely structural features, or they may indicate magma withdrawal beneath the graben. The latter explanation suggests that the graben may be the product of tensile deformation associated with the subsurface emplacement of dykes. Several authors have proposed that the giant radiating systems of grabens and fractures which surround many tectono-volcanic features on Venus may be formed by dyke emplacement (McKenzie et al.,1992b; Parfitt and Head, 1993a,b; Grosfils and Head, 1994). The graben which become radial to Ozza Mons may also be manifestations of dykes.

The fractures and graben within Dali Chasma exhibit a variable spatial density, with regions of intense deformation separated by comparatively un-deformed regions. These structures cut an older fabric of east-north-east trending lineaments which may represent an earlier phase of rifting. Within C100N197 Dali Chasma lacks a clear flanking rim along its western margin, and exhibits a confused topographic signature within its interior.

[6] in plan view.

However, the eastern margin rises by up to 2.9 km above the adjacent terrain, to a height of 5.1 km above mpr. It is possible that many of the structures on the eastern side of this portion of Dali Chasma are due to gravitational collapse of the elevated crust.

The majority of Parga Chasma and the two un-named rifts lie outside the mapped region, and only those portions closest to Ozza Mons have been mapped in this study (A, B, and C, Figures 5.5 and 5.6). As this is where the rifts converge, there is considerable overlap between them, and a complex fabric of cross-cutting fractures and graben has resulted. Some of these structures may also be due to a combination of radial fracturing and/or dyke emplacement about Ozza Mons, as well as faulting within the rift zones. These structures may also have been the result of repeated episodes of deformation under variable stress conditions, resulting from changes in the pattern of upper mantle flow and/or the position and movement of magma bodies beneath Ozza Mons.

Both Parga Chasma and the more northerly of the two un-named rifts are less well defined than Ganis Chasma, are composed of structures with a wider spacing, exhibit asymmetric topography, and contain chains of coronae and corona-like features (see below). Within C100N197 Parga Chasma is comprised of a complex swarm of predominantly north-west and east-west trending fractures and graben, including north-west trending collapse pit chains (C, Figure 5.6). Parga extends for over 10,000 km between Atla and Themis Regiones, and is predominantly characterised by graben systems containing numerous coronae and corona-like features with abundant volcanic flows and edifices (Stofan et al., 1993). East-west and north-east trending fractures and graben radiate from the east and north-east flank of Ozza Mons, marking the west and south-west portions of the un-named rifts (A and B, Figures 5.5 and 5.6). Cross-cutting relations between these different structures are obscure and do not allow the determination of the relative ages of the different rifts. However, there is no evidence to suggest that the rift zones did not develop simultaneously. The development of rift zones within and around Atla Regio is attributed to modest amounts of lithospheric extension resulting from a major mantle upwelling beneath this region of Venus.

5.4 VOLCANISM

The earliest volcanic activity in the region is recorded by the radar-dark plains themselves, although the source regions and extent of these earlier plains-forming lava flow fields are now obscure. Many other volcanic features have been formed since the plains, including radar-bright and dark lava flow fields associated with chains of coronae and fissures on the plains, large volcanoes, and clusters of small volcanoes. The relative ages of the different features are uncertain, although it appears that the large volcanoes may represent the youngest volcanic features in the area.

5.4.1 Coronae, corona-like centres, and associated lava flow fields

Eigin Corona (5.0° S, 175.0° E), and several other tectono-volcanic centres occur in the south-west corner of C100N180, and are the source of an extensive area of lava flow fields (Figure 5.3). These centres from part of a longer chain of coronae and corona-like features which extends north for 2270 km from Sith Corona (10.5° S, 176.5° E) in Aphrodite Terra into Rusalka Planitia. Eigin is a somewhat oval corona, classed as concentric by Stofan et al. (1992), measuring 180 km north-south by 140 km east-west, with its major axis oriented north-south (Figure 5.17). Eigin is defined by concentrations of ridges in the north-west, north and east, which correspond with the position of an annular moat. This moat is about 400 m deep with respect to the interior floor of the corona, which is mostly at the same level as the surrounding plains. However, the centre of the corona is elevated by up to 400 m above the rest of the floor. The annular ridges in the eastern part of the corona are continuous with a belt of sinuous ridges which otherwise cut the annular ridges in the north-west of the corona and deform its floor (Figure 5.17). These sinuous ridges are generally younger than the annulus and floor of Eigin, but combine with pre-existing annular structures in the east of the corona. The southernmost third of the corona is marked by radar-bright swarms of extensional lineaments, which are also found to the south-west of Eigin (Figure 5.17). These lineaments have an east-west trend, normal to that of the sinuous ridges to the north, and are typically separated by about 2 km. East-west trending extensional lineaments with spacings of just a few hundred metres also occur within the belt of sinuous ridges to the north of Eigin.

North of Eigin the sinuous ridges are separated by up to 4 km, and converge towards a possible tectonic centre at 2.5° S, 174.2° E (Figure 5.3). This centre is poorly defined by concentric structures which are just visible in the SAR image, and surround a knot of radar-bright lineaments. The centre is surrounded by a moat which is typically 900 m in depth. A 35 km wide, 270 km long ridge runs in a north-north-east orientation, obliquely across the sinuous ridges between Eigin Corona and the centre at 2.5° S, 174.2° E. The broad crest of this ridge lies up to 700 m above the adjacent terrain, and appears to have formed prior to the sinuous ridges which cross it. The convergence of the sinuous ridges towards these centres suggests that the coronae acted as strain magnets, localising the compression as manifested by the ridges. The ridges appear to have formed either during the latter most stages of coronae development, or later.

Another corona-like tectono-volcanic centre occurs at 1.7° S, 173.4° E, and is 90 km in diameter (Figure 5.18). The southern and northern boundaries of this feature are defined by north-west trending lineaments of uncertain nature. The eastern and western perimeter are also defined by lineament concentrations, including graben. An annular ridge surrounds the feature, and has a typical height of 600 m, although it rises by up to 1.3 km above the floor of the feature in the south-west. The lineaments may be extensional structures developed upon this ridge as a result of gravitational collapse. The interior is

Figure 5.17 Detail of Eigin Corona (5.0° S, 175.0° E). The corona has controlled the density and orientation of generally north-west trending sinuous ridges, which are best developed around the annulus of the corona. These ridges cross-cut a fabric of east-west trending lineaments with a spacing of one kilometre. The centre of the corona is marked by a radar-bright knot of ridges and other lineaments. A radar-bright swarm of east-north-east fractures is located in the south-west part of the corona. Image is centred on 4.6° S, 174.8° E and measures 110 x 80 km.

Figure 5.18 Details of corona-like tectono-volcanic centres in Rusalka Planitia. Centres at 1.7° S, 173.4° E and 1.4° S, 172.2° E occur in the upper right and upper left portions of the image respectively. Both centres are approximately 90 km across, are somewhat polygonal in shape, and are defined by north-west and north-north-east sets of concentric ridges, and some north-north-east graben. Northeast trending graben also radiate from the southern and northern margin of the centre at 1.4° S, 172.2° E (Figure 5.19). Both centres contain small volcanoes and associated deposits, which are also found in lower left of the image. Image is centred on 2.1° S, 172.5° E, and measures 240 x 185 km.

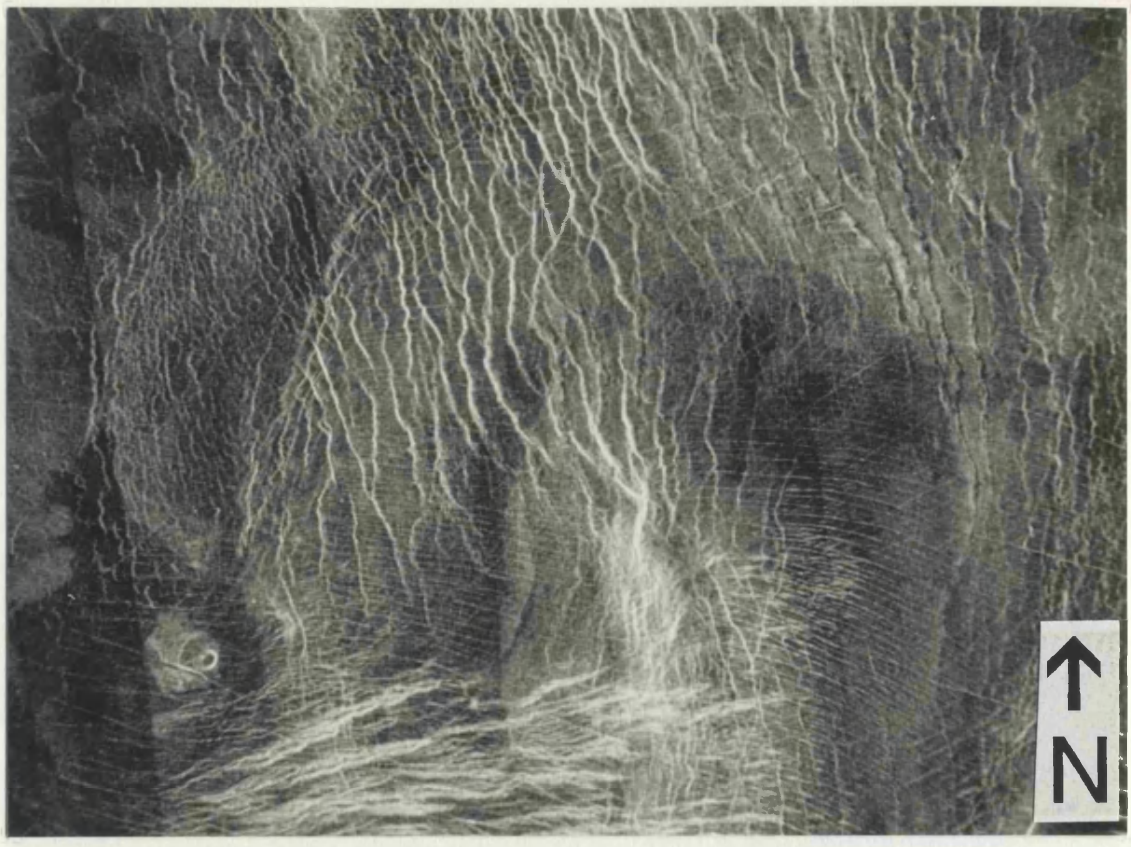
N


N

covered by radar-dark lava and small volcanoes, and lies at an elevation of 100 m below mpr.

A further tectono-volcanic centre is found at 1.4° S, 172.2° E, and is only vaguely defined as an approximately 90 km diameter polygonal feature bounded by orthogonal belts of lineaments of uncertain, but possibly extensional, nature. Lineaments also radiate from the southern margin of the feature (Figure 5.18). These radial lineaments may be fractures formed by the doming of the surface around the feature, or may be the expression of subsurface dykes. The centre contains both radar-bright and dark lava flows, and a 10 km diameter shield volcano. Smaller centres occur at 0.5° S, 172.0° E, and 0.3° S, 172.6° E. The former is merely a knot of radar-bright lineaments, while the latter is a circular caldera-like feature with a radar-dark interior, 80 km in diameter. North-north-east trending graben radiate from the northern margin of these tectono-volcanic centres onto the radar-dark plains to the north, where they are associated with a cluster of small volcanic edifices and pits (Figure 5.19). The association between the graben and the volcanic features, together with the observation that they extend well beyond the positive topography of the corona-like centres, suggests that they are the surface manifestations of dykes, rather than features formed by up-doming along the corona-chain.

The corona-like centres are the source of extensive radar-bright plains-forming lava flow fields, which predate most of the structures associated with the centres, and also predate the regional sinuous ridges (Figures 5.3 and 5.7). These lava flows have flowed up to 900 km to the north, and 270 km west of Eigin Corona and the other centres, and include a transitional flow field at least 200,000 km^2 in extent, which is listed in Chapter 3, Table 3.1. These lava flows are evidence of considerable magmatic activity at the corona-like centres, with which they appear to be contemporaneous.

Extensive lava flow fields are also associated with a number of tectono-volcanic centres in the north-east and east of C115N197 (Figure 5.5). However these flow fields exhibit a more variable backscatter, and are spatially less continuous than those in the south-west region of C100N180. A couple of centres occur at 21.2° N, 199.9° E, and 21.7° N, 201.3° E. The former is composed of a quasi-triangular central ridge-like annulus of lineaments with scarp-like sides some 30 km across. The other centre comprises a central ovoid of concentric lineaments, 20 km across, with several associated, incomplete, and overlapping annulae of lineaments to the south-east. Both these centres are the source of radial lava flow aprons up to 200 km across, and have been mapped as large volcanoes (Figure 5.5). A corona-like centre composed of concentric lineaments, and some 100 km across, occurs at 16.5° N, 202.3° E, but is not surrounded by a flow apron.

In common with the centres in the south-west part of C100N180 these centres in the north-east of C115N197 have controlled the distribution and direction of the post-volcanic sinuous ridges (Figure 5.5). The generally north-west trending sinuous ridges converge on the centre at 21.7° N, 201.3° E, cutting across its flow apron. Around 21.4° N, 204.0° E, a north-west trending set of sinuous ridges diverges into two separate sets,

Figure 5.19 Graben radiating from the northern margin of the corona-like centre at 1.4° S, 172.2° E. Individual graben are up to 1 km wide and are associated with a cluster of small volcanoes visible in the right-central portion of the image. Some of these volcanoes are aligned along the trend of the graben, and in the upper left of the image small radar-bright pits surrounded by radar-grey flow aprons are sited upon the same swarm of graben. Image measures 230 x 170 km and is centred upon 0.2° N, 172.5° E.

Figure 5.20 A small, radar-bright, fissure-fed flow field on the plains of Rusalka Planitia at 13.5° N, 174.2° E. The field appears to have been erupted from a north-west trending radar-dark fissure (arrowed) and flowed to the south-west. The fissure is one of several such lineaments in the area, which are subparallel to north-west trending sinuous ridges. These lineaments might mark the position of thrust faults formed at the same time as the sinuous ridges. Image measures 110 x 80 km.

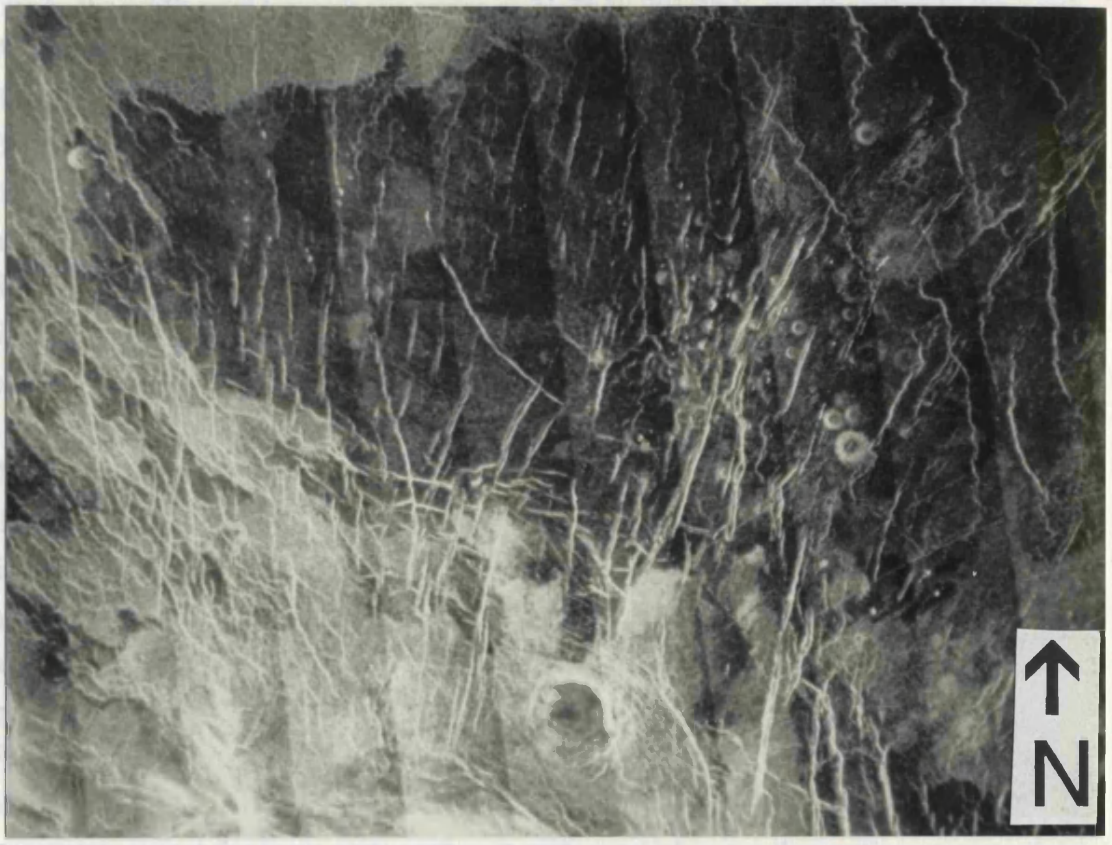
N

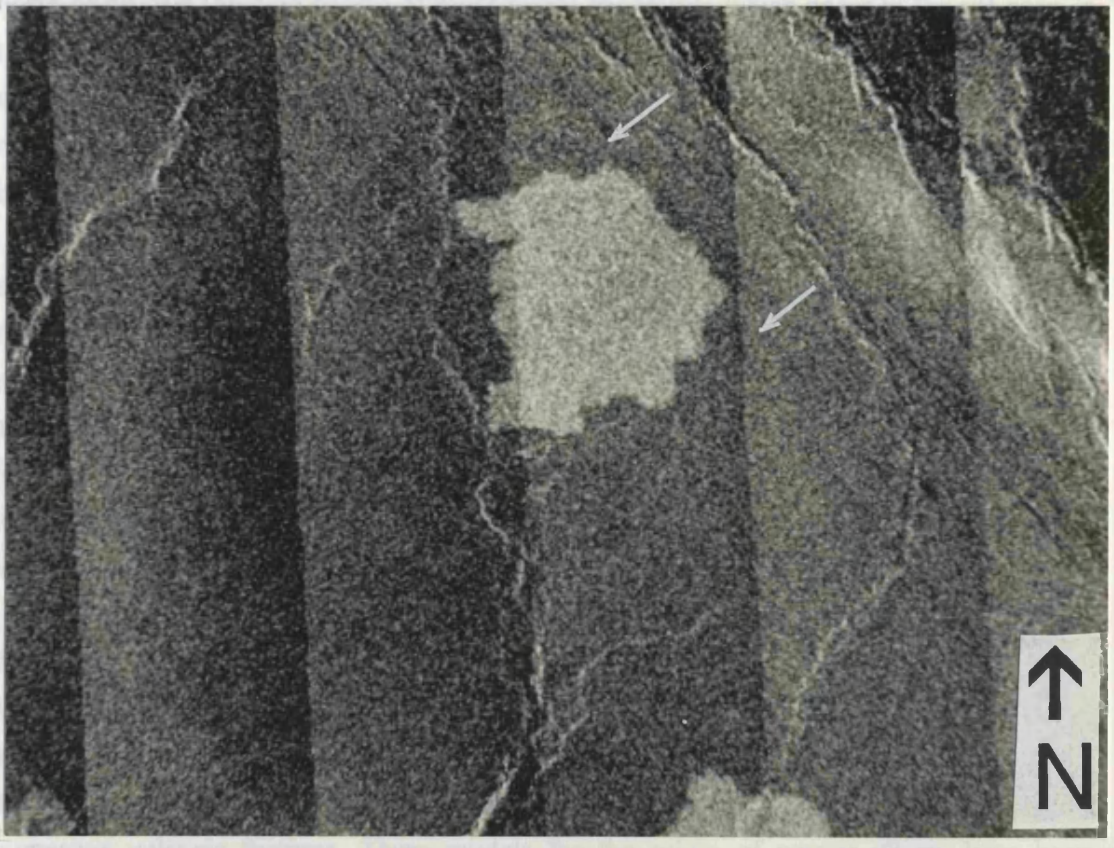
N

one to the north-west towards the centre at 21.7° N, 201.3° E, and the other to the north. A 260 km diameter corona-like feature centred on 18.5° N, 206° E is revealed by the deflection of otherwise north-west trending sinuous ridges about its western perimeter (Figure 5.5). A radar-bright concentration of lineaments on the north-west side of the feature suggest a narrow annulus has partially developed. Magellan altimetry reveals an annular ridge up to 700 m high, and 40 km wide in the south-west and north-east of the feature, the centre of which is elevated up to 800 m above mpr. The centre of this corona-like feature is located 290 km north-west of the axis of the rift zone which extends north-east from Ozza Mons (A, Figure 5.5).

A major corona is located at 14.3° N, 204.7° E, and is the source of an extensive flow apron which measures over 450 km across, and has been mapped as a large volcano (Figure 5.5). The corona itself is formed by a discontinuous annular concentration of lineaments, which surround an interior plateau, some 140 km across, with an elevation of up to 3.1 km above mpr. In the north the annulus is composed of a swarm of east-west trending en-echelon lineaments, while in the east and south, the annulus is partly obscured by the north-east trending lineaments at the western margin of the un-named rift zone (A, Figure 5.5). Several arcuate lineaments with west facing scarps occur on the western side of the corona. The interior plateau contains radar-dark lava flows with relatively few structures, except for some east-north-east graben which enter the south-east part of the interior. Some concentric graben are also found on the north-east side of the corona.

A 110 km diameter corona-like feature is centred on 10.1° N, 205.2° E, within the north-north-east trending swarm of radar-bright lineaments which occur in the rift zone in that area (A, Figure 5.5). Concentric lineaments define a central annulus to the feature, which is cross-cut by many north-north-east trending lineaments. Straight lineaments radiate from the centre in all directions and may mark the position of dykes, and a radar-bright lava flow field has been erupted from the southern flank of the feature.

A corona-like centre is also found within Dali Chasma at 6.0° S, 195.3° E, and measures 180 km diameter (Figure 5.6). This centre is defined by an annulus of intense deformation, enclosing a region of lower backscatter and less intense deformation. Rift-related structures cut across the feature, which has a small cluster of caldera-like features at its centre. The radar-dark interior is suggestive of volcanic flooding, while the caldera-like features imply magma-withdrawal and surface collapse. Cross-cutting relationships indicate that this centre was formed simultaneously with the rift-zone, but prior to the more recent extension of the rift.

Both the chain of coronae and corona-like centres in Rusalka Planitia and those occurring north-east of Ozza Mons are similar to other chains occurring elsewhere on Venus, including Parga and Hecate Chasmata, and a chain of corona-like centres in Kawelu Planitia (Chapter 3, Section 3.2.1.2). These corona-chains are characterised by an abundance of extensional features including graben, faults and fractures, together with numerous volcanic features. Three models for the origin of corona chains have been

proposed and include: (1) a hot-spot model, (2) subduction and/or delamination, and (3) extension and upwelling. The first of these models proposes that the chains of coronae represent hot-spot tracks, similar to the Hawaii-Emperor seamount chain (Stofan et al., 1984; 1992). This model has been rejected on the grounds that Venus lacks evidence for large-scale plate motions (Solomon et al., 1992). In addition there are no systematic and evolutionary changes in corona morphology along the belts, which would indicate an age progression (Stofan et al., 1993). The second model invokes subduction and/or delamination beneath the corona-chains, on the basis of the curvature and the asymmetry of topographic profiles along sections of the chains (Stofan et al., 1984; Sandwell and Schubert, 1992). However this model is inconsistent with the abundance of extensional features and the general lack of compressional ones. The sinuous ridges which occur in association with the corona-chains in the mapped region are related to regional compression, and appear to have formed after the chains were created. Despite the asymmetry in topography of the zone of deformation associated with the corona chain north-east of Ozza Mons (A, Figure 5.5), an association with adjacent rifts and the major zone of upwelling beneath Atla has already been demonstrated. The third model proposes that the chains are major zones of extension, along which diapiric upwellings form coronae and corona-like features (Stofan et al., 1984; 1992). This model is consistent with the abundance of extensional structures and the proposed origin of coronae and similar features as sites of upwelling (Stofan et al., 1992; Squyres et al., 1992a). This model is also consistent with the association of Parga Chasma and the corona-chain "A" (Figure 5.5) with Atla Regio and converging rift zones.

Atla Regio and the chains of coronae may represent different scales of mantle upwelling. Whereas volcanic rises such as Atla may be the site of a deep and long-lived mantle plume generated at the core-mantle boundary, the corona chains may arise from the alignment of upper mantle plumes along great circles to form integrated networks of upwelling and rifting (Ghail and Wilson, 1994). In this case the intersection of deep and upper mantle plumes at Atla has produced copious amounts of volcanism and a major tectonic junction. The corona chain on Rusalka Planitia exhibits less extensional deformation or rifting than Parga, Hecate, and the corona chain north-east of Ozza Mons, and has a more subdued topographic signature. This may indicate that only a very limited amount of extension or rifting took place in this chain. Alternatively the extensional structures have been buried by corona-related volcanism, and/or the topography may have relaxed. The presence of relatively recent sinuous ridges, together with the lack of extensional structures and tectonic signature, suggests that the chain is no longer tectonically active, and has most recently been subject to regional compression. This corona chain is interpreted as having formed from a relatively short-lived and modest amount of upper mantle upwelling after most of the background plains in Rusalka Planitia had been formed. This upwelling may now have been replaced by a well established regime

of mantle downwelling within Rusalka, while the longer lived and deep-seated upwelling beneath Atla continues.

5.4.2 Large Volcanoes

Atla Regio is dominated by the large volcanoes Maat and Ozza Mons (Figure 5.6). A third volcano, Sapas Mons (9.5° N, 187.5° E), lies on the western side of the broad volcanic rise (Figure 5.10). Ozza Mons is surrounded by an extensive flow apron, covering over 900,000 km^2, comprising distal radar-bright flows with a relatively uniform backscatter of -7.7 dB to the north of Ozza, and a proximal region of numerous flank-fed flows with a relatively high backscatter of -0.1 dB (Figure 5.1). South of about 8° N these lava flows both flood and are cut by faults and graben within Ganis Chasma, indicating that deformation and volcanism were contemporaneous (Figures 5.5 and 5.6). North-north-east trending graben of 4 km width and up to 100 km or more in length cut the proximal flow apron around 5.5° N, 200.2° E (Figure 5.6). A 100 km x 50 km radar-dark plateau marks the summit of Ozza Mons, and contains many pits and collapse features (Senske et al., 1992). A field of small volcanic domes lies immediately to the north of the summit, and fills and post-dates the rift-related faulting (Figure 5.6). These domes appear to represent the latest volcanic activity at Ozza, although there may have been more recent flank eruptions.

A quasi-polygonal fault-bounded plateau of relatively un-deformed terrain, with a lower backscatter than the terrain that surrounds it, lies to the south-east of the summit of Ozza Mons (Figures 5.1 and 5.6). This plateau is over 200 km across, and is tilted to the north-east, with elevations ranging from 5.3 km above mpr in the south-west to 4.5 km in the north-east. The western and southern sides exhibit steep scarps which drop by up to 1 km over a distance of about 20 km. Both radial and concentric fractures occur at the base of these scarps, and were probably formed by fracturing due to updoming or gravitational collapse. This plateau is interpreted as a fault bounded, structurally contiguous block of crust that has been tilted and uplifted by magmatic and/or tectonic activity beneath Ozza Mons.

Maat Mons lies 640 km to the south-west of Ozza Mons, and is offset by 320 km from the axis of the Dali Chasma rift (Figure 5.6). Maat is surrounded by a flow apron over 190,000 km^2 in area, composed of digitate flow lobes which extend up to 590 km from the centre of the volcano (Figure 5.9). Much of the distal apron is composed of radar-bright flows with a uniform backscatter (-8.1 dB), but the proximal area contains both radar-bright and -dark flows (Figure 5.1). A region of short flanking flows with a relatively high backscatter lie to the south-east of the summit. Flows from Maat Mons infill the Dali rift, and superpose the most westerly flows of Ozza Mons, indicating that Maat is the younger of these two large volcanoes (Figure 5.6). Klose et al. (1992) found that Maat

Mons is the only high mountain top on Venus that does not exhibit a high reflectivity at its summit. They attribute the high reflectivities on most Venus mountain tops as due to the presence of a weathered mineral assemblage. Thus the absence of high reflectivity materials at the summit of Maat suggests that the high altitude lava flows are negligibly weathered (Klose et al., 1992), which in turn supports a relatively young age for Maat, a conclusion which was also reached by Robinson and Wood (1993).

The flow aprons of both Maat and Ozza Mons lie upon older lava flows which are themselves younger than most of the radar-dark plains in the area (Figures 5.1 and 5.6). These older lava flows are cut by Dali Chasma and the other rift zones, and by faults and graben radiating from Ozza Mons. These lavas may represent the earliest volcanic activity associated with the volcanic centres at Atla Regio. These flows are also deformed by sinuous ridges, indicating that Atla was a major volcanic centre before the development of these structures. Radial fractures (suggestive of dykes) converge upon a possible volcanic centre at 1.5° S, 203.7° E, which is also marked by concentric fractures and may have been the source for some of the older flows to the south of Ozza Mons (Figure 5.6).

The third major shield volcano in the area is Sapas Mons (9.5° N, 187.5° E), which is situated on the north-western flank of Atla Regio, measures 2.4 km from base to summit, and is surrounded by a flow apron covering 175,000 km^2, with flows up to 320 km in length (Chapter 3, Table 3.1; Figure 5.10). Keddie and Head (1992) identified 6 emplacement phases in the flow apron of this volcano, which is notable in having two scalloped margin domes at its summit. Sapas is located nearly 1300 km north-west of the centre of the volcanic rise of Atla Regio, is isolated on the plains, and is not associated with any rift zone (Figure 5.1). Numerous radial lineaments occur on the west, south, south-east and north-east sides of the volcano, which both cut and are covered by the flow apron (Figures 5.3 to 5.6). Like radial lineaments around other volcanic centres on Venus, these may be the surface expression of dykes. A swarm of east-west trending lineaments lies to the south of Sapas Mons, the western portions of which turn north to become radial to the volcano (Figures 5.3 and 5.6). Cross-cutting relationships indicate that radial and east-west lineament swarms developed contemporaneously with the emplacement of the distal flow apron of Sapas Mons. The summit of Sapas contains a discontinuous ring of fractures and graben that is 75 to 100 km in diameter, which Keddie and Head (1994) cite as evidence for collapse over a large magma chamber. Sapas may have been formed by a relatively small and isolated plume that was unrelated to the upwelling in Atla Regio. Nevertheless, the presence of such an isolated large volcano on the plains is unusual, and a possible association with the abundant volcanic activity in Atla Regio cannot be ruled out.

The relative ages of Sapas Mons and the other large volcanoes in Atla Regio is unclear. Like Maat and Ozza Mons, Sapas Mons post-dates an indistinct sheet flow field which lies around 2° N to 10° N, 190 to 195° E, as well as north-west trending sinuous ridges to the north of Maat (Figures 5.5 and 5.6). Similar stratigraphic relations between these three volcanoes and adjacent units, and the weak spatial association of Sapas with

the Atla volcanic rise, suggest that Sapas Mons was formed at about the same time as Maat and Ozza. Both Sapas and Ozza exhibit high reflectivity summit material which is not seen at a similar altitude on Maat. Klose et al. (1992) and Robinson and Wood (1993) interpret the high summit reflectivities of Sapas and Ozza as indicating the presence of a weathered mineral assemblage. Furthermore, they take the lack of high reflectivity material on the summit of Maat to indicate the presence of relatively young, unweathered material. Therefore it would appear that Maat Mons is the youngest of the three volcanoes.

Three impact craters in Atla Regio have been embayed by the flow aprons of Maat and/or Ozza Mons. These craters are Richards (2.5° N, 196.1° E; Figure 5.21), Melba (4.7° N, 193.5° E; Figure 5.9), and an un-named crater at 2.3° N, 198.3° E (Figure 5.6). Note that, at the time of writing, the names of impact craters within the mapped area have only been given provisional approval by the International Astronomical Union. In addition, the crater Bashkirtseff (14.7° N, 194.0° E) has been embayed by the large volcano at 17° N, 194° E, and Zamudio (9.7° N, 189.2° E) has been embayed by Sapas Mons (Figure 5.5). It is the ejecta rather than the crater itself which has been embayed in all these cases except Richards, whose floor is covered by lava flows from Maat and Ozza Mons (Figure 5.21). These embayments are further evidence that the volcanism in the area is comparatively recent.

Other large volcanoes occur at 6.3° S, 172.5° E, 11.0° N, 174.2° E, and 10.0° N, 200.7° E. The volcano at 6.3° S, 172.5° E lies over 300 km to the south-west of Eigin Corona, and is surrounded by a 160 km diameter flow apron (Figure 5.3). This volcano is associated with an east-west trending lineament swarm, and is associated with the chain of corona-like centres and associated flow fields in the south-west corner of C100N180. The volcano at 11.0° N, 174.2° E lies 290 km north-east of the impact crater Rowena (Figure 5.4), and is characterised by a circular apron with a somewhat patchy appearance and lacking any visibly digitate flow lobes. The apron is 180 km across and the centre is marked by a radar-dark spot, approximately 10 km in diameter, which marks the central vent. This volcano is similar to that at 10.0° N, 200.7° E (Figure 5.5), which is also about 180 km in diameter and lacks any visible flow lobes, but by contrast is of lower backscatter, and has a radar-bright central vent. Both of these volcanoes are deformed by north-south trending sinuous ridges. To the south of the volcano at 10.0° N, 200.7° E, these ridges are embayed by the flow apron of Ozza Mons, implying that Ozza Mons is the younger feature.

Large volcanoes primarily occur within Atla Regio and adjacent rifts, and account for essentially all the rift-associated volcanism. The volcanoes of Atla are characterised by very extensive flow aprons and have developed simultaneously with the rifting. Maat Mons appears to be the youngest volcano in the region, and indeed may be the youngest such feature on Venus. Radial fractures and graben surrounding many centres within Atla and adjacent rifts may be evidence for considerable intrusive activity in the form of dykes. The evidence for such massive amounts of effusive and intrusive activity is consistent with the

Figure 5.21 Impact crater Richards (2.5° N, 196.1° E; 29.0 km in diameter) has been partially buried by lava flows from Maat and Ozza Mons. Portions of the hummocky and radar-bright ejecta are still visible to the north-west, south, and east of the crater. The partial burial of this and other craters in Atla Regio suggest that formation of large volcanoes was a relatively recent event in the area. Image measures 210 x 150 km.

Figure 5.22 Image demonstrating the appearance of different lava flow fields and deposits with respect to each other and to the plains in an area of Rusalka Planitia centred upon 4.4° S, 183.5° E. The emplacement of the radar-bright flow field at the left of the image (a) has been controlled by fractures. This field was emplaced upon a more extensive area of radar-grey plains (b), which in places show a relatively sharp boundary to radar-dark plains (arrowed, c). This boundary is interpreted as a flow margin with the radar-grey plains as the younger unit. Elsewhere this boundary cannot be traced with any certainty (d). This illustrates the problem in tracing and mapping flow boundaries across an image. An area of radar-bright flows and a number of small volcanoes occur in the right hand side of the image. Image measures 210 x 150 km.

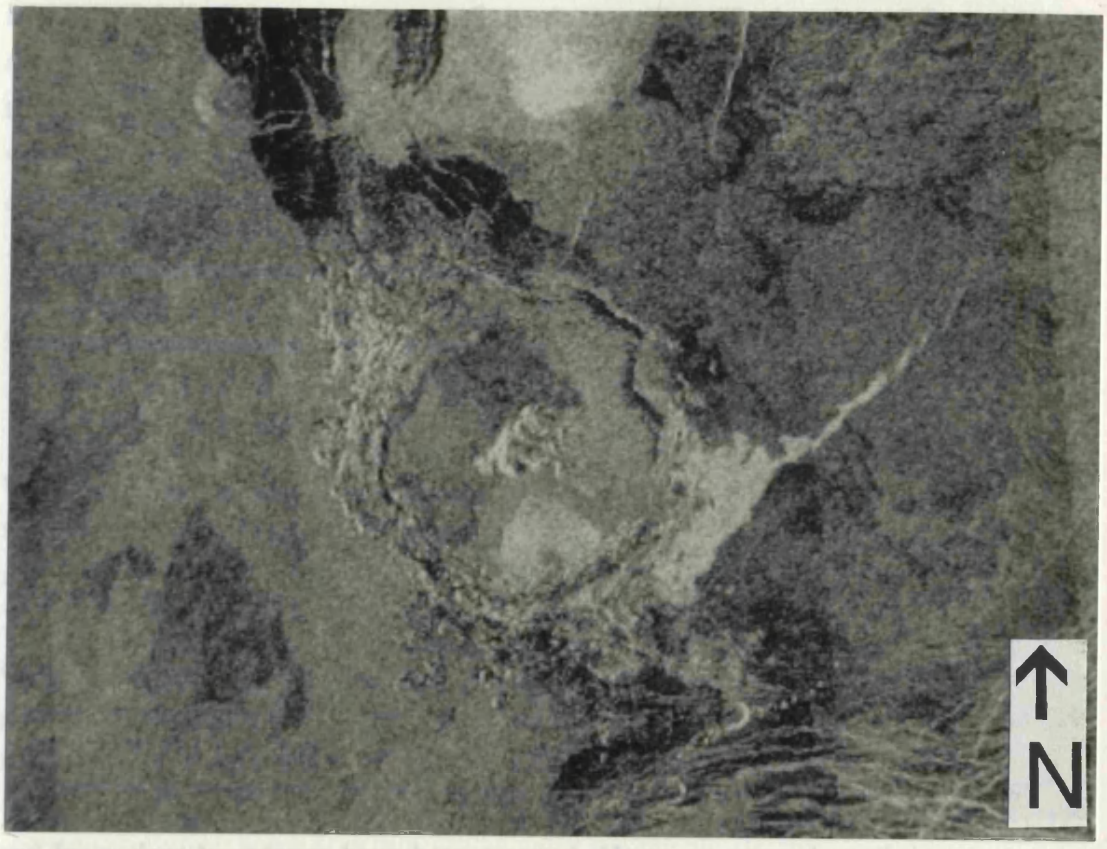
N

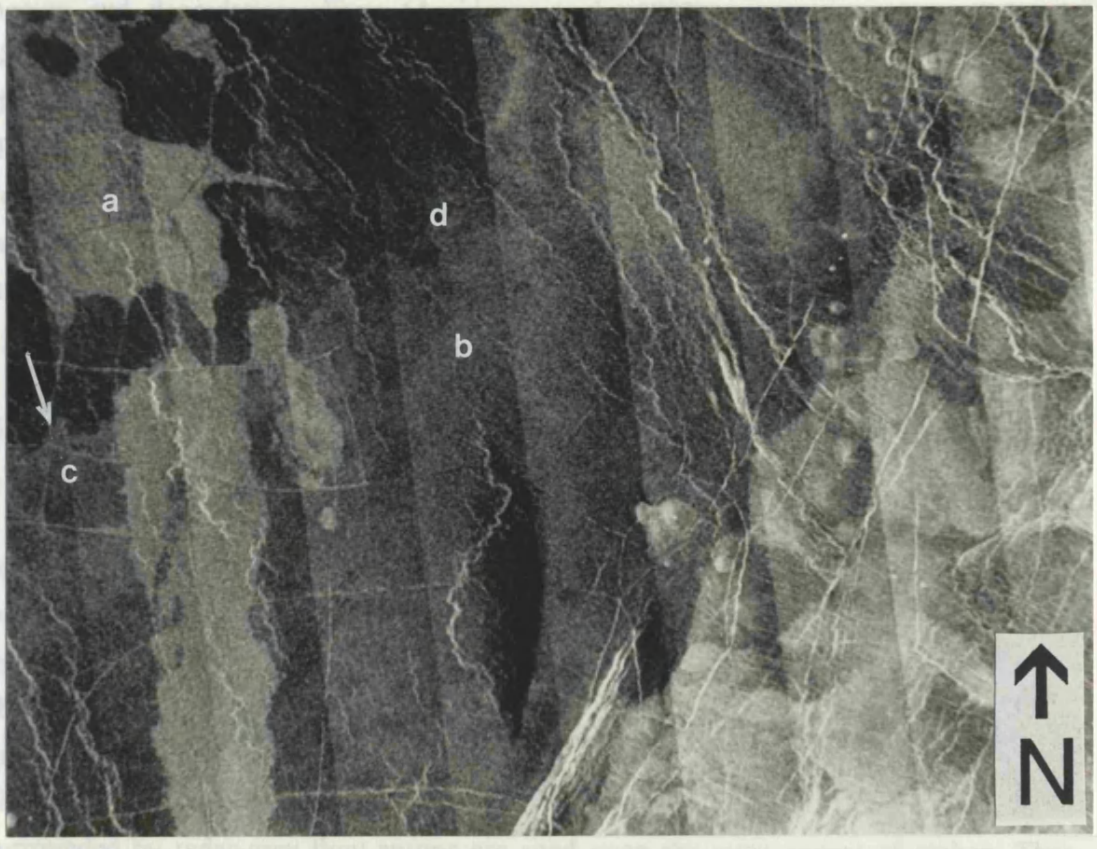
a
d
b
c
N

location of Atla above a major area of mantle upwelling. The location of Sapas Mons is anomalous in the sense that it is not situated within the volcanic rise, but it may indicate the impingement of a small and isolated plume under the plains. The number of smaller volcanoes of 160 to 180 km diameter which are also found in the plains attest to comparatively minor amounts of centralised volcanism since large scale plains formation.

5.4.3 Other Lava Flow Fields

Apart from the lava flow fields already described, there are many other flow fields which are scattered across the plains throughout the region. These lava fields are mostly sheet-like in morphology, with irregular boundaries controlled by local topography, and range in area from a few hundred to several tens of thousands of square kilometres in area. They are interpreted as the products of localised fissure eruptions, and one such example can be seen in the small flow field at 13.5° N, 174.2° E (Figure 5.20). These fields are generally of a higher backscatter than the surrounding plains, although several radar-dark fields are found around 16.0 to 22.0° N, 180 to 184° E (Figure 5.4), and at 19.0° N, 186.0° E (Figure 5.13). Only those flow fields which contrast with the surrounding plains and have clear boundaries have been mapped. However, many less distinct and more ghostly traces of flow fields exist on the plains, and are sometimes gradational to more distinct flow fields (Figure 5.22). These differences in contrast and visibility may be due to ageing and degradation effects (Arvidson et al., 1992), or to textural or dielectric differences between fields of broadly similar age. In general the mapped flow fields post-date the background of radar-dark plains, and most are deformed by the sinuous ridges. These relationships imply that these fields were formed after the major episode(s) of plains resurfacing, but prior to the more recent period of regional compression. These fields might record the very last and waning stages of plains resurfacing, formed during a tail-off in magmatic activity and mantle overturn.

5.4.4 Clusters of small volcanoes

Like the lava-flow fields, clusters of small volcanoes are found throughout the region. The clusters may contain a few tens to several hundred small volcanoes, typically occupying a region up to several hundred kilometres across. Individual volcanoes are generally shield shaped and less than 20 km in diameter. An example at 0.5° N, 173.0° E is shown in Figure 5.19, where a field of small volcanoes has developed in association with graben radial to the volcanic centres further south. Some of these volcanoes are aligned along the trend of these graben, and to the west of this field small radar-bright pits surrounded by radar-grey flow aprons are sited upon the same swarm of graben. Thus

these structures may represent the position of dykes feeding some the small volcanoes, and radiating from magmatic centres within the corona-chain to the south (see Section 5.4.1). Similar relations between linear structures and clusters of small volcanoes are seen elsewhere in the region, such as at 18.8° N, 186.5° E (Figure 5.13). These observations are taken to indicate that the clusters of small volcanoes most commonly develop in association with dyke swarms and/or regions of limited and localised extension. Such regions may relate to local anomalies in the thermal or structural properties of the upper crust, where melt formation may be encouraged. As with many of the mapped flow fields, these clusters of small volcanoes are generally younger than the surrounding plains, and they do not appear to represent a major component of plains formation.

5.5 THE IMPACT CRATERING RECORD

This investigation of the geological history of the region would not be complete without due consideration of the impact cratering record. As with the rest of Venus, the impact cratering record of the region is sparse. Fourteen impact craters have been identified within the boundary of mapping, translating to an average density of 1.1 craters per 10^6 km^2. This is nearly half the planetary average of 2.0 craters per 10^6 km^2. (Schaber et al., 1992), suggesting that this region may be significantly younger than many areas of Venus. This is consistent with the considerable tectonism and volcanic resurfacing in Atla Regio, which may have obliterated the cratering record, and mapping shows to be comparatively recent in age. Apart from supporting a relatively young age for volcanism in Atla Regio, all the craters in the region are younger than the radar-dark plains. This is consistent with the plains having been formed by resurfacing events which obliterated the earlier crater record (Schaber et al., 1992). Several impact craters are also younger than some of the radar-bright sheet flow fields that have been mapped in the region (e.g. Rowena, 10.4° N, 171.4° E, Figure 5.4; Fossey, 2.0° N, 188.8° E, Figure 5.3; and Melba, Figure 5.6). This suggests that these particular flow fields may have formed relatively soon after regional plains emplacement, before the accumulation of the impact population, and are older than the large volcanoes within Atla Regio. The very low density of impact craters does not allow the relative timing and duration of events within the region to be constrained more rigorously.

5.6 TECTONO-VOLCANIC HISTORY AND STRATIGRAPHY

The region records a long and complex history of volcanism and tectonism, but the general sequence of events is interpreted as follows (Figure 5.23). An ancient surface (which may have originally consisted of lava plains) was subject to a long and complex

Figure 5.23 Generalised stratigraphy for eastern Rusalka Planitia and Atla Regio. Younging is towards the top of the diagram. The sequence of plains formation and deformation in eastern Rusalka Planitia is at the left hand side of the diagram, while events in Atla Regio are portrayed to the right (although plains and sinuous ridges occur throughout the region). The vertical lines indicate that the formation of plains, sinuous ridges, ridge belts and rift zones may have occurred over an extended period of time. The relative timing of crater formation with respect to certain features is indicated (for example Blackburne is younger than ridge belts on C115N180, whereas Richards is older than Maat and Ozza Mons).

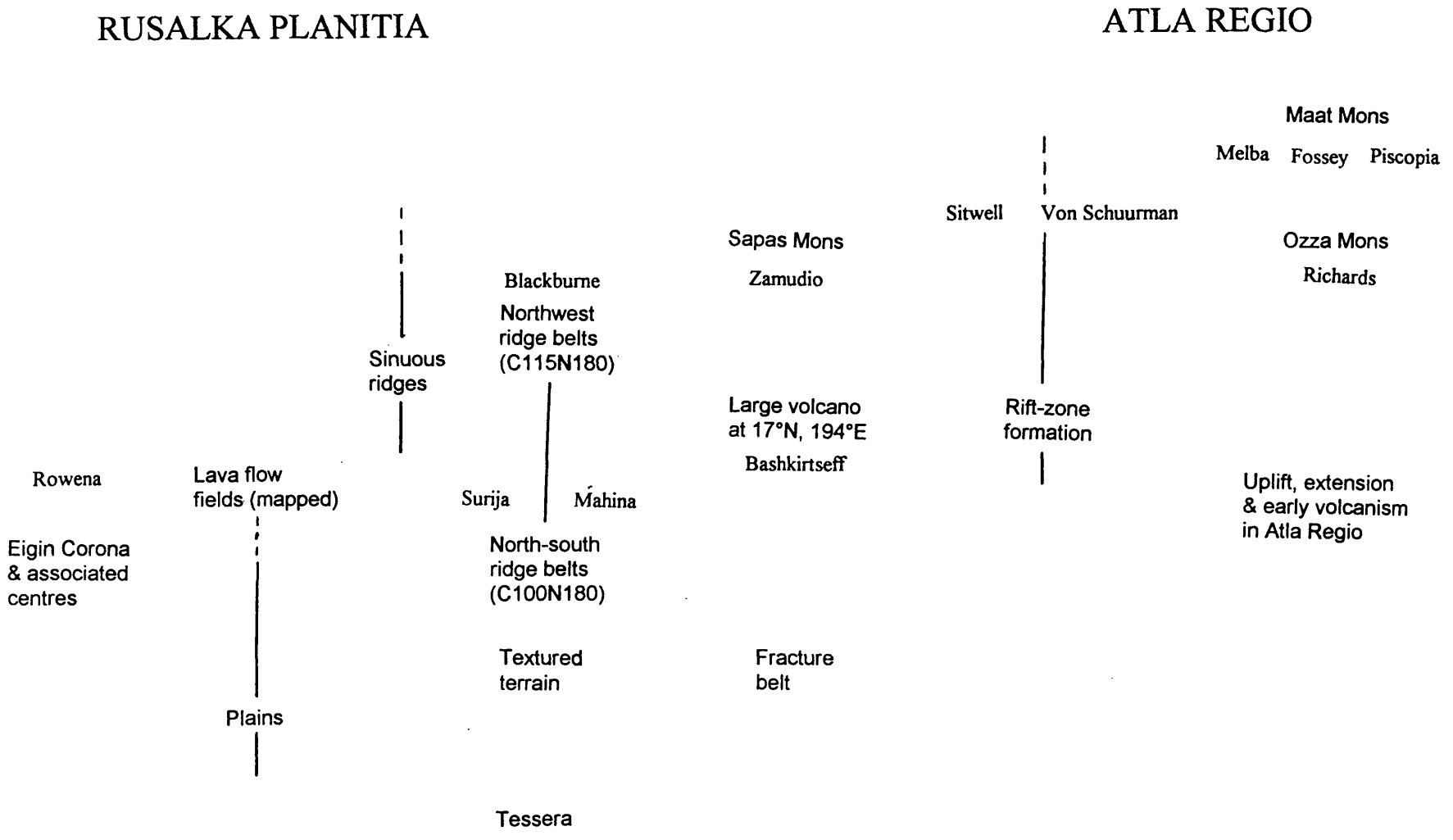
RUSALKA PLANITIA
ATLA REGIO
Maat Mons
Melba
Fossey
Piscopia
Sitwell
Von Schuurman
Sapas Mons
Zamudio
Ozza Mons
Richards
Blackburne
Northwest ridge belts (C115N180)
Sinuous ridges
Large volcano at 17°N, 194°E
Bashkirtseff
Rift-zone formation
Rowena
Lava flow fields (mapped)
Surija
Mahina
Uplift, extension & early volcanism in Atla Regio
Eigin Corona & associated centres
North-south ridge belts (C100N180)
Textured terrain
Fracture belt
Plains
Tessera

history of repeated compressional and extensional deformation. The resulting terrain is now recognised as tessera. The tectonic activity responsible for the deformation of the tessera had ceased before much of this tessera was then buried by widespread volcanic flooding and plains formation, possibly as part of the global resurfacing event or events which Schaber et al. (1992) invoke to explain the global cratering record. This event or events were related to a period of major mantle overturn which may have been in the form of episodic crustal recycling (Parmentier and Hess, 1992), or episodic plate tectonics (Turcotte, 1993). Plains formed by the earlier resurfacing episodes were deformed into areas of textured terrain, which were further deformed by east-west compression producing the north-south trending ridge belts on C100N180. North-south extension generated the fracture belt in the north central part of the region, which deformed tesserae as well as plains. Further volcanic flooding buried sections of the north-south trending ridge belts on C100N180 and areas of the fracture belt. Most of the plains had been emplaced by this time, although relatively minor amounts of volcanic resurfacing produced a number of sheet-like flow fields on Rusalka Planitia.

The period of mantle overturn and regional resurfacing was followed by a relatively short lived and modest amount of upper mantle upwelling beneath Rusalka Planitia. This activity formed a chain of coronae and corona-like features and associated intrusive and extrusive activity, including dyke swarms and extensive lava flow fields. This upwelling was succeeded by the establishment of a major and long-lived system of mantle dynamics, during which the major physiographic characteristics of the region were established. The upwelling and spreading of a large plume form the deep mantle caused major uplift, extension and volcanism in Atla Regio. At the same time an adjacent system of downwelling (and possible return flow) was established, forming the lowland basin of Rusalka Planitia. Early extension was accompanied by the emplacement of extensive lava flow fields in central Atla Regio, as well as the formation of the large volcano at 17° N, 194° E. Continued extension and rifting produced Ganis, Dali, Parga, and two un-named rifts, radiating out from central Atla Regio. The earlier fracture belt, and the large volcano at 17° N, 194° E were all dissected by Ganis Chasma. Several of these rifts developed in association with smaller and more transient upper mantle plumes, which formed coronae and corona-like centres. The rift zones cut early flow fields in Atla Regio, and tessera in Nokomis Montes. Rifting, volcanism, and intrusion occurred simultaneously at Atla.

The downwelling beneath Rusalka, coupled with the adjacent upwelling and spreading of the plume beneath Atla, resulted in a compressive stress regime which formed a regional pattern of generally north-west trending sinuous ridges in Rusalka Planitia and elsewhere. This compression also formed north-west trending ridge belts in C115N180. Volcanism continued within Atla Regio with the formation of Ozza Mons, which infilled the adjacent rifts with lava, covered earlier flow fields, and buried some sinuous ridges. Rifting and extensional activity continued during and after the emplacement of the flow apron of Ozza Mons. Sapas Mons may have been formed at about this time from an

isolated plume, and these two volcanoes were followed by the formation of Maat Mons and the infilling of parts of Dali Chasma with lava. Gravitational data suggest that mantle downwelling and upwelling may be ongoing processes beneath Rusalka Planitia and Atla Regio respectively.

5.7 CONCLUSIONS

The region of eastern Rusalka Planitia and Atla Regio has experienced a long and complex history of volcanic and tectonic activity. Nevertheless, this history can be divided into three main phases, each of which is characterised by different terrains and styles of deformation and volcanism. The first phase is recorded by the tessera as a prolonged history of multiple episodes of compression and extension. The second phase may have involved a major period of mantle overturn and regional resurfacing by plains-forming flood lavas, which buried large areas of tessera. Some tectonic activity occurred between episodes of lava flooding, and deformed resurfaced areas into textured terrain and ridge belts. The final phase was characterised by major and prolonged systems of mantle downwelling and upwelling, which produced the broad scale physiography of the region, and was responsible for major tectonic and volcanic activity. Downwelling created the lowland basin of Rusalka, while a large mantle plume gave rise to uplift, extension, and the eruption of large volcanoes within Atla Regio. Minor upwelling and upper mantle diapirism during the early part of this final phase produced a corona chain and associated volcanic activity in Rusalka Planitia, and rift-associated corona-like centres around Atla Regio. This system of mantle dynamics was also responsible for sinuous ridge and ridge belt formation within Rusalka Planitia and elsewhere.

In addition to these events, a population of impact craters has been formed since the widespread plains formation, and has undergone partial destruction by the later volcanism in Atla Regio. Some of the most recent volcanism on Venus may have occurred in Atla Regio, and mantle upwelling and downwelling, rifting, volcanism, and sinuous ridge formation may be ongoing processes. The overall sequence of events for Rusalka Planitia and Atla Regio is broadly similar to that of other areas of Venus, such as Eistla Regio/Guinevere Planitia (McGill, et al., 1991) and Lavinia Planitia (Squyres et al., 1992), showing that widely separated regions of the planet appear to have undergone the same general sequence of events.

CHAPTER 6

CONCLUSIONS

We shall not cease from exploration
And the end of all our exploring
Will be to arrive where we started
And know the place for the first time

– T. S. Eliot, *Four Quartets*

Magellan has confirmed that the surface of Venus is dominated by volcanic features, and that the planet has been subjected to a long and varied tectonic history. Volcanic activity has produced both the background plains, and a generally younger population of several thousand individual volcanic features. The areal distribution and characteristics of these features suggests that they are the surface manifestation of mantle plumes or hot-spots. The majority of plains and volcanic features are consistent with basaltic compositions. However, more evolved compositions may be represented by steep-sided domes, and some lava channels may have been produced by more fluid lava.

Magellan has revealed a wide variety of tectonic features at scales of a few kilometres to thousands of kilometres. Deformation occurs both as widely distributed strain of modest magnitude exhibited by the regular patterns of sinuous ridges and fractures found on the plains, and as areas of concentrated extension and shortening as manifested by the chasmata, mountain, ridge, and fracture belts. The most intense deformation is exhibited by the tessera, which record a long and complex history of compressional and extensional deformation. No evidence for Earth-style plate tectonics has been found, although some features associated with coronae and arcuate troughs within the Dali-Diana chasmata resemble terrestrial subduction trenches (McKenzie et al., 1992a).

The most readily identifiable volcanic features are the large flood-type lava flow fields, which have typical areas of several hundred thousand square kilometres, lengths of a few hundred to over one thousand kilometres, and widths of several hundred kilometres. A survey of fifty of those fields with areas greater than 50,000 km^2 (great flow fields) has enabled the major characteristics of these fields to be identified. The great flow fields have been classed as sheet-like, transitional or digitate in morphology. The sheet flow fields appear to represent single large flow fields with irregular margins and an absence of distinctive individual flow units, the transitional fields contain several broadly lobate flows, while the digitate flow fields are composed of many discrete flow units. The principle

difference in morphology is attributed to a combination of emplacement style and source characteristics, with the digitate fields erupted as numerous individual cooling-limited flows from mostly centralised sources, and the sheet flows as single massive volume-limited eruptions from laterally extensive fissure systems onto essentially horizontal terrain. The digitate fields have been subdivided further into aprons, fans and subparallel fields. Source elevations lie between 1.0 km below to 8.7 km above the mean planetary radius (mpr), with most between 0 and 2.2 km above the mpr. The average topographic slopes of the fields range up to 0.77°.

An analysis of the average specific radar backscatter of the great flow fields as compared to terrestrial pahoehoe and aa fields on Kilauea Volcano, Hawaii, suggests that most of these fields are characterised by extremely smooth pavement-like flow surfaces. The backscatter of individual sheet flow fields is remarkably uniform over large areas. However, there is much variation in the backscatter of different flow units within individual digitate and transitional fields. Many of the flow units with the highest backscatter may have aa-type textures. The radar properties, planform morphology, and tectonic associations of the great flows, together with the sparse Venera lander data, imply that they are basaltic in composition. In future the use of multi-incidence angle data from different mapping cycles, where available, together with the rms slope, reflectivity and emissivity data should allow a better characterisation of the surface roughness of individual flow units.

Many of the flow units within the digitate fields were apparently channel-fed and cooling-limited. First-order estimates of eruption rate of between 10^5 and 10^6 m^3s^{-1} have been made for flow units of several hundred to a thousand kilometres in length in these fields, by application of the Walker (1973) and Kilburn and Lopes (1991) models of flow emplacement, together with the consideration of likely eruption parameters for laterally extensive fissure eruptions. The flow units have typical estimated volumes of several hundred to over one thousand cubic kilometres. Together with the estimated effusion rates these volumes yield typical eruption durations of weeks to months.

Mylitta Fluctus is a sub-parallel flow field in southern Lavinia Planitia, which has been the subject of detailed investigation. The field covers 300,000 km^2 and measures 1000 km north-south by 450 km east-west. Maximum flow lengths range between 400 and 1000 km, and flow widths between 30 and 100 km in the medial and distal parts of the field. The total volume of the complex is estimated as 2×10^4 km^3. Well developed channels characterise the proximal and medial parts of the field. The geological setting of Mylitta is complex, and the source is located within an east-west trending belt of sub-parallel faults, scarps and troughs, which is interpreted as a rift zone. Volcanism at Mylitta post-dates the rifting, and may be a consequence of decompression melting resulting from extension at the rift. No evidence for fissure-fed eruptions is seen, and the majority of flows appear to have been erupted from a caldera located on the northern flank of the rift zone. Several other tectono-volcanic centres are located along the rift zone, including a

160 km diameter corona-like structure, and smaller centres to the east of Mylitta. Like Mylitta, these centres appear to post-date the rifting, but are only associated with minor amounts of volcanism.

Six constituent flow fields have been identified within Mylitta, and each comprises a separate episode in the emplacement of the complex. The initial episode produced a 400 km diameter shield volcano with a central caldera. This was followed by the emplacement of extensive flow units up to 1000 km long in a progressively easterly sequence forming flow fields 2 to 4. Radar-dark flows from an obscure source on the plains were erupted during the later stages of the second episode to form flow field 3. The development of the complex was completed by the eruption of flow field 5 to the north-west of flow field 4, and the emplacement of relatively short flows to the north and north-west of the caldera during the final episode.

Estimated eruption rates of between 10^4 and 10^6 m^3s^{-1} have been obtained from extrapolation of the plot of length versus effusion rate derived by Walker (1973). Flow field 1 took at least 70 years to be emplaced, with the remaining fields taking the order of weeks or months to be erupted. These figures are preliminary, and do not take into account periods of inactivity between the emplacement of individual flow units. More detailed analyses of individual flow units and application of more complex models of flow emplacement should provide more rigorous constraints on eruption rates and durations.

Most of the set of fifty great flow fields are associated with zones of lithospheric extension and rifting, including volcanic rises, corona-chains, highland marginal fracture belts, and mixed ridge and fracture belts. The majority of this volcanism is centred on coronae, corona-like features and large volcanoes, and typically occurs in the form of flow aprons, with a lesser number of subparallel, transitional, and sheet-like fields. More rarely the great flows are related to both centred and non-centred volcanism on the plains, which are not associated with rift zones. The rift-related settings reflect a spectrum of volcanic and tectonic activity, which may be related to varying amounts of active and passive upwelling. Major deep mantle upwellings may produce the volcanic rises and generate the largest volumes of melt through a combination of both active upwelling and rift-generated decompression melting. Smaller amounts of upper mantle upwelling may produce the corona chains, while passive rifting may produce the highland-marginal fracture belts and mixed ridge and fracture belt associations. Isolated upwellings and localised extension and melting beneath the plains may produce smaller aprons, transitional and sheet flow fields.

The set of fifty great flow fields was chosen for clarity and contrast against the surrounding plains, and consequently represent relatively recent volcanism. In addition, the visible population of great flow fields is mostly related to zones of lithospheric extension and thinning which have developed in the pre-existing plains. These observations are consistent with models which propose that the bulk of the background plains were formed during a period of catastrophic mantle overturn and global resurfacing (Schaber et al., 1992; Parmentier and Hess, 1992; Turcotte, 1993). This plains resurfacing may have been

characterised by sheet-type flow fields, which are now largely invisible due to "homogenisation" to uniform radar properties. The emplacement of plains may also be related to canali-type lava channels (Komatsu et al., 1993), although few examples of associated flow fields have been seen. Indistinct flows with no obvious tectonic associations which are seen on many areas of plains may have been formed during global resurfacing, or may have been formed during ongoing volcanic activity since that time. In terms of planimetric dimensions, predicted eruption rates, inferred compositions and surface textures, together with an association with zones of lithospheric thinning and extension, the great flow fields are considered to be Venusian analogues of terrestrial flood basalt volcanism. Moreover, the role of central volcanism in generating terrestrial flood basalts may merit further attention.

A regional study and mapping of volcanism and tectonism in eastern Rusalka Planitia and northern Atla Regio has revealed the relationships between volcanic and tectonic processes, provided further insight into the origin of plains, and allowed the regional stratigraphy to be determined. The region has experienced a long and complex history of volcanic and tectonic activity. This activity has produced a wide range of features including tessera, textured terrain, a fracture belt, ridge belts, sinuous ridges, rift zones, coronae, corona-like centres, large volcanoes, lava flow fields, and clusters of small volcanoes. Despite this complexity, three main phases in the geological history of the region are recognised, each with a characteristic style of volcanic and tectonic activity. The initial phase was characterised by a prolonged history of extensional and compressional deformation which formed the tessera. Large areas of this tessera were then buried by widespread plains-forming volcanism during the second phase of activity. This volcanism may have been part of a catastrophic global resurfacing related to major mantle overturn (Schaber et al., 1992; Parmentier and Hess, 1992; Turcotte, 1993). The relationship between plains, textured terrain and ridge belts in the region implies that resurfacing was interrupted by one or more periods of plains deformation. The broad-scale physiography and current state of the region was established during the final phase of activity, which was probably characterised by major and prolonged systems of mantle upwelling and downwelling. Downwelling created the lowland basin of Rusalka, while a large mantle plume gave rise to uplift, extension, and the eruption of large volcanoes within Atla Regio. These systems of mantle dynamics appear to be currently active, as evidenced by Magellan gravity data (Bindschadler, 1994). Minor upwelling and upper mantle diapirism during the early part of this final phase produced a corona chain and associated volcanic activity in Rusalka Planitia, and rift-associated corona-like centres around Atla Regio. This system of mantle dynamics may have also been responsible for the formation of sinuous ridges and some late-stage ridge belts in Rusalka Planitia and elsewhere in the region. Analysis of high resolution Magellan gravity data over this region and elsewhere should provide finer constraints on the relationships between interior dynamics and surface features.

A population of impact craters has accumulated across the region since widespread plains formation, and has undergone partial destruction by the later volcanism in Atla Regio. The average density of impact craters within the region is 1.1 craters per 10^6 km^2. This is nearly half the global average of 2.0 craters per 10^6 km^2 (Schaber et al., 1992), suggesting that this region may be significantly younger than many areas of Venus. Indeed, some of the most recent volcanism on Venus may have occurred in Atla Regio, and mantle upwelling, downwelling, rifting, volcanism and sinuous ridge formation may be ongoing processes in the area. The overall sequence of events for Rusalka Planitia and Atla Regio is broadly similar to that of other areas of Venus, such as Eistla Regio/Guinevere Planitia (McGill, et al., 1991) and Lavinia Planitia (Squyres et al.,1992b), showing that widely separated regions of the planet appear to have undergone the same general sequence of events. The similarity in stratigraphic sequences means that either the events were globally synchronous, or that the sequence represents a typical series of events which occurred at different times in different places.

The present global volcanic flux and rate of crustal formation remain unclear. The most recent volcanic activity appears to be related to hot-spot style mantle upwelling, with the plains having formed during earlier episodes of global resurfacing when the global volcanic flux was at its peak. The presence of many indistinct flows on the plains suggests that plains resurfacing continued on a more regional and local scale, with the more recent volcanic activity being represented by the most distinctive great flow fields. Further detailed regional mapping of the plains with particular emphasis on the indistinct flow features is required, in order to adequately address questions of global resurfacing and plains formation.

REFERENCES

Anderson, D. L., Tectonics and composition of Venus, *Geophys. Res. Lett.*, **7**, 101-102, 1980.

Anderson, D. L., Plate tectonics on Venus, *Geophys. Res. Lett.*, **8**, 309-311, 1981.

Arvidson, R. E., R. Greeley, M. C. Malin, R. S. Saunders, N. Izenberg, J. J. Plaut, E. R. Stofan, and M. K. Shepard, Surface Modification of Venus as Inferred From Magellan Observations of Plains, *J. Geophys. Res.*, **97**, 13,303-13,317, 1992.

Arvidson, R. E., J. J. Plaut, R. F. Jurgens, R. S. Saunders, and M. A. Slade, Geology of Southern Guinevere Planitia (abstract), *Lunar Planet. Sci. XX*, 25-26, 1989.

Aubele, J. C., and E. N. Slyuta, Small domes on Venus: Characteristics and origin, *Earth Moon Planets*, **50/51**, 493-532, 1990.

Baker, V. R., G. Komatsu, T. J. Parker, V. C. Gulick, J. S. Kargel, and J. S. Lewis, Channels and Valleys on Venus: Preliminary Analysis of Magellan Data, *J. Geophys. Res.*, **97**, 13,421-13,444, 1992.

Banerdt, W. B., and M. P. Golombek, Deformational models of rifting and folding on Venus, *J. Geophys. Res.*, **93**, 4759-4772, 1988.

Barsukov, V. L., Basilevsky, A. T., Kuzmin, R. O., Pronin, A. A., Kryuchkov, V. P., Nikolayeva, O. V., Chernaya, I. M., Burba, G. A., Bobina, N. N., Shaskina, V. P., Markov, M. S., and A. L. Sukhanov, Geology of Venus from the results of analysis of radar images taken by Venera 15 and 16 probes: Preliminary data, *Geokhimiya*, **12**, 1811-1820, 1984. (*Geochem. Inst.* Engl. Transl., **22**, 135-143, 1985.)

Barsukov, V. L., A. T. Basilevsky, G. A. Burba, N. N. Bobinna, V. P. Kryuchkov, R. O. Kuzmin, O. V. Nikolaeva, A. A. Pronin, L. B. Ronca, I. M. Chernaya, V. P. Shaskina, A. V. Garanin, E. R. Kushky, M. S. Markov, A. L. Sukhanov, V. A. Kotelnikov, O. N. Rzhiga, G. M. Petrov, Yu. N. Alexandrov, A. I. Sidorenko, A. F. Bogomolov, G. I. Skrypnik, M. Yu. Bergman, L. V. Kudrin, I. M. Bohshtein, M. A. Kronrod, P. A. Chochia, Yu. S. Tyuflin, S. A. Kadnichansky, and E. L. Akim, The Geology and Geomorphology of the Venus Surface as Revealed by the Radar Images Obtained by Veneras 15 and 16, *Proc. Lunar. Planet. Sci. Conf. 16th*, Part 2, *J. Geophys. Res.*, **91**, suppl., D378-D398, 1986a.

Barsukov, V. L., Yu. A. Surkov, L. V. Dmitriev, and I. L. Khodakovsky, Geochemical studies of Venus by Vega 1 and Vega 2 landers (in Russian), *Geokhimiya,* **3**, 275-288, 1986b.

Basaltic Volcanism Study Project (BVSP), *Basaltic Volcanism on the Terrestrial Planets,* 1286 pp., Pergamon, New York, 1981.

Basilevsky, A. T., Structure of central and eastern areas of Ishtar Terra and some problems of Venusian tectonics, *Geotectonics,* **20**, 282-288, 1986.

Basilevsky, A. T., and J. W. Head, The Geology of Venus, *Annu. Rev. Earth Planet. Sci.,* **16**, 295-317, 1988.

Basilevsky, A. T., R. O. Kuzmin, O. V. Nikolaeva, A. A. Pronin, L. B. Ronca, V. S. Avduevsky, G. R. Uspensky, Z. P. Cheremukhina, and V. V. Semenchenko, The surface of Venus as revealed by the Venera landings, *Geol. Soc. Am. Bull.*, **96**, 137-144, 1985.

Basilevsky, A. T., O. V. Nikolaeva, and C. M. Weitz, Geology of the Venera 8 Landing Site Region From Magellan Data: Morphological and Geochemical Considerations, *J. Geophys. Res.*, **97**, 16,315-16,335, 1992.

Basilevsky, A. T., A. A. Pronin, L. B. Ronca, V. P. Kryuchkov, A. L. Sukhanov, and M. S. Markov, Styles of tectonic deformations on Venus: Analysis of Venera 15 and 16 data, *Proc. Lunar. Planet. Sci. Conf. 16th*, Part 2, *J. Geophys. Res.*, **91**, suppl., D399-D411, 1986.

Beatty, J. K., B. O'Leary, and A. Chaikin, eds., *The New Solar System*, 240 pp., Cambridge University Press and Sky Publishing Corporation, New York, 1981.

Beurlen, K., *Geologie von Brasilien*, 427pp., Borntraeger, Berlin, 1970.

Bills, B. G., W. S. Kiefer, and R. L. Jones, Venus gravity: A harmonic analysis, *J. Geophys. Res.*, **92**, 10,335-10,351, 1987.

Bindschadler, D. L., Magellan LOS Gravity of Venus Plains Regions: Lithospheric Properties, and Implications for Global Tectonics, *Lunar Planet. Sci.* XXV, 113-114, 1994.

Bindschadler, D. L., and J. W. Head, Diffuse scattering on the surface of Venus: Origin and implications for the distribution of soils, *Earth Moon Planets,* **42**, 133-149, 1988.

Bindschadler, D. L., and J. W. Head, Characterization of Venera 15/16 geologic units from Pioneer Venus reflectivity and roughness data, *Icarus*, 77, 3-20, 1989.

Bindschadler, D. L., and J. W. Head, Tessera terrain, Venus: Characterization and models for origin and evolution, *J. Geophys. Res.*, **96**, 5889-5907, 1991.

Bindschadler, D. L., and E. M. Parmentier, Mantle flow tectonics: The influence of a ductile lower crust and implications for the formation of topographic uplands on Venus, *J. Geophys. Res.*, **95**, 21,329-21,344, 1990.

Bindschadler, D. L., M. A. Kreslavsky, M. A. Ivanov, J. W. Head, A. T. Basilevsky, and Yu. G. Shkuratov, Distribution of tessera terrain on Venus: Prediction for Magellan, *Geophys. Res. Lett.*, **17**, 171-174, 1990a.

Bindschadler, D. L., G. Schubert, W. M. Kaula, Mantle flow tectonics and the origin of Ishtar Terra, Venus, *Geophys. Res. Lett.*, **17**, 1345-1348, 1990b.

Bindschadler, D. L., A. deCharon, K. K. Beratan, S. E. Smrekar, and J. W. Head, Magellan Observations of Alpha Regio: Implications for Formation of Complex Ridged Terrains on Venus, *J. Geophys. Res.*, **97**, 13,563-13,577, 1992a.

Bindschadler, D. L., G. Schubert, W. M. Kaula, Coldspots and Hotspots: Global Tectonics and Mantle Dynamics of Venus, *J. Geophys. Res.*, **97**, 13,495-13,532, 1992b.

Bullock, M. A., D. H. Grinspoon, and J. W. Head, Venus resurfacing rates: constraints provided by 3-D Monte Carlo simulations, *Geophys. Res. Lett.*, **20**, 2147-2150, 1993.

Campbell, B. A., Comparison of Magellan measurements of surface roughness on Venus to topographic profiles of terrestrial basaltic lava flows (abstract), *Lunar Planet. Sci. XXIII*, 201-202, 1992.

Campbell, B. A., and D. B. Campbell, Western Eistla Regio, Venus: Radar properties of volcanic deposits, *Geophys. Res. Lett.*, **17**, 1353-1356, 1990.

Campbell, B. A., and D. B. Campbell, Comparison of 1988 Arecibo radar images of Western Eistla Regio, Venus, and multipolarization airborne radar images of terrestrial terrains (abstract), *Lunar Planet. Sci. XX*, 175-176, 1991.

Campbell, B. A., and D. B. Campbell, Analysis of volcanic surface morphology on Venus from comparison of Arecibo, Magellan, and terrestrial airborne radar data, *J. Geophys. Res.*, **97**, 16,293-16,314, 1992.

Campbell, B. A., and P. G. Rogers, Geology and surface characteristics of Bell Regio, Venus, *Lunar Planet. Sci. XXIV*, 247-248, 1993.

Campbell, D. B., and B. A. Burns, Earth-Based Radar Imagery of Venus, *J. Geophys. Res.*, **85**, 8271-8281, 1980.

Campbell, D. B., J. W. Head, J. K. Harmon, and A. A. Hine, Venus: Identification of banded terrain in the mountains of Ishtar Terra, *Science*, **221**, 644-647, 1983.

Campbell, D. B., J. W. Head, J. K. Harmon, and A. A. Hine, Venus: Volcanism and rift formation in Beta Regio, *Science*, **226**, 167-170, 1984.

Campbell, D. B., J. W. Head, A. A. Hine, J. K. Harmon, D. A. Senske, P. C. Fisher, Styles of Volcanism on Venus: New Arecibo High Resolution Radar Data, *Science*, **246**, 373-377, 1989.

Campbell, D. B., J. W. Head, N. J. S. Stacy, and A. A. Hine, Venus: Crater distributions at low northern latitudes and in the southern hemisphere from new Arecibo observations, *Geophys. Res. Lett.*, **17**, 1389-1392, 1990.

Campbell, D. B., D. A. Senske, J. W. Head, A. A. Hine, and P. C. Fisher, Venus southern hemisphere: Character and age of terrains in the Themis-Alpha-Lada region, *Science*, **251**, 180-183, 1991.

Campbell, I. H., and R. W. Griffiths, Implications of mantle plume structure for the evolution of flood basalts, *Earth Planet. Sci. Lett.*, **99**, 79-93, 1990.

Campbell, I. H., R. W. Griffiths, and R. I. Hill, Melting in an Archean mantle plume: Heads it's basalts, tails it's komatiites, *Nature*, **339**, 697-699, 1989.

Chester, D. K., A. M. Duncan, J. E. Guest, and C. R. J. Kilburn, *Mount Etna, The Anatomy of a Volcano*, 404 pp., Stanford University Press, Stanford, Calif., 1985.

Cox, K. G., The Karroo volcanic cycle, *J. Geol. Soc. London*, **128**, 311-336, 1972.

Crumpler, L. S., J. C. Aubele, and J. W. Head, The Magellan volcanic and magmatic feature catalog (abstract), *Lunar Planet. Sci. XXIV*, 361-362, 1993.

Crumpler, L. S., and J. W. Head, Bilateral topographic symmetry patterns across Aphrodite Terra, Venus, *J. Geophys. Res.*, **93**, 301-312, 1988.

Crumpler, L. S., J. W. Head, and D. B. Campbell, Orogenic belts on Venus, *Geology*, **14**, 1031-1034, 1986.

Crumpler, L. S., J. W. Head, and J. K. Harmon, Regional linear cross-strike discontinuities in western Aphrodite Terra, Venus, *Geophys. Res. Lett.*, **14**, 607-610, 1987.

Dewey, J. F., and K. Burke, Hot spots and continental break-up: Implications for collisional orogeny, *Geology*, **2**, 57-60, 1974.

Florensky, C. P., A. T. Basilevsky, V. P. Kryuchkov, R. O. Kusmin, O. V. Nikolaeva, A. Pronin, I. M. Chernaya, Yu. S. Tyuflin, A. S. Selivanov, M. K. Naraeva, and L. B. Ronca, Venera 13 and Venera 14: Sedimentary rocks on Venus?, Science, **221**, 57-59, 1983.

Florensky, C. P., L. B. Ronca, A. T. Basilevsky, G. A. Burba, O. V. Nikolaeva, A. A. Pronin, A. M. Trakhtman, V. P. Volkov, and V. V. Zasetsky, The surface of Venus as revealed by Soviet Venera 9 and 10, *Geol. Soc. Am. Bull.*, **88**, 1537-1545, 1977.

Ford, P. G., *Guide to GIPS*, Massachusetts Institute of Technology, 1992.

Ford, P. G., R. G. Blom, J. A. Crisp, C. Elachi, T. G. Farr, R. S. Saunders, E. E. Theilig, S. D. Wall, and S. B. Yewell, *Spaceborne Radar Observations*, JPL Publication 89-41, 1989.

Ford, P. G., and G. H. Pettengill, Venus Topography and Kilometer-Scale Slopes, *J. Geophys. Res.*, **97**, 13,103-13,114, 1992.

Ford, P. G., J. J. Plaut, C. M. Weitz, T. G. Farr, D. A. Senske, E. R. Stofan, G. Michaels, and T. J. Parker, *Guide to Magellan Image Interpretation*, JPL Publication 93-24, 1993.

Frank, S. L., and Head, J. W., Ridge belts on Venus: Morphology and origin, *Earth Moon Planets*, **50/51**, 421-470, 1990.

Gaddis, L., P. Mouginis-Mark, R. Singer, and V. Kaupp, Geologic analyses of shuttle imaging radar (SIR-B) data of Kilauea Volcano, Hawaii, *Geol. Soc. Am. Bull.*, **101**, 317-332, 1989.

Garvin, J. B., J. W. Head, M. T. Zuber, and P. Helfenstein, Venus: The nature of the surface from Venera panoramas, *J. Geophys. Res.*, **89**, 3381-3399, 1984.

Ghail, R. C. and L. Wilson, Plate Tectonics, Venusian Style, *Lunar. Planet. Sci. XXV*, 421-422, 1994.

Ghose, N. C., Chemical characteristics of some basaltic rocks of India, *Bull. Volcanol.*, **35**, 1022-1036, 1972.

Goldstein, R. M., R. R. Green, and H. C. Rumsey, Venus Radar Images, *J. Geophys. Res.*, **81**, 4807-4817, 1976.

Goldstein, R. M., R. R. Green, and H. C. Rumsey, Venus Radar Brightness and Altitude Images, *Icarus*, **36**, 334-352, 1978.

Greeley, R., and R. E. Arvidson, Aeolian processes on Venus, *Earth Moon Planets*, **50/51**, 127-157, 1990.

Greeley, R. and J. S. King (Eds.), *Volcanism of the Eastern Snake River Plain, Idaho*, NASA Contract Report CR-154621, 308pp., NASA, Washington, D. C., 1977.

Green, J. C., North Shore Volcanic Group, in *Geology of Minnesota: A Centennial Volume*, edited by P K. Sims and G. B. Morey, pp.2940-3320, Minnesota Geological Survey, St. Paul, 1972.

Grimm, R. E., and R. J. Phillips, Tectonics of Lakshmi Planum, Venus: Tests for Magellan, *Geophys. Res. Lett.*, **17**, 1349-1352, 1990.

Grosfils, E. B., and J. W. Head, Determining stress states using dike swarms: the Lauma Dorsa example, *Papers Presented to the International Colloquium on Venus, Pasadena, California*, 62-64, 1992.

Grosfils, E. B., and J. W. Head, Modes of origin for giant radiating lineament systems on Venus, *Lunar Planet. Sci. XXV*, 1994.

Guest, J. E., M. H. Bulmer, J. C. Aubele, K. Beratan, R. Greeley, J. W. Head, G. Michaels, C. Weitz, and C. R Wiles, Small Volcanic Edifices and Volcanism on the Plains of Venus, *J. Geophys. Res.*, **97**, 15,949-15,966, 1992.

Guest, J. E., C. R. J. Kilburn, H. Pinkerton, and A. M. Duncan, The evolution of lava flow fields: Observations of the 1981 and 1983 eruptions of Mount Etna, Sicily, *Bull. Volcanol.*, **49**, 527-540, 1987.

Hagfors, T., Remote probing of the Moon by infrared and microwave emissions and by radar, *Radio Sci.*, **2**, 445-465, 1970.

Head, J. W., Formation of mountain belts on Venus: Evidence for large-scale convergence, underthrusting, and crustal imbrication in Freyja Montes, Ishtar Terra, *Geology*, **18**, 99-102, 1990a.

Head, J. W., Venus trough-and-ridge tessera: Analog to Earth oceanic crust formed at spreading centers?, *J. Geophys. Res.*, **95**, 7119-7132, 1990b.

Head, J. W., D. B. Campbell, C. Elachi, J. E. Guest, D. P. McKenzie, R. S. Saunders, G. G. Schaber, and G. Schubert, Venus Volcanism: Initial Analysis from Magellan Data, *Science*, **252**, 276-287, 1991.

Head, J. W., and L. S. Crumpler, Evidence for divergent plate boundary characteristics and crustal spreading on Venus, *Science*, **238**, 1380-1385, 1987.

Head, J. W., and L. S. Crumpler, Venus geology and tectonics: Hotspot and crustal spreading models and questions for the Magellan mission, *Nature*, **346**, 525-533, 1990.

Head, J. W., L. S. Crumpler, J. C. Aubele, J. E. Guest, and R. S. Saunders, Venus Volcanism: Classification of Volcanic Features and Structures, Associations, and Global Distribution from Magellan Data, *J. Geophys. Res.*, **97**, 13,153-13,197, 1992.

Head, J. W., R. W. Vorder Bruegge, and L. S. Crumpler, Venus orogenic belt environments: Architecture and origin, *Geophys. Res. Lett.*, **17**, 1337-1340, 1990.

Head, J. W. and L. Wilson, Volcanic processes and landforms on Venus: Theory, predictions and observations, *J. Geophys. Res.*, **91**, 9407-9446, 1986.

Herrick, R. R., and R. J. Phillips, Blob tectonics: A prediction for western Aphrodite Terra, Venus, Geophys. Res. Lett., **17**, 2192-2132, 1990.

Hill, R. I., Starting plumes and continental break-up, *Earth Planet. Sci. Lett.*, **104**, 398-416, 1991.

Hooper, P. R., The timing of crustal extension and the eruption of continental flood basalts, *Nature*, **345**, 246-249, 1990.

Hulme, G., The interpretation of lava flow morphology, *Geophys. J. R. Astron. Soc.*, **39**, 361-383, 1974.

Hultgrien, L. K., and L. R. Gaddis, Characterization of lava-flow surface textures in different eruptive environments on Venus (abstract), *Lunar. Planet. Sci. XXV*, 577-578, 1994.

Ivanov, B. A., A. T. Basilevsky, V. P. Kryuchkov, and I. M. Chernaya, Impact craters of Venus: Analysis of Venera 15 and 16 data, *Proc. Lunar. Planet. Sci. Conf. 16th*, Part 2, *J. Geophys. Res.*, **91**, suppl., D413-D430, 1986.

Janes, D. M., S. W. Squyres, D. L. Bindschadler, G. Baer, G. Schubert, V. L. Sharpton, and E. R. Stofan, Geophysical Models for the Formation and Evolution of Coronae on Venus, *J. Geophys. Res.*, **97**, 16,055-16,067, 1992.

Kargel, J. S., G. Komatsu, V. R. Baker, and R. G. Strom, The Volcanology of Venera and Vega Landing Sites and the Geochemistry of Venus, *Icarus*, **103**, 253-275, 1993.

Kaula, W. M., D. L. Bindschadler, R. E. Grimm, V. L. Hansen, K. M. Roberts, and S. E. Smrekar, Styles of Deformation in Ishtar Terra and Their Implications, *J. Geophys. Res.*, **97**, 16,085-16,120, 1992.

Kaula, W. M., and L. Muradian, Is plate tectonics on Venus concealed by volcanism?, *Geophys. Res. Lett.*, **9**, 1021-1024, 1982.

Kaula, W. M., and R. J. Phillips, Quantitative tests for plate tectonics on Venus, *Geophys. Res. Lett.*, **8**, 1187-1190, 1981.

Keddie, S. T., and J. W. Head, Sapas Mons, Venus: Sequence of events in a large shield volcano, *Lunar Planet. Sci. XXIII*, 669-670, 1992.

Keddie, S. T., and J. W. Head, Sapas Mons: Evolution of a type-shield volcano on Venus, *Lunar Planet. Sci. XXV*, 679-680, 1994.

Keldysh, M. V., Venus exploration with the Venera 9 and Venera 10 spacecraft, *Icarus,* **30**, 606-625, 1977.

Kiefer, W. S., and B. H. Hager, Mantle downwelling and crustal convergence: A model for Ishtar Terra, Venus, *J. Geophys. Res.*, **96**, 20,967-20,980, 1991.

Kiefer, W. S., M. A. Richards, and B. H. Hager, A dynamic model of Venus' gravity field, *Geophys. Res. Lett.*, **13**, 14-17, 1986.

Kilburn, C. R. J., and R. M. C. Lopes, The growth of aa flow fields on Mount Etna, Sicily, *J. Geophys. Res.*, **93**, 14,759-14,772, 1988.

Kilburn, C. R. J., and R. M. C. Lopes, General Patterns of Flow Field Growth: Aa and Blocky Lavas, *J. Geophys. Res.*, **96**, 19,721-19,732, 1991.

Klose, K. B., J. A. Wood, and A. Hashimoto, Mineral Equilibria and the High Radar Reflectivity of Venus Mountaintops, *J. Geophys. Res.*, **97**, 16,353-16,369, 1992.

Komatsu, G., V. R. Baker, V. C. Gulick, and T. J. Parker, Venusian Channels and Valleys: Distribution and Volcanological Implications, *Icarus*, **102**, 1-25, 1993.

Kozak, R. C., and G. G. Schaber, Gravity-spreading origin of the Venusian tesserae (abstract), *Lunar Planet. Sci.* XVII, 444-445, 1986.

Kryuchkov, V. P., Ridge belts on the plains of Venus, 1 (abstract), *Lunar Planet. Sci. XIX,* 649-650, 1988.

Lancaster, M. G., and J. E. Guest, Possible sites of explosive volcanism in southern Guinevere Planitia (abstract), *Lunar Planet. Sci. XXII,* 773, 1991.

Lancaster, M. G., J. E. Guest, and K. M. Roberts, Sheet Flow Fields on Venus (abstract), *Lunar Planet. Sci. XXIV*, 843-844, 1993.

Lancaster, M. G., J. E. Guest, K. M. Roberts, and J. W. Head, "Great" Lava Fields on Venus (abstract), *Lunar Planet. Sci. XXIII*, 753-754, 1992a.

Lancaster, M. G., J. E. Guest, K. M. Roberts, and J. W. Head, Large Volume Lava Flow Fields on Venus: Dimensions and Morphology (abstract), *Papers Presented to the International Colloquium on Venus, Pasadena, California,* 62-64, 1992b.

Leinz, V., A. Bartorelli, G. R. Sadowski, and C. A. L. Isotta, Sobre o comportamento espacial do trapp basalticode bacia do Paraná, *Bol. Soc. Bras. Geol.*, **15**, 79-81, 1966.

Lopes, R. M. C., and C. R. J. Kilburn, Emplacement of lava flow fields: Application of terrestrial studies to Alba Patera, Mars, *J. Geophys. Res.*, **95**, 14,383-14,397, 1990.

Maack, R., Die Entwicklung der Gondwana-Schichten Suedbrasiliens und ihre Beziehungen zur Karru-Formation Suedafrikas, *International Geological Congress 19, Algiers, Sympos. sur les Series de Gondwana*, pp. 339-372, 1952.

Mackin, J. H., A Stratigraphic Section in the Yakima Basalt and the Ellensburg Formation in South-Central Washington, *Washington Div. Mines and Geology, Rept. Inv. 19*, 1961.

Magee, K. P. and J. W. Head, The Role of Rifting in the Generation of Melt: Implications for the Origin and Evolution of the Lada Terra - Lavinia Planitia Region of Venus, submitted to *J. Geophys. Res.*, 1993.

Magee, K. P. and J. W. Head, Characteristics and Distribution of Large Flow Fields on Venus: Implications for Plains Emplacement and Origin of Possible Flood Basalts, *Trans. AGU Spring Meeting*, 1994.

Magee Roberts, K., J. E. Guest, J. W. Head, and M. G. Lancaster, Mylitta Fluctus, Venus: Rift-related, centralized volcanism and the emplacement of large volume flow units, *J. Geophys. Res.*, **97**, 15,991-16,015, 1992.

Magee Roberts, K. and J. W. Head, Large-scale volcanism associated with coronae on Venus: implications for formation and evolution, *Geophys. Res. Lett.*, **20**, 1111-1114, 1993.

Mahoney, J. J., Deccan Traps, *in* Macdougall., J. D. (ed.), *Continental Flood Basalts*, Kluwer, Dordrecht, The Netherlands, pp. 151-194, 1988.

Malin, M. C., Lengths of Hawaiian lava flows, *Geology*, **8**, 306-308, 1980.

Masursky, H., E. Eliason, P. G. Ford, G. E. McGill, G. H. Pettengill, G. G. Schaber, and G. Schubert, Pioneer Venus radar results: Geology from images and altimetry, *J. Geophys. Res.*, **85**, 8232-8260, 1980.

McGill, G. E., S. J. Steenstrup, C. Barton, and P. G. Ford, Continental rifting and the origin of Beta Regio, Venus, *Geophys. Res. Lett*, **8**, 737-740, 1981.

McGill, G. E., E. R. Stofan, R. S. Saunders, and P. G. Ford, Depositional and structural sequence revealed by mapping on Magellan radar images, Eistla Regio/Guinevere Planitia area, Venus (abstract), *Lunar Planet. Sci. XXII*, 877-878, 1991.

McGill, G. E., J. L. Warner, M. C. Malin, R. E. Arvidson, E. Eliason, S. Nozette, and R. D. Reasenberg, Topography, surface properties, and tectonic evolution, *in* Hunten, D. M. et al. (eds.), *Venus*, University of Arizona Press, Tucson, pp. 159-214, 1983.

McKenzie, D., and M. J. Bickle, The volume and composition of melt generated by extension of the lithosphere, *J. Petrol.*, **29**, 625-679, 1988.

McKenzie, D., P. G. Ford, C. Johnson, B. Parsons, D. Sandwell, S. Saunders, and S. C. Solomon, Features on Venus Generated by Plate Boundary Processes, *J. Geophys. Res.*, **97**, 13,533-13,544, 1992a.

McKenzie, D., J. M. McKenzie, and R. S. Saunders, Dike Emplacement on Venus and on Earth, *J. Geophys. Res.*, **97**, 15,977-15,990, 1992b.

Michaels, G., *Guide for the Interpretation of Magellan SAR Images*, Jet Propulsion Laboratory, 18 February 1992.

Muhleman, D. O., Radar scattering from Venus and the Moon, *Astron. J.*, **69**, 34-41, 1964.

Navlivkin, D. U., *Geology of the U. S. S. R.*, translated by N. Rast, 855 pp., Oliver and Boyd, Edinburgh, 1973.

Nikolayeva, O. V., Geochemistry of the Venera 8 material demonstrates the presence of continental crust on Venus, *Earth, Moon, and Planets*, **50/51**, 329-342, 1990.

Parfitt, E. A., and J. W. Head, Radial Fracture Systems on Venus: Conditions of Formation (abstract), *Lunar Planet. Sci. XXIII*, 1027-1028, 1992a.

Parfitt, E. A., and J. W. Head, A survey of radial fracture systems on Venus (abstract), *Lunar Planet. Sci. XXIII*, 1029-1030, 1992b.

Parfitt, E. A., and J. W. Head, Formation and evolution of radial fracture systems on Venus (abstract), *Lunar Planet. Sci. XXIV*, 1113-1114, 1993a.

Parfitt, E. A., and J. W. Head, Buffered and unbuffered dike emplacement on Earth and Venus: implications for magma reservoir size, depth, and rate of magma replenishment, *Earth, Moon and Planets*, **61**, 249-281, 1993b.

Parmentier, E. M., and P. C. Hess, Chemical differentiation of a convecting planetary interior: consequences for a one-plate planet such as Venus, *Geophys. Res. Lett.*, **19**, 2015-2018, 1992.

Pavri, B, J. W. Head, K. B. Klose, and L. Wilson, Steep-Sided Domes on Venus: Characteristics, Geologic Setting, and Eruption Conditions from Magellan Data, *J. Geophys. Res.*, **97**, 13,445-13,478, 1992.

Pettengill, G. H., E. Eliason, P. G. Ford, G. B. Loriot, H. Masursky, and G. E. McGill, Pioneer Venus radar results: Altimetry and surface properties, *J. Geophys. Res.*, **85**, 8261-8270, 1980.

Pettengill, G. H., P. G. Ford, and B. D. Chapman, Venus: Surface electromagnetic properties, *J. Geophys. Res.*, **92**, 14,881-14,892, 1988.

Pettengill, G. H., P. G. Ford, W. T. K. Johnson, K. R. Raney, and L. A. Soderblom, Magellan: Radar Performance and Data Products, *Science*, **252**, 260-265, 1991.

Phillips, R. J., R. E. Arvidson, J. M. Boyce, D. B. Campbell, J. E. Guest, G. G. Schaber, L. A. Soderblom, Impact Craters on Venus: Initial Analysis from Magellan, *Science*, **252**, 288-297, 1991a.

Phillips, R. J., R. E. Grimm, and M. C. Malin, Hot-spot evolution and the global tectonics of Venus, *Science*, **252**, 651-658, 1991b.

Phillips, R. J., W. M. Kaula, G. E. McGill, and M. C. Malin, Tectonics and evolution of Venus, *Science*, **212**, 879-887, 1981.

Phillips, R. J., and M. C. Malin, The interior of Venus and tectonic implications, *in* Hunten, D. M. et al. (eds.), *Venus*, University of Arizona Press, Tucson, pp. 159-214, 1983.

Phillips, R. J., and M. C. Malin, Tectonics of Venus, *Annu. Rev. Earth Planet Sci.*, **12**, 411-443, 1984.

Phillips, R. J., R. F. Raubertas, R. E. Arvidson, I. C. Sarkar, R. R. Herrick, N. Izenberg, and R. E. Grimm, Impact Craters and Venus Resurfacing History, *J. Geophys. Res.*, **97**, 15,923-15,948, 1992.

Piccirillo, E. M., A. J. Melfi, P. Comin-Chiaramonti, G. Bellieni, M. Ernesto, L. S. Margues, A. J. R. Nardy, I. G. Pacca, A. Roisenberg, and D. Stolfa, Continental flood volcanism from the Paraná Basin (Brazil), *in* Macdougall., J. D. (ed.), *Continental Flood Basalts*, Kluwer, Dordrecht, The Netherlands, 195-238, 1988.

Pieri, D. C., and S. M. Baloga, Eruption rate, area, and length relationships for some Hawaiian lava flows, *J. Volcanol. Geotherm. Res.*, **30**, 29-45, 1986.

Pinkerton, H., and L. Wilson, The lengths of lava flows (abstract), *Lunar. Planet. Sci. XIX*, 937-938, 1988.

Pinkerton, H., and L. Wilson, The dynamics of channel-fed lava flows (abstract), *Lunar. Planet. Sci. XXIII*, 1083-1084, 1992.

Plaut, J. J., and Arvidson, R. E., 1992, Comparison of Goldstone and Magellan radar data in the equatorial plains of Venus, *J. Geophys. Res.*, **97**, 16,279-16,291, 1992.

Plescia, J. B., and M. P. Golombek, Origin of planetary wrinkle ridges based on the study of terrestrial analogs, *Geol. Soc. Am. Bull.*, **97**, 1289-1299, 1986.

Pronin, A. A., The structure of Lakshmi Plateau, an indication of asthenosphere horizontal flows on Venus, *Geotectonics*, **20**, 271-280, 1986.

Pronin, A. A., and E. R. Stofan, Coronae on Venus: Morphology and distribution, *Icarus*, **87**, 452-474, 1990.

Reidel, S. P., T. L. Tolan, P. R. Hooper, M. H. Beeson, K. R. Fecht, R. D. Bentley, and J. L. Anderson, The Grande Ronde Basalt, Columbia River Basalt Group: Stratigraphic descriptions and correlations in Washington, Oregon, and Idaho, in *Geol. Soc. Amer. Spec. Pap. 239, Volcanism and Tectonism in the Columbia River Flood Basalt Province* (S. P. Reidel and P. R. Hooper, eds.), pp. 21-53, 1989.

Richards, M. A., A. R. Duncan, and V. E. Courtillot, Flood basalts and hot-spot tracks: Plume heads and tails, *Science,* **246**, 103-107, 1989.

Roberts, K. M., and J. W. Head, Lakshmi Planum, Venus: Characteristics and models of origin, *Earth Moon Planets,* **50/51**, 193-249, 1990.

Roberts, K. M., J. W. Head, and J. E. Guest, Mylitta Fluctus, Venus: Flow characteristics and sources (abstract), *Lunar Planet. Sci. XXII*, 1121-1122, 1991.

Roberts, K. M., J. W. Head, M. G. Lancaster, and J. E. Guest, Volcanism and rifting along the northern edge of Lada Terra, Venus (abstract), *Lunar Planet. Sci. XXIII,* 1157-1158, 1992.

Robinson, C. A., and J. A. Wood, Recent Volcanic Activity on Venus: Evidence from Radiothermal Emissivity Measurements, *Icarus,* **102**, 26-39,1993.

Rowland, S. K., and G. P L. Walker, Pahoehoe and aa in Hawaii: Volumetric flow rate controls the lava structure, *Bull. Volcanol.*, **52**, 615-628, 1990.

Sandwell, D. T., and G. Schubert, Flexural Ridges, Trenches, and Outer Rises Around Coronae on Venus, *J. Geophys. Res.*, **97**, 16,069-16,083, 1992.

Saunders, A. D., M. Storey, R. W. Kent, and M. J. Norry, Consequences of plume-lithosphere interactions, in Storey, B. C., Alabaster, T. and R. J. Pankhurst, (eds), *Magmatism and the Causes of Continental Break-up*, Geological Society Special Publication No. 68, pp. 41-60, 1992.

Saunders, R. S., R. E. Arvidson, J. W. Head III, G. G. Schaber, E. R. Stofan, and S. C. Solomon, An Overview of Venus Geology, *Science,* **252**, 249-252, 1991.

Saunders, R. S., and G. H. Pettengill, Magellan Mission Summary, *Science,* **252**, 247-249, 1991.

Saunders, R. S., G. H. Pettengill, R. E. Arvidson, W. L. Sjogren, W. T. K. Johnson and L. Pieri, The Magellan Venus Radar Mapping Mission, *J. Geophys. Res.*, **95**, 8339-8355, 1990.

Saunders, R. S., A. J. Spear, P. C. Allin, R. S. Austin, A. L. Berman, R. C. Chandlee, J. Clark, A. V. DeCharon, E. M. DeJong, D. G. Griffith, J. M. Gunn, S. Hensley, W. T. K. Johnson, C. E. Kirby, K. S. Leung, D. T. Lyons, G. A. Michaels, J. Miller, R. B.

Morris, A. D. Morrison, R. G. Piereson, J. F. Scott, S. J. Shaffer, J. P. Slonski, E. R. Stofan, T. W. Thompson, and S. D. Wall, Magellan Mission Summary, *J. Geophys. Res.*, **97**, 13067-13090, 1992.

Schaber, G. G., Eratosthenian volcanism in Mare Imbrium: Source of the youngest lava, in Apollo 17 Preliminary Science Report, *NASA Spec. Publ. SP-330*, 30.17-30.21, 1973a.

Schaber, G. G., Lava flows in Mare Imbrium: Geologic evidence from Apollo orbital photography, *Proc. Lunar. Sci. Conf., 4th*, 73-92, 1973b.

Schaber, G. G., Venus: Limited extension and volcanism along zones of lithospheric weakness, *Geophys. Res. Lett.*, **9**, 499-502, 1982.

Schaber, G. G., Venus: Quantitative Analysis of Terrain Units Identified from Venera 15/16 Data and Described in Open-File Report 90-24, *U. S. Geol. Surv. Open-File Rep. 90-468*, 1990.

Schaber, G. G., Volcanism on Venus as inferred from the morphometry of large shields, *Proc. Lunar Planet Sci. Conf. XXI*, 3-11, 1991.

Schaber, G. G., and R. C. Kozak, *U. S. Geol. Surv. Open-File Map 90-24*, 1:15,000,000 scale, 1990.

Schaber, G. G., E. M. Shoemaker, and R. C. Kozak, The surface age of Venus: Use of the terrestrial cratering record, *Solar Syst. Res.*, **21**, 89-94, 1987.

Schaber, G. G., R. G. Strom, H. J. Moore, L. A. Soderblom, R. L. Kirk, D. J. Chadwick, D. D. Dawson, L. R. Gaddis, J. M. Boyce, and J. Russell, Geology and Distribution of Impact Craters on Venus: What Are They Telling Us?, *J. Geophys. Res.*, **97**, 13,257-13,301, 1992.

Self, S., S. Finnemore, T. Thordarson, and G. P. L. Walker, Importance of compound lava and lava-rise mechanism in emplacement of flood basalts (abstract), *Trans. AGU*, **72**, 566-567, 1991.

Senske, D. A., Geology of the Venus equatorial region from Pioneer Venus radar imaging, *Earth Moon Planets*, **50/51**, 305-327, 1990.

Senske, D., D. Campbell, J. Head, P. Fisher, A. deCharon, S. Frank, S. Keddie, K. Roberts, E. Stofan, J. Aubele, L. Crumpler, and N. Stacy, Geology and tectonics of the

Themis Regio-Lavinia Planitia-Alpha Regio-Lada Terra area, Venus: Results from Arecibo image data, *Earth Moon Planets*, **55**, 97-161, 1991a.

Senske, D. A., and J. W. Head, Zones of extension and rifting on Venus: characteristics and distribution (abstract), *Lunar Planet. Sci. XXIII*, 1269-1270, 1992.

Senske, D. A., J. W. Head, E. R. Stofan, and D. B. Campbell, Geology and structure of Beta Regio, Venus: Results from Arecibo radar imaging, *Geophys. Res. Lett.*, **18**, 1159-1162, 1991b.

Senske, D. A., G. G. Schaber, and E. R. Stofan, Regional Topographic Rises on Venus: Geology of Western Eistla Regio and Comparison to Beta Regio and Atla Regio, *J. Geophys. Res.*, **97**, 13,395-13,420, 1992.

Shaw, H. R., and D. A. Swanson, Eruption and flow rates of flood basalts, in Proc. Second Columbia River Basalt Symposium (E. H. Gilmour and D. Stradling, eds.), pp. 271-299, Cheney, Eastern Washington State College Press, 1970.

Simpson, R. A., G. L. Tyler, M. J. Maurer, and E. Holmann, Scattering properties of Venus' surface (abstract), *Lunar Planet. Sci. XXIII*, 1301-1302, 1992.

Sjogren, W. L., B. G. Bills, P. W. Birkeland, P. B. Esposito, A. R. Konopliv, N. A. Mottinger, S. J. Ritke, and R. J. Phillips, Venus gravity anomalies and their correlations with topography, *J. Geophys. Res.*, **88**, 1119-1128, 1983.

Slyuta, E. N., Large shield volcanoes (> 100 km in diameter) on Venus: morphologic types (abstract), *Lunar Planet. Sci. XXI*, 1172-1173, 1990.

Slyuta, E. N., and M. A. Kreslavsky, Intermediate (20-100 km) sized shield volcanic edifices on Venus (abstract), *Lunar Planet. Sci. XXI*, 1174-1175, 1990.

Smrekar, S. E., and R. J. Phillips, Venusian highlands: Geoid to topography ratios and their implications, *Earth Planet. Sci. Lett.*, **107**, 582-597, 1991.

Smrekar, S. E., and S. C. Solomon, Gravitational Spreading of High Terrain in Ishtar Terra, Venus, *J. Geophys. Res.*, **97**, 16,121-16,148, 1992.

Solomon, S. C., and J. W. Head, Lithospheric flexure beneath the Freyja Montes foredeep, Venus: Constraints on lithospheric thermal gradient and heat flow, *Geophys. Res. Lett.*, **17**, 1393-1396, 1990.

Solomon, S. C., J. W. Head, W. M. Kaula, D. McKenzie, B. Parsons, R. J. Phillips, G. Schubert, and M. Talwani, Venus Tectonics: Initial Analysis from Magellan Data, *Science*, **252**, 297-312, 1991.

Solomon, S. C., S. E. Smrekar, D. L. Bindschadler, R. E. Grimm, W. M. Kaula, G. E. McGill, R. J. Phillips, R. S. Saunders, G. Schubert, S. W. Squyres, and E. R. Stofan, Venus Tectonics: An Overview of Magellan Observations, *J. Geophys. Res.*, **97**, 13,199-13,255, 1992.

Squyres, S. W., D. M. Janes, G. Baer, D. L. Bindschadler, G. Schubert, V. L. Sharpton, and E. R. Stofan, The morphology and evolution of coronae on Venus, *J. Geophys. Res.*, **97**, 13,611-13,634, 1992a.

Squyres, S. W., D. G. Jankowski, M. Simons, S. C. Solomon, B. H. Hager, and G. E. McGill, Plains Tectonism on Venus: The Deformation Belts of Lavinia Planitia, *J. Geophys. Res.*, **97**, 13,579-13,599, 1992b.

Stofan, E. R., D. L. Bindschadler, J. W. Head, and E. M. Parmentier, Coronae on Venus: Models of origin, *J. Geophys. Res.*, **96**, 20,933-20,946, 1991.

Stofan, E. R., V. E. Hamilton, and K. Cotugno, Parga and Hecate Chasmata, Venus: Structure, Volcanism and Models of Formation, *Lunar Planet. Sci. XXIV*, 1361-1362, 1993.

Stofan, E. R., and J. W. Head, Coronae of Mnemosyne Regio, Venus: Morphology and origin, *Icarus*, **83**, 216-243, 1990.

Stofan, E. R., J. W. Head, and D. B. Campbell, Multiple ring features in Themis Regio: Evidence for endogenic origin, *Lunar Planet. Sci. XVI*, 825-826, 1984.

Stofan, E. R. and R. S. Saunders, Geologic evidence of hotspot activity on Venus: Predictions for Magellan, *Geophys. Res. Lett.*, **17**, 1377-1380, 1990.

Stofan, E. R., V. L. Sharpton, G. Schubert, G. Baer, D. L. Bindschadler, D. M. Janes, and S. W. Squyres, Global Distribution and Characteristics of Coronae and Related Features on Venus: Implications for Origin and Relation to Mantle Processes, *J. Geophys. Res.*, **97**, 13,347-13,378, 1992.

Sukeswala, R. N. and A. Poldervaart, Deccan basalts of the Bombay area, India, *Geol. Soc. Am. Bull.*, **69**, 1475-1494, 1958.

Sukhanov, A. L., Parquet: Regions of areal plastic dislocations, *Geotectonics*, **20**, 294-305, 1986.

Sukhanov, A. L. and A. A. Pronin, Ridged Belts on Venus as Extensional Features, *Proc. Lunar. Planet. Sci. Conf. 19th*, 335-348, 1989.

Sukhanov, A. L., A. A. Pronin, G. A. Burba, A. M. Nikishin, V. P. Kryuchkov, A. T. Basilevsky, M. S. Markov, R. O. Kuzmin, N. N. Bobina, V. P. Shaskina, E. N. Slyuta, and I. M. Chernaya, Geomorphic/geologic map of part of the northern hemisphere of Venus, *U. S. Geol. Surv. Map I-2059, V15M90/0G*, 1989.

Surkov, Yu. A., Geochemical studies of Venus by Venera 9 and 10 automatic interplanetary stations, *Proc. Lunar. Sci. Conf. 8th.*, 2665-2689, 1977.

Surkov, Yu. A., V. L. Barsukov, L. P. Moskalyova, V. P. Kharyukova, and A. L. Kemurdzhian, New data on the composition, structure, and properties of Venus rock obtained by Venera 13 and 14, *Proc. Lunar. Planet. Sci. Conf. 14th*, Part 2, *J. Geophys. Res.*, **89**, suppl., B393-B402, 1984.

Surkov, Yu. A, L. P. Moskalyova, V. P. Kharyukova, A. D. Dudin, G. G. Smimov, and S. E. Zaitseva, Venus rock composition at the Vega 2 landing site, *Proc. Lunar. Planet. Sci. Conf.*, Part 1, *J. Geophys. Res.*, **91**, suppl., E215-E218, 1986.

Swanson, D. A., Yakima basalt of the Teiton River area, south-central Washington, *Geol. Soc. Am. Bull.*, **78**, 1077-1110, 1967.

Swanson, D. A., T. L. Wright, and R. T. Helz, Linear vent systems and estimated rates of magma production and eruption for the Yakima basalt on the Columbia River Plateau, *Am. J. Sci.*, **275**, 1975.

Taylor, G. J., B. C. Bruno, and S. Self, Slow emplacement of flood basalts: evidence from fractal properties of lava flows (abstract), *Lunar Planet. Sci. XXV*, 1383-1384, 1994.

Theilig, E., S. Wall, and R. S. Saunders, Radar interpretation of lava fields as a function of incidence angle: Implications for interpretation of Magellan SAR data of Venus, *Proc. Lunar Planet. Sci. Conf., 19th*, 323-333, 1989.

Thompson, T. W., and the Magellan Flight Team, Magellan mission progress report, *Lunar Planet. Sci. XXIV*, 1427-1428, 1993.

Thompson, T. W., and the Magellan Flight Team, Magellan mission progress report, *Lunar Planet. Sci. XXV*, 1401-1402, 1994.

Tolan, T. L., S. P. Reidel, M. H. Beeson, J. L. Anderson, K. R. Fecht, and D. A. Swanson, Revisions to the Estimates of the Areal Extent and Volume of the Columbia River Basalt Group, in *Geol. Soc. Amer. Spec. Pap. 239, Volcanism and Tectonism in the Columbia River Flood Basalt Province* (S.P. Reidel and P.R. Hooper, eds.), 1-20, 1989.

Turcotte, D. L., An episodic hypothesis for Venusian tectonics, *J. Geophys. Res.*, **98**, 17,061-17,068, 1993.

Vorder Bruegge, R. W., and J. W. Head, Fortuna Tessera, Venus: Evidence of horizontal convergence and crustal thickening, *Geophys. Res. Lett.*, **16**, 699-702, 1989.

Walker, G. P. L., Lengths of lava flows, *Philos. Trans. R. Soc. London, Ser. A*, **274**, 107-118, 1973.

Watters, T. R., Wrinkle ridge assemblages on the terrestrial planets, *J. Geophys. Res.*, **93**, 10,236-10,254, 1988.

White, R. S., Magmatism during and after continental break-up, *in* Storey, B. C., Alabaster, T. and R. J. Pankhurst, (eds), *Magmatism and the Causes of Continental Break-up*, Geological Society Special Publication No. 68, pp. 1-16, 1992.

White, R. and D. McKenzie, Magmatism at rift zones: The generation of volcanic continental margins and flood basalts, *J. Geophys. Res.*, **94**, 7685-7729, 1989.

Whitford-Stark, J., and L. Wilson, Atmospheric motions produced by hot lava, *Weather*, **31**, 25-27, 1976.

Zuber, M. T., Constraints on the lithospheric structure of Venus from mechanical models and tectonic surface features, *Proc. Lunar Planet. Sci. Conf. 17th*, Part 2, *J. Geophys. Res.*, **92**, suppl., E541-E551, 1987.

Zuber, M. T., Ridge belts: Evidence for regional and local-scale deformation on the surface of Venus, *Geophys. Res. Lett.*, **17**, 1369-1372, 1990.

Zuber, M. T., and E. M. Parmentier, On the relationship between isostatic elevation and the wavelengths of tectonic surface features on Venus, *Icarus*, **85**, 290-308, 1990.

JOURNAL OF GEOPHYSICAL RESEARCH, VOL. 97, NO. E10, PAGES 15,991-16,015, OCTOBER 25, 1992

Mylitta Fluctus, Venus: Rift-Related, Centralized Volcanism and the Emplacement of Large-Volume Flow Units

KARI MAGEE ROBERTS,[1] JOHN E. GUEST,[2] JAMES W. HEAD,[1] AND MICHAEL G. LANCASTER[2]

Mylitta Fluctus is a volcanic flow field that covers approximately 300,000 km^2 in southern Lavinia Planitia. The flows are typically radar-bright with uniform surface textures. Central channels are common. Maximum flow lengths range from 400 to 1000 km; flow widths range 30-100 km in the medial and distal portions of the flow field. The total volume of the flow field, based on estimates of flow thickness, is of the order of 2 x 10^4 km^3. The flow field is composed of six smaller flow fields that are interpreted to represent major eruption events in the evolution of Mylitta. An asymmetric shield volcano 200 km in radius with a central caldera has been identified as the single major source. It is located along a possible rift zone at the northern edge of Lada Terra. No evidence for fissure-fed eruptions is observed, although eruptions may have occurred along fissures within the rift before the main vent centralized. Mylitta is similar in scale to many terrestrial flood basalt provinces, although it is lower in total estimated volume and is distinguished by the presence of a central source edifice. The origin of Mylitta is proposed to be linked to regional extension and possible hotspot activity in a manner similar to that suggested for the origin of terrestrial flood basalts. The lower apparent volume of Mylitta relative to terrestrial flood basalts suggests that the amount of material upwelling from the mantle may have been lower in this case or that the formation of the flow field has not yet finished. Detailed studies of the morphology and distribution of flow fields similar to Mylitta should yield insight into the variation and evolution of hotspot-related volcanism and the formation of possible flood basalts on Venus.

INTRODUCTION

Recent radar images of Venus acquired by the Arecibo Observatory in Puerto Rico and the orbiting Magellan spacecraft have revealed the presence of a massive lava flow field that covers an area of approximately three hundred thousand square kilometers within Lavinia Planitia [*Campbell et al.*, 1991; *Senske et al.*, 1991; *Roberts et al.*, 1991; *Head et al.*, 1991]. Tentatively named "Mylitta Fluctus" ("fluctus" is from the Latin for "flow"), this flow field is characterized by generally radar-bright, lobate lava flows superposed on darker plains (Figures 1 and 2). The interpretation of these lobate features as lava flows is based on the presence of surface features such as channels, levees, and lobate perimeters typically associated with lava flows observed on the other terrestrial planets and their association with an apparent volcanic vent (Figure 2). Flows within Mylitta Fluctus have traveled downslope from their source at the edge of Lada Terra to the north into the lowlands of Lavinia to form a complex that extends approximately 1000 km north-south and 460 km east-west. The entire complex is interpreted as a massive lava flow field similar in area to the Columbia River, Keweenawan and West Greenland flood basalt provinces on Earth [*Basaltic Volcanism Study Project*, 1981].

The purpose of this analysis is to characterize the flow morphology, stratigraphy, and evolution of the flow field and to examine the link between its origin and the local tectonics. We first review the regional setting of the flow field. Subsequently, we develop a model for the stratigraphy and emplacement history of Mylitta, discuss flow morphology, and present some preliminary estimates of effusion rates and eruption durations that may have characterized its emplacement. In the final section we discuss the origin of Mylitta in relation to local rifting and possible hotspot activity and compare the emplacement of Mylitta to the origin of terrestrial flood basalts.

REGIONAL SETTING

The regional setting of Mylitta is complex (Figure 3). The source area for the flow field is located within an east-west trending portion of a linear tectonic belt at the northern edge of Lada Terra. This tectonic belt extends several thousand kilometers along the border of Lavinia Planitia and Lada Terra [*Senske et al.*, 1991]. East of Mylitta it meets a north-south trending belt that extends toward Alpha Regio, where the regional structure is complicated by the presence of tessera along the rift zone (Figure 1). Near Mylitta, the belt is characterized by a broad, low topographic arch 400-1000 m in elevation above the surrounding plains and semi-continuous interior lows exhibiting 500-2500 m in total relief from the outer rise (Figure 4). Within the belt are multiple, subparallel, linear fractures, scarps and troughs spaced from 2-25 km apart. Maximum lengths are obscured by volcanic flooding but are of the order of 250-800 km (Figures 1-3). The topographic and structural characteristics of this belt and its association with volcanic sources suggest that it is extensional in origin [*Campbell et al.*, 1991] and may be a site of local crustal rifting. Along this proposed rift zone are a variety of volcanic centers, including the source vent for Mylitta (Figures 2 and 3).

The source vent for Mylitta (Figures 3 and 5) was first predicted from the Arecibo data [*Senske et al.*, 1991] and later confirmed in the Magellan images [*Roberts et al.*, 1991; Head *et al.*, 1991]. The vast majority of flows within Mylitta appear to emanate from this vent. It is characterized by an elongate caldera approximately 40 x 20 km in width that is circumscribed by multiple, closely spaced arcuate ridges and scarps that produce a hummocky surface, particularly to the southwest (Figure 5). The depression associated with the caldera varies from 700 to 1500 m in depth and extends up to

[1]Department of Geological Sciences, Brown University, Providence, Rhode Island.
[2]University of London Observatory, University College London, England.

Paper Number 92JE01245.
0148-0227/92/92JE-01245$05.00

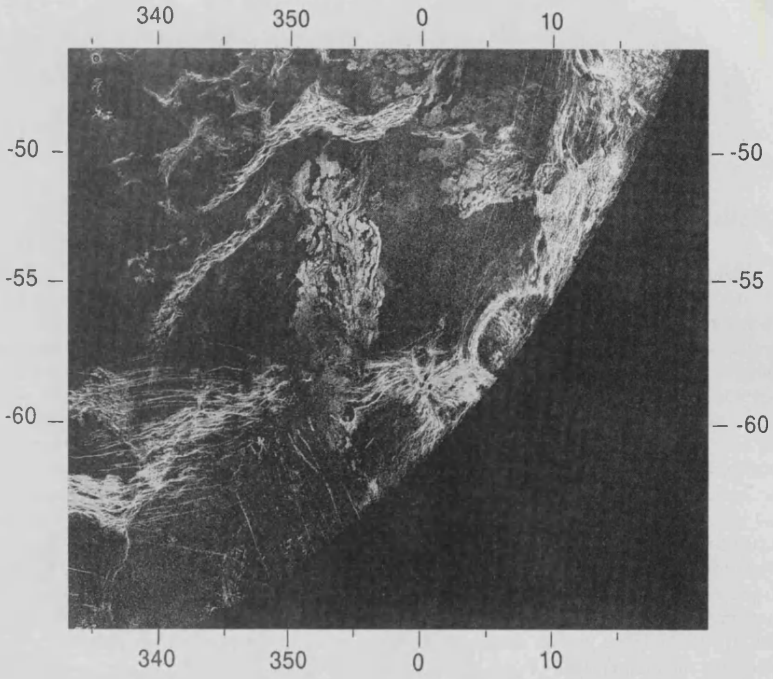

Fig. 1. Arecibo radar image (12.6 cm wavelength) of Mylitta Fluctus and structures within southern Lavinia Planitia and northern Lada Terra. Over the region of Mylitta, incidence angles range from 52° to 62° [*Senske et al.*, 1991]. The resolution is 1.5-4 km [*Campbell et al.*, 1991]. Mylitta extends approximately 1000 km north-south and 460 km east-west.

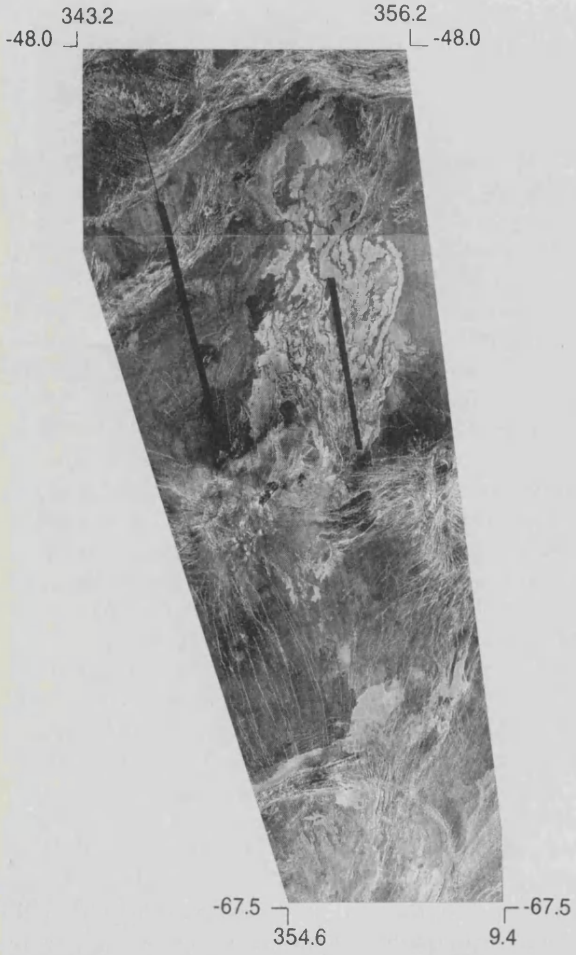

Fig. 2. Magellan radar image (12.6 cm wavelength) of Mylitta Fluctus and nearby structures. Incidence angles vary from 20° to 25° over the flow field. The image is a compressed mosaic of C1-MIDRPs 60s347 and 45s350 with a resolution of approximately 225 m. The image covers an area approximately 2000 x 900 km wide. Individual orbit swaths are ~20 km wide. Illumination is from the west.

100 km in width, approximately 60 km beyond the edge of the caldera walls (Figure 4). Within the caldera is at least one small volcanic shield approximately 3 km in diameter that has been partially buried by radar-dark material that filled the interior of the caldera. Dark material is also observed in the area immediately to the northeast. This radar-dark material is most likely ponded lava or air fall deposits that have collected in local topographic lows. Radial troughs approximately 0.6-5.0 km in width extend up to 60 km to the northwest, northeast and southeast from the caldera walls (see arrows, Figure 5*b*). In all three locations, the radial troughs disrupt the caldera wall at their juncture. This observation and the fact that flows may be directly traced to these radial structures suggest they may be channels along which flows have been directed downslope away from the caldera.

Other volcanic centers are located along the rift zone to the west and east of the caldera (Figures 2 and 3). The two closest to Mylitta are not associated with a complex of flows as extensive as that of Mylitta. Adjacent and to the west of the Mylitta source region is an ovoid structure approximately 160 km in diameter defined by complex, radial and semiconcentric fractures, scarps and troughs (B, Figure 3) [*Solomon et al.*, 1991]. Within the interior of the ovoid are numerous lava channels, pits, and volcanic shields 2-12 km in diameter. The southern portion of the ovoid and the cluster of small shields rest on a topographic high that rises approximately 500-700 m above the source vent of Mylitta (Figure 4). The eastern portion of the ovoid has been heavily embayed by volcanic flows. Approximately 470 km to the east of Mylitta is a highly deformed volcanic center (C, Figure 3) characterized by an interior circular structure 50 km in diameter from which radiate numerous closely spaced fractures possibly related to subsurface dike emplacement. A few lobate flows approximately 50 km long are visible extending to the northwest from this structure. Additional volcanic centers, including ovoids and coronae and a similar flow field (Kaiwan

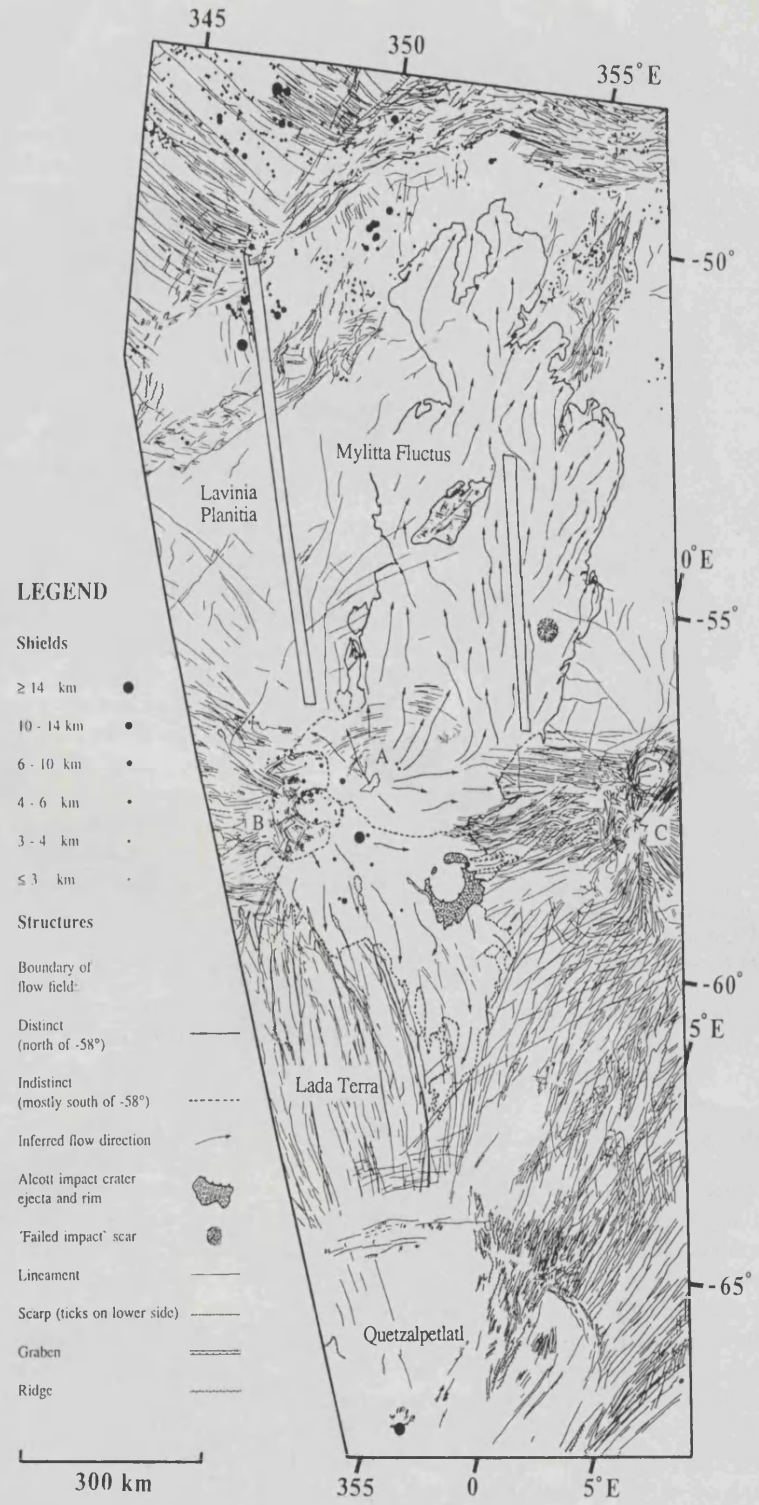

Fig. 3. Sketch map of region shown in Figure 2. The boundary of Mylitta and the orientation and distribution of regional structures are shown. A, B, and C refer to volcanic centers located along the northern edge of Lada Terra as discussed in the text. Diagonal bars outline data gaps.

Fluctus), are located along the north-south extension of the rift zone at spacings of 200 km to over 1300 km (Figure 1).

South of Mylitta the regional tectonics are dominated by Quetzalpetlatl, a large corona 800 km in diameter [*Solomon et al.*, 1991] and over 500 km distant (Figures 2 and 3). Linear fractures and troughs up to 530 km long extend between the corona and the volcanic centers along the rift zone. The fractures oriented north-northwest and east-northeast appear to radiate from the volcanic centers along the rift zone, while those oriented north-northeast appear to originate from Quetzalpetlatl. These fractures are most likely related to subsurface dike emplacement. Crosscutting relationships indicate that tectonic and volcanic activity associated with Quetzalpetlatl at least in part postdate activity associated with the rift zone.

North and west of the rift zone the regional tectonics of Lavinia Planitia are dominated by generally east-west trending tectonic belts thought to be of compressional origin (Figures 1-3) [*Frank and Squyres*, 1991; *Squyres et al.*, 1991; *Solomon et al.*, 1991]. These ridge belts are heavily flooded and

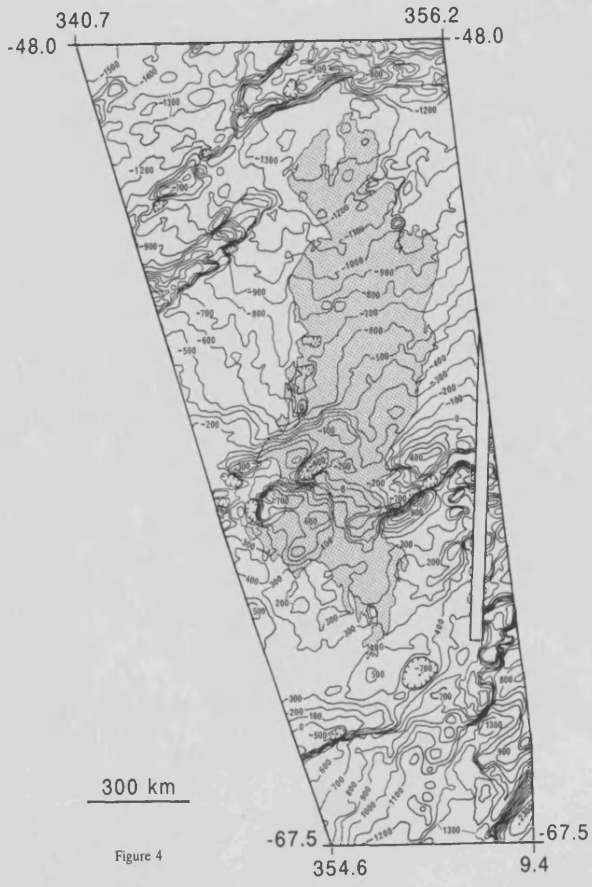

Fig. 4. Magellan topographic map of region in Figures 2 and 3. Contour interval is 100 m. Datum corresponds to 6052.0 km. Stippled pattern locates volcanic flows associated with Mylitta Fluctus.

embayed by flows within Mylitta and the underlying plains. They appear to predate most of the tectonic and volcanic activity associated with the rift zone and northernmost Lada Terra.

Flow Stratigraphy

We have identified six major flow fields within Mylitta that we consider to represent different eruptive episodes within its emplacement. The boundaries and sequence of emplacement of each flow field are shown in Plate 1*a*. These boundaries are admittedly subject to a degree of uncertainty due to the inherent difficulties of mapping flow units from radar images. Recent studies of terrestrial volcanic terrain by *Gaddis et al.* [1989] and *Theilig et al.* [1989] indicate that it is often difficult to distinguish and separate adjacent lava flows, particularly smooth pahoehoe flows, in radar images. This admits uncertainty in any estimation of emplacement history and eruption conditions based on mapping and measurements of flow dimensions. Within the Magellan images of Mylitta, there are a few instances where it is difficult to distinguish individual flows in the proximal portion of the flow field owing to their narrow widths, close spacings and complex, branching morphologies. In addition, there is at least one relatively broad flow unit in the western half of the flow field that consists of several individual flows that are difficult to distinguish. The majority of individual flow units within Mylitta, however, appear distinct and are easily separated in the Magellan data. The large flow units mapped in the distal region of Mylitta that measure many hundreds of kilometers in length and several tens of kilometers in width are thought to represent individual flows due to the presence of central channels in many of these flows and the fact that overlapping flows of smaller dimensions are also observed elsewhere in the flow field. Flow units identified in the Magellan data were also identified in the Arecibo images, despite the large difference in incidence angle represented by the two data sets. Mylitta was imaged at a range of incidence angle of 20-25° by Magellan [*Pettengill et al.*, 1991] and 52-62° by Arecibo [*Senske et al.*, 1991]. Little variation in gross morphology within the flow field is observed between the two data sets, although the Magellan data have revealed an abundance of detail, particularly with regard to stratigraphic relations, that was previously unseen. The greatest difference is seen in the proximal zone of the flow field which appears much darker in the Arecibo image, although faint outlines of flows visible in the Magellan data are detectable. Therefore, by utilizing radar data sets acquired at different viewing geometries we were able to reduce some of the uncertainty in identifying individual flow units.

Individual flow episodes within Mylitta were identified by continuities in flow boundaries and central channels and by similarities in radar backscatter and surface texture. Superposition relationships between flow units were then used to determine relative ages and flow stratigraphy (Plate 1). Flow boundaries obscured by superposed units were mapped such that only the exposed portions of the flow are connected. Uncertainties in the flow boundaries are indicated by dashed lines or question marks. The sequential growth of Mylitta is shown in Plate 1*a*; each new episode is highlighted in color. The complete flow field and the superposition of each episode is shown in Plate 1*b*.

Flow field 1. Initial eruptions in the history of Mylitta produced a flow field (shown in green in Plate 1) characterized, to the north, by multiple, closely spaced lobate flows that extend up to 200 km from the central source. Flow widths are of the order of 1-4 km and are much narrower than the 30-50 km widths typical of later episodes. These flows comprise an asymmetric shield that is approximately 200 km in radius and 700 m in elevation above the northern plains. It is located on the northern flank of the rift zone. The exposed portion of the shield is relatively flat and steep-sided, dropping 400 m in elevation over the outer 20-45 km of its radius. The shield is crosscut by multiple arcuate lineaments, most of which appear to be scarps and troughs, that are approximately 1.5 km wide and spaced 1-3 km apart [*Roberts et al.*, 1991]. These structures may be the result of continued extension along the rift zone or gravitational relaxation of the unbuttressed flank. Two broad topographic depressions or troughs 100-400 m deep trend north-south and northeast across the flanks of the shield and appear to have directed the vast majority of flows downslope into Lavinia (arrows, Figure 4). The origin of these troughs is unclear. The northeast trending trough may have formed as a result of continued extension within the rift zone; this does not explain the formation of the trough oriented north-south. The total volume of the shield is of the order of 1.7×10^4 km^3, by far the largest of all the flow fields (Table 1). The total volume as well as the uniform lengths, narrow widths, and closely spaced nature of flows in this flow field suggest that it was emplaced over a much longer time period (during multiple eruptions) than later flow fields.

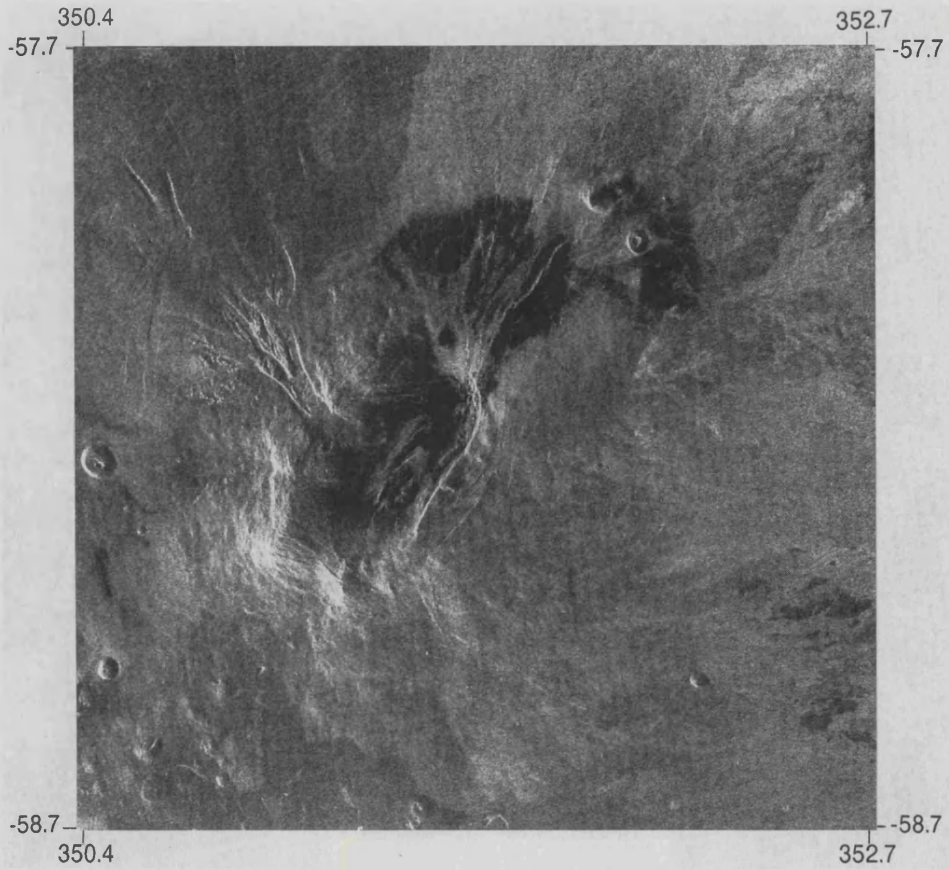

Fig. 5*a*. Magellan image of the source vent of Mylitta. The image is approximately 140 km across at the base.

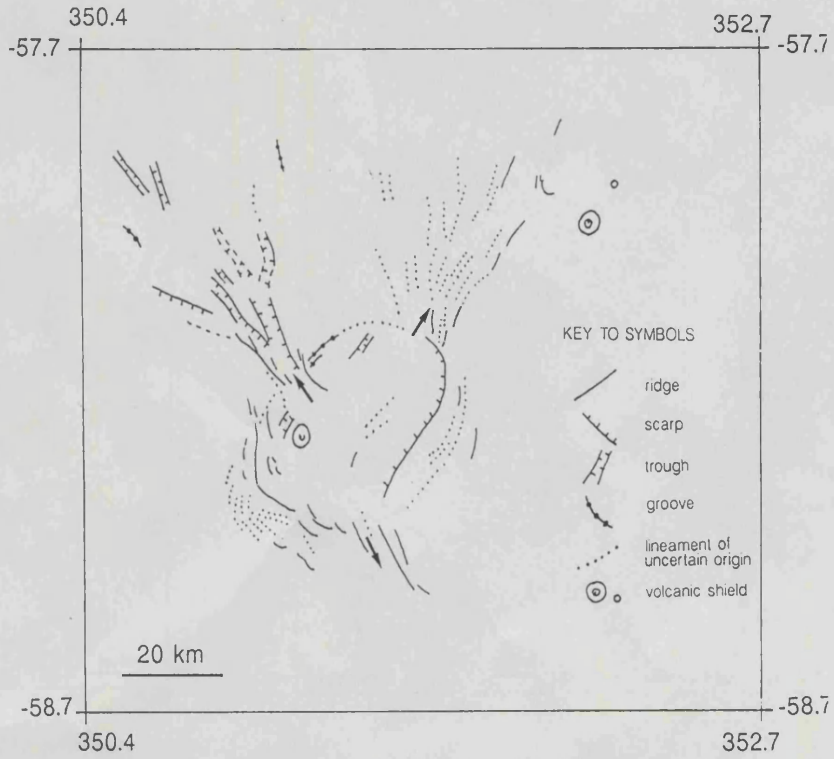

Fig. 5*b*. Sketch map of Figure 5*a*. Arrows indicate the location and orientation of channels radiating from the caldera rim.

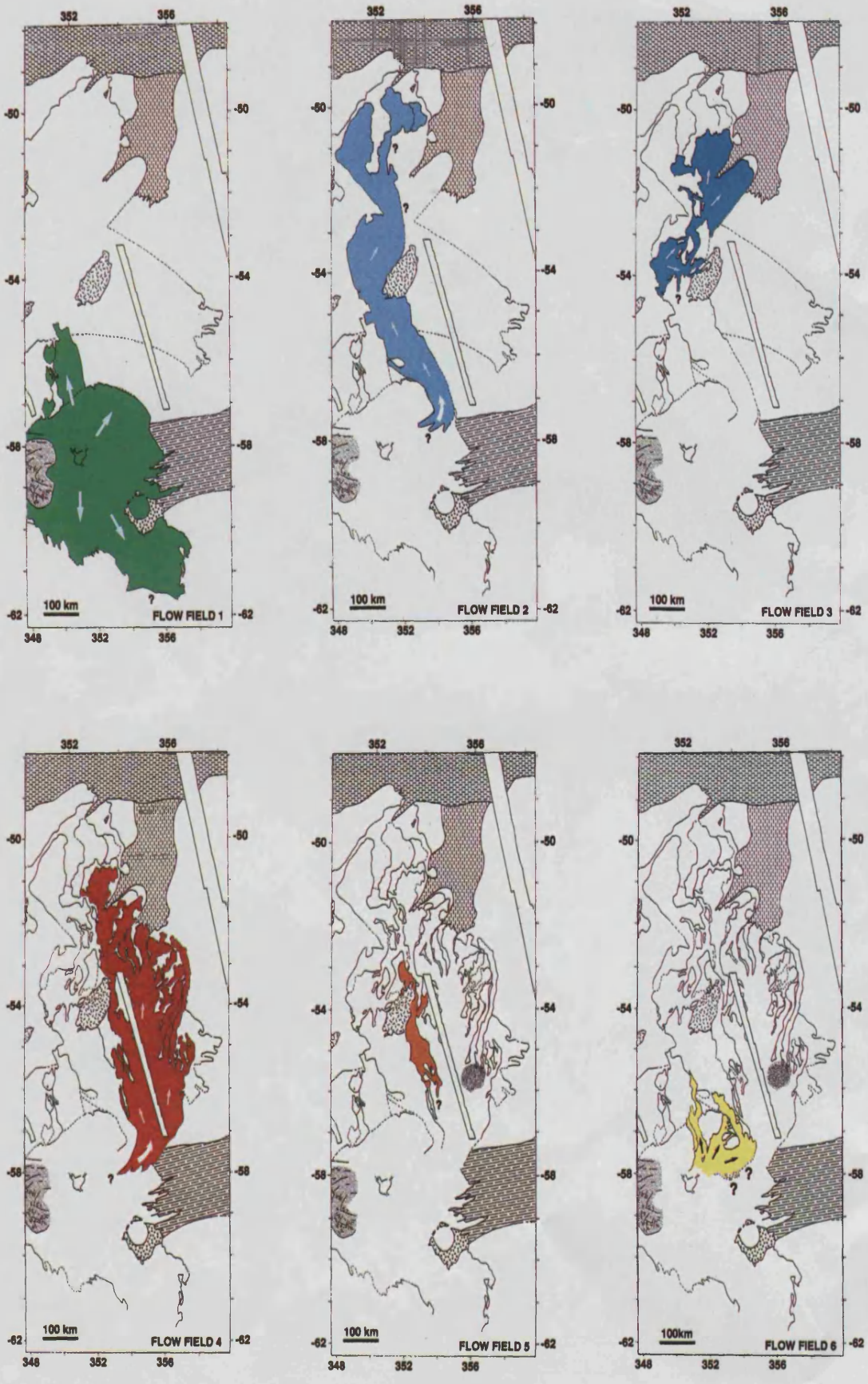

Plate 1*a*. Maps illustrating the evolution of Mylitta Fluctus. The addition of each new flow field is highlighted in color. Arrows indicate inferred flow directions. A key to symbols is given in the accompanying legend.

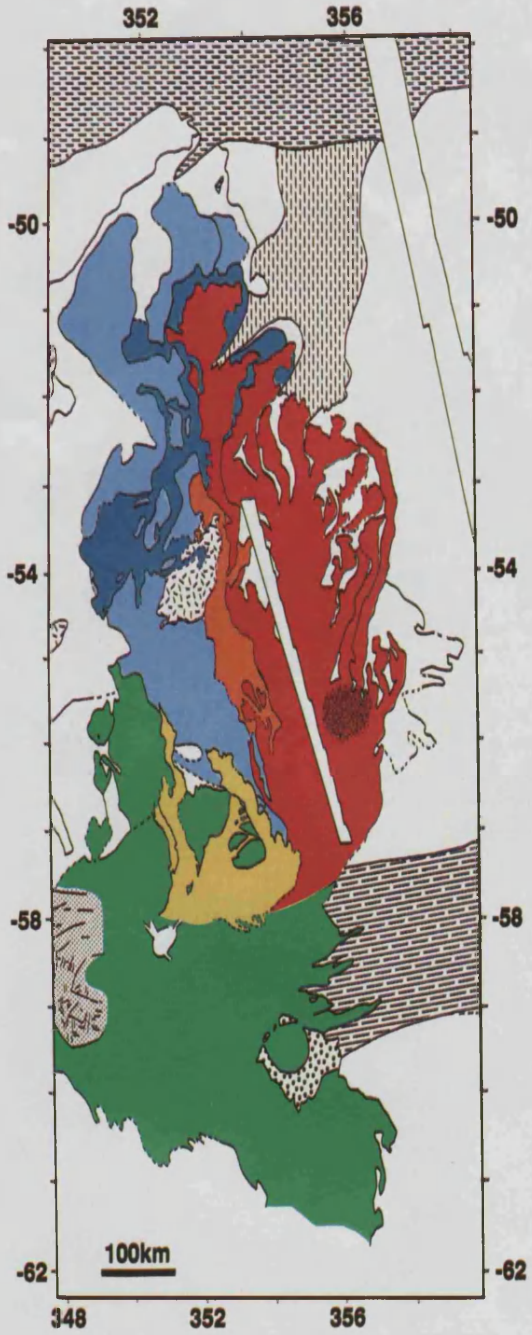

FLOW MAP LEGEND

- flows associated with phase depicted
- diffuse dark deposits of possible impact origin
- ovoid
- outline of flows from previous phases
- rift zone
- impact materials
- ridge belt
- tectonically deformed terrain

The timing of caldera formation relative to the formation of the shield is uncertain. The flows appear to be associated with the central caldera, although initially they may have emanated from fissures along the rift zone before the main source centralized. There is otherwise no direct evidence for fissure-fed eruptions. The fact that channels that radiate from the caldera are partially buried suggests the caldera formed relatively early in the evolution of Mylitta.

South of the caldera, the flows appear more sheetlike and lack the closely spaced, lobate character of the northern flows. They appear to be associated with the same source region along the rift zone but may be related to eruptions that occurred before the source centralized. This is consistent with the observation that Alcott, an impact crater 60 km in diameter located 200 km to the southeast of the caldera, is both flooded by and situated on flows associated with this portion of the rift. Alcott may have been emplaced on flows, now seen south of the caldera, that erupted before the main source of Mylitta centralized. These flows may have erupted from fissures within the rift zone or from one or more sources associated with the ovoid and/or cluster of small shields southwest of the caldera. Topographic data indicate these flows may have traveled south-southeast from the local high associated with the ovoid and shield cluster (Figure 4). Later flows from the caldera subsequently flooded and partially filled the crater and formed the shield edifice now seen to the north.

Apparently associated with this episode is a region of longer flows that extends over 200 km beyond the base of the shield. The maximum flow length measured in this region is approximately 440 km (Table 1). The flows are closely spaced and appear to overlap. Where individual flows are observed, widths are approximately 3-6 km. The relative superposition of these flows and those of the shield is obscured by a superficial layer of diffuse, dark material that partially covers the flows at the base of the shield. However, the flows appear to be related to radiating channels superposed on the shield, indicating that these flows may be the youngest of episode 1. Just west of this region are a lava channel and "fan" and an irregular shield approximately 50 km in diameter. The precise age relationships between these structures are unclear but the shield appears to have been emplaced before the eruptions of episode 1 were complete.

The borders of mottled plains underlying Mylitta (seen most clearly near the northernmost border of the flow field; Figure 2) are outlined in Plate 1*a*. These plains may have originated in the same manner as Mylitta, a result of volcanism along the rift zone, but are not related to the same source that fed Mylitta. The inferred flow directions (northeast and east-southeast) of this older flow field suggest the regional slopes within Lavinia have changed since its emplacement.

Flow field 2 . The second major episode in the evolution of Mylitta Fluctus produced the first flow field of extensive length (shown in light blue in Plate 1). The maximum flow length is of the order of 1000 km (Table 1). Flow widths are obscured by the superposition of later flow fields but exceed 60-100 km in the distal portions of the field where the flows pond and embay the northern ridge belts. Flows emplaced during this episode are generally radar-bright and of uniform surface texture. Channel development is extensive in the proximal and medial

Plate 1*b*. Map of the complete flow field showing the relative positions of individual phases. Flow dimensions are given in Table 1.

TABLE 1. Dimensions of Episodes for Mylitta Fluctus

Episode	Area, km^2	Maximum Length,[a] km	Maximum width,[b] km	Volume,[c] km^3
1	117,960	440	-	16,966[d]
2	62,320	1000	140	623
3	32,100	390[e]	100	321
4	106,660	960	160	1,741
5	7,900	630	60	79
6	16,180	340	140	162
Entire flow field	300,000[f]	1000[g]	460	19,892

[a]The maximum continuous length of each episode, measured from the source caldera to the most distal part.

[b]The maximum continous width of individual episodes. Episode 1 completely surrounds the source caldera. The maximum width of the whole field crosses several episodes.

[c]Volumes are based on a minimum estimate of flow thickness of 10 m. Figures are quoted to the nearest cubic kilometer to avoid rounding errors during summation, but this precision is not implied. Volume for episode 4 was derived separately (see Table 2).

[d]Based on a cone 700 m in height with a basal radius of 150 km representing the source edifice, surrounded by a 10-m-thick pile of episode 1 lavas.

[e]Measured from the most proximal to distal part along the longest continual portion (flow) of the episode. This length was not extended to the source caldera, since for this episode the source appears to be local.

[f]Area of the envelope formed by the episodes (which overlap), includes southern extension of the flow field beyond 58.5° S.

[g]The maximum length of the longest episode, namely, episode 2.

portions of the flow field but only faintly detected in the distal regions. Flows within this episode cannot be traced directly to the source vent because of burial by subsequent flow units but appear to have originated at the caldera and flowed downslope to the northeast across the shield (following regional topography; Figure 4) before turning northwest to form the bulk of the western boundary of Mylitta. A remnant of what appears to have been an older ridge belt within Lavinia has been partially embayed by flows within this episode.

Flow field 3 . Shown in dark blue in Plate 1, the third flow field emplaced in the formation of Mylitta appears to have been locally derived and unrelated to eruptions at the rift zone. The source of this flow field is not obvious but appears to be situated at the extreme western edge of Mylitta. From this location, flows traveled up to 390 km northeast across flow field 2 and the mottled plains underlying Mylitta. The flows of this episode are radar-dark and have a uniform surface texture. There is no clear evidence for the presence of channels or other flow structures. At its distal end the flow field appears to have ponded against a northern ridge belt and achieves a maximum width of 100 km (Table 1). Much narrower widths of 3-6 km are observed near the source, where the flows followed relatively tortuous pathways. The low radar backscatter, uniform surface texture, apparent lack of central channels, and narrow pathways of the flows in this episode suggest that the eruption was characterized by extremely fluid lavas.

This episode generally postdates episode 2. However, there is some uncertainty in the local stratigraphy within flow field 2 such that the superposition relationships appear reversed. These relationships are difficult to unravel due to complexities in radar backscatter of flows in this area (see question mark in Plate 1; flow field 3). The reversed stratigraphy appears to be the result of the superposition of both episodes 2 and 3 by a younger flow characterized by a long sinuous channel and a radar-bright lava "fan."

Flow field 4. The fourth episode in the evolution of Mylitta was the emplacement of the most distinctive flow field of the Fluctus. It is shown in red in Plate 1 and forms the entire eastern half of Mylitta. It consists of a series of subparallel, lobate, radar-bright flows that appear to have been emplaced in a progressively eastward direction in response to changes in local topographic slopes due to the emplacement of previous flow fields and phases within episode 4. Four phases in the formation of this flow field are recognized (Figure 6); their dimensions are listed in Table 2. Individual flows emplaced during this episode are up to 460-960 km long and 30-80 km

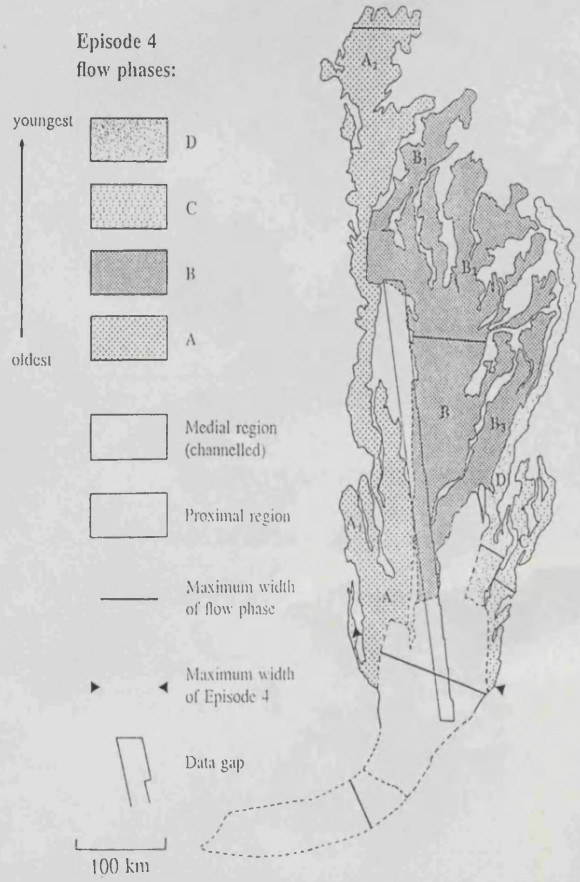

Fig. 6. Sketch map of episode 4 showing the location and relative ages of individual flows within this flow field. Flow dimensions are given in Table 2.

wide; the maximum continuous width of the entire flow field is 160 km (Tables 1 and 2). There is a general trend toward decreasing length and estimated volume with each phase that is consistent with a waning effusion rate. The long eastern flow (phase D) is an exception to this trend. The entire flow field has a surface area of over 100,000 km^2 which is exceeded only slightly by that of the first episode (Table 1). Channels and levees are well-developed and dominate the proximal, upslope portion of the flow field. Channel development in the distal portion of the flow field is not as extensive.

Superposed on the medial portion of flow field 4 is a circular-shaped region of diffuse, radar-dark material approximately 75 km in diameter (Figure 2). This feature possesses a fine radial texture and becomes gradually darker toward its center. There the texture is somewhat speckled, possibly due to a cluster of small blocks. It is interpreted to be the scar of an impact event produced by the shock or pressure wave of a meteoroid that was destroyed before it reached the surface, and is similar in appearance to other such features on Venus [*Phillips et al.*, 1991].

Flow field 5. This flow field (shown in orange in Plate 1) is distinctive for the extreme mottling and heterogeneity in radar brightness it exhibits. In terms of surface area, it is the smallest of all the flow fields (Table 1). It cannot be traced directly back to the source area and as there is no evidence for superpositioning of later flows, it may have been tube-fed. It was emplaced in the central portion of Mylitta, adjacent to and superposed on the western boundary of flow field 4. The mottled character of this flow field and its proximity to flow field 4 suggest that it may not actually represent a separate episode in the evolution of Mylitta but rather the waning stages of the eruption of episode 4. In this case, as the eruption of episode 4 neared completion, lowered effusion rates may have produced numerous, overlapping flow units of shorter lengths and different textures. Such a process has been documented for terrestrial eruptions [*Guest et al.*, 1987] and might have caused the distinct surface textures of flow field 5. If this flow field is indeed a later phase of the previous episode, then its emplacement along the western edge of flow field 4 is inconsistent with the eastward younging trend of the other phases in that episode and may be due to changes in topographic slopes caused by the emplacement of the bulk of flow field 4.

Flow field 6. The youngest flow field is shown in yellow in Plate 1 and contains flows that may be traced directly back to the source. The flows are generally radar-bright with local variations in backscatter due to channel development and superficial deposits of diffuse, radar-dark material. They are shorter in length than those of previous episodes (Table 1) and do not extend more than 110 km beyond the base of the shield. Flow directions are to the north and northwest and reflect changes in local slope due to the emplacement of flow field 4.

To summarize, the evolution of Mylitta Fluctus began with a phase of eruptions that flooded the rift zone and constructed an asymmetric edifice on the northern flank. These eruptions produced the greatest volume of material (Table 1) within Mylitta and was emplaced over a longer period of time than any of the later flow fields. Two subsequent eruptions or series of eruptions (flow fields 2 and 4/5) produced flow fields of extensive length that define the bulk of Mylitta away from the source. These episodes were separated by an intermediate eruption of radar-dark flows (flow field 3) that were locally derived (did not erupt from the central caldera). The latest series of eruptions (flow field 6) produced the least extensive flow field, with flows not traveling much farther than the base of the shield. Within Mylitta, flow fields were emplaced progressively west to east and then back toward the west in response to changes in local topographic slope. Except for the

TABLE 2. Flow Dimensions of Episode 4, Mylitta Fluctus

Flow Phase	Area,[a] km^2	Total length,[b] km	Maximum width,[c] km	Volume, km^3
A	27,410	A_1 460 A_2 960	80	274[d]
B	45,010	B_1 930 B_2 810 B_3 640	80	450[d]
C	4,580	560	30	46[d]
D	7,180	810	30	72[d]
Medial Region	15,420	510	130	617[e]
Proximal Region	7,060	200	50	282[e]
Whole Episode	106,660	960[f]	160	1,741

[a]For flow phases the distal area is quoted.

[b]Measured from the source caldera to the most distal part of the flow phase.

[c]The maximum continuous width.

[d]Distal volumes use, as an example, an average flow thickness of 10 m (see text). Figures are quoted to the nearest cubic kilometer to avoid rounding errors during summation, but this precision is not implied.

[e]Medial and proximal volumes use an example thickness of 40 m (four overlapping flows of 10 m thickness).

[f]The maximum length of the longest flow phase, namely, phase A.

episode of shield formation, the evolution of Mylitta appears to have been similar to the growth of flow fields on Mount Etna on Earth and Alba Patera on Mars, which progressed from stages of early time lengthening to subsequent widening and thickening [*Kilburn and Lopes*, 1988; Lopes and Kilburn, 1990]. In general, with the eruption of each of the major episodes, including the shield-building phase (episode 1), the episodes that formed the most extensive flow fields (2, 4/5), and the youngest episode (6), there has been a decrease in both the surface area and estimated volume of erupted materials. The total surface area of Mylitta is 3 x 10^5 km^2 and the total volume is of the order of 2 x 10^4 km^3 (Table 1). For comparison, the dimensions of various flow fields and flood basalt provinces on the Earth and Mars are given in Table 3. Mylitta compares favorably to many of these regions in terms of surface area (of the entire complex and individual flows) but is lower in total volume by at least one order of magnitude. In addition, Mylitta is distinguished from most terrestrial flood basalt provinces by the presence of a central shield edifice. Mylitta is also similar in volume to many of the large shield volcanoes on Earth and Mars [Schaber, 1991] but is distinguished from these structures by the presence of flow fields that extend to great distances from the shield edifice.

FLOW MORPHOLOGY

Individual flows within Mylitta Fluctus vary in dimension, brightness, and channel development. Variations in morphology are well documented between flows of different episodes. For example, flows within episodes 1, 3, and 5 are distinct from flows elsewhere in Mylitta. Flow field 1 is characterized by closely spaced, overlapping flows of much shorter lengths and narrower widths than flows in other episodes. Flow field 3 is the only region of sheetlike, radar-dark flows and flow field 5 is characterized by a mottling not observed in any other portion of Mylitta. In contrast, the flows of episodes 2, 4, and 6 are morphologically similar. Variations in flow morphology are also observed between phases of single episodes and along the length of individual flows.

Flow dimensions. Variations in flow length have been discussed previously and maximum lengths are given for each episode in Table 1. The maximum widths of entire flow fields are also given for each episode in Table 1; maximum widths for individual flows are given in Table 2 for episode 4 only. Widths of individual flows vary systematically with distance from the source. Widths and spacings are most narrow (1-8 km) in the proximal portions of Mylitta (Figure 7) although widths as large as 20 km are also measured in this region. In the medial portions of the flow field, flow widths broaden to about 15-40 km, locally exceeding 50 km (Figure 8). The greatest widths are observed in the distal portions of Mylitta (Figure 9) where values in excess of 100 km are common. Flows are thought to broaden with distance from the source as a result of decreasing topographic slopes. Maximum slopes of 0.4° are observed from the caldera to the base of the exposed portion of the shield; north of this, slopes decrease to approximately 0.1°. The greatest widths are due to ponding at the base of ridge belts within central Lavinia Planitia. Maximum width to length ratios obtained for individual flows in episode 4 range from 0.25 to 0.04. These values are similar to those estimated for basaltic aa flow fields on Mount Etna [*Kilburn and Lopes*, 1988].

It is difficult to obtain precise thickness estimates for individual flows due to the approximately 20-km-diameter footprint of the Magellan altimeter over this portion of the planet [*Pettengill et al.*, 1991]. However, analysis of the regional topography contoured at 100-m intervals indicates the flows are probably less than 100 m thick in the distal portion of Mylitta where there is little overlap between flow units because (1) individual contours do not bend or kink as they cross the flow field (Figure 4) and (2) profiles taken across this region are relatively flat (Figure 10*d*). Flow thickness may be constrained further by an independent observation. Several flows in the proximal and medial portions of Mylitta are contained by narrow concentric lineaments that cross the flow field in multiple locations (Figures 3, 11, and 12). These arcuate lineaments are less than 1.5 km wide and probably no more than a few meters to tens of meters in relief (they lack expression in the Magellan topographic data which has a height resolution of 5-50 m; *Pettengill et al.* [1991]). Therefore, where flows have been stopped by these structures they are probably 10-30 m thick.

The thickness of the entire flow field varies along its length as the amount of overlap in flow units increases toward the source. In the distal region where no more than three sequences of flows overlap, the total thickness is probably 30-90 m (Figure 10*d*). Profiles taken across the medial and proximal portions of Mylitta yield a thickness of approximately 150-250 m (Figures 10*b* and 10*d*). The shield has a total elevation of about 700 m but it is difficult to determine how much of this elevation is due to uplift along the rift zone and how much is actually due to flow emplacement. As described earlier, there is a 400 m elevation difference between the outer 20-45 km of the shield and the northern plains (Figure 10*a*). Therefore, a maximum estimate for the thickness of the proximal portion of Mylitta is probably of the order of 400 m. The total thickness may be greater if subsidence has occurred and underlying flow layers have been obscured. The fact that underlying plains are clearly visible in proximal, medial, and distal portions of the flow field indicates that great thicknesses of underlying flow layers have not been obscured and that if subsidence has occurred, it probably is not significant.

Channel development. Central channels are observed in flows throughout Mylitta, although they are most common in the proximal region. Channels in this portion of Mylitta are generally radar-dark with brighter, well-defined levees. They are typically less than 2 km wide and form complex, braided, and branching networks (Figure 7). Many are associated with distal fans. Medial and distal channels are broadly sinuous and radar-dark (Figure 13). Widths vary from 6 to 2.5 km and are extremely constant along the length of an individual channel. Most are typified by broad overflows and less distinctive levees than those observed in the proximal portions of Mylitta. The negative relief of one channel is clearly demonstrated in Figure 13: a superposed flow has traveled along the underlying channel a short distance before filling it sufficiently to cross over. Two flows within Mylitta exhibit unusual, mottled surface textures such that the margins of the flow appear rougher than the interior (Figures 13 and 14). This pattern is consistent with levee and channel development although dramatically different in morphology from the majority of channels observed in Mylitta. As these patterns are observed at the distal portions of individual flows, they may be related to processes that occur at the flow toe.

TABLE 3. Comparison of Flow Fields on the Terrestrial Planets

Flow Field or Province	Present (and Possible Original) Area, km^2	Maximum (and average) Thickness, m	Approximate Total Volume, km^3	Individual Flow Areas, km^2	Individual Flow Thicknesses, m	Individual Flow Volumes, km^3
Parana Basin	1.2×10^6 [a] (2×10^6?)	1,500 - 1,800[b] (650)	650,000[c] (1.5×10^6?)		average = 50[d] maximum > 100	
Karroo Province	140,000 (2×10^6?)[f]	8,000 - 9,000[d] (1,000?)	420,000[f] (2×10^6?)[e]		average = 10[d] (Lesotho)	
Siberian Platform	> 1.5×10^6[g] includes intrusions	3,500[d] (1,000)	250,000[g]		average = 30[d]	
Lake Superior Basin (Keweenawan)	100,000 in Lake Superior area[d] (125,000?)	800 - 12,000[d] (5,000?) for several basins[d]	> 300,000 in Lake Superior area[d]		3 - 30[h] average = 25[h] maximum = 400[h]	
Columbia River Basalt Group	163,700 ± 5,000[i]		174,300 ± 31,000[i]	(Grande Ronde Basalt) 149,000[j]	(Grande Ronde Basalt) ~3 to >100; average = 30[j]	maximum = 2,000 - 3,000[i]
Deccan Traps	520,000[k]	2,000[l]	700,000[k] (1.5×10^6?)			
Alba Patera, Mars				S-type fields: 33 - 1,800 M-type fields: 25,500 - 28,880[m]	S-type fields: 34 - 97 M-type fields: 80 ± 50%[m]	S-type fields: 1.6 - 174.8 M-type fields: 2,040 - 2,310[m]
Mare Imbrium			3×10^6[d]		average = 30 - 35[n]	
Mylitta Fluctus, Venus	300,000	400 - 250?	19,892 (see Table 1)	7,900 - 117,960 (flow episodes)	10 - 30 m?	80 - 16,970 (using 10 m thickness)

[a] *Maack* [1952]
[b] *Beurlen* [1970]
[c] *Leinz et al.* [1966]
[d] *Basaltic Volcanism Study Project* [1981]
[e] *Richards et al.* [1989]
[f] *Cox* [1972]
[g] *Navlivkin* [1973]
[h] *Green* [1972]
[i] *Tolan et al.* [1989]
[j] *Reidel et al.* [1989]
[k] *Ghose* [1972]
[l] *Sukeswala and Poldevaart* [1958]
[m] *Lopes and Kilburn* [1990]
[n] *Schaber* [1973a, b]

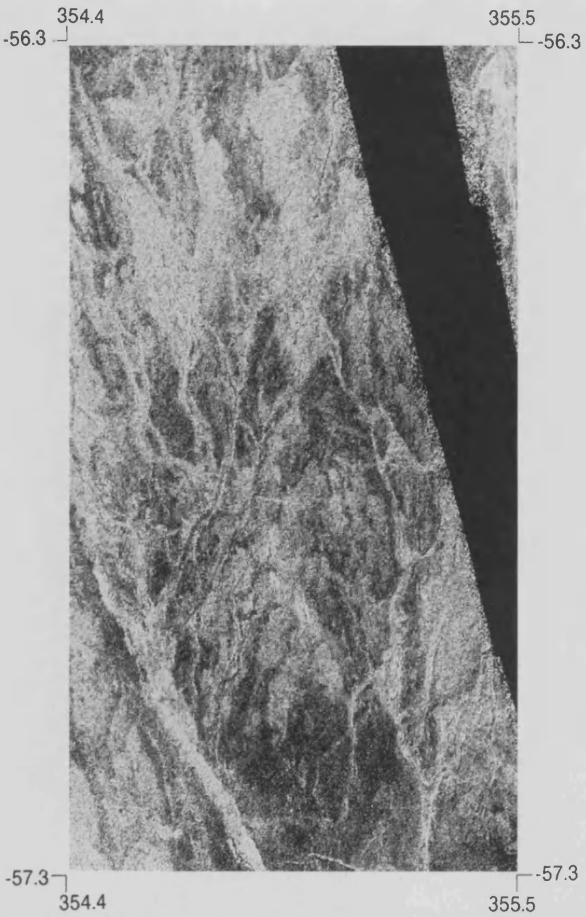

Fig. 7*a*. Magellan image of narrow, braided, and branching channels in the proximal region of Mylitta. The image is approximately 65 km across.

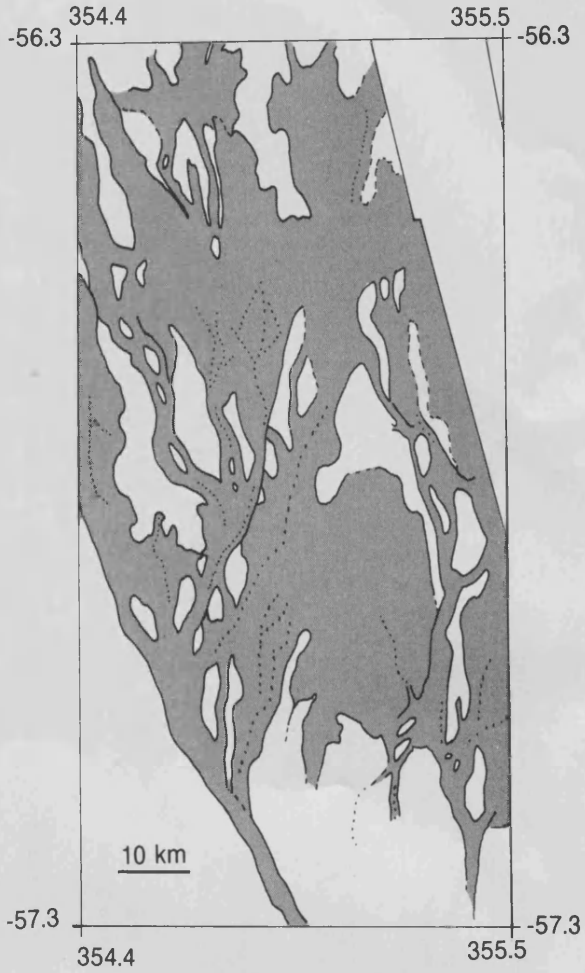

Fig. 7*b*. Sketch map of Figure 7*a*. Bright flows and channels are shaded and the location of some of the most narrow channels are shown by dotted lines.

Channel origin is generally attributed to flow drainage. Where channels are not observed, it is presumed that, if the flow was channel-fed, little or no drainage occurred subsequent to its emplacement. Faint channels observed in some flows (Figure 13; dotted lines) are probably due to lower amounts of drainage. Some of the medial and distal channels within Mylitta (e.g., the dark channel in Figure 13) are very similar in appearance to the extensive channels or "canali" seen elsewhere on Venus in terms of their sinuousity, great length, relatively constant widths and lack of obvious levees [*Head et al.*, 1991; *Baker et al.*, this issue]. The similarity of channels within Mylitta to these features suggests that channel formation may have been complex, possibly involving thermal erosion [*Baker et al.*, this issue], although constructional processes of channel formation cannot be dismissed [Gregg and Greeley, 1992].

The differences between proximal and distal flows in terms of channel width, abundance and complexity are similar to those documented for terrestrial flow fields [*Guest et al.*, 1987] and are probably due to changes in topographic slope and/or cooling rate. Although there is a general decrease in topographic slope away from the source of Mylitta, the region of most pronounced channel development in the proximal portion of the flow field occurs along the same local slope as the regions of medial and distal channel development. Therefore, changes in channel morphology are probably not the result of changes in local slope and may be related instead to changes in cooling rate during flow emplacement. Theoretical studies by *Crisp and Baloga* [1990*a*] and observations of active flow fields on Mount Etna by J. E. Guest and C. R. J. Kilburn (manuscript in preparation, 1991) indicate that during the initial stages of an eruption, near the vent, a flow has no crust or has one that is extremely thin and continuously broken up. During this stage, flows are often narrow, channel-fed and cool rapidly due to the large percentage of exposed core. As they cool, they slow, widen, and form crusts that reduce the rate of subsequent cooling. These observations may explain the relative abundance and narrow widths of channels in the proximal portion of Mylitta.

Surface brightness. Flows within Mylitta are typically radar-bright and remarkably uniform in surface texture (Figure 8), but some variation in surface brightness is observed. Dark flows, also of relatively uniform surface texture, are observed in flow field 3 (Figure 15) in the northwest portion of Mylitta. These flows are less rough relative to the 12.6-cm wavelength of the Magellan and Arecibo radar systems than brighter flows in the Fluctus. Extremely mottled flows are observed in portions of flow fields 4 (Figure 13) and 6 (Figure 14) and dominate flow field 5 (Figure 16). This mottling is thought to be the result of enhanced roughness due to channel and levee formation and, in the case of episode 5, the presence of numerous, overlapping flow units emplaced during the waning stages of episode 4. Changes in brightness and surface texture occur along the lengths of individual flows (e.g., Figures 7, 8,

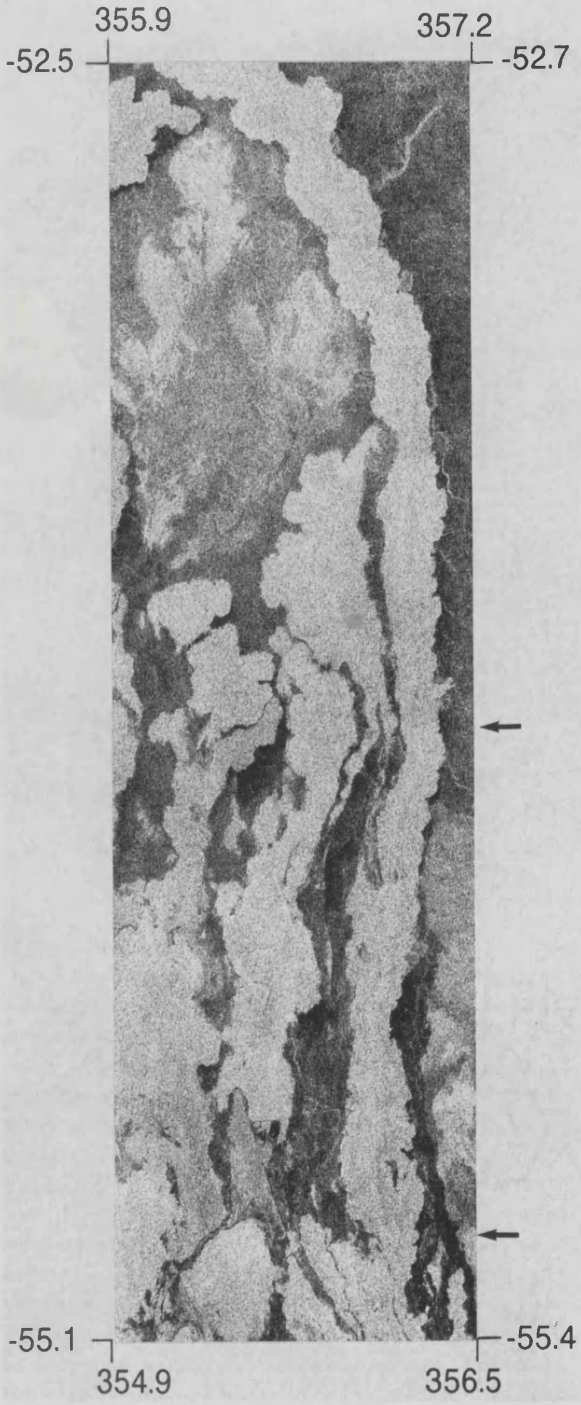

Fig. 8. Magellan image of medial and distal flows of episode 4 (portions of flow phases B_2, B_3, and C from Figure 6). The image is approximately 95 km across. Flows in this region have fairly uniform surface textures and widths of ~20-30 km. Arrows indicate changes in brightness along the length of phase B_3.

and 12) and are probably due to changes in lava rheology as a result of cooling and changes in local slope.

Analyses of radar backscatter of flows within Mylitta do not show a very strong correlation of radar brightness with age; only a slight trend toward lower values with increasing age is observed [Campbell and Campbell, this issue]. Processes of surface modification (including small-scale mass wasting, weathering, eolian activity, and emplacement of impact ejecta) are expected to slowly and continuously homogenize initial surface properties such that there should be a systematic muting of flow brightness with increasing age [*Arvidson et al.*, this issue]. Because no strong, systematic muting or darkening of flow brightness is observed among flow fields of different ages, it is possible that flow units within Mylitta were emplaced in a geologically rapid succession.

The perimeters of many flows, particularly those of flow field 4, are often bounded by diffuse, radar-dark regions 2-20 km wide (Figures 8 and 17). The origin of these features is unclear. They do not appear to be darker, underlying flow units but, instead, related to the emplacement of the bright flows that they surround. It is possible they have formed in a manner similar to the "dark margins" observed about many impact craters on Venus. Such features are thought to be due to the scouring of wavelength-scale material from existing terrain by the atmospheric shock or pressure wave of the incoming meteoroid [*Phillips et al.*, 1991]. In an analogous manner, dark flow margins may have been produced by the scouring of adjacent terrain by strong atmospheric convection cells caused by the rapid emplacement of a massive, hot lava flow. Similar effects have been observed along active flows on Mount Etna [e.g., *Whitford-Stark and Wilson*, 1976; *Chester et al.*, 1985]. The nearby redeposition of scoured fragments may also produce radar-dark signatures.

Radar-dark regions are also observed within the proximal portion of Mylitta (Figure 18). These regions are thought to be covered by superficial deposits of loose pyroclastic or fragmental material produced by other processes and windblown from more distant sources.

ERUPTION STYLE

Preliminary observations and conclusions regarding eruption style and duration can be made based on the morphology and dimensions of flow fields within Mylitta Fluctus. These conclusions are only tentative and subject to the uncertainties associated with accurately obtaining precise flow field measurements from the available radar data as well as the inherent limitations of using such measurements to describe the complex physical parameters associated with the eruption and emplacement of lava flows [Crisp and Baloga, 1990*a*].

Flow composition and type. The lobate flows within Mylitta are thought to be basaltic in general composition on the basis of their great lengths, morphologies that are suggestive of extremely fluid lavas, and measurements of reflectivity and dielectric constant similar to values for terrestrial basalt *Campbell and Campbell* [this issue]. In addition, morphologies exhibited by the flow field bear no similarities to flows and constructs observed elsewhere on Venus that are thought to be associated with the eruption of highly viscous magmas [e.g., *Head et al.*, 1991; *Moore et al.*, this issue]. Flows within Mylitta are not thought to be pyroclastic in origin due to their extreme lengths [*Head and Wilson*, 1986] and the abundance of channels.

Based on morphology and radar characteristics, it is difficult to determine whether flows in Mylitta have textures most similar to aa, pahoehoe, or blocky basaltic lavas. Flow structure is important as it provides information on the manner of flow emplacement. For example, recent work by *Rowland and Walker* [1990] has shown that volumetric flow rate controls the formation of pahoehoe and aa, such that pahoehoe forms at a lower volumetric flow rate (<5-10 m^3/s) than aa (>5-10 m^3/s).

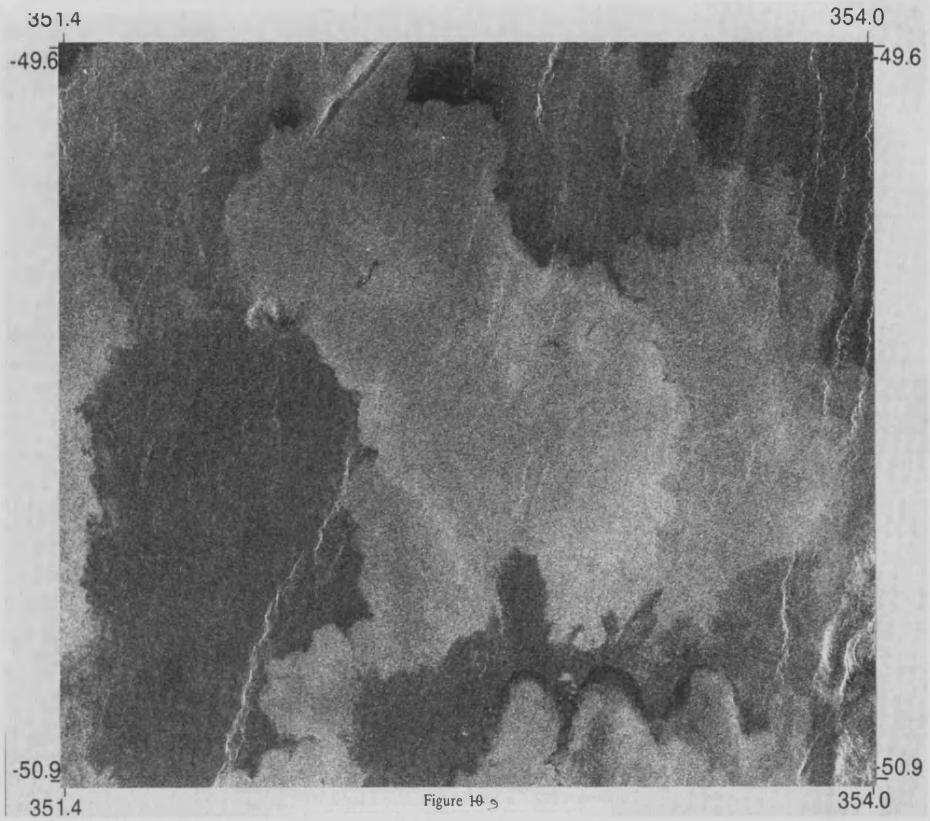

Fig. 9. Magellan image of a ponded flow in the distal portion of Mylitta. The image covers an area approximately 180 km across. The maximum flow width is ~120 km.

A comparison of Magellan and Arecibo radar images of flows in Mylitta Fluctus, Western Eistla Regio, and Sedna Planitia to airborne radar images of terrestrial flows by *Campbell and Campbell* [1991, this issue] has shown that the bright flows in these regions of Venus bear little resemblance in terms of polarization ratio to terrestrial aa flows and probably represent variations from very smooth "pavements" to pahoehoe textures. Backscatter cross sections for all but the brightest flows in this region are similar to those of terrestrial pahoehoe flows; moderately rough surfaces and enhanced reflectivity are thought to produce the brightest flow signatures [*Campbell and Campbell*, this issue]. However, *Arvidson et al.* [this issue] have proposed that the most radar-bright flows of Mylitta Fluctus (and other regions on Venus) are comparable to terrestrial aa based on comparisons to data obtained by an airborne radar system at incidence angles similar to those used by Magellan over Mylitta. A similarity to terrestrial aa was also reported for flows in Mylitta in a recent comparative fractal analysis of flow margins by *Bruno et al.* [1992*a*, *b*]. Results of this study indicate that two bright flows examined from episode 4 have fractal dimensions similar to those determined for a range of terrestrial aa flows. Thus, although pahoehoe flows are predicted on the basis of polarization ratio data, aa flows are predicted on the basis of radar backscatter data and recent estimates and comparisons of the fractal dimensions of flow margins.

Given the similarity of Mylitta to terrestrial flood basalt provinces, it is perhaps interesting to note that "planar to slightly undulatory" surfaces were described by *Swanson* [1967] for flows in the Yakima Basalt of the Columbia River Group. Swanson observed no flow top breccia, clinker, or pressure ridges within these flows. "Apparently the flows were very fluid during movement and cooled evenly after they had stopped and ponded, without the crust being disrupted by late flowage. Any crust that formed during flowage was probably continuously broken, engulfed in the fluid lava, and remelted, the process continuing until movement ceased" [*Swanson*, 1967, p. 1083]. Smoothly undulating to ropey pahoehoe textures also have been reported for flows elsewhere in the Columbia River, Keweenawan, and Snake River Plain flood and plains basalt provinces [e.g., *Swanson et al.*, 1975; *Greeley and King*, 1977; *Basaltic Volcanism Study Project*, 1981].

Eruption rate and duration. Having documented the morphology and apparent stratigraphic relations between flows of Mylitta, we would like to make some preliminary observations regarding the eruption conditions that may have characterized its emplacement. Numerous studies have attempted to infer eruption conditions from flow field morphology on the basis that flow field growth is systematic and strongly correlated to effusion rate, eruption duration, and local topography [e.g., *Walker*, 1973; *Hulme*, 1974; *Crisp and Baloga*, 1990b; *Lopes and Kilburn*, 1990]. A strong correlation between effusion rate and flow length was observed by *Walker* [1973] who examined 41 terrestrial basalt, basaltic andesite, and dacite flows. Walker concluded that effusion rate is the factor that largely determines lava flow length. The simplicity of this model is such that effusion rates may be estimated from measurements of flow length alone. Given an estimate of total flow volume, eruption duration also may be calculated.

This empirical relationship between flow length and effusion rate has been criticized, however, and additional correlations between flow length and total flow volume [*Malin*, 1980] and eruption rate and planimetric area [*Pieri and Baloga*,

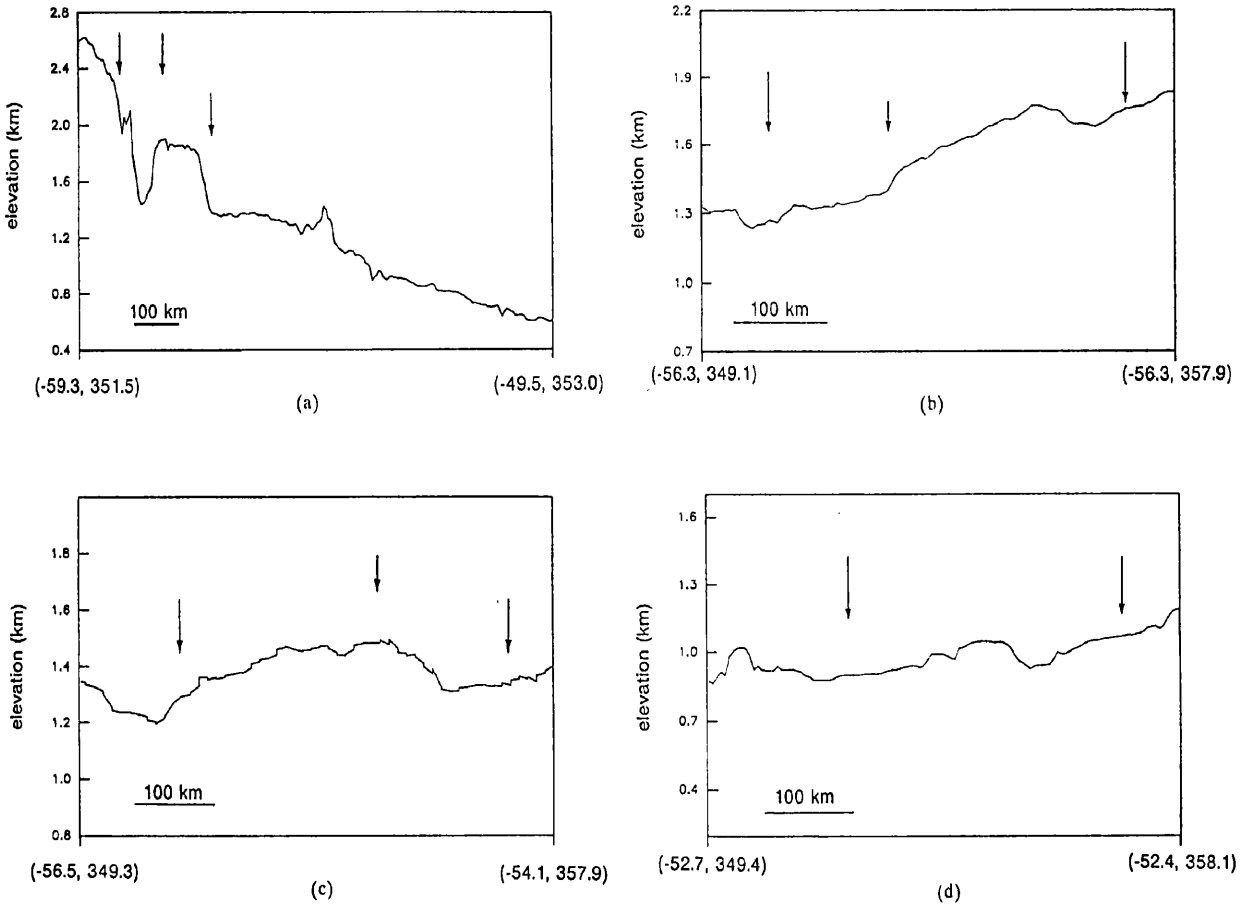

Fig. 10. Topographic profiles across Mylitta obtained from Magellan altimetry. Elevations are given in reference to a mean planetary radius or datum of 6050 km. The latitude and longitude of the endpoints of each profile are specified. (*a*) North-south profile from the source to the distal flow margins. The depression associated with the source vent is indicated by the two left arrows, the base of the shield by the third. The regional slope from the edge of Lada Terra into Lavinia Planitia is clearly shown. The slight rise approximately half the distance from the source to the northern flow margin corresponds to the remnant tectonic belt that has been heavily embayed by flows along the western margin of Mylitta. (*b*) East-west profile across the central portion of Mylitta. The large arrows mark the boundaries of entire flow field, the small arrow indicates the western edge of flows emplaced after episode 1. A maximum elevation above the regional slope or flow thickness of 150 m is measured in this portion of Mylitta. (*c*) Oblique profile across central Mylitta with the effects of regional slope essentially removed. Large arrows indicate boundaries of entire flow field; a smaller arrow marks the central region of episode 4. A maximum total flow thickness of 200 m is observed in the central portion of Mylitta; the flow margins thin substantially. (*d*) East-west profile across the distal portion of the flow field. Flow margins are indicated by arrows. Little to no relief is observed between the margins of the flow field and the adjacent plains.

1986] have been demonstrated for several Hawaiian basaltic flows. Recently, *Pinkerton and Wilson* [1988, 1992] have reanalyzed the Hawaiian flows examined by *Malin* [1980] and found that those flows whose lengths were longer than predicted from Walker's relationship were tube-fed flows and that those shorter had eruption durations less than 2 days. The positive relationship between effusion rate and flow length is related to flow cooling; the more rapidly a flow is erupted, the farther it may travel before it is stopped by cooling [e.g., *Kilburn and Lopes*, 1988]. Therefore, only relatively long duration, cooling-limited flows are going to have lengths dependent on effusion rate. If tube-fed flows and "immature" flows with eruption durations less than two days are omitted, then all of Malin's data fit within Walker's limits [*Pinkerton and Wilson*, 1988, 1992]. Flows that are volume-limited, tube-fed, channelled down preexisting depressions, or breached due to blockages in the main channel do not have lengths determined by effusion rate. However, Walker's relationship has been confirmed for all mature, channel-fed flows and can be used to predict flow length within a factor of 7 [*Pinkerton and Wilson*, 1992]. The relationship between flow length and effusion rate also has been supported by observations of channel-fed flows on Mount Etna [*Guest et al.*, 1987; *Kilburn and Lopes*, 1988].

Clearly this model is simplistic and its usage is limited to estimating order-of-magnitude values of effusion rate for those flows that are channel-fed. Effusion rate is only one significant factor among many that influence the final length of a channel-fed flow. Other factors include changes in the property of the lava downstream and at the source (e.g., changes in volatile content, amount of crystallization, viscosity, and yield strength) [*Guest et al.*, 1987; *Baloga and Pieri*, 1986] and variations in the amount of radiative cooling due to variations in the fraction of exposed core [*Crisp and Baloga*, 1990*a*,*b*]. None of these factors are addressed by *Walker*'s [1973] empirical model. Our use of it here is merely as a first-order estimate of effusion rate.

Although the relationship between flow length and effusion rate was documented for flows on the Earth, its application to flows on Venus should be valid as theoretical studies by *Head*

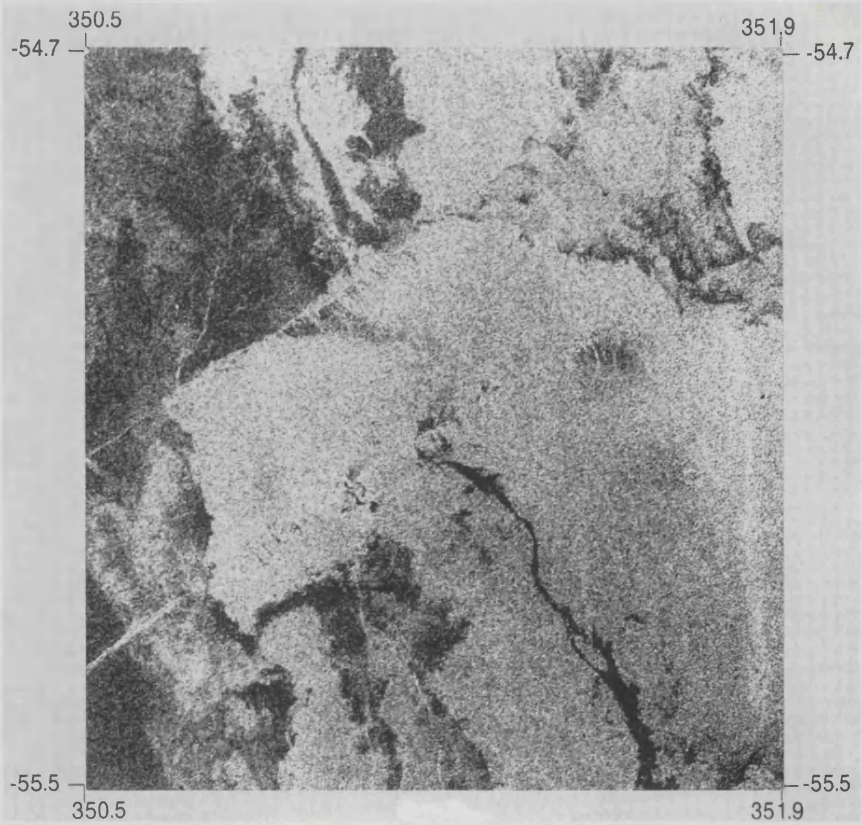

Fig. 11*a*. Magellan image of flows both superposed on and abutted against arcuate lineations mapped within Mylitta. The image is approximately 85 km across.

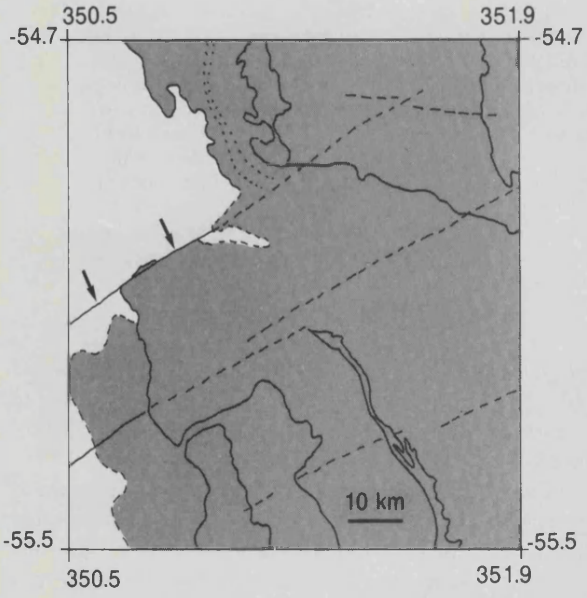

Fig. 11*b*. Sketch map of Figure 11*a*. Arrows indicate one lineation against which flows have stopped. These relations are used to estimate flow thickness as discussed in the text.

and Wilson [1986] have shown that no significant differences between lava flow morphologies on the two planets are expected unless there exist significant differences in lava rheology. The most significant differences for eruptions on Venus are (1) less cooling of magma in its final stage of ascent, (2) higher rates of convective cooling during only the first hour of emplacement, and (3) less exsolution of volatiles. These differences are due to the higher ambient temperature and greater atmospheric pressure of Venus and have been predicted to effect little change in the flow emplacement process as understood for Earth [*Head and Wilson*, 1986].

From the presence of abundant channels within Mylitta Fluctus (Figures 7, 13, and 14) we may infer that many flows were channel-fed and cooling-limited. Although analyses of flow surface texture are inconclusive, there is no strong evidence for tube-fed, compound pahoehoe flow fields within Mylitta (with the possible exception of flows within episode 5). As discussed above, the positive relationship between length and effusion rate published by *Walker* [1973] is thought to be valid for such flows, and we have attempted to estimate in a very preliminary fashion the eruption rates of flow fields within Mylitta by extrapolating the plot of flow length versus effusion rate to lengths of the order of 1000 km. The upper and lower bounds and the average trend of this plot were used to obtain minimum, intermediate, and maximum effusion rates. These estimates vary by about a factor of 8 or approximately one order of magnitude. By dividing the total volume of an individual episode (Tables 1 and 2) by the estimated effusion rate, estimates of eruption duration were calculated (Tables 4 and 5).

Estimates of effusion rate vary from about 460-4600 x 10^3 m^3/s for flows 900-1000 km long, to 12-70 x 10^3 m^3/s for flows 200 km long. The maximum rates listed in Tables 4 and 5, which exceed 6-23 x 10^6 m^3/s, correspond to eruption durations of less than 2 days and are not considered further. The estimated time of emplacement for flow field 1, using an estimate for effusion rate based on an average flow length of 200 km and a total volume as given in Table 1, is 10-70 years. As suggested earlier, the emplacement of this flow field occurred over a much longer time period than later flow fields.

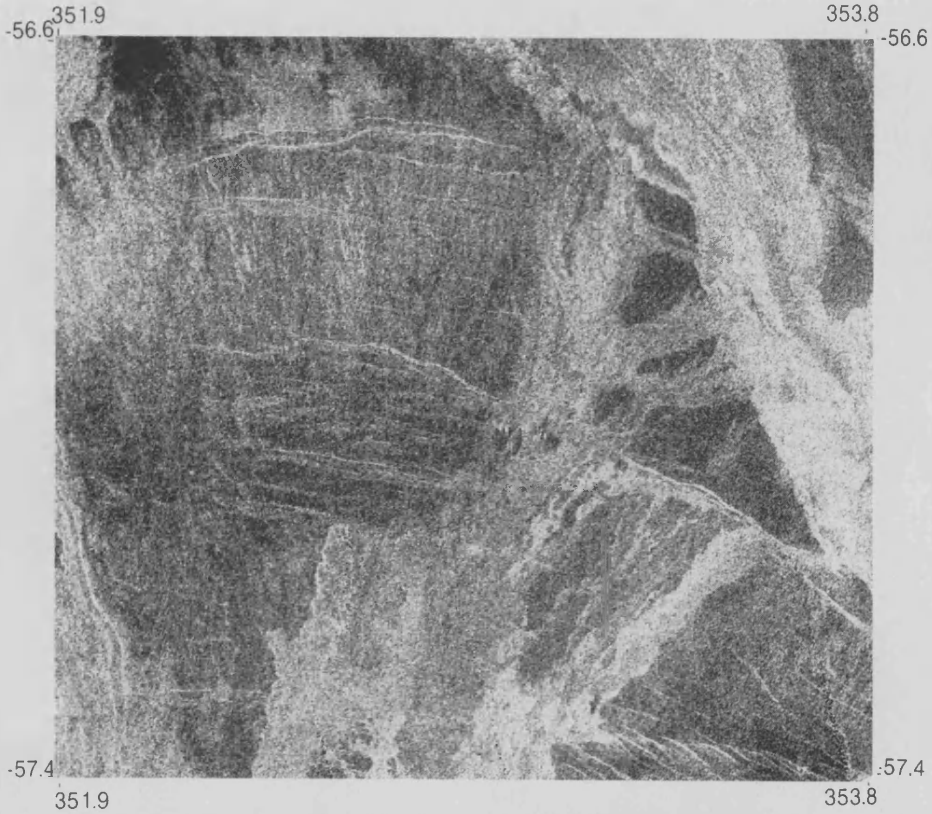

Fig. 12. Magellan image of arcuate lineations, most of which appear to be scarps or troughs, superposed on the flank of the shield. Flows from episode 6 superpose and abut against these structures. The image covers an area approximately 130 km wide.

However, this emplacement time is based on a single continuous eruption; it is most likely that the flows of episode 1 were emplaced over a much longer period during multiple eruptions. According to these calculations, the remaining flow fields were emplaced over a total period of 20-165 days. The emplacement of flow field 4 took from 5 to 35 days with the eruption of individual phases lasting from 15 hours to 5 days. These values are similar to those predicted by *Head and Wilson* [1986] for extensive flows in Venus lowlands. Their calculations were based on the model of lava flow morphology of *Hulme* [1974] and assumed values of slope (0.17°), lava density (2600 kg/m^3), yield strength (100 Pa), and viscosity (1500 Pa s). Flows 20-50 km wide and 350 to over 2300 km long were predicted to erupt at rates of 10^5-10^6 m^3/s over periods of 6-14 days. These estimates are similar to those listed in Table 5 for the individual phases of episode 4 and suggest that the rheological parameters assumed by *Head and Wilson* [1986] are appropriate for flows in Mylitta and that our simplistic approach to calculating effusion rate is valid as an order of magnitude estimate. We are currently examining more complex models of lava flow emplacement to more rigorously constrain effusion rates and eruption duration for flows within Mylitta.

Swanson et al. [1975] found that estimates of effusion rate and eruption duration for portions of the Roza Member of the Columbia River Basalt Group calculated from a cooling model compared favorably to those obtained by extrapolating the plot of length versus effusion rate presented by *Walker* [1973] in a manner similar to the one used above. The cooling unit examined from the Roza Member has an approximate volume of 700 km^3 and maximum lengths of 300 km. It was erupted from a fissure system 100 km long that was assumed to have been active along its entire length during eruption. The theoretical model used by *Shaw and Swanson* [1970] predicted an eruption duration of approximately 7 days and therefore an eruption rate of 100 km^3/d (1.2 x 10^6 m^3/s) for cooling units as voluminous as those in the Roza Member. From the extrapolation of Walker's plot, a maximum effusion rate of 1.5 x 10^6 m^3/s was estimated for this unit of the Roza Member from which was calculated an eruption duration of 5 days. These values are similar to those estimated from the cooling model and are also similar to the values estimated for Mylitta.

Are effusion rates of 10^5-10^6 m^3/s physically plausible? Unfortunately, there have been no documented observations of flood-type eruptions on the Earth so there are no direct measurements of effusion rates of this magnitude. However, during extensive geologic mapping of the Yakima Basalt Subgroup of the Columbia River Basalt province, *Wright et al.* [1989] observed flat upper flow surfaces and columnar jointing which they attributed to widespread ponding of flows, and similar crystallinities within samples of dikes and pillow basalts of the same flow unit separated by distances in excess of 100 km. On the basis of these observations, *Wright et al.* [1989] concluded that the emplacement of the voluminous Yakima basalts was "virtually instantaneous." In addition, there is no evidence of caldera collapse, discrete volcanic centers, or rhyolitic flows in the Yakima Basalt Subgroup, all of which are associated with basaltic provinces known to have shallow crustal magma reservoirs. These observations indicate that magma associated with these eruptions must have originated from deep crustal or subcrustal storage zones [*Wright et al.*, 1989]. Theoretical modeling of dike emplacement from deep magma reservoirs (through several tens of kilometers of brittle crust) indicate that there is no physical

Fig. 13*a*. Magellan image of channels in the medial and distal regions of Mylitta (episode 4).

Fig. 13*b*. Sketch map of Figure 13*a*. Bright flows are shaded in gray; the extremely mottled flow is shown in a speckled pattern. Channels are colored black or outlined with dashed and dotted lines. The stippled pattern maps the remnant tectonic belt near the western edge of the flow field.

reason that eruption rates as high or higher than 10^5-10^6 m^3/s could not occur; in fact, they appear to be necessary for the eruptions to occur at all (E. A. Parfitt and L. Wilson, personal communication, 1992).

Mylitta Fluctus is clearly associated with a caldera and shield edifice which would suggest the presence of a relatively shallow magma reservoir. However, the extensive flows that comprise the bulk of the fluctus postdate the shield edifice and may have originated from greater depths. Recent work by *Head and Wilson* [1992] has shown that the high atmospheric pressure on Venus hinders volatile exsolution and therefore inhibits the formation of neutral buoyancy zones at shallow levels within the crust. This effect is enhanced at low elevations on the planet due to the greater atmospheric pressure in these regions. Therefore, the presence of a deep magma storage zone is predicted for Mylitta, and high effusion rates appear highly plausible.

Much lower effusion rates of 30-60 m^3/s (1-2 km^3/yr) have been estimated for the Deccan, Parana, and Karroo flood basalt provinces [e.g., *Richards et al.*, 1989]. However, these rates were calculated on the assumption that eruptions occurred continuously over the entire age span of these basalts. It is more probable that the basalts were emplaced during a series of shorter lived pulses erupted at much higher effusion rates, perhaps similar to those described above. Recently, *Self et al.* [1991] have identified compound pahoehoe flow units within the Columbia River Basalt province and suggested that much lower effusion rates, associated with compound flow formation and the injection of lava into preexisting, cooler flow units (the "lava rise mechanism"), may have characterized at least a portion of the eruption of these basalts. This is certainly plausible and may be related to a decrease in effusion rate with time. As discussed previously, waning effusion rates appear to characterize the latter stages of the formation of Mylitta.

To summarize, the formation of Mylitta Fluctus appears to have been characterized by the effusive eruption of basaltic lavas at rates varying from 460 to 4600 x 10^3 m^3/s. The first episode produced an asymmetric shield along the rift zone and

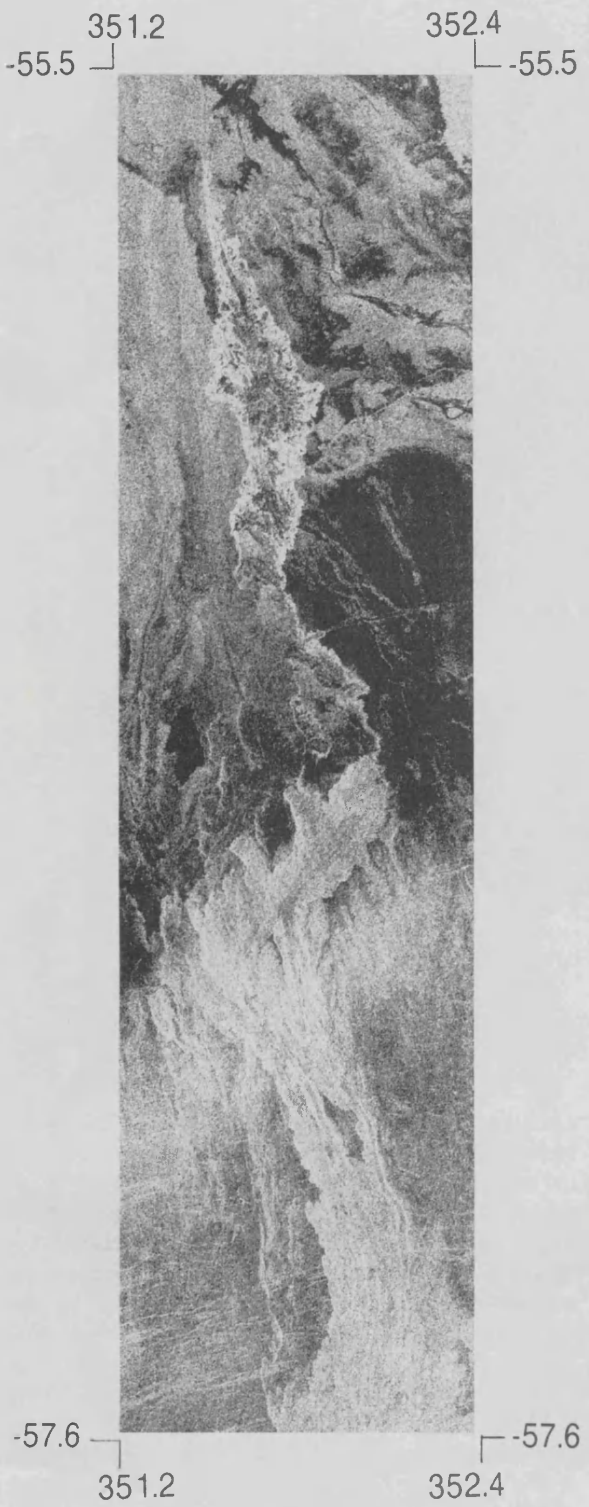

Fig 14*a*. Magellan image of a flow in the proximal region of Mylitta (episode 6) that exhibits extreme heterogeneity in surface brightness. The flow is relatively uniform in surface brightness and contains channels with distinct levees near the source. As it crosses the base of the shield (marked by arrows in Figure 14*b*) its surface texture becomes extremely mottled such that it appears to be rougher at the flow margins than in the flow interior. This roughness pattern may be due to an unusual form of channel and levee development. A similar morphology is exhibited by the mottled flow in Figure 13.

Fig. 14*b*. Sketch map of Figure 14*a*.

was emplaced over a much greater period of time than later flow fields. The subsequent episodes emplaced massive flows that flooded parts of Lavinia Planitia over a time period of several months. Individual flows were emplaced during eruptions that are estimated to have lasted of the order of days. These estimates are comparable to those obtained for a flow field of similar magnitude within the Roza Member of the Columbia River Basalt Group and are consistent with theoretical predictions made by *Head and Wilson* [1986] for extensive flows on Venus.

ORIGIN AND LINK TO TECTONIC ENVIRONMENT

The origin of Mylitta Fluctus is thought to be related to the processes of uplift and extension that characterize northern Lada Terra [*Roberts et al.*, 1991]. Volcanism associated with Mylitta was typified by eruptions of large volumes of fluid basaltic lavas that rapidly emplaced extensive flow fields with

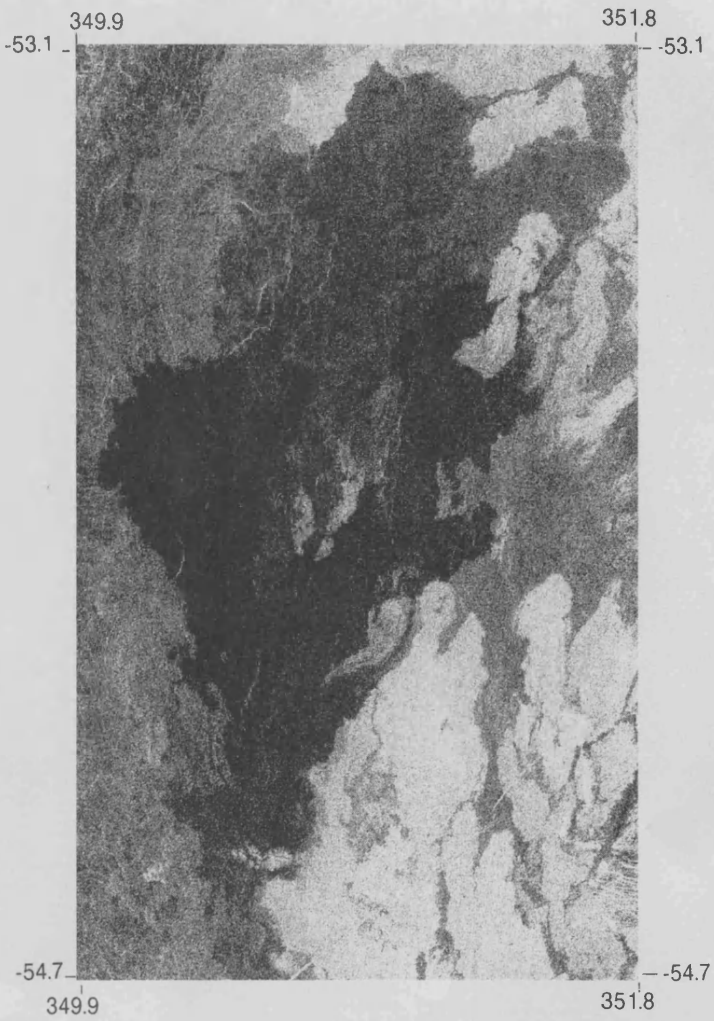

Fig 15. Magellan image of radar-dark flows within Mylitta (episode 3). The image is approximately 120 km across.

maximum areas of the order of 10^5 km^2. The extreme lengths of individual flows and the total area of Mylitta are of a scale similar to terrestrial flood basalt provinces (Tables 1-3). Recent studies have related the origin of terrestrial flood basalts to the initiation of mantle plumes [*Campbell et al.*, 1989; *Richards et al.*, 1989; *Campbell and Griffiths*, 1990] and the intersection of hotspots with spreading centers or continental rifts [*White and McKenzie*, 1989]. We propose that the origin of Mylitta and, possibly, the rifting along northern Lada Terra, is linked to large-scale mantle diapirism or hotspot activity. As Venusian mantle plumes are predicted to be 100-150°C hotter than terrestrial plumes, their associated melts are likely to be MgO-rich tholeiites and basaltic komatiites [*Hess and Head*, 1990]. The large volumes, high temperatures, and low viscosities of such plume-related melts easily could have produced the areally extensive flows of Mylitta.

The exact relationship between rifting and possible hotspot activity along northern Lada Terra is unclear. Several possibilities exist, including the intersection of a preexisting rift zone and a stable hotspot, the intersection of a preexisting rift zone and a plume head, and dynamic rifting caused by the impingement of a mantle plume against the lithosphere. The fact that the rift zone extends thousands of kilometers along the northern edge of Lada Terra beyond Mylitta indicates that extension probably was not initiated by any local mantle upwelling or hotspot in the region of Mylitta. This is also supported by the different morphologies exhibited by Mylitta and areas on Venus inferred to be related to hotspot activity and plume-initiated rifting such as Beta Regio, Western Eistla Regio, and Atla Regio. These regions are all characterized by broad domal uplifts and multiple radiating rift zones at the junctures of which are located large shield volcanoes that have been highly deformed as a result of continued extension along the rift zones [*Senske et al.*, this issue]. This is in contrast to the situation at Mylitta, where an asymmetric but relatively undeformed volcanic center sits on a single linear rift zone located at the edge of an extensive highland, not at the center of a domal uplift.

The presence of numerous volcanic centers along the rift zone, including the massive flow field of Mylitta and coronae 200-450 km in diameter, indicates that magmatic upwellings have occurred at various times along its length. The scale and spacing of these volcanic centers, however, suggest that each may be the result of individual plumes, possibly short-lived, rather than passive, intermittent upwellings of material due to lithospheric extension [e.g., *Stofan and Head*, 1990]. It is possible that these hotspots have directed, if not initiated, rifting along the northern edge of Lada Terra. The rift may have been emplaced between zones of thermally weakened lithosphere (due to the presence of local mantle plumes) when the region underwent subsequent extension. However, the vast

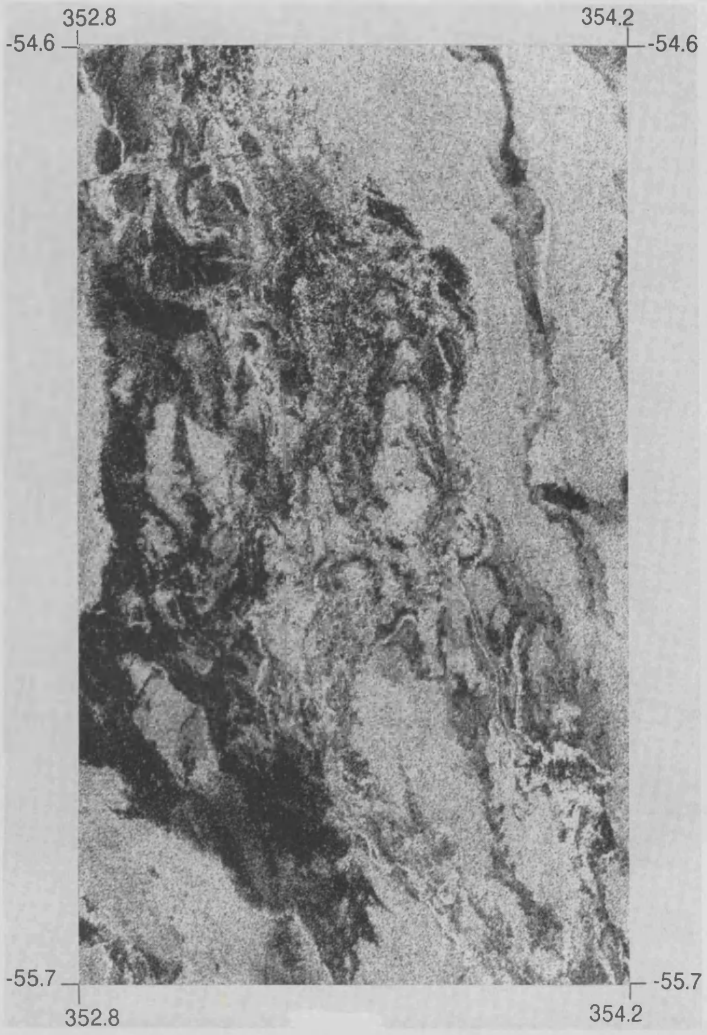

Fig. 16. Magellan image of mottled flows within central Mylitta (episode 5). This mottled texture is thought to be the result of overlapping flows of shorter length produced during the waning stages of episode 4. The image is approximately 80 km across.

majority of volcanism in Mylitta appears to postdate the onset of rifting in the region. In fact, there is little evidence for rifting of the source of Mylitta nor the crater Alcott, which has been extensively embayed by flows of Mylitta. Therefore, the proposed hotspot associated with the origin of Mylitta may be one of the youngest of the region (but older or shorter-lived than any hotspot associated with the corona Quetzalpetlatl). In addition, the fact that the total estimated volume of Mylitta is 1-2 orders of magnitude lower than the volumes of typical terrestrial flood basalts indicates that either the hotspot associated with the formation of Mylitta was smaller than those associated with terrestrial flood basalts or that the formation of Mylitta is not yet complete. These ideas will be tested in future studies by comparing the volume of Mylitta to that predicted by models of passive mantle upwelling along zones of extension and by examining the regional geology, topography, and age relationships of volcanic centers and rifting along the boundary between Lavinia Planitia and Lada Terra.

SUMMARY AND CONCLUSIONS

Mylitta Fluctus is an extensive complex of lava flows that covers over 300,000 km^2 in southern Lavinia Planitia. The flows are typically radar-bright with uniform surface textures and contain structures such as channels, levees, overflows, and lobate perimeters that are characteristic of lava flows observed on Earth and the other terrestrial planets. They appear to have originated from a single major source characterized by a caldera 40 km wide and an asymmetric shield approximately 200 km in radius that is located within a proposed tectonic rift zone along the northern edge of Lada Terra. There is no direct evidence of fissure-fed eruptions, although flows may have erupted from fractures within the rift zone before the main source centralized. Fissure vents may have been subsequently buried and are no longer discernible.

The emplacement of Mylitta occurred during six major eruptions of fluid basaltic lavas that produced individual flow fields up to 120,000 km^2 in area that are similar in scale to many terrestrial flood basalt provinces. Based on the relationship of effusion rate and flow length developed by *Walker* [1973], eruption rates are estimated to have been as high as 460-4600 x 10^3 m^3/s. From these values and estimates of flow volume, preliminary eruption durations have been calculated. The initial phase occurred over a minimum period of approximately 10-70 years and produced the greatest volume of lava (~1.7 x 10^4 km^3) that flooded the rift zone and built an asymmetric shield on the northern flank. Subsequent eruptions were characterized by flows of extensive length that

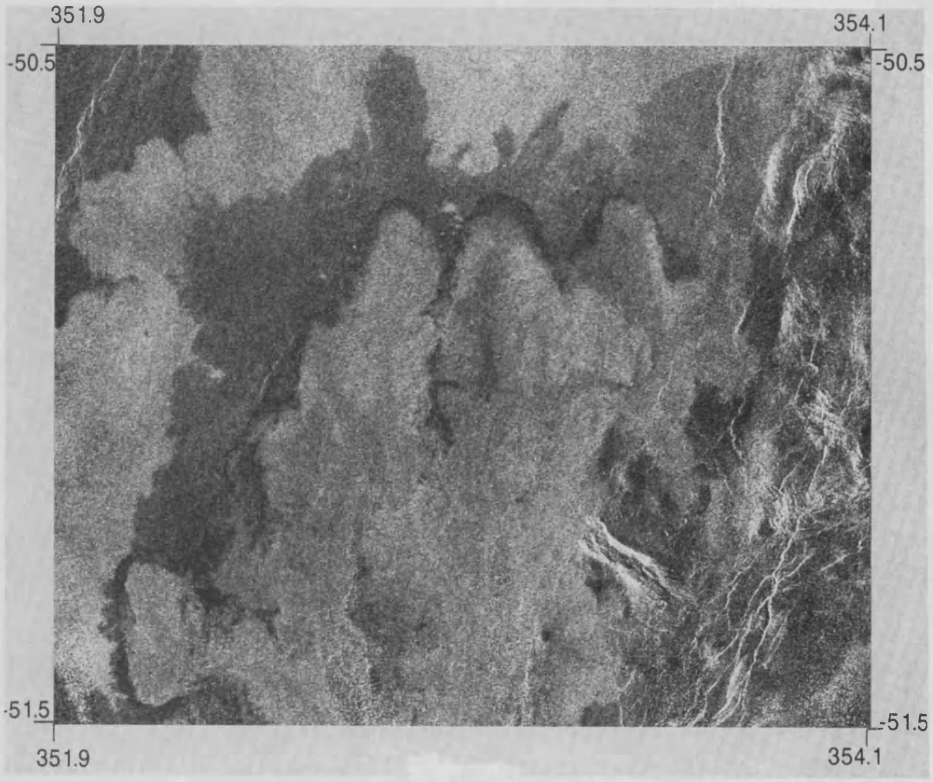

Fig. 17. Magellan image of a radar-bright flow with dark margins. Such margins are proposed to be the result of scouring and, possibly, redeposition of adjacent plains materials due to atmospheric interaction with the lava during flow emplacement. The image is approximately 145 km across.

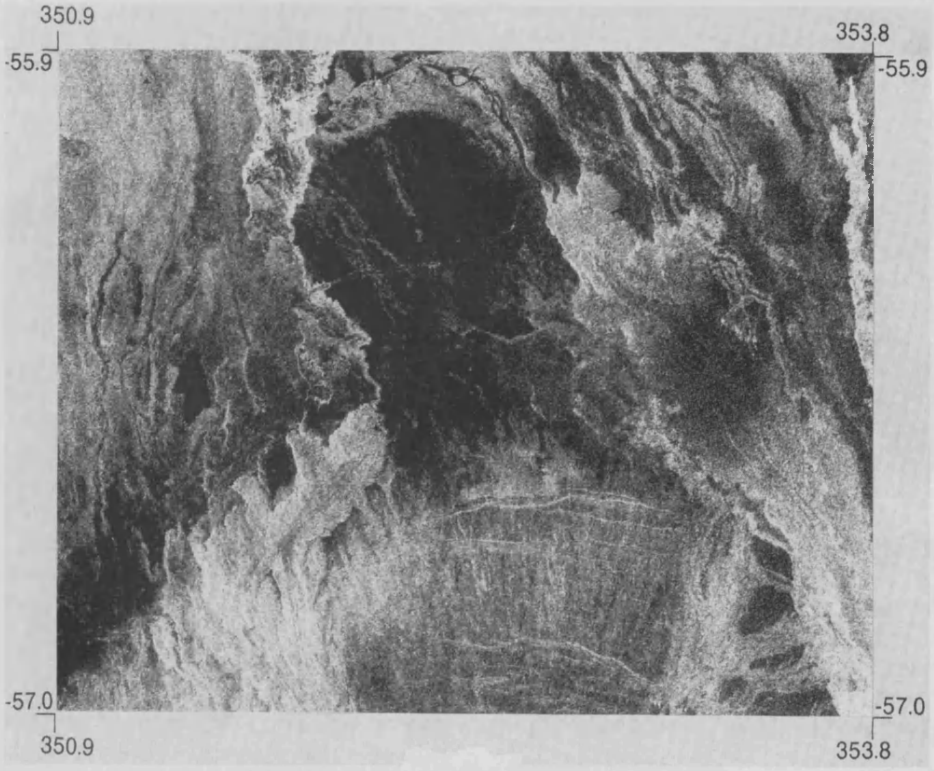

Fig. 18. Magellan image of diffuse, radar-dark deposits in the proximal region of Mylitta near the base of the shield. These deposits are thought to be superficial and windblown from more distant locations. The image is approximately 165 km across.

TABLE 4. Estimates of Effusion Rate and Eruption Duration

Episode	Flow Length,[a] km	Volume,[b] km^3	Effusion rate,[c] m^3/s	Duration
1	200	17,000	8.1×10^3	67 years
			7.0×10^4	8 years
			5.0×10^5	395 days
	400	17,000	4.6×10^4	12 years
			4.1×10^5	1 year
			3.0×10^6	66 days
2	1,000	623	6.0×10^5	12 days
			4.5×10^6	2 days
			3.0×10^7	6 hours
3	400	321	4.6×10^4	80 days
			4.1×10^5	9 days
			3.0×10^6	1 day
4	1,000	1,741	6.0×10^5	34 days
			4.5×10^6	5 days
			3.0×10^7	16 hours
5	600	79	1.5×10^5	6 days
			1.3×10^6	17 hours
			9.0×10^6	2 hours
6	400	162	4.6×10^4	41 days
			4.1×10^5	5 days
			3.0×10^6	15 hours
Roza Member Columbia River Basalt cooling unit[d]	300	700	2.3×10^4	350 days
			2.0×10^5	41 days
			1.5×10^6	5 days

[a] Lengths are rounded to nearest hundred from Table 1.

[b] Volumes are from Table 1.

[c] Eruption rates are extrapolated from a plot of length versus effusion rate as calculated by *Walker* [1973].

[d] *Swanson et al.* [1975].

produced the bulk of Mylitta away from the rift over a time period of several months. Individual flows within these episodes were emplaced during eruptions that are estimated to have lasted several days. Within Mylitta, flow fields were emplaced west to east and then back toward the west in response to changes in topographic slope produced by the emplacement of previous flow units. There is a general decrease in both surface area and estimated volume of each episode with time, although actual effusion rates are estimated to have been greatest during episodes 2-4, when the longest flows were emplaced. Values of eruption rate and duration estimated for episodes within Mylitta are similar to values determined for at least one flow unit of similar size and volume in the Columbia River Basalt Group [*Swanson et al.*, 1975]. They are also similar to theoretical values predicted for extensive flows on Venus by *Head and Wilson* [1986] based on a model of lava flow morphology [*Hulme*, 1974] and assumed values of lava density (2600 kg/m^3), yield strength (100 Pa), and viscosity (1500 Pa s). We are currently examining more complex models of flow emplacement to better constrain effusion rates and eruption durations for flows within Mylitta.

The total volume of Mylitta is approximately 2×10^4 km^3. The thickness of individual flows is estimated to be of the order of 10-30 m; maximum thicknesses of 200-400 m in the proximal portion of the flow field are the result of overlap in flow units. The total volume is 1-2 orders of magnitude less than estimated volumes of terrestrial flood basalts of similar area. Relative to terrestrial flood basalts, the formation of Mylitta appears to have been relatively short-lived (or is perhaps not yet complete) and did not produce the massive volumes of multiple flow layers observed in the Deccan, Karroo, and other large terrestrial basalt provinces.

In a manner similar to that suggested for the production of many terrestrial flood basalts, the origin of Mylitta is proposed to be the result of a large-scale mantle upwelling along a preexisting tectonic rift. Rifting is not thought to have been initiated by hotspot activity but may have been directed along zones of thermal weakness when the region,

TABLE 5. Eruption Rates and Durations for Episode 4 Phases

Phase	Length,[a] km	Volume,[b] km^3	Effusion rate,[c] m^3/s	Duration
A_1	500	59	9.3×10^4	7 days
			8.0×10^5	21 hours
			6.0×10^6	3 hours
A_2	1,000	216	6.0×10^5	4 days
			4.5×10^6	13 hours
			3.0×10^7	2 hours
B_1	900	205	5.0×10^5	5 days
			4.0×10^6	14 hours
			2.5×10^7	2 hours
B_2	800	166	3.0×10^5	6 days
			2.5×10^6	18 hours
			2.0×10^7	2 hours
B_3	600	79	1.5×10^5	6 days
			1.3×10^6	17 hours
			9.0×10^6	2 hours
C	600	46	1.5×10^5	4 days
			1.3×10^6	10 hours
			9.0×10^6	1 hour
D	800	72	3.0×10^5	3 days
			2.5×10^6	8 hours
			2.0×10^7	1 hour

[a]Lengths are rounded to the nearest hundred from Table 2.

[b]Volumes are from Table 2.

[c]Eruption rates are extrapolated from a plot of length versus effusion rate as calculated by *Walker* [1973].

characterized by multiple sites of mantle upwelling and possible hotspots, deformed under tension. We will test this hypothesis in a future study of the geology and age relationships of volcanic centers and rifting along the northern edge of Lada Terra.

Volcanism at Mylitta appears to postdate the onset of rifting and there is little evidence of continued rifting and subsequent deformation of the shield and related flows. In addition, the lower estimated volume of Mylitta relative to typical terrestrial flood basalts indicates either that the mantle plume associated with the formation of Mylitta was smaller than those associated with terrestrial flood basalts or that the formation of Mylitta is not yet finished. Thus, Mylitta may be one of the youngest sites of volcanism in the region. In fact, the lack of significant deformation of the shield along the rift zone and the bright, crisp flow outlines indicate that Mylitta may be a site of currently active volcanism. Only the presence of a possible "failed" impact scar suggests that flows within the Mylitta may be relatively old.

If indeed Mylitta Fluctus is a Venusian flood basalt, then examination of its flow characteristics and the characteristics of similar flow fields may yield new insight into the nature of terrestrial flood basalts as the lack of significant erosion on Venus [*Bindschadler and Head*, 1988; *Saunders et al.*, 1991] preserves surface features in relatively pristine states. Mylitta may represent the early stages of hotspot volcanism and flood basalt emplacement. Future studies of the character, distribution, age and tectonic environment of similar large flow fields should provide information on the evolution of hotspot-related volcanism and its modification by regional crustal structure.

Acknowledgments. We gratefully acknowledge funding provided by the NASA Magellan project (grant 957088) and the William F. Marlar Memorial Foundation (J. W. H. and K. M. R.) and the UK Natural Environment Research Council (J. E. G. and M. G. L.). Elisabeth Parfitt and Lionel Wilson provided helpful discussions of several aspects of this work. Constructive reviews were provided by Stephen Baloga and Charles Wood. Thanks are also extended to Peter Nievert for photographic assistance.

REFERENCES

Arvidson, R. E., R. Greeley, M. Malin, R. S. Saunders, N. Izenberg, J. J. Plaut, M. Shepard, and E. Stofan, Surface modification of Venus as inferred from Magellan observations of plains, *J. Geophys. Res.*, this issue.

Baker, V. R., G. Komatsu, T. J. Parker, V. C. Gulick, J. S. Kargel, and J. S. Lewis, Channels and valleys on Venus: Preliminary analysis of Magellan data, *J. Geophys. Res.*, this issue.

Baloga, S. and D. Pieri, Time-dependent profiles of lava flows, *J. Geophys. Res., 91*, 9543-9552, 1986.

Basaltic Volcanism Study Project (BVSP), *Basaltic Volcanism on the Terrestrial Planets*, 1286 pp., Pergamon, New York, 1981.

Beurlen, K., *Geologie von Brasilien*, 427 pp., Borntraeger, Berlin, 1970.

Bindschadler, D. L., and J. W. Head, Diffuse scattering of radar on the surface of Venus: Origin and implications for the distribution of soils, *Earth Moon Planets, 42*, 133-149, 1988.

Bruno, B. C., G. J. Taylor, S. K. Rowland, P. G. Lucey, and S. Self, Lava flows are fractals, *Geophys. Res. Lett., 19*, 305-308, 1992*a*.

Bruno, B. C., G. J. Taylor, S. K. Rowland, P. G. Lucey, and S. Self, Fractal analysis: a new remote sensing tool for lava flows (abstract), *Lunar Planet. Sci., XXIII*, 171-172, 1992*b*.

Campbell, B. A. and D. B. Campbell, Comparison of 1988 Arecibo radar images of Western Eistla Regio, Venus, and multipolarization airborne radar images of terrestrial terrains (abstract), *Lunar Planet. Sci., XXII*, 175-176, 1991.

Campbell, B. A., and D. B. Campbell, Analysis of volcanic surface morphology on Venus from comparison of Arecibo, Magellan, and terrestrial airborne radar data, *J. Geophys. Res.*, this issue.

Campbell, D. B., D. A. Senske, J. W. Head, A. A. Hine, and P. C. Fisher, Venus southern hemisphere: Character and age of terrains in the Themis-Alpha-Lada region, *Science, 251*, 180-183, 1991.

Campbell, I. H. and R. W. Griffiths, Implications of mantle plume structure for the evolution of flood basalts, *Earth Planet. Sci. Lett., 99*, 79-93, 1990.

Campbell, I. H., R. W. Griffiths, and R. I. Hill, Melting in an Archean mantle plume: Heads it's basalts, tails it's komatiites, *Nature, 339*, 697-699, 1989.

Chester, D. K., A. M. Duncan, J. E. Guest, and C. R. J. Kilburn, *Mount Etna, The Anatomy of a Volcano*, 404 pp., Stanford University Press, Stanford, Calif., 1985.

Cox, K. G., The Karroo volcanic cycle, *J. Geol. Soc. London, 128*, 311-336, 1972.

Crisp, J., and S. Baloga, A model for lava flows with two thermal components, *J. Geophys. Res., 95*, 1255-1270, 1990*a*.

Crisp, J., and S. Baloga, A method for estimating eruption rates of planetary lava flows, Icarus, 85, 512-515, 1990*b*.

Frank, S. L., and S. W. Squyres, Ridge belts in Lavinia Planitia, Venus: Description and sequence of events (abstract), *Lunar Planet. Sci., XXII*, 407-408, 1991.

Gaddis, L., P. Mouginis-Mark, R. Singer, and V. Kaupp, Geologic analyses of shuttle imaging radar (SIR-B) data of Kilauea Volcano, Hawaii, *Geol. Soc. Am. Bull., 101*, 317-332, 1989.

Ghose, N. C., Chemical characteristics of some basaltic rocks of India, *Bull. Volcanol., 35*, 1022-1036, 1972.

Greeley, R. and J. S. King (Eds.),Volcanism of the Eastern Snake River Plain, Idaho, NASA Contract Report CR-154621, 308 pp., NASA, Washington, D. C., 1977.

Green, J. C., North Shore Volcanic Group, in *Geology of Minnesota: A Centennial Volume* , edited by P. K. Sims and G. B. Morey, pp. 2940-332, Minnesota Geological Survey, St. Paul, 1972.

Gregg, T. K. P., and R. Greeley, Formational constraints on Venusian "canali" (abstract), *Lunar Planet. Sci., XXIII*, 449-450, 1992.

Guest, J. E., C. R. J. Kilburn, H. Pinkerton, and A. M. Duncan, The evolution of lava flow-fields: Observations of the 1981 and 1983 eruptions of Mount Etna, Sicily, *Bull. Volcanol., 49*, 527-540, 1987.

Head, J. W., and L. Wilson, Volcanic processes and landforms on Venus: Theory, predictions and observations, *J. Geophys. Res., 91*, 9407-9446, 1986.

Head, J. W., and L. Wilson, Magma reservoirs and neutral buoyancy zones on Venus: implications for the formation and evolution of volcanic landforms, *J. Geophys. Res., 97*, 3877-3903, 1992.

Head, J. W., D. B. Campbell, C. Elachi, J. E. Guest, D. P. McKenzie, R. S. Saunders, G. G. Schaber, and G. Schubert, Venus volcanism: Initial analysis from Magellan data, *Science, 252*, 276-288, 1991.

Hess, P. C. and J. W. Head, Derivation of primary magmas and melting of crustal materials on Venus: Some preliminary considerations, *Earth Moon Planets, 50/51*, 57-80, 1990.

Hulme, G., The interpretation of lava flow morphology, *Geophys. J. R. Astron. Soc., 39*, 361-383, 1974.

Kilburn, C. R. J., and R. M. C. Lopes, The growth of aa flow fields on Mount Etna, Sicily, *J. Geophys. Res., 93*, 14,759-14,772, 1988.

Leinz, V., A. Bartorelli, G. R. Sadowski, and C. A. L. Isotta, Sobre o comportamento espacial do trapp basaltico da bacia do Parana, *Bol. Soc. Bras. Geol., 15*, 79-81, 1966.

Lopes, R. M. C. and C. R. J. Kilburn, Emplacement of lava flow fields: Application of terrestrial studies to Alba Patera, Mars, *J. Geophys. Res., 95*, 14,383-14,397, 1990.

Maack, R. Die Entwicklung der Gondwana-Schichten Suedbrasiliens und ihre Beziehungen zur Karru-Formation Suedafrikas, International Geological Congress 19, Algiers, Sympos. sur les Series de Gondwana, pp. 339-372, 1952.

Malin, M. C., Lengths of Hawaiian lava flows, *Geology, 8*, 306-308, 1980.

Moore, H. J., J. J. Plaut, P. M. Schenk, and J. W. Head, An unusual volcano on Venus, *J. Geophys. Res.*, this issue.

Nalivkin, D. U., *Geology of the U. S. S. R.*, translated by N. Rast, 855 pp., Oliver and Boyd, Edinburgh, 1973.

Pettengill, G. H., P. G. Ford, W. T. K. Johnson, R. K. Raney, and L. A. Soderblom, Magellan: Radar performance and data products, *Science, 252*, 260-265, 1991.

Phillips, R. J., R. E. Arvidson, J. M. Boyce, D. B. Campbell, J. E. Guest, G. G. Schaber, and L. A. Soderblom, Impact craters on Venus: Initial analysis from Magellan, *Science, 252*, 288-297, 1991.

Pieri, D. C. and S. M. Baloga, Eruption rate, area, and length relationships for some Hawaiian lava flows, *J. Volcanol Geotherm. Res., 30*, 29-45, 1986.

Pinkerton, H., and L. Wilson, The lengths of lava flows (abstract), *Lunar Planet. Sci., XIX*, 937-938, 1988.

Pinkerton, H., and L. Wilson, The dynamics of channel-fed lava flows (abstract), *Lunar Planet. Sci. XXIII*, 1083-1084, 1992.

Reidel, S. P., T. L. Tolan, P. R. Hooper, M. H. Beeson, K. R. Fecht, R. D. Bentley, and J. L. Anderson, The Grande Ronde Basalt, Columbia River Basalt Group: Stratigraphic descriptions and correlations in Washington, Oregon, and Idaho, in Volcanism and Tectonism in the Columbia River Flood Basalt Province, edited by S. P. Reidel and P. R. Hooper, *Geol. Soc. Amer. Spec. Pap. 239*, 21-53, 1989.

Richards, M. A., R. A. Duncan, and V. E. Courtillot, Flood basalts and hot-spot tracks: Plume heads and tails, *Science, 246*, 103-107, 1989.

Roberts, K. M., J. W. Head, and J. E. Guest, Mylitta Fluctus, Venus: Flow characteristics and sources (abstract), *Lunar Planet. Sci., XXII*, 1121-1122, 1991.

Rowland, S. K. and G. P. L. Walker, Pahoehoe and aa in Hawaii: Volumetric flow rate controls the lava structure, *Bull. Volcanol., 52*, 615-628, 1990.

Saunders, R. S., R. E. Arvidson, J. W. Head, G. G. Schaber, E. R. Stofan, and S. C. Solomon, An overview of Venus geology, *Science, 252*, 249-252, 1991.

Schaber, G. G. Eratosthenian volcanism in Mare Imbrium: Source of the youngest lava, in Apollo 17 Preliminary Science Report, *NASA Spec. Publ. SP-330*, 30.17-30.21, 1973*a*.

Schaber, G. G., Lava flows in Mare Imbrium: Geologic evidence from Apollo orbital photography, *Proc. Lunar Sci. Conf., 4th*, 73-92, 1973*b*.

Schaber, G. G., Volcanism on Venus as inferred from the morphometry of large shields, *Proc. Lunar Planet. Sci. Conf., 21*, 3-11, 1991.

Self, S., S. Finnemore, T. Thordarson, and G. P. L. Walker, Importance of compound lava and lava-rise mechanism in emplacement of flood basalts (abstract), *Trans. AGU, 72*, 566-567, 1991.

Senske, D., D. Campbell, J. Head, P. Fisher, A. deCharon, S. Frank, S. Keddie, K. Roberts, E. Stofan, J. Aubele, L. Crumpler, and N. Stacy, Geology and tectonics of the Themis Regio-Lavinia Planitia-Alpha Regio-Lada Terra area, Venus: Results from Arecibo image data, *Earth Moon Planets, 55*, 97-161, 1991.

Senske, D. A., J. W. Head, G. G. Schaber, and E. R. Stofan, Regional topographic rises on Venus: Geology of Western Eistla Regio and comparison to Beta Regio and Atla Regio, *J. Geophys. Res.*, this issue.

Shaw, H. R., and D. A. Swanson, Eruption and flow rates of flood basalts, in Proc. Second Columbia River Basalt Symposium, edited by E. H. Gilmour and D. Stradling, pp. 271-299, Cheney, Eastern Washington State Coll. Press, 1970.

Solomon, S. C., J. W. Head, W. M. Kaula, D. McKenzie, B. Parsons, R. J. Phillips, G. Schubert, and M. Talwani, Venus tectonics: Initial analysis from Magellan, *Science, 252*, 297-312, 1991.

Squyres, S. W., S. L. Frank, G. E. McGill, D. McKenzie, B. E. Parsons, and S. C. Solomon, Tectonic evolution of Lavinia Planitia, Venus (abstract), *Lunar Planet. Sci., XXII*, 1309-1310, 1991.

Stofan, E. R. and J. W. Head, Coronae of Mnemosyne Regio: Morphology and origin, *Icarus, 83*, 216-243, 1990.

Sukeswala, R. N. and A. Poldervaart, Deccan basalts of the Bombay area, India, *Geol. Soc. Am. Bull., 69*, 1475-1494, 1958.

Swanson, D. A., Yakima basalt of the Teiton River area, south-central Washington, *Geol. Soc. Am. Bull., 78*, 1077-1110, 1967.

Swanson, D. A., T. L. Wright, and R. T. Helz, Linear vent systems and estimated rates of magma production and eruption for the Yakima basalt on the Columbia River Plateau, *Am. J. Sci., 275*, 1975.

Theilig, E., S. Wall, and R. S. Saunders, Radar interpretation of lava fields as a function of incidence angle: Implications for interpretation of Magellan SAR data of Venus, *Proc. Lunar Planet. Sci. Conf., 19th*, 323-333, 1989.

Tolan, T. L., S. P. Reidel, M. H. Beeson, J. L. Anderson, K. R. Fecht, and D. A. Swanson, Revisions to the estimates of the areal extent and volume of the Columbia River Basalt Group, in Volcanism and Tectonism in the Columbia River Flood Basalt Province, edited by S. P. Reidel and P. R. Hooper, *Spec. Pap. Geol. Soc. Am. 239*, 1-20, 1989.

Walker, G. P. L., Lengths of lava flows, *Philos. Trans. R. Soc. London, Ser. A, 274*, 107-118, 1973.

White, R. and D. McKenzie, Magmatism at rift zones: The generation of volcanic continental margins and flood basalts, *J. Geophys. Res., 94*, 7685-7729, 1989.

Whitford-Stark, J., and L. Wilson, Atmospheric motions produced by hot lava, *Weather, 31*, 25-27, 1976.

Wright, T. L., M. Mangan, and D. Swanson, Chemical data for flows and feeder dikes of the Yakima Basalt Subgroup, Columbia River Basalt Group, Washington, Oregon, and Idaho, and their bearing on a petrogenetic model, *U.S. Geol. Surv Bull., 1821*, 71 pp., 1989.

J. E. Guest and M. G. Lancaster, University of London, Observatory, University College London, Mill Hill Park, London, NW7 2QS, England.

J. W. Head and K. Magee Roberts, Department of Geological Sciences, Brown University, Providence, RI 02912.

(Received October 15, 1991;
revised May 14, 1992;
accepted June 2, 1992.)